Composites manufacturing by injection of reactive thermoplastic resin in a fibrous preform

William Han

Université Fédérale
Toulouse Midi-Pyrénées

THÈSE

En vue de l'obtention du

DOCTORAT DE L'UNIVERSITÉ DE TOULOUSE

délivré par

IMT – École Nationale Supérieure des Mines d'Albi-Carmaux

présentée et soutenue par

William HAN

le 17 mai 2022

Titre :

Composites manufacturing by injection of reactive thermoplastic resin in a fibrous preform

École doctorale et discipline ou spécialité :

MEGEP : Génie Mécanique, Mécanique des Matériaux

Unité de recherche :

Institut Clément Ader, UMR CNRS 5312, IMT Mines Albi

Directeurs de thèse :

Fabrice SCHMIDT, Professeur, IMT Mines Albi

Arthur CANTAREL, Maître de Conférences, IUT de Tarbes - Université Toulouse III

Autres membres du jury :

Jöel BRÉARD, Professeur, Université de Caen Normandie, Rapporteur

Gilles AUSIAS, Maître de Conférences, Université Bretagne Sud, Rapporteur

Vincent SOBOTKA, Professeur, Université de Nantes, Président

Conchúr Ó BRÁDAIGH, Professor, University of Edinburgh, Examinateur

France CHABERT, Maître de Conférences, ENI de Tarbes, Examinatrice

Quentin GOVIGNON, Maître-assistant, IMT Mines Albi, Examinateur

Philippe OLIVIER, Professeur, IUT Paul Sabatier - Université Toulouse III, Invité

Cédric SAMUEL, Maître-assistant, IMT Nord Europe, Invité

Remerciements

Cette thèse a été réalisée au laboratoire de l'Institut Clément Ader de l'IMT Mines Albi. Je voudrais donc remercier les directeurs successifs du centre Thierry Cutard et Thierry Sentenac pour leur accueil. Je remercie aussi la région Occitanie et IMT Mines Albi pour avoir co-financé ces recherches.

Je souhaite exprimer ma sincère gratitude envers mes directeurs et encadrants de thèses, Fabrice Schmidt, Arthur Cantarel et Quentin Govignon, pour leur accompagnement, leur disponibilité, leur conseils précieux ainsi que pour la confiance qu'ils m'ont accordée au long de ces années.

Je tiens à remercier les membres du jury, Joël Bréard, Gilles Ausias, Vincent Sobotka, Conchúr Ó Brádaigh, France Chabert, Phillipe Olivier et Cédric Samuel pour m'avoir fait l'honneur d'examiner mon travail, ainsi que pour les remarques et discussions enrichissantes qui ont suivies la soutenance.

Je voudrais adresser des remerciements supplémentaires à Cédric Samuel au centre TPCIM à Douai, ainsi qu'à Etienne Roussel à Thermo Fischer Scientific à Courtaboeuf pour m'avoir permis de réaliser des essais sur leur rhéomètre respectif.

Je souhaite adresser ma reconnaissance à l'ensemble des enseignants-chercheurs et techniciens de l'ICA-A pour leur assistance au fil des années, que ce soit scientifiquement ou pour la réalisation des essais. Merci aussi à Esther, Cathy, Christel, ainsi qu'au bureau des doctorants et au centre de documentation, qui m'ont permis d'aborder sereinement tous les aléas administratifs qui ont pu survenir durant ces années, de mes déplacements jusqu'à la soutenance.

J'aimerais ensuite dédier ce paragraphe afin de remercier les collègues de l'ICA-A doctorants et docteurs, ingénieurs de recherche, et stagiaires que j'ai côtoyé et avec qui il y avait toujours une bonne ambiance. J'ai une pensée particulière à tous mes anciens collègues du bureau 1M15, avec qui j'ai passé de très bons moments.

Je souhaite finalement remercier mes amis de toujours, ainsi que ma famille, ma mère en particulier pour son soutien sans faille, et mon frère.

Un dernier mot pour les personnes lisant ces lignes. Je vous remercie pour votre intérêt, en espérant que vous trouverez ce que vous y cherchiez, dans ce document ou ailleurs.

Table of contents

Résumé long en français

Introduction

Les matériaux composites ont une popularité grandissante dans l'industrie car ils offrent la possibilité d'obtenir des propriétés mécaniques spécifiques inaccessibles pour les matériaux plus conventionnels. Un type de matériau composite inclut les matériaux (alors appelés « matrices ») renforcés par des fibres. Les matériaux polymères sont un choix populaire pour constituer les matrices de composites renforcés par des fibres grâce à leur poids et leur polyvalence. Notamment, les thermoplastiques intéressent car contrairement aux thermodurcissables, ils peuvent être refondus. Cependant, à cause de leur viscosité élevée à l'état fondu [1], ils sont difficilement utilisables dans des procédés de fabrication par voie liquide comme le moulage par transfert de résine (procédé RTM, voir Figure 2).

Or, ces derniers sont très intéressants pour industrialiser la production de pièces composites. Ainsi, pour fabriquer des composites à matrices thermoplastiques, des résines de faible viscosité ont été conçues afin de les employer dans le procédé TP-RTM (moulage par transfert de résine thermoplastique). Cela implique d'utiliser des mélanges réactifs permettant de polymériser la matrice in-situ [8-11], ou d'utiliser une résine spécialement conçue pour être peu visqueuse [12,13]. Dans les travaux de thèse de Vicard [14], un mélange réactif synthétisant le polyamide 6 (PA6) a été étudié (voir Figure 3). À l'aide de mesures par calorimétrie différentielle (DSC), Vicard et al. [15,16] ont montré le lien ténu entre polymérisation et cristallisation. Un modèle permettant de décrire l'exothermie de la synthèse en situation isotherme leur a permis de produire un diagramme Temps-Transformation-Température (TTT) (Figure 4).

En outre, la présence d'une préforme fibreuse lors de l'injection d'une résine réactive va affecter le remplissage. Notamment, si la préforme est de type tressé ou « non-crimp », les mèches sont alors organisées régulièrement et forment un milieu poreux double-échelle [17,18]. En général, les forces visqueuses dominent l'écoulement durant le procédé et les mèches imprègnent durant un laps de temps beaucoup plus long que le remplissage des espaces inter-mèches (Figure 6). Ce phénomène affecte les propriétés du composite fabriqué, car non seulement des bulles vont être formées, mais l'imprégnation non uniforme du domaine implique que la réaction de la résine sera aussi non uniforme dans le domaine.

Objectifs et structure de la thèse

L'objectif de cette thèse est d'étendre la compréhension via une simulation de l'injection d'un mélange réactif de PA6 dans une préforme fibreuse pour la fabrication de composite, à partir

des travaux de Vicard [14]. Pour ce faire, les phénomènes susmentionnés, l'écoulement double-échelle et la réaction exothermique de la synthèse du PA6 doivent être modélisés et testés expérimentalement.

Par conséquent, le manuscrit est divisé en trois chapitres. Chaque chapitre commence par une partie bibliographique concernant le volet concerné des travaux de thèse. Le premier chapitre traite de la simulation de l'écoulement double échelle dans OpenFOAM®, d'abord dans des configurations géométriques simples puis dans un textile numérisé, qui a été partagé gracieusement par Wijaya et son équipe de l'université de Auckland, Nouvelle-Zélande [21].

Dans le deuxième chapitre, les DSC effectuées par Vicard [14] sont réétudiées et un nouveau modèle, adaptable selon la variabilité expérimentale, et décrivant la synthèse du PA6 permettant de faciliter son calcul numérique est proposé. A partir d'essais rhéologiques réalisés respectivement à Thermo Fischer Scientific à Courtaboeuf, et au TPCIM (*Technologie des polymères et composites & ingénierie mécanique*, IMT Nord Europe, Douai), un modèle rhéocinétique est aussi proposé.

Le dernier chapitre se concentre sur les problématiques entourant la simulation du procédé incluant réaction, température et écoulement. L'intégration du modèle de synthèse et en particulier de la cristallisation non-isotherme est discutée. Une simulation intégrant cette synthèse pour le remplissage de résine est présentée, avant de donner des éléments pour confronter une simulation d'injection dans une préforme fibreuse avec un essai expérimental.

Une conclusion termine le manuscrit, commentant les travaux réalisés et ceux à approfondir.

Chapitre 1 : Simulation de l'écoulement dans une préforme fibreuse

Pour contrôler les procédés de fabrication de composites par voie liquide, l'effet de la présence de la préforme sur l'écoulement doit être pris en compte. La première approche est d'utiliser la loi de Darcy [23], applicable à l'échelle macroscopique, et dans laquelle la préforme est caractérisée par son tenseur de perméabilité. Cependant, une telle modélisation ne permet pas de prendre en compte l'écoulement double-échelle se déroulant dans la préforme, capable d'influer sur les propriétés finales du composite. Comme la représentation à l'échelle microscopique de la totalité des fibres de la préforme est virtuellement infaisable dans l'état actuel des capacités de calculs, l'utilisation d'un volume élémentaire représentatif (REV) à l'échelle mésoscopique est une solution alternative intéressante. C'est un cadre intermédiaire (voir schématisation des échelles dans la Figure 1.1), qui permet d'observer l'écoulement à l'échelle des mèches de fibres.

1.1 Modélisation de l'écoulement dans une préforme fibreuse

En moyennant les propriétés géométriques et hydrauliques de la préforme fibreuse, une vitesse moyenne est définie (équation 1.1), avec laquelle la loi de Darcy (équation 1.2, [23]) permet de calculer le gradient de pression. Cependant, caractériser l'écoulement dans une préforme fibreuse avec une double échelle de porosité cause une perte d'informations

importantes sur l'écoulement, comme le montrent la non-adéquation des différents modèles analytiques développés pour prédire la perméabilité d'une préforme [33,34]. Avec les défis causés par la standardisation des essais de perméabilité [29-31], des techniques numériques ont été étudiées afin d'aider à la compréhension de la caractérisation de la perméabilité. Elles se basent sur l'utilisation d'un REV à l'échelle mésoscopique, déterminé en isolant un motif caractéristique des mèches de la préforme. La numérisation du motif textile peut se faire avec des outils logiciels de conception tels que WiseTex [35] ou TexGen [36], ou en utilisant des méthodes d'imagerie 3D comme la tomographie rayon X [37].

Une fois le REV obtenu, il existe trois approches principales (Figure 1.4) pour y modéliser l'écoulement. La plus simple utilise l'équation de Stokes (équation 1.7) et considère que la mèche peut être considérée imperméable. Cependant, l'information sur l'écoulement dans la mèche est perdue dans ce cas. Pour s'intéresser à l'écoulement dans la mèche, il faut distinguer le comportement inter-mèche de type Stokes du comportement intra-mèche de type Darcy. Cela peut se faire en utilisant une équation de type Brinkman (équation 1.8, [43]), ou en couplant les équations de Stokes et Darcy avec la condition limite de Beaver, Joseph et Saffman (équation 1.11, [40-42]). Ces deux dernières méthodes ont été utilisées pour la détermination de la perméabilité de textiles par simulation numérique [34,51-54].

Enfin, à la modélisation de l'écoulement doit s'ajouter la modélisation de la saturation pour simuler le remplissage. En général, le terme de saturation, dépendant du volume de fibre (équation 1.12) est utilisé pour suivre le remplissage. Une perméabilité insaturée peut alors être définie, dépendant de la perméabilité saturée et de la saturation (équation 1.13, [45]). Une alternative au paramètre de saturation est l'utilisation d'un terme puits (équation 1.15). Cette méthode permet de distinguer le remplissage intra-mèche et inter-mèche sans avoir à définir la géométrie des mèches [26,64,67]. La détermination expérimentale de ce terme puits est alors importante. Par exemple, Imbert et al. [67] propose un terme plus complexe, combinant un comportement source et puits, et qui correspondrait plus précisément aux observations expérimentales de remplissage de préformes.

1.2 Tests pour la simulation de la perméabilité saturée

Les simulations sont effectuées avec la boîte à outils open-source de calcul de fluide numérique OpenFOAM® v8 [55] qui utilise la méthode des volumes finis (FVM). Elle inclut une implémentation de l'équation de Navier-Stokes-Brinkman (équation 1.16). La méthode pour son couplage avec l'équation de continuité est présentée dans les équations 1.17 à 1.21 [72-74]. Ces équations décrivent les étapes de l'algorithme présenté Figure 1.5. Pour tester la performance de l'implémentation, des tests ont été effectués avec des géométries simples d'agencement de cylindres (Figure 1.6 et Figure 1.7), qui ont été l'objet de solutions analytiques déterminées par Gebart (Table 1.1, [32]) avec des hypothèses d'écoulement Darcien dans une cellule de Hele-Shaw [75]. Dans la littérature, les cylindres modélisent généralement des fibres imperméables, mais dans cette étude, ils représenteront des mèches de perméabilité variable.

Les premiers tests sont simulés suivant la géométrie présentée Figure 1.8, où un écoulement se fait dans des mèches cylindriques perméables en configuration hexagonale transverse, avec

les paramètres de la Table 1.2. Les résultats sont présentés Figure 1.9, où la perméabilité effective du domaine, calculée en fonction de la perméabilité des mèches à partir de l'équation 1.22, est comparée avec la perméabilité analytique imperméable correspondante de Gebart. Plus la perméabilité des mèches est faible, plus la perméabilité effective déterminée par la simulation se rapproche de la valeur analytique. Le fort écart dans ce cas est expliqué par la mauvaise qualité de la géométrie.

Ensuite, une géométrie plus simple a été simulée avec une seule mèche cylindrique modélisant un arrangement quadratique transverse. Trois cas sont étudiés : le cas d'une mèche imperméable (voir Figure 1.11, Figure 1.12 et Table 1.4 pour les conditions limites, la géométrie et le maillage), le cas d'une mèche quasi imperméable, (voir Figure 1.14 et Figure 1.15) et le cas d'une mèche perméable (voir Figure 1.19 et Figure 1.20). Le maillage est cette fois réalisé de manière conforme au cylindre. Cela permet d'obtenir des résultats plus proches de la valeur analytique de Gebart dans le cas imperméable lorsque le maillage est suffisamment fin (voir la courbe de l'erreur relative en fonction du nombre d'éléments Figure 1.13). Dans le cas quasi imperméable, un maillage suffisamment fin permet de converger quasiment à la même valeur que dans le cas imperméable (Figure 1.18). Cependant, dans le cas perméable, la représentation de la perméabilité simulée en fonction du nombre d'éléments (Figure 1.20) montre que le maillage influe peu sur la valeur de la perméabilité effective.

1.3 Simulation dans une géométrie réaliste

Des simulations ont été réalisés sur une géométrie numérisée de textile tressée de fibres de verres, transmise gracieusement par Wilsen Wijaya de l'université d'Auckland en Nouvelle-Zélande (Figure 1.21). A partir de la densité linéique de la mèche et de la surface des mèches, la fraction volumique de fibre (FVF) est déterminée dans chaque voxel de la géométrie, et la perméabilité correspondante de Gebart a été calculée ([21], voir Figure 1.24 représentant la FVF dans la géométrie). Cela a permis d'attribuer des perméabilités moyennes aux mèches de trame et de chaîne (équation 1.25). Des mesures expérimentales sur la perméabilité du textile ont été effectuées par Wijaya [21] (Table 1.10). Ces mesures peuvent être comparées avec une simulation saturée en calculant la perméabilité effective du domaine. Dans un premier temps, la simulation est effectuée avec des mèches imperméable (voir conditions limites Figure 1.26). Les résultats présentés Figure 1.27 ne permettent pas de retrouver la valeur expérimentale. Une raison probable de cette différence se trouve dans la dissymétrie des canaux observés entre les mèches de chaîne et de trame dans la section normale à la direction de l'écoulement. En effet, en comparant la Figure 1.28 avec la Figure 1.29, on remarque que pour la surface normale à la direction de trame, l'espace entre les mèches est bien plus conséquent que pour la surface normale à la direction de chaîne. Ensuite, des simulations avec des mèches perméables et utilisant l'équation 1.26 ont permis de retrouver des résultats similaires à la simulation imperméable, due à la faible perméabilité des mèches. Finalement, un exemple de simulation de remplissage du domaine utilisant l'équation 1.27 avec la géométrie réaliste est présenté (Figure 1.35, Figure 1.36 et Figure 1.37).

Chapitre 2 : Modélisation de la synthèse du PA6 réactif

L'objectif de la modélisation est de prédire la durée et l'exothermie de la réaction, ainsi que les caractéristiques du polymère synthétisé. À cause des fortes interactions entre la polymérisation et la cristallisation, dont les phénomènes peuvent se chevaucher durant la synthèse, la stratégie de modélisation revêt une importance particulière. Une nouvelle méthode de modélisation est proposée et permet de remédier aux difficultés de calculer le modèle de Vicard et al. [16] dans un domaine 3D, et une étude préliminaire de la rhéologie du mélange réactif est effectuée.

2.1 État de l'art de la modélisation de la synthèse anionique du PA6

Différents paramètres sont établis pour décrire les caractéristiques de la synthèse. Notamment, la fraction massique de polymère et la cristallinité sont respectivement distincts du degré de polymérisation et du degré de cristallisation (équations 2.1 et 2.2). Dans l'équation 2.3, la vitesse de polymérisation et de cristallisation sont définis à partir de leurs flux respectifs de chaleur. Le flux de la synthèse φ_s est généralement mesuré par DSC [15,92], et il est considéré comme la somme de ceux de la polymérisation φ_p et de la cristallisation φ_c (équation 2.6).

La dépendance de la cristallisation sur la polymérisation est simple à visualiser, vu que la cristallisation se fait à partir de chaînes polymériques (Figure 2.1). La dépendance inverse a été aussi considérée [87], mais son effet a été majoritairement négligé dans la littérature. Cette dépendance, ainsi que la possible simultanéité des deux phénomènes a rendu nécessaire de les séparer sur les mesures DSC.

Pour pouvoir séparer ces phénomènes dans le cas où ils sont simultanés, deux méthodes ont été utilisées dans la littérature. La première suppose que les flux de chaleur de la polymérisation et de la cristallisation suivent chacun une courbe gaussienne [92,95,96]. La seconde se base sur la caractérisation d'un des phénomènes dans des conditions où il se déroule seul (généralement la polymérisation), ce qui permet d'obtenir le comportement de l'autre phénomène par soustraction [16,91,97-99].

Pour pouvoir soustraire l'effet de la polymérisation au reste de la synthèse, il faut modéliser l'avancée de la polymérisation. En général des modèles semi-empiriques basés sur la loi d'Arrhenius sont utilisés (équation 2.8). Les modèles utilisés récemment pour la polymérisation du PA6 incluent Malkin et Camargo (équation 2.10, [14,101-104]) et Kamal-Sourour (équation 2.11, [91,105]). Ces modèles pondèrent la loi d'Arrhenius avec la quantité non polymérisée de monomère et y ajoutent un effet auto-catalysant des chaînes polymérisées. Le modèle de Kamal-Sourour ajoute à l'autocatalyse un comportement non-linéaire et dépendant de la température, mais son utilisation n'a pas forcément montré d'amélioration significative de la description de la cinétique [14,106].

Une fois effectuée la soustraction de l'effet de polymérisation, des hypothèses doivent être faites sur le flux restant attribué à la cristallisation. Pour pouvoir y calquer des modèles provenant d'études sur la cristallisation isolée de la polymérisation, le modèle de couplage

doit prendre en compte l'influence des chaînes nouvellement polymérisées. La méthode décrite par Bolgov et Malkin (équation 2.15, [97,98]) n'ayant pas donné de résultats satisfaisants dans l'étude effectuée par Vicard et al. [16], ces derniers ont adapté le couplage de Hillier [108] pour conjuguer les effets de la polymérisation et de cristallisation (équations 2.16, 2.17, 2.18, 2.19 et 2.20). La cristallisation, dont la cinétique a été déterminée de manière séparée à partir de PA6 déjà polymérisé suit alors le modèle de Nakamura (équation 2.24) avec une dépendance en température de type Hoffman-Lauritzen (équation 2.22).

2.2 Modélisation isotherme initiale de la synthèse

Dans l'étude effectuée par Vicard et al. [14-16], le mélange réactif utilisé est décrit Table 2.1, avec une proportion de catalyste et d'activateur de 0,79/1,10mol.% du monomère. Les propriétés du PA6 et de sa synthèse y avaient été déterminées à l'aide de mesures DSC, d'analyse thermogravimétrique (TGA) (voir Table 2.2) et les paramètres des modèles avaient été déterminés avec des méthodes de minimisation numérique. Les paramètres présentés Table 2.3 et Table 2.4 pour les modèles de polymérisation et cristallisation ont été retenus pour la suite de l'étude.

2.3 Etude du couplage entre la polymérisation et cristallisation et nouvelle méthode

La faible variation du taux de polymérisation massique ($\overline{X_p^\infty} = 94.2 \pm 1.4\%$, [15]) rend possible de l'approximer comme une constante indépendante de la cristallisation. Cependant, il est probable que la cristallisation affecte le taux de conversion à petite échelle (Figure 2.4, [2,87,94]). Ainsi, la complexité du couplage est causée par la fenêtre temporelle différente de la polymérisation et de la cristallisation, comme le montre la Figure 2.5 où les temps caractéristiques ont été calculés avec les équations 2.18, 2.30 et 2.31. La cinétique de cristallisation est virtuellement instantanée comparée à celle de polymérisation en dessous de 423 K. Néanmoins, elle devient de plus en plus longue si la température est plus élevée, et au-dessus de 455 K, le temps caractéristique de la cinétique de cristallisation dépasse celui de la polymérisation. Cela explique pourquoi les modèles simples de couplage (équations 2.33, 2.34 et 2.36) ne permettent pas de décrire le comportement du flux de chaleur mesuré par DSC (voir les exemples de comparaisons des flux de chaleurs expérimentaux et simulés sur la Figure 2.6 et la Figure 2.7). En effet, ces couplages ne prennent pas en compte la temporalité très différente des deux phénomènes.

En outre, la méthode proposée par Vicard et al. [16] est difficile à discrétiser (voir section 3.2). Par conséquent, une nouvelle méthode est proposée, dont le principe est de calculer la cinétique de cristallisation en considérant uniquement la fraction polymérisée, à l'aide du degré local de cristallisation (équation 2.38). En modifiant le modèle de Nakamura afin que la vitesse de cristallisation soit pondérée en fonction de la quantité polymérisée (équations 2.39, 2.40), la Figure 2.8 comparant le nouveau modèle à l'expérimental prouve la performance de la méthode par rapport aux modèles simples. La Figure 2.9 montre une comparaison

graphique de l'estimation de la cristallisation entre Hillier-Vicard et la nouvelle méthode et la Figure 2.10 montre leurs degrés de corrélation selon la température. Ces figures démontrent les résultats très similaires des modèles, malgré la différence d'interprétation avec la méthode de Hillier et Vicard, qui considère la cinétique de cristallisation comme la somme des cristallisations prise individuellement de chaque quantité infinitésimale de chaînes polymérisées. Enfin, l'ajout du facteur de diffusion (équation 2.41) permet d'affiner la quantité de chaînes polymérisées disponible à la cristallisation, et améliore nettement la performance du modèle (voir comparaison avec une mesure expérimentale dans la Figure 2.11).

2.4 Optimisation du modèle de synthèse du PA6

Cette section reprend partiellement l'optimisation du modèle de synthèse décrite dans l'article "*Efficient polymerization and crystallization kinetics coupling of polyamide 6 synthesis for liquid composite molding process modeling"* publié dans *Polymer Engineering and Science* en 2022.

Comme une forte variabilité sur la durée de la synthèse a été observée à chaque isotherme (voir l'exemple à 433 K sur la Figure 2.12), une étude a été effectuée pour appréhender ses conséquences. Sur la Table 2.6, il peut être observé que la variabilité sur la durée de synthèse n'entraîne pas une variabilité de la même magnitude sur l'enthalpie totale de réaction. En outre, la Figure 2.12 montre une forme similaire pour chaque courbe de mesures DSC. Dès alors, l'hypothèse choisie a été que la variabilité sur les courbes DSC découle d'une variabilité sur la vitesse de polymérisation, avec la cristallisation affectée uniquement par le changement de quantité de chaînes polymères disponibles dans le temps.

Pour contrôler cette variabilité, l'étude s'est portée en particulier sur le paramètre autocatalytique B_0, pour deux raisons. La première est une performance légèrement meilleure lors de l'optimisation du paramètre pour décrire les courbes expérimentales (voir exemple Figure 2.13). La deuxième raison est d'investiguer la présence d'une éventuelle thermo-dépendance du paramètre, qui aurait éventuellement échappée à l'étude de Vicard et al. [16], et qui aurait permis de confirmer l'étude de Teuwen et al. [91] (qui avait favorisé le modèle de Kamal-Sourour). Une polymérisation initiale et un temps d'initiation de la polymérisation ont été rajouté à l'équation de polymérisation (équation 2.42), dont l'objectif est de corriger d'éventuelles erreur sur les hypothèses concernant l'initiation de la polymérisation, et sur la préparation des courbes de mesures DSC.

L'optimisation s'est alors faite avec une méthode différente selon l'emplacement du pic de cristallisation sur la mesure DSC. La méthode d'optimisation est décrite
Figure 2.14, et a été réalisée sur chaque mesure afin d'obtenir les paramètres moyens des paramètres optimisés (Table 2.7 et Table 2.8), dont le comportement est comparé aux DSC les plus lentes et les plus rapides mesurées aux isothermes 413 K, 433 K et 453 K dans la Figure 2.27.

2.5 Rhéocinétique de la synthèse du PA6

Pour modéliser la rhéocinétique du PA6 réactif, deux paramètres sont importants, la température et les caractéristiques de la synthèse. Dans la littérature, pour modéliser

l'influence de la température, la viscosité du monomère a généralement été caractérisée par une loi d'Arrhenius (équation 2.49, [90,126]). La polymérisation et éventuellement la cristallisation étaient ensuite ajoutés suivant une loi exponentielle (équations 2.50 et 2.51, [14,90,126]), ou suivant une loi de type Castro et Macosko (équation 2.52, [96,127]).

Plusieurs essais de rhéologie à disques parallèles ont été effectués en plus de ceux réalisés par Vicard [14] afin d'affiner l'évaluation de la faible viscosité initiale du mélange réactif. Ils ont ensuite été étudiés pour comprendre le comportement rhéologique du mélange réactif. Les différentes conditions des essais sont détaillées Table 2.9, et la phase de de montée en température en fonction du temps est montrée Figure 2.18. Le mode rotationnel est utilisé pour les basses viscosités (< 0.1 ou 1 Pa s), avant de passer au mode oscillatoire lorsque le rhéomètre le permettait. La viscosité complexe est alors interprétée en utilisant la relation de Cox-Merz (équation 2.53). La Figure 2.20 montre l'allure de la montée de la viscosité à 453 K. De nombreux problèmes ont été observés lors des mesures. La Figure 2.23 montre notamment la porosité finale des échantillons, qui ont pu être causés par le débordement du mélange réactif hors de la zone d'essai (Figure 2.21) ou par son évaporation (Figure 2.22). En outre, le stockage des échantillons à vide dans des sacs de polyuréthane s'est révélé être un choix non optimal car les essais provenant de ces échantillons ont présenté un comportement dégradé (voir les courbes de viscosité en fonction du temps selon le stockage de l'échantillon dans la Figure 2.24).

Néanmoins, certains éléments pour modéliser le comportement en viscosité du mélange réactif ont été proposés. Tout d'abord, comme un temps d'induction a été observé avant le début de la montée en viscosité des échantillons, une loi d'Arrhenius a été déterminée pour la dépendance de la viscosité initiale en température (équation 2.55, Figure 2.25). Une loi exponentielle est proposée pour la dépendance en polymérisation (équation 2.56), de manière similaire à ce qui a été réalisé dans la littérature [90,126] car elle est capable de décrire correctement la montée en viscosité sur des mesures où la cristallisation ne s'initie quasiment pas (à 473 K, voir Figure 2.26). Dans le cas où la cristallisation affecte la viscosité, la méthode présentées équations 2.57 à 2.61 proposent une modélisation dépendant non pas des degrés de polymérisation et de cristallisation, mais de leur proportion massique respective. Le modèle empirique de Hieber et al. [130] a été choisi pour modéliser la dépendance en viscosité à la cristallinité. La Figure 2.27 comparant le modèle proposé de viscosité aux mesures expérimentales à 443 K et 453 K montre ses performances prometteuses.

Chapitre 3 : Simulation du procédé de fabrication de composites PA6 renforcés par des fibres

Dans ce chapitre, l'objectif est de combiner les études des deux chapitres précédents afin de proposer une simulation du procédé capable de prédire l'interaction de la synthèse du PA6 et de l'écoulement de la résine dans une préforme fibreuse. Un banc d'essai pour tester une telle simulation est aussi présenté.

3.1 Méthodes de simulation pour les procédés voies liquides

La méthode la plus utilisée pour simuler les procédés voies liquides est la méthode CVFEM (méthode des éléments finis avec volumes de contrôles, [24,135-139]). L'alternative principale est la méthode FVM (méthode des volumes finis, [148-151]). En général, la méthode CVFEM ou FVM est alors couplée avec une méthode de suivi de l'interface. Les principales sont la méthode VOF (volume de fluide, équation 3.1, [141]), « level set » (équation 3.2, [157-161]) et « phase-field » (équation 3.3, [162,163]).

Le couplage de l'écoulement de résine avec les paramètres décrivant la réaction non-isotherme se fait généralement en calculant dans l'espace l'équation de transport pertinente (équation 3.4) après les équations dirigeant l'écoulement [67,148,149,167].

3.2 Simulation non-isotherme de la synthèse de la cinétique de cristallisation

Pour effectuer la simulation non-isotherme de la synthèse de la cinétique de cristallisation, le calcul de la synthèse et de la température doit s'ajouter au calcul de la pression et de la vélocité. Par conséquent, la procédure présentée dans la Figure 3.2 est considérée, qui ajoute notamment le calcul du flux de chaleur de la synthèse (équation 3.8) et l'équation de transfert de la chaleur (équation 3.6).

Pour pouvoir calculer le flux de la synthèse, il faut avoir celui de la polymérisation et de la cristallisation. L'équation 3.9 permet de calculer le taux de polymérisation et d'arriver au flux correspondant. Cependant, la dépendance en température de la cristallinité (Table 2.2, équation 3.12) oblige de coupler le degré de cristallisation avec la variation de température. Cette étude propose de réaliser ce couplage en utilisant la procédure décrite dans la Figure 3.3. Le degré de cristallisation y est alors mis à jour à chaque itération temporelle (équation 3.16) afin de pouvoir appliquer le modèle de cristallisation du chapitre 2. Le suivi réel de la cristallisation durant la synthèse non-isotherme se fait alors par l'enthalpie de cristallisation, considérée comme directement proportionnelle à la cristallinité.

Dans le chapitre 2, un nouveau modèle de cristallisation couplé (équation 2.40) a été présenté comme une alternative à celui de Vicard et al. [16] (équation 2.16). C'est pourquoi, pour la simulation de la cristallisation du PA6 par la méthode des volumes finis, ce nouveau modèle a été retenu sous la forme de l'équation 3.27, car aucune discrétisation satisfaisante n'a été trouvée pour l'intégrale de convolution nécessaire au calcul du modèle de Hillier-Vicard. Les équations 3.28 et 3.29 sont alors calculées afin de suivre la quantité disponible de polymère à la cristallisation, en suivant la procédure de la Figure 3.4.

Enfin, les propriétés du mélange réactif varient en fonction de la température, et avaient été compilées par Teuwen [170]. Comme les simulations sont faites avec une hypothèse d'incompressibilité des fluides, la masse volumique du mélange réactif et du PA6 sont supposés égales et constantes (fixés à 1000 kg m^{-3}), bien que ce ne soit pas le cas en réalité. Pour la capacité thermique massique et la conductivité thermique, une loi des mélanges entre les différentes phases du mélange en cours de réaction est effectuée (équations 3.30 et 3.31).

3.3 Comparaison avec des mesures de DSC non-isotherme

La méthode de simulation non-isotherme de la synthèse a été testée en la comparant aux DSC de synthèses à vitesse de chauffe constante du PA6 effectuées par Vicard et al. [15] (voir Figure 3.5). La Figure 3.6 montre que la simulation non-isotherme arrive à prédire raisonnablement bien l'enthalpie de synthèse, et donc la cristallinité finale à chaque vitesse de chauffe sauf à 5 K/min, où la simulation prédit un comportement avec deux pics de flux de chaleur qui a été observé une seule fois expérimentalement. Cependant, la Figure 3.7 montre que la courbe simulée ne reproduit pas complètement le comportement expérimental. En observant quelques cas particuliers sur la Figure 3.9, l'hypothèse d'une avance de la synthèse simulée par rapport à la réalité est probable. Cela pourrait s'expliquer par l'inertie en température des mesures DSC, non prise en compte dans la simulation. En revanche, il semble peu probable que ce décalage soit la preuve d'un temps d'initiation de la réaction, car dans le cas échéant l'accélération de la polymérisation avec l'augmentation de la température aurait rattrapé le retard, et donc la forme des courbes ne serait pas conservée.

3.4 Simulation de l'injection réactive

Cette section reprend la simulation réactive de remplissage présentée dans l'article "*Efficient polymerization and crystallization kinetics coupling of polyamide 6 synthesis for liquid composite molding process modeling"* publié dans *Polymer Engineering and Science* en 2022.

Une simulation de remplissage où la résine suit le modèle du PA6 réactif a été réalisée en condition adiabatique. La procédure de la simulation suit la Figure 3.10, intégrant le calcul de la synthèse à une simulation d'écoulement biphasique. La résine est injectée à 413 K, et les autres paramètres de la simulation sont présentés dans la Figure 3.11 et dans la Table 3.4. Les résultats montrent qu'en condition adiabatique, l'exothermie de la réaction augmente la température du domaine, ce qui cause en fin de simulation, une cristallinité inférieure à celle qui est attendue d'après les mesures DSC à 413 K (Figure 3.14). En outre, le remplissage imparfait ainsi que la différence de température entre les bords et le centre du domaine mènent à une cristallinité pas complètement uniforme dans le domaine (voir Figure 3.15).

3.5 Éléments pour la confrontation expérimentale de la simulation

Dans le but de confirmer la pertinence de la simulation, ses résultats doivent être confrontés expérimentalement. Un dispositif expérimental est proposé pour permettre cette confrontation. Un moule a été réalisé suivant la géométrie décrite Figure 3.16. Le domaine d'injection est formé par deux couches de silicone vulcanisée, bloqués entre un bâti en aluminium et une plaque de verre trempée afin de pouvoir observer le front d'injection (Figure 3.17).

Une injection test y a été réalisée avec de l'eau dans un textile tressé de fibres de verre, dont les propriétés ont été extensivement caractérisée [30,31,171]. Le domaine d'injection est chauffé grâce à une table chauffante, le front a été enregistré à l'aide d'une caméra CCD et la

température a été mesurée à plusieurs points du domaine d'injection à l'aide de thermocouples (Figure 3.20, Figure 3.21 et Figure 3.22). Une simulation non-isotherme de l'injection de l'eau a été réalisée pour la comparer aux résultats expérimentaux. L'équation de la chaleur a été modifiée afin de prendre en compte la présence des fibres (équation 3.32). Les comparaisons entre la simulation et les mesures expérimentales ont montré des résultats prometteurs (voir Figure 3.31 pour la comparaison des fronts, et Figure 3.32 pour la comparaison des températures), et la simulation de la synthèse Figure 3.33 montre l'inhomogénéité de la cristallisation qu'on peut obtenir dans des conditions d'essai. Cependant, une injection avec le mélange réactif doit être réalisé pour confronter ces observations.

Conclusion

Pour améliorer la compréhension de la fabrication de composites thermoplastiques par voie liquide réactive, à la suite de travaux déjà réalisé à l'institut Clément Ader [14-16], une étude sur la simulation du procédé d'injection de résine réactive dans une préforme fibreuse est réalisée.

Des simulations d'écoulement en milieu fibreux ont été testé avec des géométries basiques et une géométrie réelle. En utilisant sur OpenFOAM® l'équation de Navier-Stokes-Brinkman, il a été observé que l'influence de la perméabilité de la mèche dépend de sa valeur comparée à la perméabilité de la géométrie imperméable. Sur la géométrie réaliste [21], les résultats simulés ont montré l'importance de la présence des canaux inter-mèches selon la direction de l'écoulement.

Ensuite, l'objectif a été d'améliorer la compréhension de l'interaction entre la polymérisation et la cristallisation lors de la synthèse du PA6 à l'aide des mesures de flux de chaleur. L'étude de ces phénomènes a permis d'établir une nouvelle méthode de coupler la modélisation des deux phénomènes, et d'évaluer sa pertinence. Une étude de la rhéologie du mélange réactif pendant la synthèse du PA6 a aussi été réalisé. Les mesures ont permis de proposer des éléments de modélisation de la rhéocinétique concernant la température, la polymérisation et la cristallinité.

Le modèle a alors été intégré pour pouvoir effectuer des simulations d'injections incluant le calcul de la polymérisation et de la cristallisation. Une procédure de résolution mettant à jour le degré de cristallisation en fonction de l'enthalpie de cristallisation et de la température a été mise au point et testé par comparaison avec des mesures DSC réalisées précédemment [15], et a permis la mise en place d'une simulation non-isotherme d'injection de résine réactive. Un banc d'essai expérimental est alors proposé, et a permis de tester une simulation d'injection d'eau dans une préforme fibreuse en condition non-isotherme.

Cependant, de nombreux points doivent être approfondis. Pour la simulation dans un textile, l'influence de la perméabilité des mèches, de leur géométrie et de leur fraction volumique dans le domaine devront être étudiés. En outre, l'influence de la tension de surface de la résine sur le phénomène de capillarité doit être étudié. La simulation à l'échelle mésoscopique pourra être utilisée pour alimenter des modèles moins gourmands en ressources calcul.

L'approfondissement de l'étude de la synthèse devra elle se porter sur les mécanismes d'initiation de la polymérisation et de la cristallisation, qui pourraient permettre de déterminer les paramètres des modèles en ayant moins recours à l'optimisation numérique. La variabilité de la cinétique devra aussi être mieux comprise et maîtrisée. De nouveaux essais rhéologiques où les causes de variabilités sont maîtrisées pourraient alors permettre d'obtenir un modèle rhéocinétique plus rigoureux.

Enfin, la procédure de simulation couplant la synthèse et l'écoulement fibreux devra être réalisée, permettant à une comparaison avec une injection expérimentale du mélange réactif de parachever cette étude.

Nomenclature

Abbreviations

LCM	Liquid Composite Moulding
RTM	Resin Transfer Moulding
TP-RTM	Thermoplastic Resin Transfer Moulding
PA6	Polyamide 6
APA6	Anionically polymerized PA6
DSC	Differential Scanning Calorimetry
FVF	Fibre Volume Fraction
REV	Representative Elementary Volume
CFD	Computational Fluid Dynamics
FVM	Finite Volume Method
VOF	Volume Of Fluid
SD	Standard deviation
Tc	Thermocouple

Character ornaments

$y_{i\in\{p,c,s\}}$	Parameter y relative to polymerization (p), crystallization (c) or the whole synthesis (s)
$y_{i\in\{r,g\}}$	Parameter y relative to the reactive mix phase (r) or the air phase (g)
y^{∞}	Parameter y at the end of a synthesis
$\dot{y}$	Rate of parameter y with regards to time during PA6 synthesis
$\bar{y}$	Volume averaged parameter y in porous media simulation
$\boldsymbol{y}$	Vector
$\boldsymbol{Y}$	Tensor

Flow simulation parameters

$\boldsymbol{u}$	Velocity vector
p	Pressure
ρ	Fluid density
η	Fluid dynamic viscosity
t	Simulation time
δt	Time step
δl	Element characteristic length

t_n	Simulation time at the n-th time step

Darcy equation parameters

$\overline{\boldsymbol{u}}$	Averaged velocity vector
V_f	Fibre volume fraction
$\tilde{\varepsilon}$	Porosity
$\boldsymbol{K}$	Permeability tensor

Heat equation parameters

$\dot{q}$	Heat equation source term
c_p	Mixed specific heat capacity
κ	Mixed thermal conductivity

Volume of Fluid parameters

$\boldsymbol{u_r}, \boldsymbol{u_g}$	Resin, gas velocity vector
α_r, α_g	Resin, gas saturation (volume fraction phase if there is only fluids)

Synthesis model parameters

R	Ideal gas constant
T	Temperature
H	Heaviside function
$\tilde{\varepsilon}$	Porosity

Reaction monitoring parameters

$\varphi_{i\in\{p,c,s\}}$	Heat flux of polymerization, crystallization, or the whole synthesis [W g^{-1}]
$X_{i\in\{p,c\}}$	Mass ratio of converted polymer or crystallinity
$\Delta H^{\infty}_{i\in\{p,c\}}$	Total polymerization or crystallization enthalpy [J g^{-1}]
$\Delta H_c^{100\%}$	Theoretical crystallization enthalpy for 100% crystallinity [J g^{-1}]
Q	Reaction enthalpy [J g^{-1}]
Q_{tot}	Total reaction enthalpy [J g^{-1}]
$t_{50\%}$	Half-time of the synthesis [s]
a	Degree of polymerization progress
b	Global degree of crystallization progress
β	Local degree of crystallization progress

Synthesis model parameters

A_p	Pre-exponential factor
E_a	Activation energy

B_0	Autocatalytic factor
n_p	Polymerization reaction order
K_N	Nakamura global kinetic constant
n_c	Avrami exponent representative crystals nucleation and growth
U^*	Activation energy of macromolecular motion in the molten state
K_0	Constant relative to molecular mass
K_g	Constant relative to crystallization growth
T_∞	Limit temperature for macromolecular motion
T_m^0	Equilibrium crystal melting temperature
$t_{c,0}$	Crystallization induction time
E_t	Activation energy for crystallization
A_t	Pre-exponential factor for crystallization induction time
f_d	Diffusion factor for polymer chains
C, D	Diffusion factor parameters
a_a	Degree of polymerization availability for crystallization

Optimization parameters

Q_{exp}	Experimental enthalpy
Q_{sim}	Simulated enthalpy
φ_{exp}	Experimental heat flow
φ_{sim}	Simulated heat flow
a_i	Initial polymerization degree
t_i	Polymerization induction time

Non-isothermal calculation parameters

t_r	Resin age
a_{tc}	Initial crystallization time delayed polymerization degree
ΔH_c	Current enthalpy of crystallization
ξ_n	Location status of the field variable is t_n
$\alpha_{r,n}$, T_n, $\Delta H_{c,n}$	Refers respectively to $\alpha_r(\xi_n, t_n)$, $T_n(t_n, \xi_{n+1})$, $\Delta H_c(t_n, \xi_n)$
δb_n	Variation of crystallization degree between t_n and t_{n+1}

Introduction

Composite materials see fast growth in industrial use. Their advantageous strength/weight compromise when compared to metal alloys makes them particularly interesting in transport industries (automobile, aeronautic…) especially with current needs to reduce greenhouse gas emissions. This is allowed by the architecture of composite materials when compared to monolithic materials: they assemble different kind of materials with specific properties in order to get the most of each component. In fibre-reinforced composite materials, as the name imply, the components include the fibre reinforcement and a matrix. The fibres are designed to carry most of the mechanical tensile loads. The matrix makes up the overall geometry of the composite pieces and contributes to improve mechanical performances, notably shear and compressive behaviour.

Thermoplastic composites

Polymers are a popular choice for matrices because of their polyvalence, weight, and ease of use. Notably, thermosets are often used since their low viscosity allows liquid composite moulding (LCM) processing. Nonetheless, thermoplastic matrices are studied more and more as compared to thermosets, they can be welded, reshaped, and recycled. They also boast higher toughness [1]. They have already been considered for wind turbine blades [2] or automobile parts [3,4]. Because of their high viscosity [1], as shown in Figure 1, pre-impregnated thermoplastics semi-products are often used for processing by matrix fusion and consolidation [5,6].

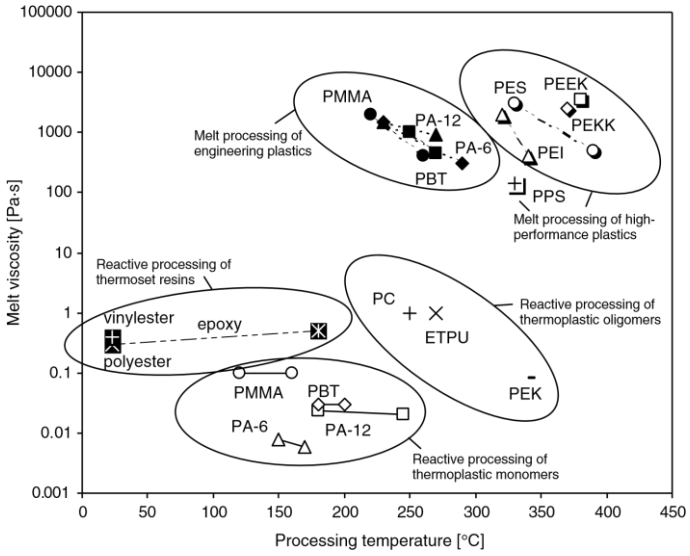

Figure 1. Viscosity and manufacturing temperature of thermosets, thermoplastics and thermoplastics reactive systems [1].

These processes are limited in the geometry shape and cycle times and involve high energy and material costs. For this reason, the use of reactive thermoplastic systems is considered. As shown by Figure 1, they combine very low viscosity and low temperature of use relatively to other polymers. This makes them suitable for LCM processes.

Thermoplastic resin transfer moulding (TP-RTM)

The resin transfer moulding (RTM) process is attractive for its capability to manufacture complex parts with moderate material and energy costs. It allows high production rates and control of both the preform constitution and the fibre orientation. During the process, a low viscosity resin is injected inside a mould with a preform under low pressure conditions (around 1 to 10 bars). The usual structure of the RTM process is presented in Figure 2.

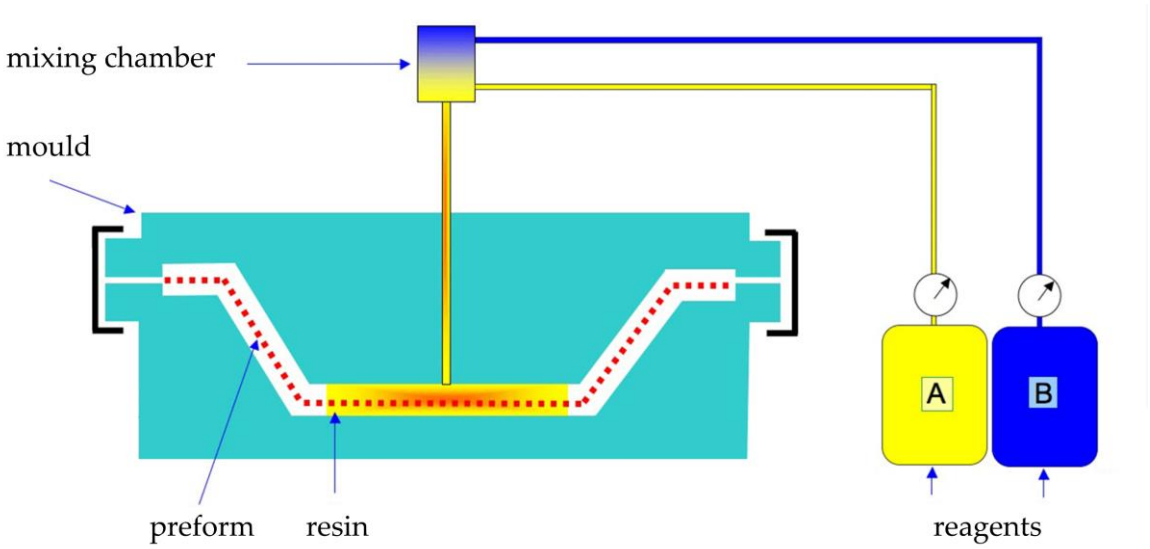

Figure 2. RTM Process (Adapted from [7]).

The process can be referred as thermoplastic resin transfer moulding (T-RTM, or TP-RTM) when the injected resin produces a thermoplastic matrix. For TP-RTM to be possible, a highly fluid resin is required. The primary option is to use the reactive mixes mentioned earlier. They have been studied for manufacturing of polyamide 12 (PA12) matrices [8–10] before interest shifted for polyamide 6 (PA6) matrices thanks to their lower viscosity and better mechanical properties (Murray et al. [11]). In their study, they highlighted the advantageous cost and mechanical properties that processing anionically polymerized PA6 (APA6) can procure. However, because of their complex behaviour, TP-RTM processing with specifically designed highly fluid thermoplastic has also been considered [12,13].

PA6 reactive mix and synthesis behaviour

During Vicard's PhD thesis [14], a reactive mix was chosen and characterized for in-situ polymerization of PA6. A catalyst – Caprolactam magnesium bromide (MgBrCL), and an activator – bifunctional hexamethylene-1,6-dicarbamoylactam (HDCL), have been mixed with the monomer, ε-caprolactam. The reactants were chosen as they combined an initiation time for polymerization which would allow the mix impregnation in the preform maintaining a

low viscosity, while keeping a short synthesis duration [2]. Their role and structural formula in the reaction are shown in Figure 3.

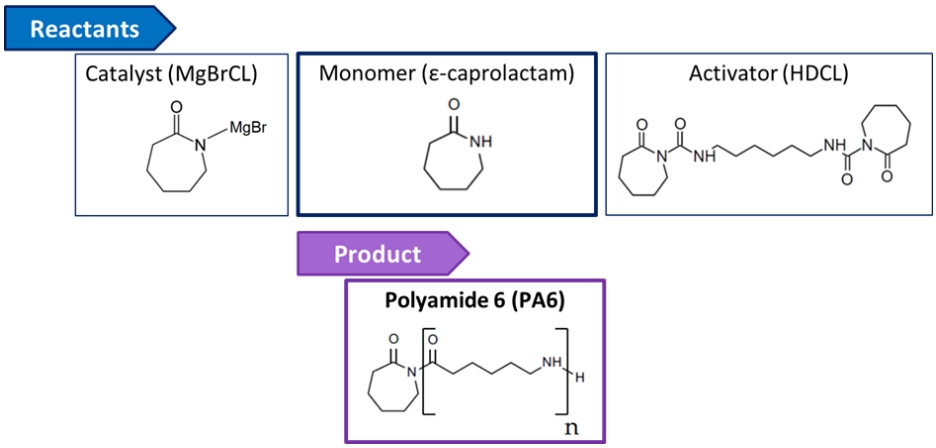

Figure 3. Structural formula of PA6 and its reactants for in-situ synthesis.

As a potentially semi-crystalline polymer, both crystallization and polymerization can occur during the synthesis of PA6. Using differential scanning calorimetry (DSC), Vicard et al. [15] observed the interaction between the two phenomena and the influence of temperature on crystallinity. Their inversed thermodependency showed a window of temperature and time during which the polymerized chain could start crystallizing before the end of monomer conversion. As an attempt to better understand the synthesis, they derived a model for the coupled phenomena [16]. As such, they were able derive a time transformation temperature (TTT) diagram for synthesis of this reactive mix (Figure 4).

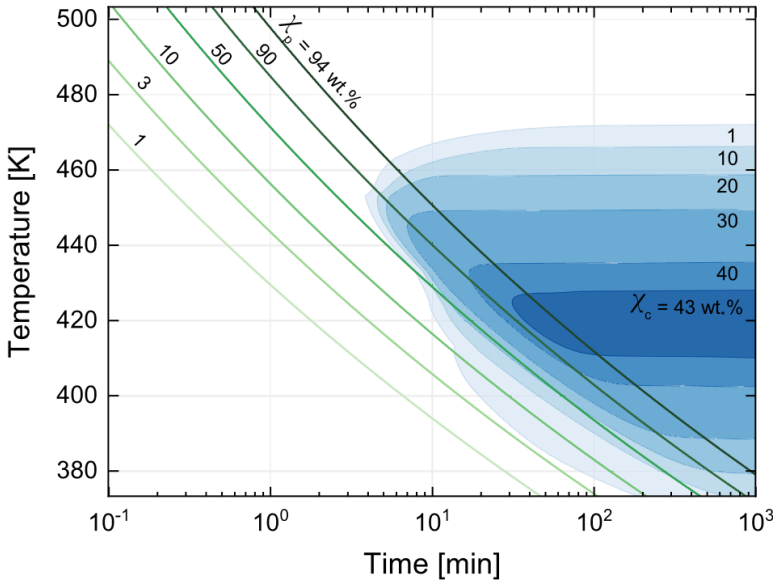

Figure 4. TTT diagram of reactive PA6 [16].

Resin flow in a continuous fibre preform

In some preforms, like non-crimp fabrics (NCF) or woven textiles (Figure 5), the continuous fibre are first aligned and organised into tows. Therefore, while the distance between fibre

inside a tow is measured in micrometres, the distance between tows is much higher and is measured in millimetres [17]. Thus, because of the different scale of gaps (or pore) in these kind of textile materials, they are classified as dual-scale porous medium [17,18].

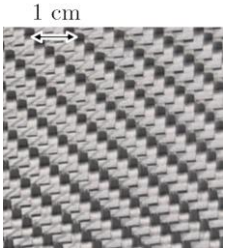

Figure 5. Example of woven glass fibre textile.

In LCM processes, the resins' low surface tension usually causes viscous forces to dominate over capillary effects [19]. In this case, the density of fibre inside the tows slows the intra-tow flow (Figure 6). This causes the presence of multiple resin fronts as the tows' impregnation is delayed. Not only it can trap gas bubbles and form voids in the manufactured piece but with a reactive resin, the resin age will be different inside and outside the tows.

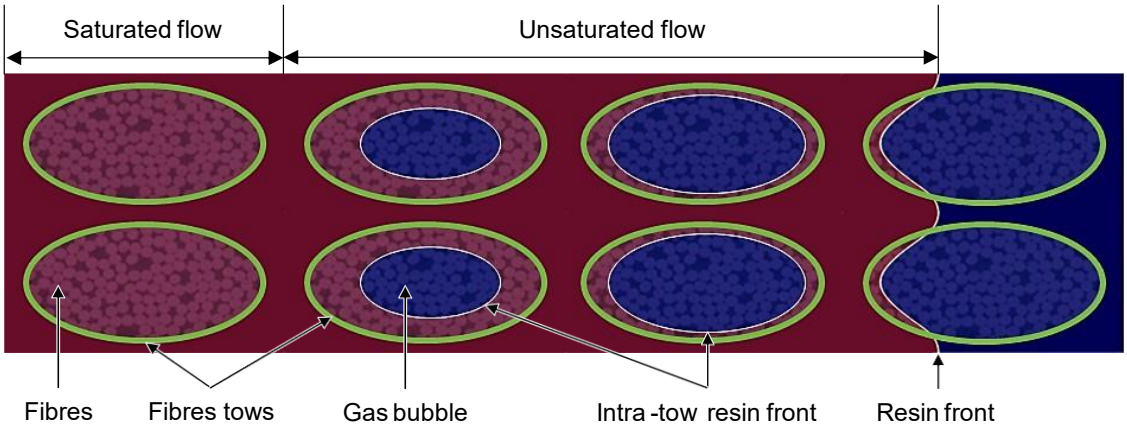

Figure 6. Schematic of fibre tow saturation.

For instance, for the PA6 reactive mix, it means that the progress of polymerization and crystallization would be different at the resin front and inside the tow during the process. As the synthesis releases heat, the different temperatures may lead to variation in crystallinity (Figure 4 and Figure 7) throughout the composite.

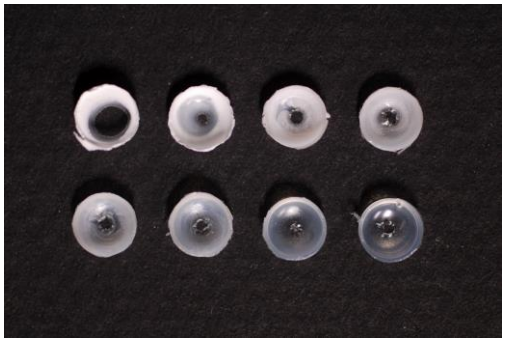

Figure 7. Different aspects of PA6 samples (~5 mm diameter) after synthesis at different temperatures for DSC measurements [14]. Samples with higher crystallinity are whiter and less transparent.

Moreover, the progress of the synthesis increases the viscosity of the reactive mix [14], and further limits the tows' impregnation. Both the formation of voids and the heterogeneous synthesis progression during the composite manufacture may affect its properties [10,20].

Objectives and manuscript organisation

This thesis work aims to capitalize on Vicard thesis work in which PA6 synthesis has been characterized [14]. The aim is to further the understanding of injection of the reactive mix in fibrous preforms for composite manufacture. Notably, modelling and simulation of the process has been considered as simulation results can be a precious tool to predict eventual manufacturing failures and improve the process' conception. Because of the dual scale porosity exhibited by long fibre textiles, the flow model needs to be able to describe flow at both scale of porosity. Then, because of the reactive mix sensibility to external factors, its model needs to be capable of accounting for variation in syntheses results. The model coupling with its rheology and the exothermic reaction is also of prime interest. Moreover, the model derived by Vicard et al. [16] for synthesis description involves uncommon functions for RTM process simulations and therefore its integration or alternatives needed exploration. Finally, the model needs to be coupled with dual-scale flow and the simulations must be compared to experiments.

As such, this manuscript is divided in three chapters. In Chapter 1, a review of modelling methods dealing with fibrous preform for saturated and unsaturated flow is conducted. Then, the performance of Brinkman equation in the open-source computational fluid dynamics (CFD) toolbox OpenFOAM® is tested by simulations using common geometrical configurations. By evaluating the effective permeabilities of the geometries, the effect of tow permeability is observed, and the influence of mesh quality on saturated flow simulation results convergence is studied. This allowed elements to interpret saturated flow simulations results realized with a realistic geometry, which was obtained and graciously shared by Wijaya and his laboratory team [21] (University of Auckland, New Zealand). An example of unsaturated flow simulation on the sample closes the chapter and shows how fast the tows' gaps is filled compared to the tows' impregnation.

In Chapter 2, synthesis models for the PA6 reactive mix are reviewed. Then, an alternative coupling method able to describe the synthesis heat contribution of polymerization, crystallization while taking their interaction into account is proposed [22]. With the variability present in Vicard et al. [15] DSC results, some key parameters have been adapted to both account for it and propose an average model. Thanks to rheological measurement performed at Thermo Fischer Scientific, Courtaboeuf (France), and at the TPCIM (*Technologie des polymères et composites & ingénierie mécanique*, IMT Nord Europe) research laboratory located at Douai (France), elements for modelling the reactive mix rheokinetics are proposed.

Chapter 3 focuses on the hurdle of full process simulation describing flow, temperature variations and synthesis together. After a review of process simulations in the literature along a review of resin front-tracking methods, integration of the synthesis model and especially crystallization in non-isothermal conditions is studied. A procedure is proposed and

compared to non-isothermal DSC measurements realized by Vicard [14]. A simulation coupling the flow and the full synthesis method is presented [22]. Then, elements are given for experimental confrontation of injection simulation of the reactive PA6 mix in a fibrous preform, and for simulation of the synthesis method in a dual-scale porosity material.

Finally, a conclusion closes the manuscript, reflecting on the work realized and perspectives.

Chapter 1

Flow simulation in a fibrous preform

To control liquid composite moulding processes, the interaction between the flow and the preform needs to be assessed. There are multiple problems associated with flow in fibrous preform. They can be linked with the process parameters (position of injection points and event, pressure, mould size and shape…), with the properties of the resin or the properties of the preform.

To model and simulate the filling step of liquid composite moulding (LCM) processes, in a first approach, the fibre preform is characterized by its permeability tensor and the flow behaviour inside can be defined described using Darcy law [23] which will be defined in the next section. Using the permeability parameters, the filling process in LCM can be simulated and the filling time can be predicted. In this case, only the process parameters, the mould geometry, the preform permeability and fibre volume fraction (FVF) and the fluid viscosity are needed. Such simulations at the scale of the mould are said to be performed at macro-scale (see Figure 1.1 for schematic description of different flow scales) and require minimal computational effort compared to smaller scales.

However, in macro-scale representation the preform is only characterized by its geometry permeability and porosity. Therefore, some information is lost concerning the specific aspects of the preform structure. Notably, such averaging fails to account for the different scales of flow velocities that occur inside the tow (intra-tow) and between the tows (inter-tow). This phenomenon is commonly referred as dual-scale flow in the literature [17,24–26]. When only the momentum is considered, ignoring it can be an acceptable approximation. However, in this case voids inside the tow cannot be predicted, not to mention that intra-tow flow is also influenced by interfacial interactions. In the case of a reactive resin, the different time and porosity scale may affect the homogeneity of the final composite through local differences in temperature which influence reaction and viscosity. Nonetheless, exact geometrical representation of the fibre preform at micro-scale is not practically feasible given the thousands of fibres that would have to be represented. Therefore, studies at micro-scale have been restricted to representative geometries with a limited number of fibres. One solution to model dual-scale flow is to consider the mesoscopic scale. At this scale, only the tows

properties are averaged instead of the whole geometry. This notably allows to observe the different resin front position inside and between the tows, as shown in Figure 1.2 obtained by numerical simulation. Moreover, assuming the periodicity of a tow arrangement, a representative elementary volume (REV) can be derived and used for numerical permeability determination [21].

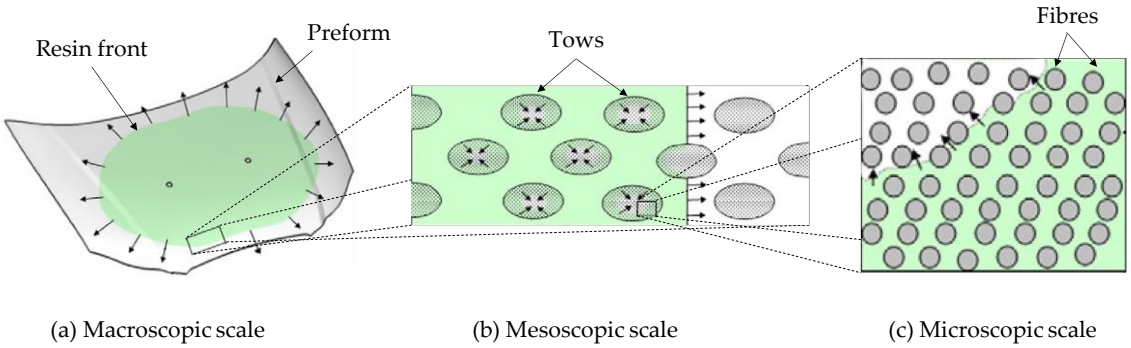

Figure 1.1. Different flow scales study (adapted from [17]).

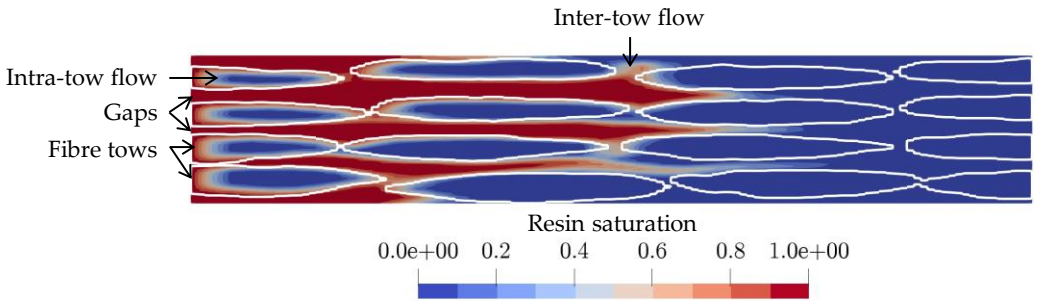

Figure 1.2. Interaction between resin and tows during a filling simulation (fully saturated spaces are in red - see section 1.3.3 for details of the simulation).

In this chapter, the focus will be on modelling and simulating the influence of a fibrous preform on the momentum of the resin flow at meso-scale. Thus, the main equations used to describe flow in LCM processes are described. In particular, the different methods to describe the influence of the reinforcement on the saturated or unsaturated flow are discussed. Then, the Navier-Stokes-Brinkman equation which is present in OpenFOAM® is employed in permanent flow simulations. It is used with regular cylinder configurations in order to compare it to Gebart's analytical model. The influence of the cylinders' permeability (simulating fibre tows) and meshing quality are studied. Then, the simulation method is tested with a real geometry obtained by Wijaya [21] using micro-tomography. Finally, a flow test is realized with unsaturated conditions. The interfacial interactions between the preform and the resin are not considered during simulations nor are the fibre preform displacement and deformation caused by the resin flow. The issues caused by reactive PA6 and non-isothermal conditions will be addressed in Chapter 2 and Chapter 3.

1.1 Flow modelling in fibrous preform

The equations used to describe one phase flow in fibrous media are presented here. The equation for porous media flow, the Darcy equation and the fundamental equations for fluid mechanics, the Navier-Stokes equations are recalled first. Then, modelling methods for mesoscopic scale flow are detailed.

1.1.1 Macro-scale modelling and issues

To simulate a flow when filling a fibre preform, the first approach is to consider the macro-scale flow in which the textile geometrical and hydraulic properties are averaged. Indeed, simulating the whole geometry is not cost-effective at the time of the writing because of the sheer number of fibres in a preform.

Darcy equation

To characterize a porous media at the macro-scale, two parameters are used, the permeability tensor $\boldsymbol{K}$ and the porosity $\tilde{\varepsilon}$ which respectively defines the hydraulic conductivity and average of volumetric geometrical properties. For fibrous preforms, the porosity can be related to the Fibre Volume Fraction V_f (FVF) as $\tilde{\varepsilon} = 1 - V_f$. In such characterization, as the flow is averaged in the whole domain, the information from the intrinsic velocity vector $\boldsymbol{u}$ is lost due to the geometry simplification. Thus an averaged velocity $\overline{\boldsymbol{u}}$, characteristic of the macro-scale flow is defined instead following the Dupuit-Forchheimer relationship [27] (equation 1.1).

$$\boldsymbol{u} = \frac{\overline{\boldsymbol{u}}}{\tilde{\varepsilon}} = \frac{\overline{\boldsymbol{u}}}{1 - V_f} \tag{1.1}$$

Given a slow laminar (or creeping) Newtonian flow in an homogeneous porous media, the averaged fluid velocity and the permeability have been related to the pressure p and the dynamic viscosity η of the fluid with Darcy equation [23,28] (equation 1.2, in which $\overline{\boldsymbol{u}}$ is also referred as Darcy's velocity).

$$\overline{\boldsymbol{u}} = -\frac{\boldsymbol{K}}{\eta}\boldsymbol{\nabla} p \tag{1.2}$$

The issue with space averaging methods is the loss of information that comes from reducing the porous media to only a few parameters [27].

Dual-scale porosity material

To separate the cases when the lost information is significant, two kinds of porous media pertaining to fibre preform for the RTM (Resin Transfer Moulding) process can be distinguished [18,26]. The first kind is the single scale fibrous material which is usually made of randomly oriented fibres. Therefore, with the random volume distribution of porosity, the macroscopic representation is pertinent. However, when the textile is made of continuous fibres with a regular configuration (non-crimp fabrics (NCF) or woven textiles), a repeatable

motif in the tow configuration can be distinguished. Such fibrous preforms can be called dual-scale porosity materials, and their study is often realized using their characteristic patterns through representative elementary volumes (REVs).

A REV can be distinguished at either the fibre scale (microscopic scale) or at the tow scale (mesoscopic scale) (see Figure 1.1). The microscopic scale gives information on the tow while the mesoscopic scale gives information on the textile preform.

1.1.2 Meso-scale modelling in fibrous media and saturated permeability

With the challenges of standardizing experimental determination of saturated permeability [29–31], modelling flow in a REV has been used as a mean for theoretical permeability determination. Numerous analytical models have been derived depending on the geometry of the fibre preform. While the Kozeny-Carman model is maybe the most general of them and has filtration theory background [27], a lot of models such as the Gebart model [32] have been developed to try and account for particular geometries and divergence from experimental results (see Bodaghi et al. [33] for a review). However, it is usually concluded that too much information about the preform geometry is lost with the assumptions taken to derive these analytical models [33,34]. One reason could be that their assumption is based on fibre repartition instead of tows'. Therefore, they pertain to either macroscopic permeability in the case of random fibre distribution or microscopic permeability for ordered configurations.

Hence, it is interesting to look at the eventual capabilities of numerical modelling and simulation to give more insight for the flow at tow scale. For a mesoscopic scale REV, a 3D geometrical description of the tows is needed. One manner to create such a geometry is through computer-aided design (CAD). Some software have been specifically developed for textile geometry design (WiseTex [35] or TexGen [36] for example). Another possibility is to use X-ray micro-tomography to obtain volumetric scan of a real textile geometry and convert them to a 3D geometry as realized by Wijaya et al. [37]. In Figure 1.3, an example of such geometry from Wijaya's thesis work [21] is shown.

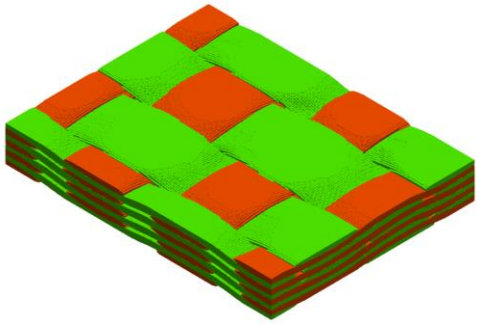

Figure 1.3. Tow geometry of a textile obtained after post-treatment of X-ray micro-tomography scans [21].

Tow modelling hypotheses

When the tow geometry has been obtained, different hypotheses for the tow behaviour with relation to the flow have been used for simulation in the domain. The tows can be either described as impermeable using a no-slip (or adherence) boundary condition (Figure 1.4, left),

(with similar hypothesis to micro-scale simulations with fully impermeable fibres), or as permeable. For the latter hypothesis, a tow permeability $\boldsymbol{K_{tow}}$ must be determined. To this endeavour, analytical models can be used at micro-scale (for instance, Wijaya et al. [37] used the Gebart model), or micro-scale REV simulation can be done (see [38,39] for example). Then, two options have been proposed to couple the flow inside and outside the permeable tow. The first option is to separately consider the porous domain and the non-porous one, and to couple the different flows with a Beaver-Joseph Saffman (BJS) [40–42] kind of boundary condition (Figure 1.4, centre). The second option is to use the Brinkman equation [43] which can be applied to the whole domain (Figure 1.4, right).

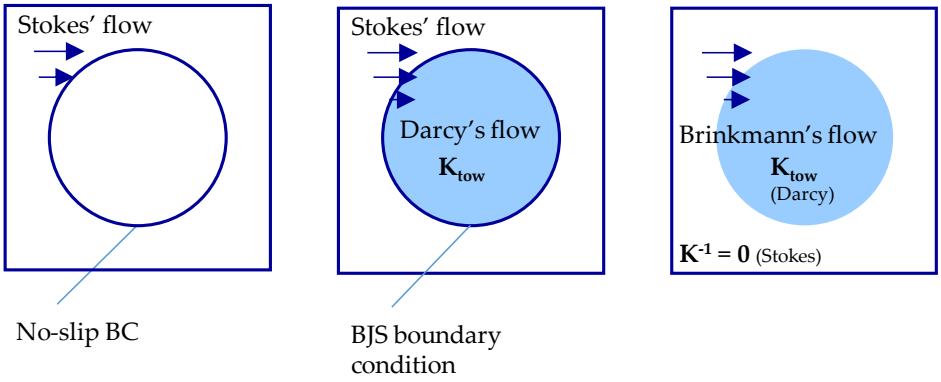

Figure 1.4. Different types of representations for tows in a geometry. Left: impermeable tow, centre: coupled Stokes-Darcy using Beavers & Joseph family of boundary conditions between two domains, right: Brinkman's equation with variable permeability in one domain.

All the aforementioned methods consider a Stokes' flow outside the tows. It can be derived from the Navier-Stokes equations.

Navier-Stokes equations

The isothermal Navier-Stokes equation consists in two equations. The first is the mass conservation equation (continuity equation), given by equation 1.3 where t is the time and ρ the density, and $\boldsymbol{u}$ the fluid velocity vector.

$$\frac{\partial \rho}{\partial t} + \boldsymbol{\nabla} \cdot (\rho \boldsymbol{u}) = 0 \tag{1.3}$$

The second is the conservation of momentum given in its general form by equation 1.4. $\boldsymbol{\tau}$ is the viscous stress tensor and $\boldsymbol{f}$ includes other forces applied to the fluid such as gravity.

$$\frac{\partial \rho \boldsymbol{u}}{\partial t} + \boldsymbol{\nabla} \cdot (\rho \boldsymbol{u} \otimes \boldsymbol{u}) = -\boldsymbol{\nabla} p + \boldsymbol{\nabla} \cdot \boldsymbol{\tau} + \rho \boldsymbol{f} \tag{1.4}$$

Usually, incompressibility of the fluid is assumed along the isothermal hypothesis. Therefore, for an incompressible Newtonian fluid with no additional forces, the Navier-Stokes equations can be rewritten following equations 1.5 and 1.6.

$$\boldsymbol{\nabla} \cdot \boldsymbol{u} = 0 \tag{1.5}$$

$$\rho\left[\frac{\partial \boldsymbol{u}}{\partial t} + \boldsymbol{u}\cdot\boldsymbol{\nabla u}\right] = -\boldsymbol{\nabla} p + \eta\boldsymbol{\Delta u} \tag{1.6}$$

As flow in fibrous preform is usually creeping, the Stokes formulation for Newtonian permit to simplify calculations (equation 1.7) as the convection term is considered negligible.

$$\rho\frac{\partial \boldsymbol{u}}{\partial t} = -\boldsymbol{\nabla} p + \eta\boldsymbol{\Delta u} \tag{1.7}$$

Using the Stokes equation, the flow outside the tows can be modelled. Supposing permeable tows, the behaviour inside the tows need to be described.

Brinkman and Brinkman-Forchheimer equation

Brinkman [43] proposed equation 1.8 as an attempt to combine Stokes' equation 1.7 and Darcy's equation 1.2.

$$\boldsymbol{\nabla} p = -\eta\boldsymbol{K^{-1}}\overline{\boldsymbol{u}} + \tilde{\eta}\boldsymbol{\Delta}\overline{\boldsymbol{u}} \tag{1.8}$$

$\tilde{\eta}$ defines an effective viscosity. Straight volume averaging as described by Ochoa-Tapia and Whitaker [44] suggests equation 1.9 to define the parameter.

$$\tilde{\eta} = \frac{\eta}{\tilde{\varepsilon}} \tag{1.9}$$

However, in porous flow theory, the effective viscosity is usually considered dependant of the domain [45]. Notably Nield and Bejan [27] report various expressions proposed for $\tilde{\eta}$ and diverging from equation 1.9 in the literature. Moreover, the fundamental physical validity and domain of usability of Brinkman equation has not been completely settled [27,46–48], especially when porosity is medium to low ($\tilde{\varepsilon} < 0.6$). Nonetheless, the viscous term is usually negligible compared to the Darcian term [48–50], which makes it a possible choice for numerical modelling in meso-scale fibrous geometry including both Stokes' flow and Darcy's flow.

A generalization of equation 1.8 has been derived in the literature [27], using Ochoa-Tapia and Whitaker [44] volume averaging and the Forchheimer term to model drag force for moderately fast flows ($Re > 1\ to\ Re \approx 10$) in equation 1.10 with c_F being a dimensionless constant depending on the porous medium [49].

$$\rho\left[\frac{1}{\tilde{\varepsilon}}\frac{\partial \overline{\boldsymbol{u}}}{\partial t} + \frac{1}{\tilde{\varepsilon}}\boldsymbol{\nabla}\left(\frac{\overline{\boldsymbol{u}}\cdot\overline{\boldsymbol{u}}}{\tilde{\varepsilon}}\right)\right] = -\boldsymbol{\nabla} p + \frac{\eta}{\tilde{\varepsilon}}\boldsymbol{\Delta}\overline{\boldsymbol{u}} - \eta\boldsymbol{K^{-1}}\overline{\boldsymbol{u}} - c_F\rho\boldsymbol{K^{-\frac{1}{2}}}\|\widetilde{\boldsymbol{u}}\|\widetilde{\boldsymbol{u}} \tag{1.10}$$

Brinkman's equation and its derivatives has been used as a basis for multiple simulations to determine textile permeability [51–53]. Indeed, for textile flow simulation, the Darcian term dominates other terms in the tows, while out of the tows, the Stokes equation can be resolved. The pressure gradient becomes then the sum between the viscous contribution and the resistance of the permeable medium to the flow. However, the aforementioned theoretical

issues coupled with numerical issues in low permeability computation [34] lead various authors to consider separate modelling of intra and inter-tow flow with a coupling boundary condition in-between.

Beavers and Joseph Saffman boundary conditions

Using boundary conditions around the tows is usually based on Beavers and Joseph [40] conditions generalized by Saffman in equation 1.11 for non-planar porous boundaries [41]. Assuming that the flow in the tow behaves as a Darcy flow, it aims to replicate the velocity drop at the tow interface, with n the normal direction of the tow interface, and $\tilde{c}$ an empirical constant. It was further generalized by Jones, who proposed for shear stress at the interface to follow the same behaviour [42], which validity seems likely but lacks experimental confirmations [27].

$$\frac{\partial \overline{\boldsymbol{u}}}{\partial n} = \tilde{c}\boldsymbol{K}^{-\frac{1}{2}}\overline{\boldsymbol{u}} + O(\boldsymbol{K}) \tag{1.11}$$

It allows to couple the Stokes' flow and the Darcy flow at the tow boundary. Uses of the method in the composite processing simulation literature includes Geoffre et al. [34] for permeability determination and Li et al. [54] for unsaturated simulations (coupled with a phase-field method for the interface).

Discussion about the methods

According to Geoffre et al. [34], equation 1.8 makes simulations with very low intra-tow permeability delicate, and needs affectation of an unphysical very high permeability for inter-tow flow. The latter problem can be solved by implementing the inverse of the permeability instead, as done in OpenFOAM® [55]. Beavers and Joseph type of boundary conditions is also favoured by Nield and Bejan [27] for its better description of boundary flow behaviour compared to Brinkman's equation although some objections on the range of validity of the boundary condition have been raised by Auriault [56].

However, Brinkman's equation and its derivatives advantage lies in its monolithic nature and the simplicity of its integration in a simulation framework [57] compared to setting a boundary conditions and coupling two regime of flows. This motivated its use in Carillo et al. work [58] for example, for a multiphase and multiscale porous flow simulation toolbox in OpenFOAM®.

1.1.3 Unsaturated flow modelling

For LCM processes simulation, the preform and the mould are filled by resin, or in other terms, they are saturated by resin. Supposing a homogeneous domain, a filling simulation can be realized using only Darcy equation and a front-tracking method. In Gantois PhD thesis [28] example of simulations using Darcy and level-set equations can be found. In Chapter 3, discussion about front-tracking methods is expanded on.

However, in practice, the preform full saturation is slower than Darcy equation predictions with the medium permeability [19]. Possible explanations are capillarity effects caused by the small gaps between fibres [19], or voids than form as a result of flow in a dual-scale porosity medium [59]. In this case, dual-scale flow occurs which refers to the division of the resin front caused by the different saturation speed inside the tows and outside the tows.

A solution to account for these effects is to model saturation in concert with unsaturated permeability, to correct the pressure distribution of the flow [60]. Another possibility is to subtract the intra-tow flow from the inter-tow flow through the use of a sink term in the macroscopic continuity equation [17].

Unsaturated permeability

To correct the permeability in Darcy equation for resin filling conditions, a saturation parameter S_r is defined and follows equation 1.12 with α_r defining the volume fraction of the resin phase.

$$S_r = \frac{\alpha_r}{1 - V_f} = \frac{\alpha_r}{\tilde{\varepsilon}} \tag{1.12}$$

To account for the microscopic front geometrical parameters at a higher scale (meso or macro) a correction of permeability in saturation conditions can be used. Hence, the unsaturated permeability K is defined by equation 1.13. K_s refers to the saturated permeability tensor, and k_r is the dimensionless relative permeability depending on saturation level. For anisotropic porous media, both K_s and k_r may depend on the considered direction [45].

$$K(S_r) = K_s k_r(S_r) \tag{1.13}$$

Assuming that the flow is dominated by viscous effects rather than capillary effects, which is often the case with viscous resin used in LCM processes, k_r is valued between 0 and 1 and various models have been developed to empirically describe its dependence to saturation [19]. It is used in conjunction with the transport equation of saturation (equation 1.14).

$$\frac{\partial S_r}{\partial t} + \boldsymbol{\nabla} \cdot S_r \overline{\boldsymbol{u}}_{\boldsymbol{r}} = 0 \tag{1.14}$$

Recent use of this method for LCM process simulation such as proposed by Gascon et al. [61,62] or Li et al. [54] also include a method to account for capillary pressure.

Sink term

The addition of a sink term in a volume-averaged framework aims to consistently model the resin absorption inside the tow [63–65]. Therefore, a sink term S defining the volumetric resin absorption rate is added in the mass balance equation 1.15. The term is distinct from the above-mentioned saturation scalar S_r which describes the impregnation state of the tow.

$$\boldsymbol{\nabla} \cdot \bar{\boldsymbol{u}} = -S \tag{1.15}$$

According to Tan and Pillai [64], it is a more elegant formulation for simulating dual-scale flow, with experimentally validated results. To further improve the model, Tan et Pillai [17] proposed a coupled macro-meso scale model, with the macro sink term simulated using data from a tow-scale simulation with its own sink term.

Equation 1.15 is however based on the basis that inter-tow flow occurs much faster than intra-tow flow (assuming viscous effects dominates the flow, as presumed before), and therefore that intra-tow flow can be reduced to resin absorption [64]. This view is challenged by Imbert et al. experimental study [66], which introduces the notion of "storage" (absorption by the tows) and "release" since the resin in the tow is not immobile. Therefore, they enriched the sink term previously defined with a "release" term to meet experimental observations [67].

Discussion about the methods

Compared to the method using unsaturated permeability, Tan and Pillai argues that the use of a sink term is more efficient [64]. This is explained by the fact that the sink term has been used to separate the simulation of impregnation conducted inside and outside the tows [26,67]. The meshing is therefore used two times, separately for averaged flow inside and outside the tow. Therefore, while its calculation is more complex because of the parallel calculation of both flows, it has been shown to be able to give information about the intra-tow flow, such as its temperature or its cure status with less refined meshing. However, to give such results careful volume averaging needs to be realized [17,25,63,64], which always implies loss of information [27]. Strong hypotheses on the flow direction or behaviour may also need correction (such as the one proposed by Imbert et al. [67]) as understanding on intra-tow flow improves. Fundamental comparison of both methods may also give insights on the subtle differences between the two modelling strategies.

1.1.4 Challenges in fibrous preform flow modelling

Various methods for modelling flow in a preform exist and have been employed to either determine permeability or simulate unsaturated flow for LCM processes. Notably, the modelling of intra-tow flow, inter-tow flow and their coupling have recently been tackled with various methods without a clear consensus on the better method. This is caused by the numerous challenges posed by the preform and its averaging. The equilibrium between lost information from volume averaging, physical conformity of the model and simulation performance is difficult to assess. Another huge challenge which has not been expanded on here is the experimental determination of the parameters for flow (saturated or unsaturated) models in dual-scale porosity medium [68].

1.2 Test for saturated permeability simulation

In this work, the open source computational fluid dynamic (CFD) toolbox OpenFOAM® v8 [55] is used for flow simulation. It uses the Finite Volume Method (FVM) to spatially discretize the (strong) integration form of general transport equations. Some details on equation resolution are given here, however for further information, Jasak [69], Weller et al. [70] and the user guide for another OpenFOAM® fork [71] can be consulted. The simulations in this section aim to test OpenFOAM® capabilities for computing both intra-tow and inter-tow flow.

1.2.1 Simulation parameters and principle

The most powerful configuration used for simulations is a virtual machine with 32 gigabytes of RAM and 8 cores of an AMD® Ryzen threadripper 3960x 24-core processor.

Navier-Stokes-Brinkman in OpenFOAM®

The resin is considered Newtonian and incompressible. The conservation of mass therefore follows equation 1.5. The simulation follows a Brinkman model of flow as equation 1.10 without accounting for porosity (equivalent to $\tilde{\varepsilon} = 1$) nor drag force as the flow is assumed to never reach a sufficient speed. Therefore, in this section, the pressure and velocity are computed following equation 1.16. The viscous term is written here with the kinematic viscosity ($\nu = \eta/\rho$) and placed here in the left-hand side of the equation to conform to its matricial expression (equation 1.17).

$$\rho\left(\frac{\partial \boldsymbol{u}}{\partial t} + \boldsymbol{u}\cdot\boldsymbol{\nabla u} - \nu\boldsymbol{\Delta u}\right) = -\boldsymbol{\nabla} p + \eta \boldsymbol{K}^{-1}\boldsymbol{u} \tag{1.16}$$

Discretization and resolution

The time derivative is computed; however, simulations are conducted until the flow reaches a permanent configuration, therefore the Euler explicit scheme is used. The viscous term is calculated with the central differencing method, while the convection term is calculated with the "limitedLinearV" scheme used with maximum emphasis on convergence. It is a Total Variation Diminshing (TVD) method which aims to improve convergence without sacrificing too much precision (see [71,72] for more details). The Darcy term is solved explicitly and pressure solving is explained in the following section.

Simulation method

The simulation method uses the OpenFOAM® integration of the pressure implicit with splitting of operators (PISO), a segregated pressure-velocity procedure developed for transient flows. Its steps are summarized below and can be found in the source code [73].

It starts from equation 1.17, in which matrix $\boldsymbol{\mathcal{M}}$ is constructed from the discretized transient, convective and viscous terms from the left-hand side of equation 1.16. The Darcian term is

calculated explicitly and is thus in the right-hand side of the equation. Index n indicates that the pressure and the velocity come from the n-th time step ($t = t_n$).

$$\boldsymbol{\mathcal{M}}\boldsymbol{u_n} = -\boldsymbol{\nabla} p_n + \eta \boldsymbol{K}^{-1}\boldsymbol{u_n} \tag{1.17}$$

Equation 1.17 is also called the momentum predictor step, as it can be used to obtain an initial velocity $\boldsymbol{u_n^0}$. This step can be skipped if its computation is not beneficial (in that case, $\boldsymbol{u_n^0} = \boldsymbol{u_n}$). Then, in equation 1.18, the diagonal terms of matrix $\boldsymbol{\mathcal{M}}$ are separated to create the easily invertible matrix $\boldsymbol{\mathcal{A}}$. The residual matrix $\boldsymbol{\mathcal{H}}$ is obtained as a result.

$$\boldsymbol{\mathcal{M}}\boldsymbol{u_n^0} = \boldsymbol{\mathcal{A}}\boldsymbol{u_n^0} - \boldsymbol{\mathcal{H}} \tag{1.18}$$

By replacing $\boldsymbol{\mathcal{M}}\boldsymbol{u_n^0}$ with the right-hand side terms of equation 1.17 and by multiplying equation 1.18 with $\boldsymbol{\mathcal{A}^{-1}}$, equation 1.19 is obtained.

$$\boldsymbol{u_n^0} = \boldsymbol{\mathcal{A}^{-1}}\left(\boldsymbol{\mathcal{H}} - \eta \boldsymbol{K}^{-1}\boldsymbol{u_n^0}\right) - \boldsymbol{\mathcal{A}^{-1}}\boldsymbol{\nabla} p_n \tag{1.19}$$

Now, as applying the incompressible continuity equation 1.5, the Laplacian equation 1.20 for pressure is obtained.

$$\boldsymbol{\nabla} \cdot \boldsymbol{\mathcal{A}^{-1}}\boldsymbol{\nabla} p_n = \boldsymbol{\nabla} \cdot \left[\boldsymbol{\mathcal{A}^{-1}}\left(\boldsymbol{\mathcal{H}} - \eta \boldsymbol{K}^{-1}\boldsymbol{u_n^0}\right)\right] \tag{1.20}$$

It is commonly called the pressure correction equation and its resolution gives an intermediate pressure value p_n^*. The corresponding intermediate velocity $\boldsymbol{u_n^*}$ is obtained with equation 1.21 by replacing the relevant terms in equation 1.19.

$$\boldsymbol{u_n^*} = \boldsymbol{\mathcal{A}^{-1}}\left(\boldsymbol{\mathcal{H}} - \eta \boldsymbol{K}^{-1}\boldsymbol{u_n^0}\right) - \boldsymbol{\mathcal{A}^{-1}}\boldsymbol{\nabla} p_n^* \tag{1.21}$$

Then, to ensure second order precision on the pressure-velocity coupling, equations 1.20 and 1.21 need to be solved at least one more time (minimum two loops in total). Three loops are often used in OpenFOAM® example cases. Thus, for the following simulations, the velocity $\boldsymbol{u_{n+1}}$ and pressure p_{n+1} are obtained on the third time equation 1.20 and 1.21 are solved ($\boldsymbol{u_{n+1}} = \boldsymbol{u_n^{***}},\ p_{n+1} = p_n^{***}$). The described calculation procedure to compute the values at t_{n+1} is illustrated with Figure 1.5.

According to Issa [74], looping back on the pressure equation enables to reach second order accuracy. While it may not necessarily be the most adapted procedure for permanent flows, it is able to give satisfactory results if the simulation timeframe is set long enough [72].

No convergence criterion for the whole simulations has been set, however they have been conducted until convergence of the residuals.

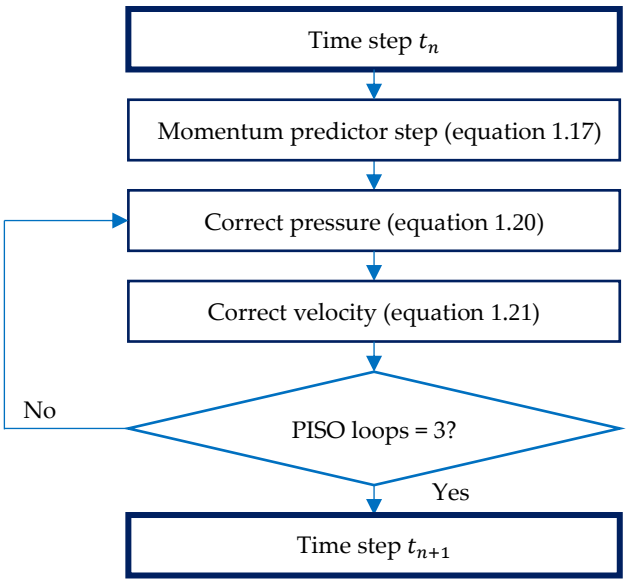

Figure 1.5. PISO method for fluid simulations.

1.2.2 Gebart analytical solution

The simulation tests were realized with geometry representing quadratic or hexagonal arrangement of cylinders. Supposing the cylinders represent impermeable fibres, Gebart [32] determined an analytical solution perpendicular to the fibres (giving the formula for transverse permeability) and along the fibres (giving the formula for longitudinal permeability). To derive the formula, creeping flow following hydrodynamical lubrification hypotheses (in a Hele-Shaw cell) adapted to curvilinear boundaries was assumed to derive velocity. The pressure can then be obtained from the conservation equation, and permeability formula from Darcy's law [75]. The geometrical configurations are shown on Figure 1.6 and Figure 1.7. The corresponding analytical values are detailed in Table 1.1, in which V_f refers to the cylinders volume fraction.

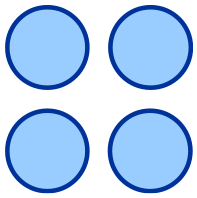

Figure 1.6. Gebart quadratic arrangement.

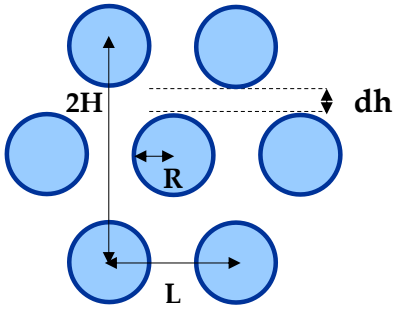

Figure 1.7. Gebart hexagonal arrangement ($2H = L\sqrt{3}$).

To compare with the Gebart theoretical permeability, the simulation geometry effective permeability K_{eff} is calculated by imputing simulation results in equation 1.22, which results from Darcy equation 1.2 application, where Q is the debit and $\mathcal{A}$ the inlet area.

$$K_{eff} = \left|\frac{\eta L Q}{\mathcal{A}\Delta P}\right| \tag{1.22}$$

Table 1.1. Gebart analytical solution

Permeability \ Arrangement	Quadratic	Hexagonal
Transverse	$K_{g\perp,q} = \frac{16R^2}{9\pi\sqrt{2}}\left(\sqrt{\frac{\pi}{4V_f}} - 1\right)^{\frac{5}{2}}$	$K_{g\perp,h} = \frac{16R^2}{9\pi\sqrt{6}}\left(\sqrt{\frac{\pi}{2\sqrt{3}V_f}} - 1\right)^{\frac{5}{2}}$
Longitudinal	$K_{g\parallel,q} = \frac{8R^2}{57}\frac{(1-V_f)^3}{{V_f}^2}$	$K_{g\parallel,q} = \frac{8R^2}{53}\frac{(1-V_f)^3}{{V_f}^2}$

The relative error ϵ_r with the theoretical permeability is calculated using equation 1.23.

$$\epsilon_r = \left|\frac{K_{eff} - K_{\perp,q}}{K_{\perp,q}}\right| \tag{1.23}$$

1.2.3 Influence of tows' permeability on the geometry's permeability

In a first approach, simulations have been performed with tows of varying permeability to observe the permeable tows influence on the effective permeability of the geometry. The tow geometry is not realistic but can be compared to Gebart analytical solution.

Simulation description

Two 3D geometries shown in Figure 1.8 were used with volumes sketched in blue representing quasi-cylindrical tows in a hexagonal configuration. The hex-dominated mesh does not smoothly follow a cylindrical form as it followed a simple meshing procedure. A simple hexagonal mesh is first realized, before refinement of tow interface by cell division. Finally, the elements inside the tow were selected. Cut elements are selected depending on their orientation relatively to the cylinders. The volumes in blue represent the selected elements representing cylindrical tows where the Darcian term in equation 1.16 is calculated. The geometry is described by Figure 1.8 and was used to compute the configuration's transverse effective permeability. The geometry characteristics, parameters of the simulation with the permeability value of the blue cylinders are described in Table 1.2. The pressure differential was chosen arbitrarily, and the viscosity high enough to have a creeping flow. The volume occupied by the cylindrical tows is characterized by V_{tow}.

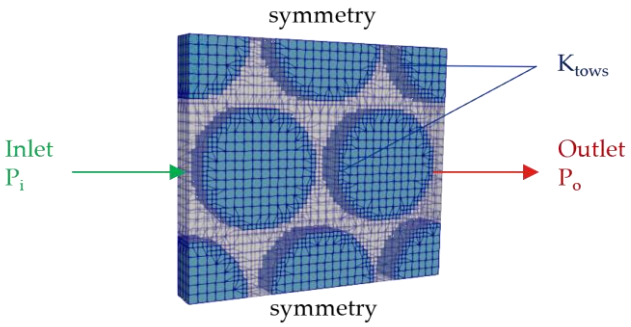

Figure 1.8. Mesh to test cylindrical hexagonal geometry effective permeabilities.

Table 1.2. Hexagonal tows simulation parameters.

Meshing	(See Figure 1.8)
Number of elements	9408 elements
Dimensions	2*0.25*1 mm^3
$\boldsymbol{\Delta P = P_i - P_o}$	1000 Pa
$\boldsymbol{\eta}$	2.37 Pa.s
$\boldsymbol{K_{tows}}$	10^{-x} $m^2, x \in [\![8,14]\!]$
$\mathbf{V_{tows}}$	60.8 %

Simulation results

In Table 1.3 and in Figure 1.9 the effective permeability K_{eff} calculated using equation 1.22 is displayed with relation to the value of the cylinders' permeability. The relative error has been calculated using equation 1.23.

Table 1.3. Simulation effective permeability results and relative error compared to Gebart analytical value.

Tows permeability [m^2]	**10^{-14}**	**10^{-13}**	**10^{-12}**	**10^{-11}**	**10^{-10}**	**10^{-9}**	**10^{-8}**
$\boldsymbol{K_{eff}}$ **[10^{-9} m^2]**	1.15	1.15	1.16	1.19	1.48	3.45	14.0
Relative error [%]	26.15	26.19	26.62	30.49	61.47	277.7	1430
Analytical value ($K_{g\perp,h}(V_{tows})$) [10^{-9} m^2]				0.914			

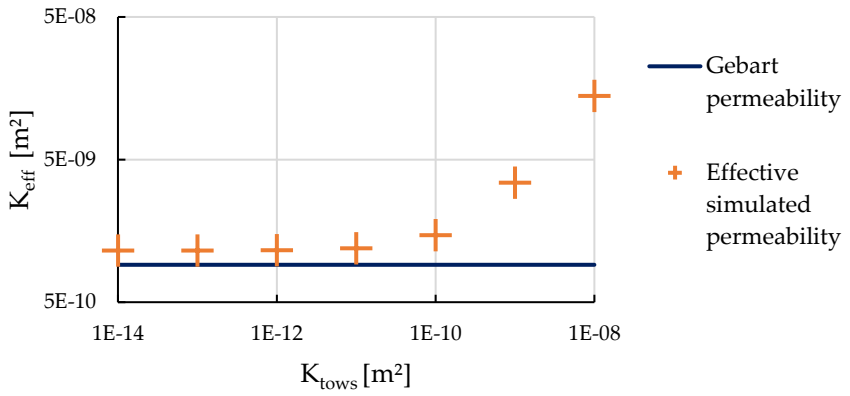

Figure 1.9. Transverse effective permeability with relation to the cylindrical tows' permeability compared to the theoretical Gebart permeability with impermeable cylinders.

The results shows that K_{eff} value converges when K_{tows} value is negligible enough compared to K_{eff}. In this case, it occurs for $K_{tows} \leq 10^{-11}$ m^2, when the tows permeability is two orders of magnitude lower than the effective permeability of the theoretical impermeable geometry. Then, when the tows permeability is higher (for $K_{tows} = 10^{-9}$ m^2 and $K_{tows} = 10^{-8}$ m^2), the effective permeability K_{eff} value increase and is valued at the same order of magnitude as K_{tows}. Thus, this shows that at very low tow permeability, the tow geometry directs the effective permeability of the medium while for higher permeabilities, the effect becomes more prominent.

This is coherent with similar observations by Geoffre et al. [34] with a different simulation method (coupled Stokes-Darcy with BJS boundary condition, see subsection 1.1.2). A more detailed study, notably on the influence of V_{tow} and empirical relations between K_{tows} and K_{eff} is realized on their paper.

From the results above, it can be hypothesized that the effective permeability converged value ($K_{eff}(K_{tows} \leq 10^{-11}$ m^2)) correspond to the geometry's permeability for impermeable tows. However, in that case the relative error when compared to Gebart theoretical permeability is high (26% compared to $K_{g\perp,h}$). The most apparent reason for this difference is the quality of the meshing.

Impermeable simulation result with conforming mesh

To test this hypothesis, an impermeable simulation was realized. The meshing method differed from above as the tows' geometry are removed from the mesh, before refinement to conform to the surface. Therefore, the geometry's description is much better (see Figure 1.10) and involved more elements (15304). The same boundary conditions as above are applied, with a no-slip boundary representing impermeable tows. For this simulation, an effective permeability of $K_{eff} = 8.67 * 10^{-10}$ m^2 was obtained, which correspond to an error of 0.74% when compared to the analytical value. The much lower error indicates the importance of good geometry description on effective permeability results.

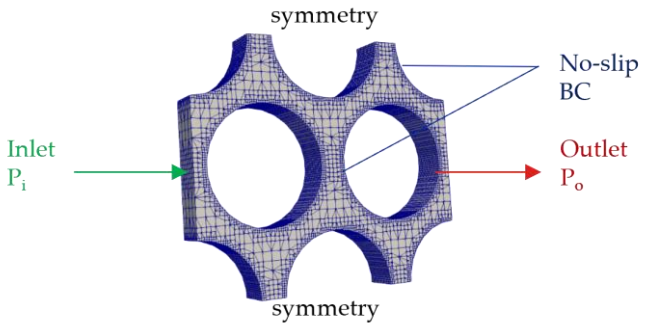

Figure 1.10. Impermeable conforming cylindrical hexagonal geometry effective permeabilities.

To create meshes that includes conforming cylindrical permeable tows, meshes of the tows and the background geometry needed to be created separately before merging the meshes individually. For the geometry in Figure 1.8, it involves merging nine set of meshes, with errors possibly occurring at each merge.

Thus, in the next subsections, a quadratic configuration for cylindrical tow is chosen. This allows reducing the number of cylindrical tows to one which simplifies the conforming meshing procedure. The improved meshing will permit a more coherent comparison between the simulated effective permeability and the geometry's analytical value. Then, it is tested with quasi-impermeable and permeable tows (respectively 10^{-14} m^2 and 10^{-8} m^2, the extreme values used in this section). Comparison between the impermeable tow simulation will also permit to confirm the hypothesis of quasi-impermeability at very low tow permeability.

1.2.4 Impermeable tow simulation

For impermeable tow simulation, only the Navier-Stokes equation is necessary, therefore equation 1.16 is solved with $\boldsymbol{K}^{-1} = \boldsymbol{0}$. The boundary conditions are described on Figure 1.11.

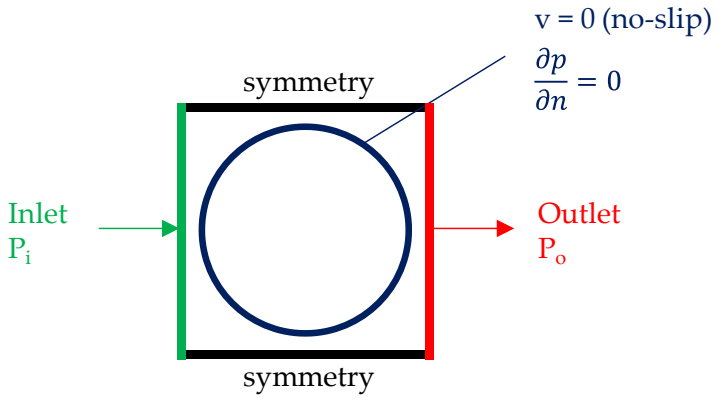

Figure 1.11. Boundary conditions for impermeable quadratic Gebart configuration.

The mesh will be dominated by hexahedrons with prisms to fit the curvilinear boundary. The mesh follows a quasi-2D configuration in which there is only one width element and symmetry boundary conditions are applied on surfaces transverse to the cylinder. Parameters

of the simulation are referenced in Table 1.4. The mesh has been realized on different level of refinement, ranked by the number of elements on the side (from 12 to 384 elements). For a configuration with 48 elements on one side of the squared geometry, the mesh is shown on Figure 1.12. The total number of elements is indicated in brackets on the first row of Table 1.5.

Table 1.4. Impermeable tow simulation parameters.

Meshing	(See Figure 1.12)
Number of elements	(See Table 1.5)
Dimensions	2.4*2.4 mm²
$\boldsymbol{\Delta P = P_i - P_o}$	1000 Pa
$\boldsymbol{\eta}$	2.37 Pa.s
$\mathbf{V_{tows}}$	54.5 %

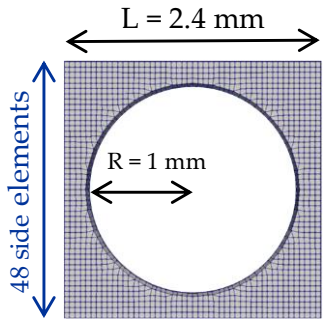

Figure 1.12. Mesh with 48 elements on the side for quadratic impermeable geometry and dimensions.

Following the transverse Gebart analytical permeability from Table 1.1, the geometry described in Figure 1.12 gives a theoretical permeability of $K_{\perp,q} = 7.11 \cdot 10^{-9}$ m^2. The results are displayed with the relative errors in Table 1.5. Here, the meshing configuration name refer to the number of elements on the side. Results shown Table 1.5 and Figure 1.13 demonstrate the convergence of the simulation when there are more than 16884 elements, with a converged relative error of -2.65 %. Therefore, the simulation slightly underestimates the geometry's permeability when compared to Gebart analytical expression. Multiple reasons may explain this gap. The first one comes from the way the theoretical expression was derived. Stronger hypotheses than Stokes' flow were employed to uses hydrodynamical lubrifaction laws and were further adapted for curvilinear surfaces. While the simulation parameters have been chosen to have creeping flow, calculations of the convective term may add some small numerical error as the inertial forces act oppositely to the viscous force, which in turn slows the flow speed and lower the permeability of the medium. Other reasons may include the geometry, as it is likely that the cylinder is not reproduced perfectly, and the simulation method in which small errors accumulates between discretization and resolution.

Table 1.5. Simulation converged effective permeability results and relative error compared to Gebart analytical value.

Meshing name (Number of elements)	192 (16884)	240 (26380)	384 (67168)
K_{eff} **[10^{-9} m^2]**	6.926	6.923	6.923
Relative error ϵ_r to theory [%]	-2.61%	-2.65 %	-2.65%
Analytical value ($K_{g\perp,q}(V_{tows})$) [10^{-9} m^2]		7.11	

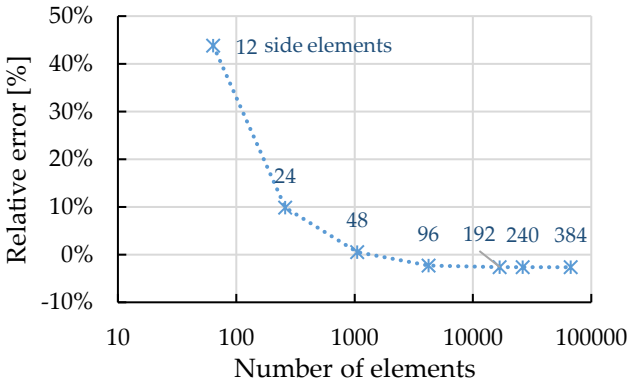

Figure 1.13. Simulation effective permeability error with relation to the number of elements in the mesh.

1.2.5 Quasi-impermeable tow simulation

Here, instead of a no-slip boundary condition around the cylinder, the flow inside the cylinder is calculated using equation 1.16 with a very low permeability of $\|\boldsymbol{K}\| = 10^{-14}$ m^2 for the cylinder as described by Figure 1.14.

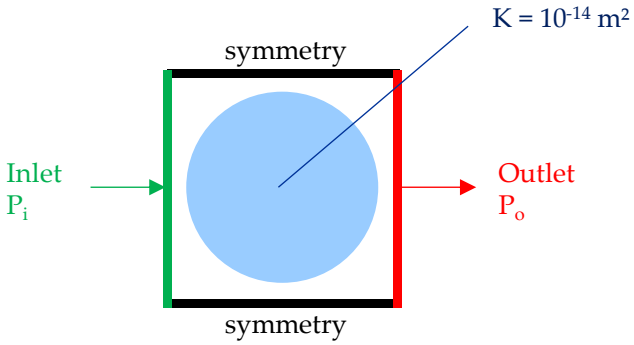

Figure 1.14. Boundary conditions and permeable zone definition for quasi-impermeable quadratic Gebart configuration.

The cylinder and the rest of the geometry are meshed separately but with the same parameters regarding the elements size and the conformation to the interface between the two geometries. The transport of numerical values at the boundary is achieved through the Arbitrary Mesh

Interface (AMI) technique present in OpenFOAM® which projects the interface elements surface between the different geometries [76,77]. First, results with non-refined meshing are presented (see Figure 1.15 for an example with 48 side elements).

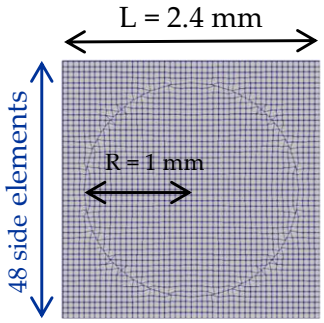

Figure 1.15. Mesh with 48 elements on the side for quadratic permeable geometry.

The results are presented in Table 1.6, and shows that the simulated effective permeability quickly approach Gebart's theoretical value. Therefore, the meshing employed in subsection 1.2.3 had results similar to the simulation with 48 elements on the side, which gives a mostly unconverged permeability result.

However, Figure 1.16 shows that even the most refined meshing (384 elements on the side) has likely not reached a converged value. Indeed, while the effective permeability is similar to Gebart theoretical permeability, it is slightly different from the converged permeability calculated with impermeable cylinders in section 1.2.4. It would be expected that with a quasi-impermeable simulation, its converged effective permeability value should approach the converged results from an impermeable simulation.

Table 1.6. Simulation effective permeability results and relative error compared to Gebart analytical value.

Mesh name (Number of elements)	48 (2304)	96 (9216)	192 (36444)	384 (147456)
$\boldsymbol{K_{eff}}$ **[10^{-9} m^2]**	8.67	7.75	7.35	7.13
Relative error ϵ_r to theory [%]	22.0	8.97	3.32	0.381
Analytical value for impermeable tows ($\boldsymbol{K_{g\perp,q}(V_{tows})}$) [$10^{-9}$ m^2]	7.11			

The relative error for the "384" quasi-impermeable simulation has a similar value to the "48" impermeable simulation. Therefore, the "384" quasi-impermeable configuration is far from convergence. As the total number of elements follows a quadratic growth for 2D representation, millions of elements could be needed to confirm convergence.

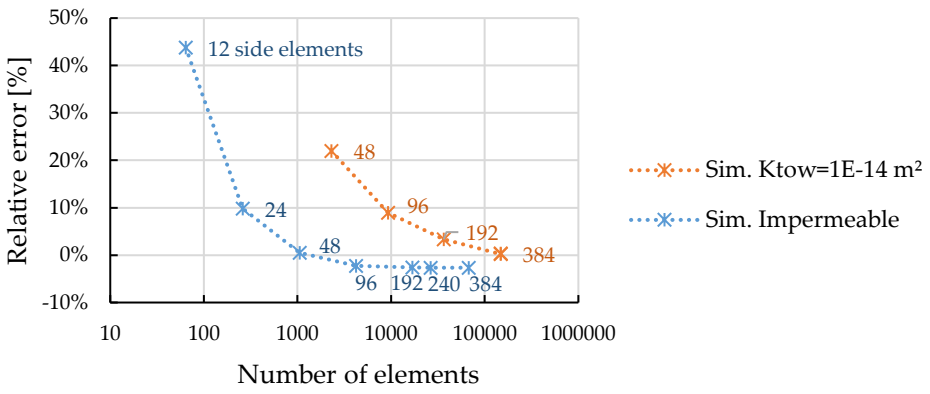

Figure 1.16. Simulation effective permeability error with relation to the number of elements in the mesh with a quasi-impermeable zone (orange) or an impermeable zone (blue).

Therefore, mesh refinement at the tow interface was sought to reduce the needed computer resource. Simulations with 240 elements on the side (the value was chosen following the impermeable configuration convergence), and with refinement on the interface inside permeable zone as shown in Figure 1.17 for "240i3", with "3" standing for the refinement level. A level *n* for refinement means *n* layers of refinement, with the third layer having a 2^{n+1} times denser mesh. The method of refinement was chosen following a study on the influence of different mesh refining and its performance is shown with the "240i3" meshing configuration, which gives a result nearer to the impermeable converged simulation with a similar number of elements with the "384" meshing configuration.

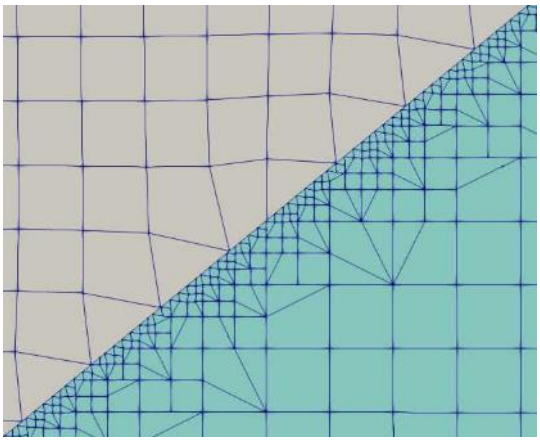

Figure 1.17. Zoom on mesh refinement for the simulation named "240i3".

In Figure 1.18, with "240i5" permeability value approaching the impermeable "240" configuration effective permeability and looking at the general tendency of the purple curve, it is assumed that the meshing is nearly converged. Indeed, the relative error decreases as low as 0.17 % (see results in Table 1.7). Thus, when the tow permeability is low compared to the geometry effective permeability, it may be approximated as an impermeable tow.

Table 1.7. Simulation effective permeability results and relative error compared to Gebart analytical value for refined mesh.

Mesh name (Number of elements)	240i3 (147988)	240i4 (427708)	240i5 (1543012)
K_{eff} [10^{-9} m^2]	6.961	6.941	6.935
Relative error ϵ_r to converged impermeable simulation [%]	0.55	0.26	0.17
Converged impermeable tows simulation ($K_{g\perp,q}(V_{tows})$) [10^{-9} m^2]		6.923	

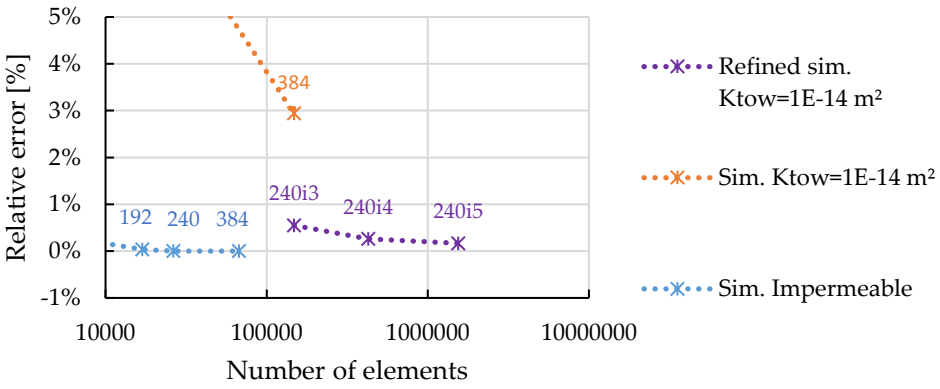

Figure 1.18 Simulation effective permeability error compared to converged impermeable simulation value with relation to the number of elements.

1.2.6 Permeable tow simulation

This time, the flow inside the cylinder is also calculated using equation 1.16, but with a higher permeability of $\|\boldsymbol{K}\| = 10^{-8}$ m^2 for the cylinder as described in Figure 1.19.

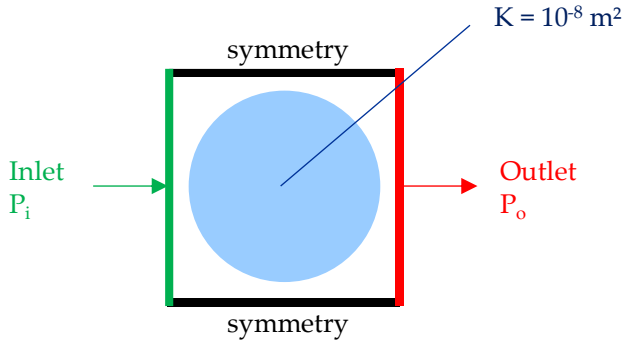

Figure 1.19. Boundary conditions and permeable zone definition for permeable quadratic Gebart configuration.

In this case, the value cannot be compared to Gebart analytical value. Therefore in Figure 1.20, it is the effective permeability of the domain which is shown with relation to the number of elements. Figure 1.20 shows that the permeability value convergence with increased meshing resolution follows a similar shape to the quasi-impermeable case (see the orange curve, Figure 1.16). It also shows that at the simulation named "384", the meshing has not been refined enough for the effective permeability value to converge.

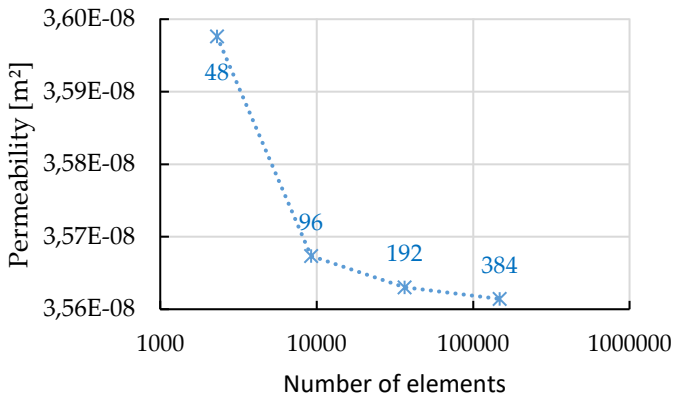

Figure 1.20. Simulation effective permeability error with relation to the number of elements in the mesh with a quasi-impermeable zone (orange) or an impermeable zone (blue).

However, the variation of the calculated effective permeability is very low, as the magnitude of the variation between the different simulations is only a few 10^{-10} m^2 (see Table 1.8). Moreover, the computed effective permeability is only a few times higher than the permeability of the cylinder.

Table 1.8. Simulation effective permeability results.

Meshing name (Number of elements)	48 (2304)	96 (9216)	192 (36444)	384 (147456)
$\boldsymbol{K_{eff}}$ **[10^{-8} m^2]**	3.598	3.567	3.563	3.561

Therefore, it is likely that the effective permeability value is much more influenced by the high permeability of the cylinder than the refinement of the meshing.

1.2.7 Discussion

OpenFOAM® resolution method for Navier-Stokes-Brinkman equation has been tested with geometry featuring ordered repartition of cylinders. Using precise meshing, it has been shown that the simulation can reach analytical values. At the same time, modelling the cylinders as a tow with permeability K_{tows}, its varying influence on the geometry effective permeability K_{eff} has been observed. Three cases can be distinguished, depending on the value of K_{tows} with relation to $K_{eff,imper}$ (the geometry permeability for impermeable tows). If the permeability of the tows is very low ($K_{tows} \ll K_{eff,imper}$), the geometry's permeability dominates, and $K_{eff} \approx K_{eff,imper}$. Therefore, to have satisfactory results, good geometry description is particularly important. If $K_{eff,imper} \gg K_{tows}$, the permeability of the tows becomes a much more important variable, and inversely, geometry description is less important to determine K_{eff}. For this configuration, $K_{eff} = O(K_{tows})$ has been observed (subsection 1.2.3 and 1.2.6). However, this assumption would need confirmation at lower K_{tows} and with different tow fraction volume. Finally, there is a transition phase when $K_{eff,imper} \sim K_{tows}$, which has not been studied in detail. However, it can be reasonably extrapolated that in this case, both geometry description and tow permeability are important.

1.3 Simulation in a realistic geometry

In this section, the simulation method is applied to a geometry obtained from a real textile reinforcement.

1.3.1 Original textile and geometry

A 3D representation of textile meshes was graciously given by Wilsen Wijaya (The University of Auckland, New Zealand, [21], Figure 1.21). It was acquired from a four layers stack E-glass plain weave specimen. Its nominal areal weight and tow linear density are respectively 800 g/m² and 2400 g/km. In the following text, a summary of relevant information coming from Wijaya's works on the textile ([21,37,78,79]) is realized.

Geometry acquisition

The acquisition was described by Wijaya et al. [37] and realized using an X-ray micro tomography (μCT) scanner. From the μCT scan which yielded volumetric data of the textile in grey-level form, they used an image processing procedure to separate the tows data from the air and convert it into a 3D object suitable for simulation. The geometry presented in Figure 1.21 is obtained from a mesh realised using a μCT scan of a textile sample. It has a global fibre volume fraction of 50% and was used in tow compression simulation study [78]. The original mesh had 121*211*158 voxels (or elements in a simulation framework). For subsequent simulations, every mesh realized will conserve the same ratio between thickness and area of the voxel (the volume thickness is 1/8 time its length and width). The 1/8 ratio was chosen by Wijaya [21] for its good geometry description.

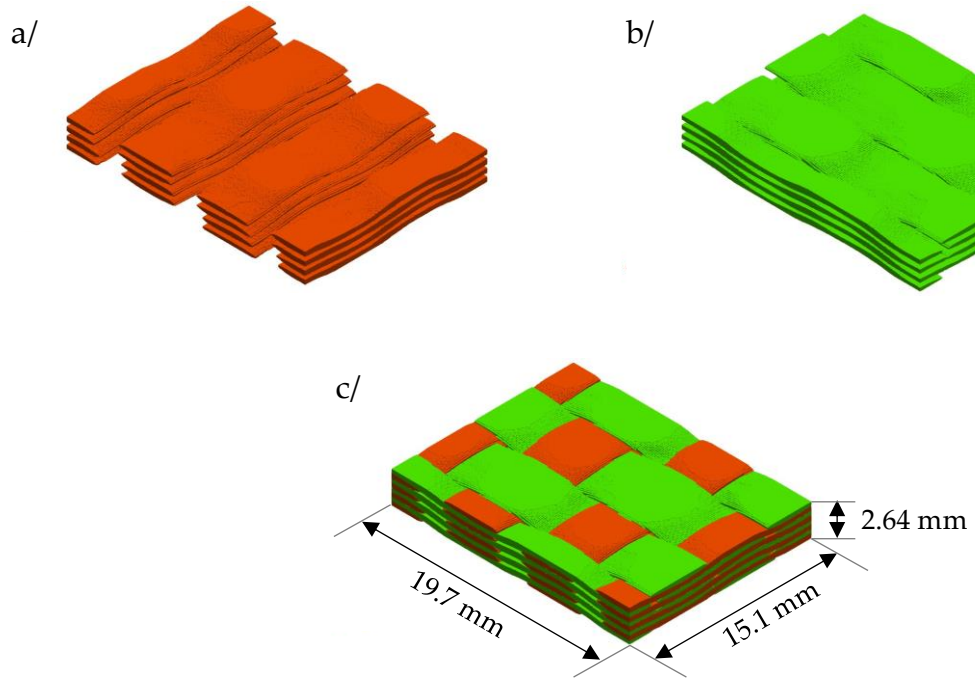

Figure 1.21. 3D tow geometries of the textile: a/ weft tows (orange), b/ warp tows (green), c/ both tows and dimensions.

In Figure 1.22 and Figure 1.23, a cross-sectional profile of the textile is shown along respectively warp tows and weft tows. A big asymmetry between the two cross-sections can be observed. There is much more space between warp tows, and more nesting along them. This discrepancy is expected to impact the sample permeability [80].

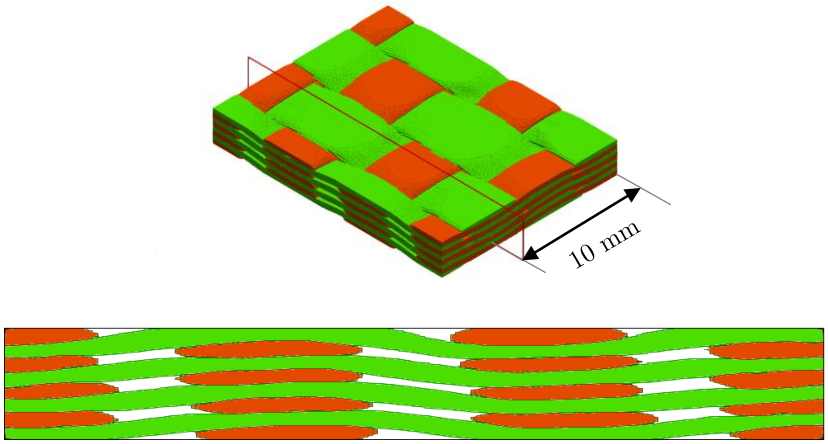

Figure 1.22. Position and cross-sectional observation of the textile geometry along warp tows.

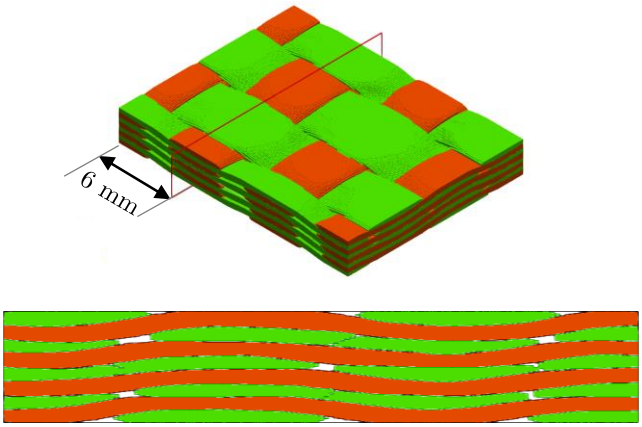

Figure 1.23. Position and cross-sectional observation of the textile geometry along weft tows.

Discrete fibre volume fraction and permeability

The fibre volume fraction V_f throughout the tows shown in Figure 1.24 was calculated in each voxel using the tow linear density and the surface description of the tows [21]. From V_f value in each voxel, Wijaya determined a longitudinal and transverse permeability throughout the tows thanks to Gebart analytical formulation for hexagonal cylinders arrangement (see Table 1.1) [21].

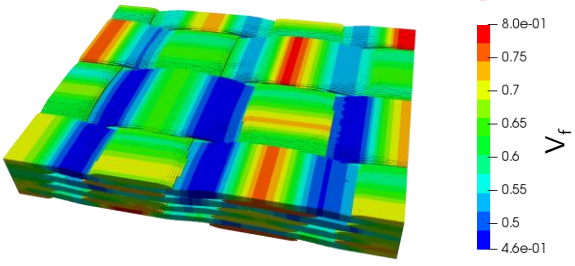

Figure 1.24. FVF inside the tows.

In Table 1.9, the value for both tow volume fraction in the domain and their sum is given. The geometrical volume fraction of the tows ($V_{warp}, V_{weft}\ and\ V_{tows}$) are calculated relatively to the volume of the rectangular parallelepiped domain of study (see Figure 1.19 c/) with $V_{channels}$ the volume fraction of the inter-tow channels. The value of V_{tows} is very high as it includes both the fibres' volume and the intra-tow channels' volume. Inclusion of voxels with low FVF in the tow geometry may also have inflated the value. $V_{domain} = 1$ is the sum of V_{tows} and the inter-tow channels. $V_{f,warp}$, $V_{f,weft}$ and $V_{f,tows}$ are respectively the FVF inside the warp, the weft and both tows. The overall FVF of the domain is obtained by calculating $V_{f,domain} = V_{tows} * V_{f,tows}$.

Table 1.9. Volume fraction of tows and fibre.

	Geometry volume fraction	FVF
Warp tows	$V_{warp} = 0.451$	$V_{f,warp} = 0.602$
Weft tows	$V_{weft} = 0.342$	$V_{f,weft} = 0.667$
Both tows	$V_{tows} = 0.792$	$V_{f,tows} = 0.631$
Tows + inter-tow channels	$V_{domain} = 1$	$V_{f,domain} = 0.500$

As the permeability in OpenFOAM® in later simulations is set by selecting the tows' volume, individual volumetric setting of permeability for each element was not practical. Thus, the average FVF was set instead of the discrete data. Moreover, the permeability values also needed averaging. Usually, for textiles, arithmetic or harmonic averages are proposed [81]. Such averages are relevant respectively for parallel configuration (textile stacking) or series configuration (textiles placed end to end) [82]. There is some order in the FVF repartition, and in a unidirectional flow simulation a combination of both averaging may be most pertinent. However, to simplify average calculation, the geometric average $\overline{K_g}$ (equation 1.24) has been used instead. It has been recommended for averaging in media with random permeability distribution in reservoir engineering [82,83]. In equation 1.24, h_i and k_i are respectively the thickness and the permeability of the individual volume.

$$\overline{K_g} = \exp\left[\frac{\sum_{i=1}^{n}(h_i \ln(k_i))}{\sum_{i=1}^{n} h_i}\right] \tag{1.24}$$

Averages were calculated separately for warp and weft tows, and for transverse and longitudinal permeability. As in average, the principal axes of the tows conformed to the axes of the domain, the permeability matrix was considered diagonal. The warp direction corresponds to the first principal direction and the weft direction to the second principal direction. Permeability matrices for the warp and weft tows are given in equation 1.25.

$$\begin{aligned} \bar{\boldsymbol{K}}_{\boldsymbol{tows,warp}} &= \begin{bmatrix} 7.68 \cdot 10^{-13} & 0 & 0 \\ 0 & 3.69 \cdot 10^{-12} & 0 \\ 0 & 0 & 7.68 \cdot 10^{-13} \end{bmatrix} \mathrm{m}^2 \\ \bar{\boldsymbol{K}}_{\boldsymbol{tows,weft}} &= \begin{bmatrix} 1.78 \cdot 10^{-12} & 0 & 0 \\ 0 & 3.59 \cdot 10^{-13} & 0 \\ 0 & 0 & 3.59 \cdot 10^{-13} \end{bmatrix} \mathrm{m}^2 \end{aligned} \tag{1.25}$$

Permeability tests on the textile

Permeability measurement have been realized by Wijaya [21] on the textile from which the geometry has been extracted. Two kinds of tests were realized, and the results with $V_f \approx 0.5$ are shown in Table 1.10. K_{warp} and K_{weft} refer to the permeability of the textile sample measured for flow in respectively the first and second principal direction.

Table 1.10. Permeability measurement results on the textile [21].

Type of permeability test	1D saturated experiment (steady-state)	2D saturating experiment (transient)
Fibre volume fraction	0.495	0.503
K_{warp} [10^{-10} m^2]	1.41 ± 0.15	1.31 ± 0.22
K_{weft} [10^{-10} m^2]	3.26 ± 0.60	2.88 ± 1.46

The 1D saturated experiment consisted in unidirectional flow of a heavy mineral oil inside the textile between opposite sides of a mould. It gives the saturated permeability calculated by evaluating the steady-state mass flow rate. The 2D saturating experiment was realized by central injection of the same oil. The unsaturated permeability is calculated instead, by measuring the front ellipse's semi-axes. Therefore, their slightly lower values compared to 1D saturated experiment result tend to indicate that viscous forces are more preponderant that capillary forces. More details on the tests can be found in the original work [21].

1.3.2 Impermeable tows simulation

To realize a simulation using the impermeable textile assumption, the mesh is realized by first creating a background rectangular mesh and then subtracting the tow geometry, which gives the meshed geometry shown in Figure 1.25.

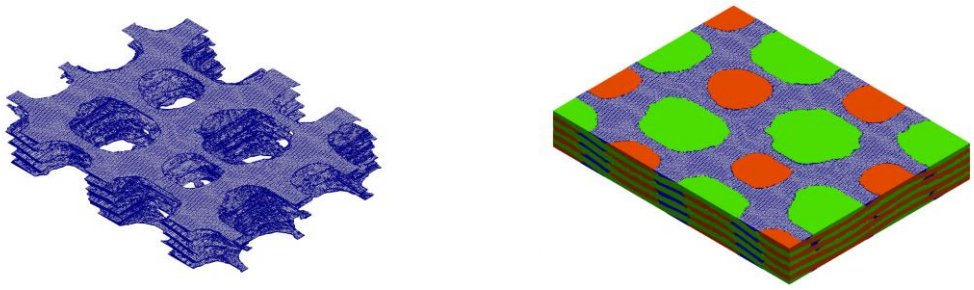

Figure 1.25. Example mesh (807225 elements) for impermeable tow simulation (left). The tows are shown indicatively with the mesh in the right-hand side figure.

The simulation method is the same as for simulations for impermeable cylinders described in subsection 1.2.4.

Boundary conditions

The boundary conditions were defined on the background mesh and stayed the same on the patches of the meshed geometry. They are defined according to the same hypotheses as the

quadratic impermeable simulation described in Figure 1.11. The upper and lower surfaces are considered to represent the mould; thus, they have a no-slip boundary condition with a normal pressure gradient equal to zero. The same boundary condition is applied to every surface representing the tow interface. Each transverse surface forms a pair with their opposite according to the flow direction and are either symmetry boundary conditions for periodicity enforcing or have inlet and outlet boundary conditions.

The flow is directed by a pressure gradient $\Delta P = 100$ Pa between the inlet and the outlet, and the viscosity is set to $\eta = 2$ mPa. s, which corresponds to the viscosity of ε-caprolactam reactive mix around 443 K (all details will be given in Chapter 2).

The boundary conditions for the simulation configuration for the warp and weft permeability determination are shown in Figure 1.26.

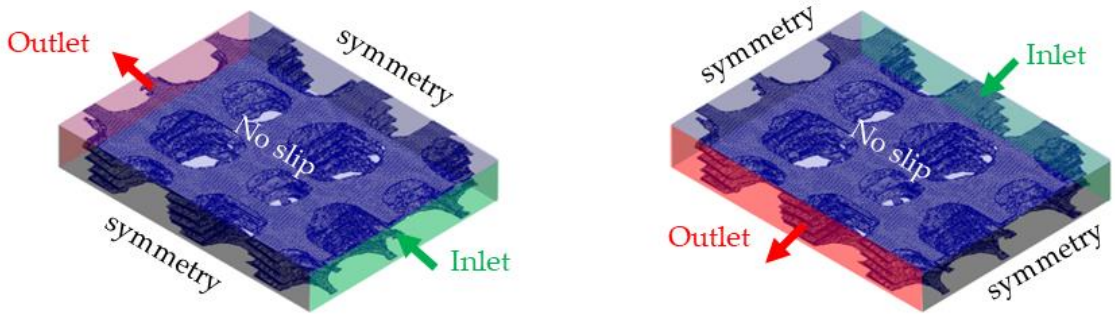

Figure 1.26. Boundary conditions for warp permeability determination (left) and weft permeability determination (right).

Simulation results and comparison with experimental results

To compare with experimental results, the effective permeability (based upon Darcy law) was calculated using equation 1.22 for each simulation. Simulation with various element numbers were realized to confirm the mesh convergence. The simulated permeability compared to the experimental results are shown in Figure 1.27, with the values detailed for each direction in Table 1.11 and Table 1.12.

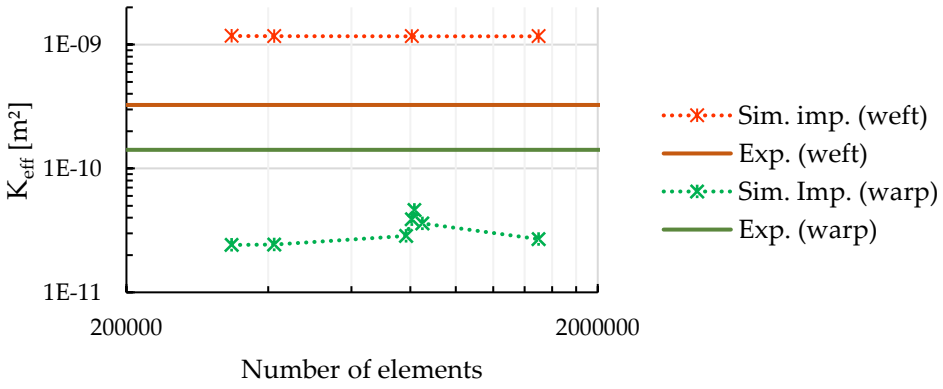

Figure 1.27. Effective permeability simulation for different number of elements compared to 1D saturated experiment by Wijaya [21].

Figure 1.27 shows that the simulation fails to predict the experimental permeability. The weft experimental permeability clearly overestimated, while it is underestimated in the warp direction. Moreover, in the warp direction, multiple results are shown for simulations around 800000 elements because of an anomaly in the results. Instead, in the weft direction, the mesh has converged without issue.

Table 1.11. Effective permeability simulation results along the weft tows direction for different number of elements compared to 1D saturated experiment by Wijaya [21].

Number of elements	334 511	412 001	807 225	1 499 547
$\boldsymbol{K_{eff,weft}}$ $\boldsymbol{[10^{-10}\ m^2]}$	11.8	11.7	11.7	11.7
$\boldsymbol{K_{weft,exp1D}}$ $\boldsymbol{[10^{-10}\ m^2]}$	3.26 ± 0.60			

Table 1.12. Effective permeability simulation results along the warp tows direction for different number of elements compared to 1D saturated experiment by Wijaya [21].

Number of elements	334 511	412 001	784 814	807 225	816 386	849 875	1 499 547
$\boldsymbol{K_{eff,warp}}$ $\boldsymbol{[10^{-10}\ m^2]}$	0.241	0.243	0.285	0.390	0.461	0.359	0.269
$\boldsymbol{K_{warp,exp1D}}$ $\boldsymbol{[10^{-10}\ m^2]}$	1.41 ± 0.15						

Both observations are likely explained by the textile sample geometry. Indeed, in the orthogonal cross-sections in Figure 1.28 and Figure 1.29, a huge assymetry in the size of inter-tow channel can be observed. They are much bigger along the weft tows than the warp tows, which results in much higher flow velocity and flow rate. Moreover, the discrepency in size is higher than the 2.3 ratio that would be suggested by experimental measurements (Table 1.10). As Darcy's law dictates proportionality between cross-section area and permeability (equation 1.22), the permeability in the weft direction is much higher than in the warp direction.

The very thin inter-tow also explains the anomaly around 800000 elements for simulated warp permeability. Indeed, in Figure 1.29 and Figure 1.30, the geometry difference between two meshes are highlighted with red ellipses. They are caused by the meshing algorithm that removes badly shaped elements, which are more likely to occur with very narrow geometries and lead to permeability underestimation if it cuts a channel. Thus, the highest obtained value for warp permeability is considered the most converged for the following discussions. The

issue is less important in the weft direction as the channels in this direction are sufficiently big to be well described (Figure 1.28) as shown by the quick convergence of the permeability values in this direction.

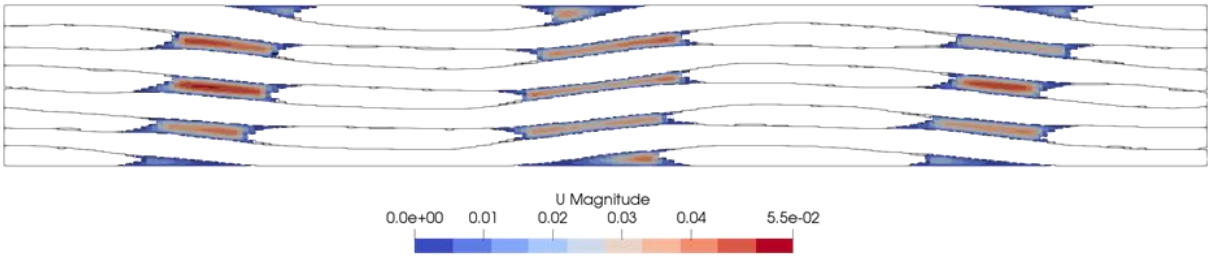

Figure 1.28. Cross section normal to the weft direction with velocity repartition for the 807225 elements simulation (see Figure 1.22 for position in the sample). The velocity magnitude is in $[m\ s^{-1}]$.

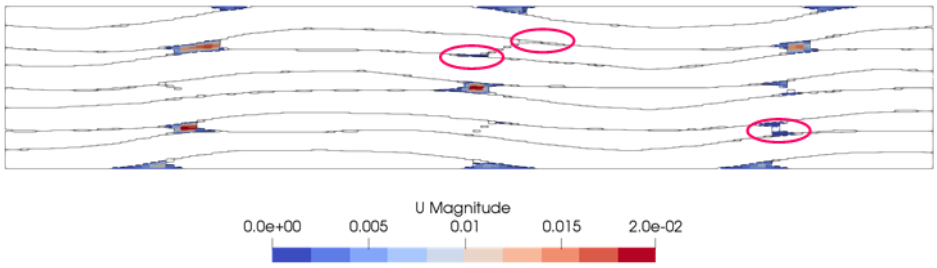

Figure 1.29. Cross section normal to the weft direction with velocity repartition for the 807 225 elements simulation (see Figure 1.23 for position in the sample). The velocity magnitude is in $[m\ s^{-1}]$.

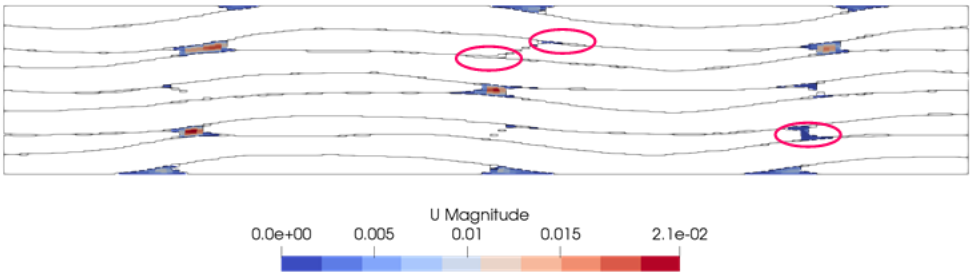

Figure 1.30. Cross section normal to the weft direction with velocity repartition for the 1 499 547elements simulation (see Figure 1.23 for position in the sample). The velocity magnitude is in $[m\ s^{-1}]$.

Therefore, it is likely that the digitalized sample geometry has a particular tow configuration which is not characteristic of the textile used for experimental measurement. As a workaround, Wijaya [21] used a representative geometry with a randomized ply repartition to perform similar flow simulations. As it reduced the asymmetry of the channels between weft and warp direction, the obtained results were more in line with their experimental results.

1.3.3 Permeable tows simulation

In this subsection, the tows are considered permeable in the simulations. Their effective permeability will be compared with the most converged value of the impermeable simulation ($K_{imp,weft} = 1.167 \cdot 10^{-9}$ m^2 and $K_{imp,warp} = 4.61 \cdot 10^{-11}$ m^2) since it has been established that

the geometry is not characteristic of the textile. The averaged permeability values (equation 1.25) are much lower than $K_{imp,weft}$, therefore quasi-impermeable results are expected in this direction. They are also lower than $K_{imp,warp}$ but to a lesser extent. With the high-volume fraction of tows (0.792), more deviation from the impermeable result may be observed.

Navier-Stokes-Brinkman and porosity

In section 1.1.4, the porosity was not included in equation 1.16 as it used the default implementation in OpenFOAM®. As it was used for saturated cases in theoretical configurations, the omission was acceptable. However, in this case, the tows' porosity $\tilde{\varepsilon}$ is known (Table 1.9), thus equation 1.26 was used (equation 1.10 without the Forchheimer term). It will also be necessary for unsaturated flow (section 1.3.4).

$$\frac{\rho}{\tilde{\varepsilon}}\left[\frac{\partial \bar{\boldsymbol{u}}}{\partial t}+\boldsymbol{\nabla}\left(\frac{\bar{\boldsymbol{u}}\cdot\bar{\boldsymbol{u}}}{\tilde{\varepsilon}}\right)-\nu\boldsymbol{\Delta}\bar{\boldsymbol{u}}\right]=-\boldsymbol{\nabla}p+\eta\boldsymbol{K}^{-1}\bar{\boldsymbol{u}} \tag{1.26}$$

The inclusion of porosity does not change the continuity equation and the solution method.

Simulation meshing and boundary condition

The simulation uses the same boundary conditions as for the impermeable simulation, which are recalled in Figure 1.31.

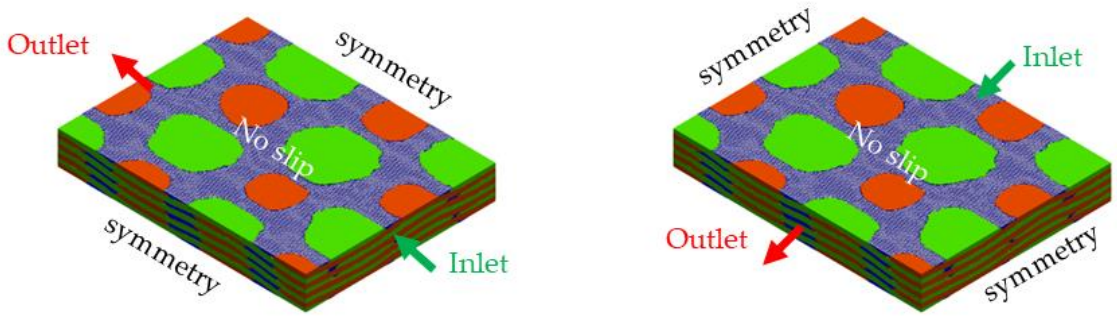

Figure 1.31. Boundary conditions for warp permeability determination (left) and weft permeability determination (right).

The meshing uses hexagonal elements with a ratio roughly equal to 1/8 between the element thickness and its length and width. No refinement has been realized as the high tow volume relatively to the domain makes it not as worth as it was in previous sections.

The permeable zones are achieved by integrating all elements that are inside the tow geometry. The interface elements (between the tows and the channels) are chosen depending on the surface orientation of the tows' geometry. Figure 1.32 and Figure 1.33 show a comparison between the 3D geometry (black borders) and the selected zone in the mesh with 154283 elements (in grey). The selected zones are faithful to the tows' geometry, although it is not perfectly reproduced, notably in Figure 1.33 where inter-tow description could be improved.

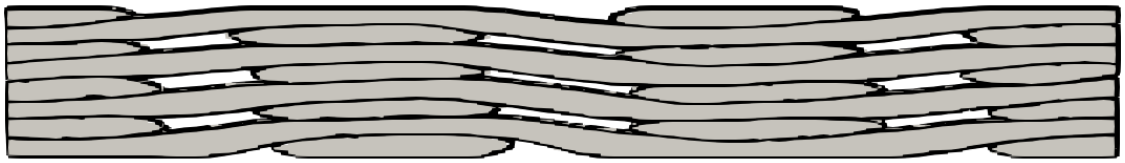

Figure 1.32. Comparison between 3D geometry tow geometry (black borders) and tows zone in the meshing (grey). Position of the cross-section is described in Figure 1.22.

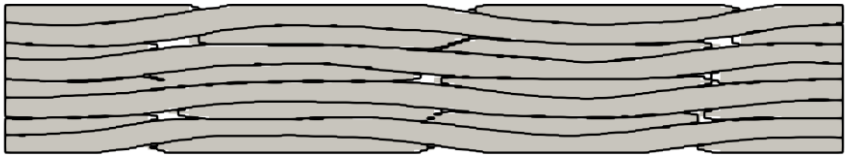

Figure 1.33. Comparison between 3D geometry tow geometry (black borders) and tows zone in the meshing (grey). Position of the cross-section is described in Figure 1.23.

Results

In Figure 1.27, the resulting effective permeability are shown compared to the converged effective permeability calculated with impermeable tow hypothesis. The numerical results are given in Table 1.13 for the weft direction and Table 1.14 for the warp direction. Due to practical issues, mesh convergence has not been reached, even with 4112376 elements. However, as expected with nearly quasi-impermeable tows, the values between the permeable simulation and the impermeable simulation are in the same order of magnitude.

The lowest value for $\boldsymbol{K_{eff,weft}}$ is lower than $\boldsymbol{K_{eff,weft,imp}}$ (Table 1.13). As theoretically, the effective permeability of the domain should be the lowest when the tows are considered impermeable, this difference is most likely caused by a bad representation of the tow geometry. Either the tows volume is underestimated in the permeable simulation, or it is overestimated in the chosen impermeable tow simulation.

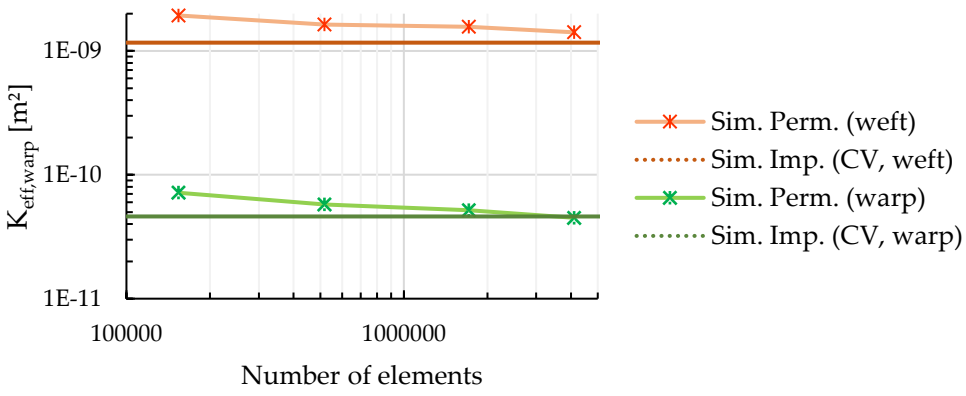

Figure 1.34. Effective permeability simulation for different number of elements with permeable tows compared to converged impermeable simulation.

Table 1.13. Effective permeability simulation results along the weft tows direction for different number of elements compared to converged impermeable value

Number of elements	154 283	517 280	1 717 200	4 112 376
$\boldsymbol{K_{eff,weft}}$ $\boldsymbol{[10^{-10}\ m^2]}$	0.716	0.578	0.517	0.450
$\boldsymbol{K_{eff,weft,imp}}$ $\boldsymbol{[10^{-10}\ m^2]}$	0.461			

Table 1.14. Effective permeability simulation results along the warp tows direction for different number of elements compared to converged impermeable value

Number of elements	154 283	517 280	1 717 200	4 112 376
$\boldsymbol{K_{eff,warp}}$ $\boldsymbol{[10^{-10}\ m^2]}$	19.3	16.3	15.6	14.1
$\boldsymbol{K_{eff,warp,imp}}$ $\boldsymbol{[10^{-10}\ m^2]}$	11.7			

1.3.4 Unsaturated flow simulation with permeable tows

In this subsection, an example of unsaturated flow simulation with permeable tows is presented. To follow the saturation of the fluid throughout the domain, the Volume Of Fluid method (VOF) present in OpenFOAM® is slightly corrected for it to describe the conservation of saturation. It is written in equation 1.27 where $S_r = \alpha_r/\tilde{\varepsilon}$ is the resin saturation varying between 0 and 1, and S_g the gas saturation ($S_g = 1 - S_r$). $\overline{\boldsymbol{u}}_{\boldsymbol{r}}$ and $\overline{\boldsymbol{u}}_{\boldsymbol{g}}$ are the resin and gas averaged velocity. They are used to calculate the second divergence term which is used to compress the fluid/fluid interface [58,84].

$$\frac{\partial \tilde{\varepsilon} S_r}{\partial t} + \boldsymbol{\nabla} \cdot (\overline{\boldsymbol{u}} S_r) + \boldsymbol{\nabla} \cdot \left(\left(\overline{\boldsymbol{u}}_{\boldsymbol{r}} - \overline{\boldsymbol{u}}_{\boldsymbol{g}} \right) \tilde{\varepsilon} S_r S_g \right) = 0 \tag{1.27}$$

The unsaturated flow simulation followed the same configuration and boundary conditions as for weft permeability determination (Figure 1.31 (left)) and using the mesh with 154283 elements. The only difference is the initial conditions inside the domain, which became $S_g = 1$ (instead of $S_r = 1$ for saturated simulation). The gas properties were taken from air at 433 K ($\eta_g = 2.42 \cdot 10^{-5}$ Pa s, $\rho_g = 0.815\ \mathrm{kg\,m^{-3}}$). The simulation was conducted until the filling time reached 0.6 s. It is a little longer than the theoretical fill time $t_{f,warp}$ calculated in equation 1.28 from fill time expression obtained with Darcy's law [85]. As the simulation computation took more than half a day, full infiltration of the tows has not been calculated due to a lack of time.

$$t_f = \left| \frac{\tilde{\varepsilon}\eta L^2}{2K\Delta P} \right| \tag{1.28}$$
$$t_{f,warp}(154\ 283\ \text{elements}) = 0.59\ \text{s}$$

The results of the filling simulation are shown relatively to the tows in Figure 1.35. Surface tension forces were not considered (capillary number is infinite). The resin in red was the part of the domain where the saturation reached at least 50% ($\alpha_r > 0.5$). Figure 1.35 shows that only the inter-tow channels were filled, with the resin having reached the other end of the domain at $t = 0.6$ s. The tows did not have the time to be impregnated.

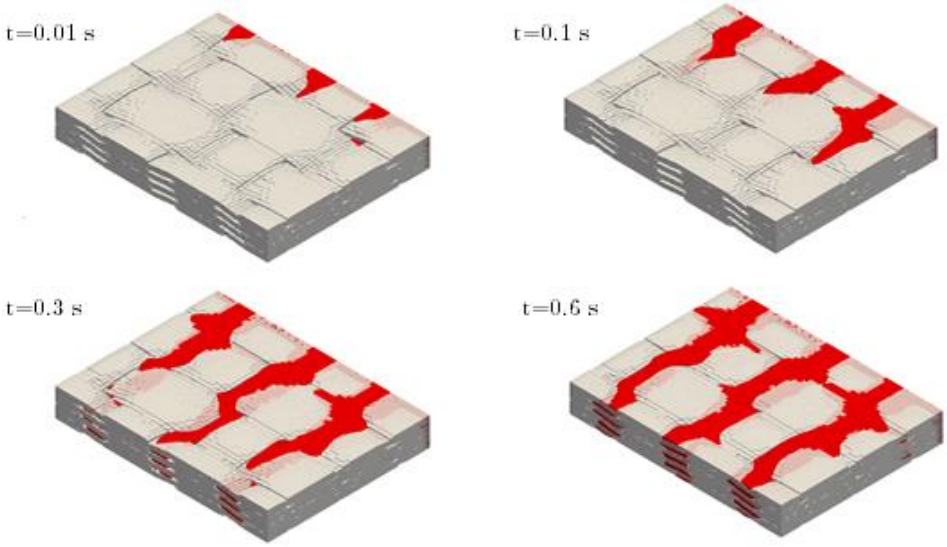

Figure 1.35. Filling simulation at different times. The tows are plotted in white, while the resin is represented in red.

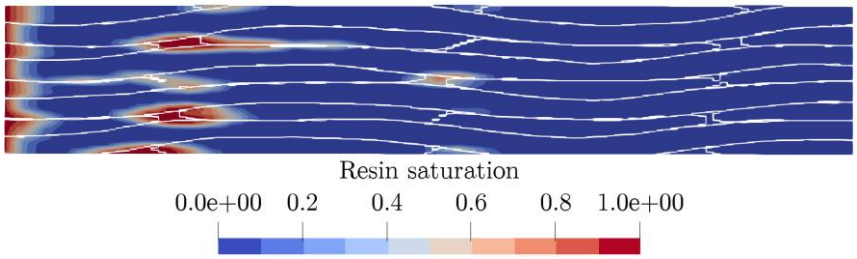

Figure 1.36. Resin saturation at $t = 0.6$ s for cross section in Figure 1.23

Thus, in Figure 1.37 the filling status is shown at different time for the median warp tows cross section. In this position, the weft tows are not present, thus the wide inter-tow channels allowed the resin to flow without resistance. It also shows that the tows have barely started to be filled, with mostly air present even at $t = 0.6$ s.

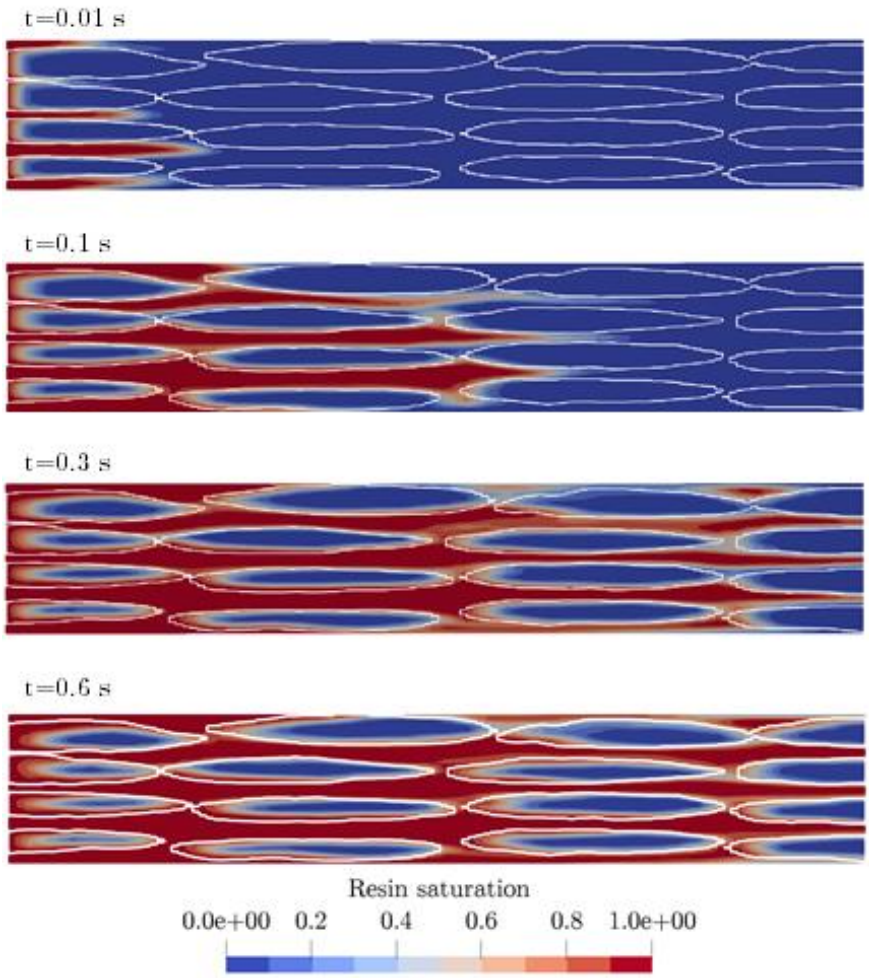

Figure 1.37. Resin saturation at different times for the weft tows median cross section.

Chapter conclusion

In this chapter, a review of resin flow modelling in a fibrous preform has been realized. Then, in order to conduct LCM process simulation with OpenFOAM®, the Navier-Stokes-Brinkman equation was tested in saturated conditions. Simulations have been conducted with cylinders arrangement that can be compared to Gebart analytical solution. The influence of the cylinder's permeability has been assessed and the results quality depending on the meshing evaluated depending on how permeable the cylinder is. The simulations showed that for a given tow geometry, effective permeability of the geometry with impermeable tow compared to the tow permeability gives information on the domain's permeability. With low enough permeability, the effective permeability of the domain can be approximated by supposing impermeable tows. Further work on this direction may involve study of different FVF, and more tow permeability values, as realized by Geoffre et al. [34]. Longitudinal flow instead of transverse could also be tested.

Then, the simulation is conducted on a geometry obtained using micro-tomography by Wijaya [21]. It is supposed that the geometry's particularity made the simulation unable to reproduce experimental results. An averaged geometry would be better suited for effective permeability determination. Acquisition of such a geometry was attempted by Wijaya by randomizing and correcting the position of the tows layers [21]. The simulation showed the particular importance of geometry description, and the influence of the inter-tow cross-section on the effective permeability on the preform.

The possibility for unsaturated simulation has been demonstrated at the end. It showed the widely different filling time between and inside tows as intra-tow filling barely started when inter-tow filling finished.

However, the study has been hampered by the complexity of the geometry and the high computational resources needed to converge. The high difference in flow velocities between intra-tow flow and inter-tow flow required very small timesteps to retain stable numerical resolution. This is especially true for unsaturated simulations, and particularly intra-tow flow simulation. Another issue concerns the capillarity effect which is not included in the unsaturated simulation. Depending on surface tension between the resin and the fibres, viscous forces and capillarity effects will compete and affect the unsaturated permeability.

Lastly, in this chapter most flows have been considered in theoretical conditions. For real applications, modelling may need to be tailored to experimental observations because of the many phenomena presents in such flows. Parameters such as capillarity, repartition of fibres in the mould, rate of tow absorption or displacement/deformation of the preform can all drastically affect the flow. Therefore, the resin and the preform and the conditions of the flow should be well characterized in order to be able to use adequate modelling and validate simulations. With quantifications of all these phenomena, simulation in a REV will be able to faithfully reproduce flow behaviour. At this point, they could be an useful tool to determine parameters such as storage and release of resin in a textile [67] for dual-scale simulations at macro-scale using the sink term approach.

Chapter 2

Reactive PA6 synthesis modelling

The section 2.4 goes over the optimized PA6 synthesis model parameters, which were first described in Han William, Quentin Govignon, Arthur Cantarel, et Fabrice Schmidt. « Efficient Polymerization and Crystallization Kinetics Coupling of Polyamide 6 Synthesis for Liquid Composite Molding Process Modeling ». *Polymer Engineering & Science* 62, nº 4 (04/2022): 999-1012. https://doi.org/10.1002/pen.25901.

Modelling PA6 synthesis aims to predict the polymerization and crystallization kinetics to evaluate reaction time, exothermy, and the polymer characteristics. As the phenomena closely interact with each other, the modelling strategy is of particular importance for good description and for implementation in process simulations.

In this chapter, we start by discussing the empiric models that have been used until now to try and tackle this problem. Vicard et al. [15,16] presented a comprehensive study of both experimental kinetics and kinetic models. Based on this work, an explanation of the dependency of crystallization to polymerisation looking at the kinetics scale of all involved phenomena is proposed. A new coupling method is detailed which propose a different interpretation of the crystallization kinetics than previous methods. Then, it is shown that it can be adapted to the difficulties of repeating the synthesis kinetics and an averaged model is proposed for further process simulation.

Finally, the kinetic influence in the PA6 rheology is succinctly reviewed and elements to understand and model it are given with the help of rheological measurement during PA6 synthesis [86].

2.1 State of the art of anionic synthesis of PA6 models

Crystallization can occur simultaneously during anionic polymerization of PA6 when the right conditions of temperature and polymer chains are met [87,88]. Thus, various strategies have been devised to measure and model the phenomena.

2.1.1 Description of the kinetics and experimental measurement

To model the reactive PA6 kinetics, experimental measurement must be conducted, and their results post processed. In the following section, normalized parameters for crystallization and polymerization modelling, and the experimental determination of the synthesis progress are described.

Parameters definition

In following equations, indexes p, c and r are used to refer respectively to the polymerization, the crystallization, and the whole reactive system. Exponents ∞ and 100% are used to differentiate between the state at the end of a synthesis and the theoretical total completion of polymerization or crystallization.

To normalize the description of the reaction, we define some parameters here. First, the final mass fraction of polymerization X_p^∞ or crystallization X_c^∞ can be defined by the ratio between the respective enthalpy at the end of the synthesis $\Delta H_{p,c}^\infty$ and the enthalpy for a theoretical total conversion of the system $\Delta H_{p,c}^{100\%}$ (equation 2.1).

$$\begin{aligned} X_p^\infty &= \frac{\Delta H_p^\infty}{\Delta H_p^{100\%}} \\ X_c^\infty &= \frac{\Delta H_c^\infty}{\Delta H_c^{100\%}} \end{aligned} \tag{2.1}$$

Thus, a normalized degree of polymerization a and crystallization b can be defined with relation to time in equation 2.2. $\Delta H_{p,c}(t)$ means the enthalpy at time t.

$$\begin{aligned} a(t) &= \frac{X_p(t)}{X_p^\infty} = \frac{\Delta H_p(t)}{\Delta H_p^\infty} \\ b(t) &= \frac{X_c(t)}{X_c^\infty} = \frac{\Delta H_c(t)}{\Delta H_c^\infty} \end{aligned} \tag{2.2}$$

The rate of polymerization $\dot{a}$ and crystallization $\dot{b}$ take the following definition, with $\varphi_{p,c}(t)$ the heat flux in equation 2.3.

$$\begin{aligned} \dot{a}(t) &= \frac{1}{\Delta H_p^\infty}\frac{d\Delta H_p(t)}{dt} = \frac{1}{\Delta H_p^\infty}\varphi_p(t) \\ \dot{b}(t) &= \frac{1}{\Delta H_c^\infty}\frac{d\Delta H_c(t)}{dt} = \frac{1}{\Delta H_c^\infty}\varphi_c(t) \end{aligned} \tag{2.3}$$

Experimental measurements

As polymerization and crystallization manifests themselves as exothermic phenomena, most studies used the adiabatic reactor method [89–91] to evaluate their influence based on the temperature variation. The difference between a reference temperature T_{ref} and the experimental temperature T_{exp} can be expressed by equation 2.4. It gives the synthesis

temperature T_s, which depends on polymerization and crystallization, and its relationship with reaction enthalpy can be obtained using the system's heat capacity.

$$T_{exp}(t) - T_{ref}(t) = T_s\big(a(t), b(t)\big) \tag{2.4}$$

More recently, the PA6 anionic synthesis has been studied using DSC [16], which allows accurate temperature control for isothermal or constant temperature rate measurement. It measures a heat flux φ_{exp} which, similarly to the aforementioned method, gives the polymerization and crystallization dependent synthesis heat flux φ_s (equation 2.5). This method was recently employed by Vicard et al. [15] and Humphry et al. [92].

$$\varphi_{exp}(t) - \varphi_{ref}(t) = \varphi_s\big(a(t), b(t)\big) \tag{2.5}$$

2.1.2 Interaction between crystallization and polymerization

Few studies of simultaneous polymerization and crystallization during reactive PA6 synthesis have been published. While polymerization influence on crystallization is self-explanatory, with crystallization being possible only if polymer chains exist (see Figure 2.1), polymerization dependence from crystallization is less evident.

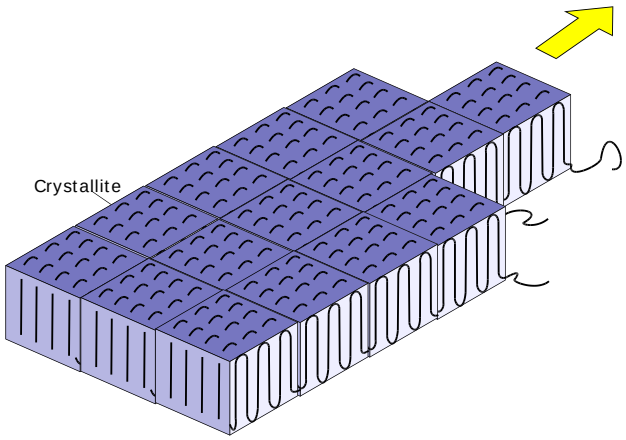

Figure 2.1. Crystal lamellae formation from polymer chains (black line) – yellow arrows indicate preferential crystal growth following temperature gradient [93].

However, possible influence of crystallization in polymerization has been evocated before [14]. The hypotheses about crystallization influence on polymerization usually consider that the crystalline phase does not physically or chemically interact with the polymerizing system. Instead, the presence of crystallization may change the situation of the reactive system: it feeds on polymer chains which will locally increase the concentration of reactants, thus affecting the polymerization kinetics. This is notably suggested by Wichterle et al. [87], based on their observation of a favourable discrepancy in the temperature dependency of the final monomer conversion rate if crystallization occurred simultaneously. They confirmed this hypothesis by correlating the final conversion rate of the amorphous phase. Another suggested influence of

crystallization would be local trapping of reactants, which could instead lower the monomer conversion rate during the synthesis [94] or at the end of the synthesis [2]. Vicard et al. experimental study [15] suggests that both mechanisms may be happening.

Nevertheless, all attempts described below of modelling polymerization and crystallization coupling have considered this effect as not significant enough.

2.1.3 Phenomena separation method

Regardless of the phenomena interactions between themselves, to model the simultaneous polymerization and crystallization phenomena, the synthesis reaction flux can be considered as the sum of the heat flux of these two phenomena since they are distinct (equation 2.6).

$$\varphi_s(t) = \varphi_p(t) + \varphi_c(t) \tag{2.6}$$

Thus, to model the PA6 anionic synthesis, a method of separation for polymerization and contribution to the increase in heat must be employed.

Dual asymmetric Gaussians

The first method presented comes from a mathematical observation of experimental reaction curves. It was initially proposed by Karger-Kocsis and Kiss [95] and was recently used by Taki et al. [96] and Humphry et al [92]. As it aims to reproduce the shape of experimental curves, it can produce good results. However, it comes with no answer about temperature, polymerization, and crystallization dependency of the separated method. Moreover, the latter study expressed the method limits when a third phenomenon, which they tentatively attributed to recrystallization or re-melting, altered the measurement curve shape.

Separation by subtracting polymerization contribution

The second method considers that polymerization is mostly independent from crystallization (which has been discussed in subsection 2.1.2). It comes from a better understanding of the lone polymerization phenomena, as crystallization does not occur if the synthesis temperature is high enough. Crystallization contribution is therefore obtained with equation 2.7.

$$\varphi_c(t) = \varphi_s(t) - \Delta H_p^{\infty} \dot{a}(t) \tag{2.7}$$

This method has been used multiple time in the literature [16,91,97–99], and we will discuss it further alongside its relation to crystallization modelling in subsection 2.1.5.

Separation by subtracting crystallization contribution

A last possibility would be to determine crystallization kinetics first from bulk polymer crystallization. Vicard et al. [16] notably observed that at temperatures where crystallization

occurs once polymerization has advanced enough, it behaved similarly to crystallization from melted polymer: if enough polymer has been synthetized, crystallization can be considered independent from polymerization. However, it is difficult to use when the phenomena are simultaneous since crystallization is limited by the amount of available polymer.

2.1.4 Polymerization modelling

To isolate the crystallization contribution in the aforementioned method, a polymerization model is necessary. Moreover, since polymerization is the driving force and most prominent phenomenon of the synthesis, a polymerization model is mandatory to model the reaction.

Historically, mechanistic approaches based on modelling anionic PA6 polymerization were first considered. They are based on trying to model the unfolding chemical reactions. For instance, such a method was employed by Greenley et al. [100].

However, semi-empirical models are much more popular due to their performance and the relative ease of parameter determination through numerical fitting. They follow an Arrhenius law at their core to ensure dependence to temperature. Thus, in this subsection, we will use the notation $k_{i\in\{1,2\}}$ to define a term following an Arrhenius law (equation 2.8), with the pre-exponential term A_i and its characteristic exponential fraction between the activation energy $E_{a,i}$ and the product of the temperature T and the ideal gas constant R.

$$k_i = A_i \exp\left(\frac{E_{a,i}}{RT}\right) \tag{2.8}$$

The most basic modelling, proposed by Wittmer et al. [89] considers that the rate of polymerization is proportional to the fraction of material that has not yet polymerized. Thus, the normalized form follows equation 2.9, where the Arrhenius law is weighted by the available reacting material left.

$$\dot{a} = k_1(1 - a) \tag{2.9}$$

Malkin and Camargo model

To achieve a more satisfactory modelling compared to experimental results, Malkin et al. [101] have enriched Wittmer's expression with an auto-catalytic term: B_0. It characterizes the acceleration of the reaction caused by the presence of growing polymer chains. It has been further expanded by Camargo et al. [102], with the degree of reaction n_p hypothesizing non-linear influence of already polymerized material (equation 2.10). This equation was able to fit experimental data in numerous studies of PA6 anionic synthesis in the literature [16].

$$\dot{a} = k_1(1 - a)^{n_p}(1 + B_0 a) \tag{2.10}$$

According to Malkin et al. [103], A_1 and B_0 can be defined with relation to the concentration of the activator $[A]$, the catalyst $[C]$ and the monomer $[M]_0$ with a pre-exponential factor K and a marker m of the degree of auto-catalysis during chain growth (equations 2.11).

$$\begin{cases} A_1 = K\dfrac{[A][C]}{[M]_0} \\ B_0 = \dfrac{m}{([A][C])^{1/2}} \end{cases} \tag{2.11}$$

Further parametrization of the model was considered regarding the value of B_0. Lin et al. [104] proposed equation 2.12 which is an attempt to weigh the autocatalytic parameter with the advancing polymerization. It also indirectly makes B_0 temperature dependent. However, in their comparison, it was not able to give better result than a constant B_0.

$$B_0(a) = \frac{B}{1 - Ba} \tag{2.12}$$

Kamal-Sourour model

Another way to parametrize the autocatalytic parameter is to use the Kamal-Sourour model [105] (equation 2.13), usually employed to describe thermoset curing. It was proposed by Teuwen et al. [91] as a better alternative to the Malkin and Camargo model.

$$\dot{a} = (k_1 + k_2 a^{m_p})(1 - a)^{n_p} \tag{2.13}$$

Compared to Malkin and Camargo model, where autocatalysis is linearly directed by the parameter B_0, in Kamal-Sourour model, the autocatalytic part is modelled as a side-reaction, with its own order and an Arrhenius thermodependance. This is better shown by rewriting the model to conform to Malkin and Camargo in equation 2.14.

$$\dot{a} = k_1(1 - a)^{n_p}\left(1 + \frac{k_2}{k_1}a^{m_p}\right) \tag{2.14}$$

The two added parameters may explain both Teuwen et al. [91] observations about its fitting capability and the lower use of the model even recently. Indeed, despite having less parameters, the Malkin and Camargo model has shown to be sufficient for modelling anionic PA6 reaction [14,106].

2.1.5 Coupled polymerization-crystallization modelling

After subtracting polymerization contribution to the synthesis, modelling crystallization is left. Contrary to what Taki et al. proposed [96], directly modelling a crystallization kinetics model to the crystallization contribution when they are coincident phenomena should not be done. In fact, since crystallization is dependent on the polymer chain availability, as mentioned in subsection 2.1.2, the crystallization model should show some dependence to polymerization. Korshak et al. [107] studied the crystallization dependence to polymerization and isolated their contributions using a gravimetric study. This led them to correlate polymerization and crystallization contributions using a piecewise linear function.

Bolgov-Malkin coupling

Korshak et al.'s study led Bolgov et al. [97] to propose a more general approach with equation (2.15), where the crystallization rate $\dot{b}(t)$ is linearly weighted by the polymerization degree, which should limit crystallization to the polymerized portion of a sample.

$$\varphi_c(t) = \Delta H_c^{\infty} \dot{b}(t) a(t) \tag{2.15}$$

Malkin et al. [98] used it with success by determining the crystallization rate model at temperatures where it happens independently from polymerization. This led both Lee et al. [99] and Teuwen et al. [91] to model the coupled polymerization-crystallization kinetics following the Bolgov-Malkin coupling.

However, Vicard et al. [16], also determining a crystallization model in conditions with no polymerization, were not able to fit the synthesis advancement using Bolgov-Malkin coupling. This is because of the conflicting timespans of the phenomena, since at lower temperatures, the crystallization of polymer chains occurs at such speed that blindly putting a crystallization model will results in equation 2.15 giving spurious results.

Hillier-Vicard coupling

To solve the aforementioned problem, Vicard et al. [16] adapted the Hillier coupling method, originally intended for describing primary and secondary crystallization [108] to model the crystallization rate (equation 2.16).

$$\dot{b}(t, a) = \frac{d}{dt} \int_0^t a(x_t) \frac{d\beta}{dx_t} (t - x_t) dx_t \tag{2.16}$$

In this equation, a local crystallization rate $\dot{\beta}$ is introduced, which expresses the difference of scale between the crystallization of already polymerized material and the global crystallization kinetics, which occurs on partially polymerized reactive materials. $\dot{\beta}$ is calculated following a crystallization kinetic model. The principle behind this method is that every part of newly polymerized materials will have its own local crystallization kinetic, and thus the global crystallization kinetic described by $\dot{b}$ should be the sum of these local kinetics. Then, the crystallization contribution to heat flux follows equation 2.17.

$$\varphi_c(t) = \Delta H_c^{\infty} \dot{b}(t, a) \tag{2.17}$$

However, this coupling still was not able to faithfully model the synthesis heat flow. Two modifications were employed by Vicard et al. [16] for better modelling. First, they added an initiation time $t_{c,0}$ for crystallization (equation 2.18), similarly described by Bolgov et al. [97]. It follows an Arrhenius like dependence to temperature (parameters A_t and E_t) and T_m^0 describe the equilibrium melting temperature of crystals.

$$t_{c,0} = A_t \exp\left(\frac{E_t}{R(T_m^0 - T)}\right) \tag{2.18}$$

Then, a diffusion factor f_d (equation 2.19) similar to the one used in thermosetting curing models to take the vitrification influence on crosslinking kinetics [109] was also added, where $C(T)$ determines the crystallization speed relative to polymerization while $D(T)$ determines the beginning of crystallization relative to polymerization.

$$f_d(a) = 1 - \frac{1}{1 + \exp\big(C(T)(a-1) + D(T)\big)} \tag{2.19}$$

Equation 2.16 is rewritten following equation 2.20 with the Heaviside function $\mathcal{H}$ to take these two modifications into account (if $x > 0$, then $\mathcal{H}(x) = 1$, else $\mathcal{H}(x) = 0$) . It aims to realize better crystallization description by delaying its kinetics relatively to polymerization.

$$\dot{b}(t,a) = \frac{d}{dt}\int_0^t \mathcal{H}\left(t - x_t - t_{c,0}(T)\right)(f_d * a)(x_t)\frac{d\beta}{dx_t}\big(t - x_t - t_{c,0}\big)dx_t \tag{2.20}$$

However, the need for a corrective factor shows the limitations caused by the lack of fine understanding of how crystallization initiates during polymerization. Another flaw lies in the complexity of the model; to find the crystallization rate, a convolution integral needs to be computed at each time step.

2.1.6 Crystallization modelling

To make better physical sense of the crystallization contribution, Malkin et al. [98] and Vicard et al. [16] used semi-empirical models to describe crystallization in fully polymerized material (also referred as bulk polymer crystallization). In bulk polymer, there is no distinction between local and global crystallization kinetics. If the whole system can be considered homogeneously polymerized and receive a homogeneous amount of energy, crystallization kinetics can be also considered homogeneous. Thus, the global and local normalized crystallization degree are equal in this situation. Since we use these crystallization models for local kinetics, in this section we will use the notation β to refer to the degree of crystallization.

The basis of most semi-empirical models for crystallization description was formulated by Avrami [110] (equation 2.21). $K_c[s^{-1}]$ refers to a thermodependant global speed parameter and is linked to germination probability and crystal growth speed, while n_c is characteristic on the kind and geometry of germination-crystallization.

$$\beta(t) = 1 - \exp(-(K_c(T)t)^{n_c}) \tag{2.21}$$

Hoffman-Lauritzen temperature dependency

To model the kinetic constant K_c dependence to temperature, Vicard et al. [16] used Hoffman-Lauritzen law [111], defined in equation 2.22 which is consistent with PA6 spherulite growth observations by Magill [112] and with fast scan DSC measurements [113,114]. They chose this model as it can take both macromolecular diffusion and nucleation into account from the glass transition temperature to the equilibrium melting temperature.

$$K_c(T) = K_0 \exp\left(-\frac{U^*}{R(T - T_\infty)}\right) \exp\left(\frac{-K_g(T_m^0 + T)}{2T^2(T_m^0 - T)}\right) \tag{2.22}$$

U^* [J mol^{-1}] defines the activation energy of macromolecular motion in the molten state, K_g [K^2] depends on the crystallization growth, T_∞ is the temperature under which no macromolecular movement is possible and T_m^0 is the equilibrium melting temperature of PA6 crystals.

Malkin crystallization model

Malkin et al. chose to adapt their polymerization model (equation 2.10) to calculate the crystallization kinetics as shown by the form of equation 2.23. It yields similar performance to Avrami model for low value of K_c [98] and considers autocatalysis of the crystallization kinetic with parameter C_0.

$$\dot{\beta} = \big(K_c(1 - \beta)\big)^{n_c}(1 + C_0\beta) \tag{2.23}$$

Nakamura model

Vicard et al. [16] used the Avrami model (equation 2.21) for isothermal crystallization modelling and proposed Nakamura et al. [115] formulation to generalize it for non-isothermal crystallization settings (equation 2.24).

$$\beta(t) = 1 - \exp\left(-\left(\int_0^t K_c\, T(x_t)dx_t\right)^{n_c}\right) \tag{2.24}$$

Then, as formulated by Patel et al. [116], Nakamura's equation's differential form follows equation 2.25.

$$\dot{\beta} = K_c\big(T(t)\big)(1 - \beta)n_c \ln\left(\frac{1}{1 - \beta}\right)^{\frac{n_c - 1}{n_c}} \tag{2.25}$$

Secondary crystallization

Crystallization is not a linear phenomenon, and previously mentioned crystallization models mostly rely on statistically describing the formation of crystals. However formed crystals can induce further germination which can lead to thicker lamellar structures and interlamellar crystallization [14]. It was notably hypothesized to occur in PA6 crystallization by Wichterle et al. [117] and suggested as a reason for misfit of aforementioned crystallization model by Vicard [14]. Thus, modelling secondary crystallization may be interesting for finer description of the thermal behaviour of PA6 synthesis. To model secondary crystallization, both crystallization phenomena were considered to be separate contributions to an overall crystallization kinetic [14]. Calling β_1 the primary degree of crystallization, and β_2 the secondary degree of crystallization, and β the overall degree, Velisaris et al. [118] consider the

crystallization kinetics to be parallel, and thus weigh linearly the two contributions in equation 2.26, each following their own kinetic:

$$\beta(t) = w_1\beta_1 + w_2\beta_2 \tag{2.26}$$

The two weights w_1 and w_2 follow $w_1 + w_2 = 1$ and aim to account for the relative importance of the two crystallization phenomena.

A more complex model, which inspired the Hillier-Vicard coupling method mentioned above (equation 2.16), considers that secondary crystallization is dependent of the existence of crystals formed with primary crystallization. Thus the overall secondary crystallization kinetic β_2, instead of following a simple kinetic law, will have the characteristic Hillier convolution integral [108], corresponding to the sum of individual secondary crystallization kinetics β_{2i} occurring as primary crystallization progresses (equation 2.27).

$$\beta_2 = \frac{d}{dt}\int_0^t \beta_1(x_t)\frac{d\beta_{2i}}{dx_t}(t - x_t)dx_t \tag{2.27}$$

2.1.7 External synthesis influences

The anionic polymerization of ε-caprolactam is known to be a very sensitive reaction, and some authors in the past even claimed non-reproducibility as a characteristic of the reaction [87]. This is because impurities can provoke parasitic side-reactions that inhibit polymerization [87]. Notably, the synthesis is very sensitive to the presence of humidity. Water can not only react and degrade the catalyst but can also terminates the propagation of growing polymer chains [14]. In fact Ueda et al. and Wilhelm et al. [119,120] observed that even a 0.1% increase of water content is capable of substantial increase of the synthesis duration. Thus, to maximize the polymer chains molecular weight Ueda et al. recommends in their study that water content in ε-caprolactam should not go above 0.013 mol%.

To model this inhibition, Wendel et al. [106] proposed an empirical modification of parameters A_1 and n_p in Malkin and Camargo model (equation 2.10), and related to a number c of reactive molecules with an inverse exponential law. A_{p0}, A_{p1}, n_{p0}, n_{p1}, t_A and t_n are numerically determined constants related to the availability of reactants (referred as molecules by Wendel et al.).

$$\begin{cases} A_1 = A_{p1}\exp\left(-\dfrac{c}{t_A}\right) + \mathrm{A}_{p0} \\ n_p = n_{p1}\exp\left(-\dfrac{c}{t_n}\right) + \mathrm{n}_{p0} \end{cases} \tag{2.28}$$

2.1.8 Conclusion

In the previous section, we described the different tools used in the literature to model the PA6 anionic synthesis. This allowed deeper insight of kinetics model used for each phenomenon.

In Vicard et al.'s experimental and modelling work [14–16], a modelling strategy to simulate the kinetic behaviour of PA6 synthesis was devised. The steps of this strategy were all described in this section. It involved the use of Malkin and Camargo model for polymerization with Nakamura-Hoffmann-Lauritzen crystallization model. Polymerization influence on crystallization was accounted using a modified Hillier coupling (equation 2.17) and polymerization and crystallization were separated by supposing that polymerization was independent. With experimental comparison, they demonstrated the performance of their strategy. Therefore, the same polymerization and crystallization models were employed in this study and their chosen parameters are described in section 2.2. Because of the difficulties of numerical integration of Hillier coupling method in simulation strategies (more information on subsection 3.2.2), other methods are discussed, and an alternative is proposed (section 2.3). Then, as the experimental variability cannot be neglected, their accounting is discussed in section 2.4, with improved parameters determination of corrective parameters.

2.2 Initial isothermal synthesis modelling

As aforementioned, modelling derived in Vicard's previous works [14–16] is used as a basis in the following study. Therefore, some parameters are used directly, and described in the following section.

2.2.1 Experimental procedure

Reactants

The reactants used for PA6 polymerization came from components provided by Brüggemann Chemical which are summarized in Table 2.1. The ratio of both the catalyst and the activator were defined at 0.79/1.10mol.% of the monomer. It was chosen by Vicard [14] because of it offers good compromise between the polymerization initiation time and synthesis duration.

Table 2.1. Components of the PA6 reactive mix..

Chemical compound	Function	Commercial name
ε-caprolactam	Monomer	AP-Nylon®
caprolactam magnesium bromide	Catalyst	Nyrim C1®
bifunctional hexamethylene-1,6-dicarbamoylactam	Activator	Brüggolen C20P®

Isothermal heat flow measurements

Using DSC measurement, the global heat flow φ_s of the synthesis was recorded multiple times at temperatures with a 10° interval between 403 K and 473 K. In Figure 2.2, one sample DSC curve is displayed for each tested isotherm. The isotherms are divided between syntheses at high and low temperatures, and the 433 K isotherm is shown in both figures to compare scale. At 473 K, only one peak is distinguishable which can be safely attributed to polymerization as crystallization barely occur at this temperature. At 463 K, a second peak can be barely distinguished. It is much more distinguishable at 453 K. In both cases, the second peak

corresponds to the slow crystallization kinetics. The lower the temperature, the faster crystallization starts relatively to polymerization, and thus between 423 K and 443 K, the two peaks merged into one. Finally, at 403 K and 413 K, crystallization starts so early relatively to polymerization that its peak is distinguishable before the polymerization peak.

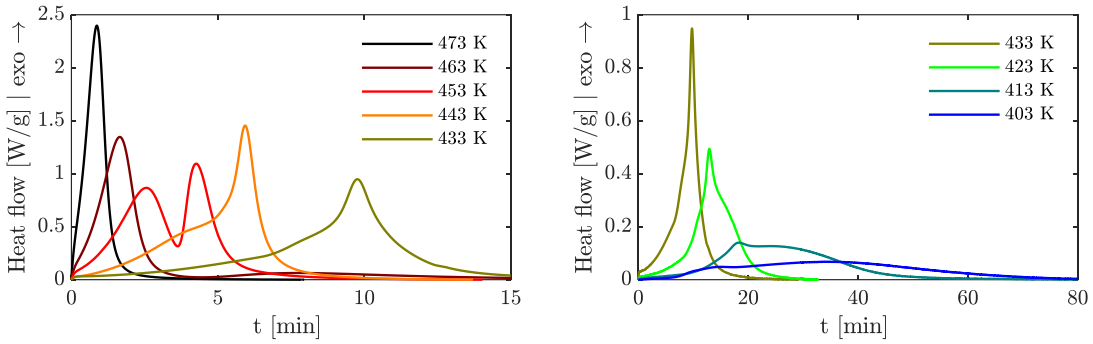

Figure 2.2. PA6 global synthesis kinetics measured in isothermal conditions using DSC [15]. Isotherms 473 K to 433 K are shown in the left, and isotherms 433 K to 403 K are shown in the right.

2.2.2 Parameters determination

Reaction enthalpies, conversion, and crystallinity

To obtain average reaction enthalpies, Vicard et al. [15] first obtained the mass ratio of polymerization X_p^∞ with thermogravimetric analysis (TGA) on the residual monomer. This allowed them to deduce $\Delta H_p^{100\%}$ at 463 K and 473 K where polymerization and crystallization are clearly decoupled. Then ΔH_p^∞ is calculated following equation 2.1. Following equation 2.6, we can consider that the synthesis enthalpy ΔH_s^∞ can be obtained from the sum of the polymerization and crystallization enthalpies (ΔH_p^∞ and ΔH_c^∞). Thus, by melting the sample after the synthesis, the crystallization enthalpy was obtained by subtracting the polymerization enthalpy from the fusion enthalpy. It was then approximated with a positive second-degree polynomial. Finally, the final degree of crystallinity X_c^∞ is obtained with equation 2.1 with the theoretical total crystallization enthalpy [121]. The parameters are compiled in Table 2.2.

Table 2.2. Polymerization and crystallization enthalpy.

Parameters	Value	Unit
X_p^∞	94.2 ± 1.4	$wt\%$
$\Delta H_p^{100\%}$	123.5 ± 4.1	$[\mathrm{J\,g^{-1}}]$
$\Delta H_C^{100\%}$	230	$[\mathrm{J\,g^{-1}}]$
$\Delta H_c^\infty(T)$		
$T \in [365.3\ \mathrm{K}, 472.3\ K]$	$-0.0354T^2 + 29.651T - 6107.5$	$[\mathrm{J\,g^{-1}}]$
$T \notin [365.3\ \mathrm{K}, 472.3\ K]$	0	

Synthesis model

To determine the crystallization model, Vicard et al. [16] used crystallization data obtained from molten polymer samples heated at temperature between 453 K and 463 K, temperatures at which crystallization occurs sufficiently late to be considered independent to polymerization. They confirmed this independence by showing the coincidence between the shapes of crystallization peaks obtained from bulk polymer and those obtained from full anionic synthesis of PA6. The parameters U^*, T_∞ and T_m^0 come from literature values of PA6 properties [122]. Therefore, they were able to numerically determine parameters with a least-square method for a combined Nakamura-Hoffman-Lauritzen model and for the crystallization initiation time (equations 2.18, 2.22, and 2.24), compiled in Table 2.3.

Table 2.3. Parameters of the crystallization model.

Parameters	Value	Unit
n_c	1.59	$[-]$
K_0	1.34×10^7	$[\mathrm{s}^{-n_c}]$
K_g	9.15×10^4	$[\mathrm{K}^2]$
U^*	6300	$[\mathrm{J\ mol}^{-1}]$
T_∞	293.15	[K]
T_m^0	533.15	[K]
A_t	5.17×10^{-2}	$[\mathrm{s}^{-1}]$
E_t	4.45×10^3	$[\mathrm{J\ mol}^{-1}]$

To determine the polymerization model, they determined preliminary parameters at temperatures where polymerization is nearly fully decoupled from crystallization, namely at 463 K and at 473 K.

Table 2.4. Parameters of Malkin and Camargo model determined independently from crystallization.

Parameters	Value	Unit
A_1	1.34×10^7	$[\mathrm{s}^{-1}]$
E_a	9.15×10^4	$[\mathrm{J\ mol}^{-1}]$
B_0	73.9	$[-]$
n_p	1.1	$[-]$

Then, they proposed another set of parameters (Table 2.5), alongside values for the diffusion factor (equation 2.19) determined using a Hillier type of coupling for polymerization and crystallization model following equations 2.6, 2.17 and 2.20. Because of the difficulty coming

from averaging the different DSC measurements, the model was fitted with one chosen measurement at each temperature.

Table 2.5. Updated Malkin and Camargo model parameters, determined concurrently with crystallization.

Parameters	Value	Unit
A_1	1.86×10^7	$[s^{-1}]$
E_a	9.12×10^4	$[J\ mol^{-1}]$
B_0	47.4	$[-]$
n_p	1.14	$[-]$

Comparing parameters from Table 2.4 and Table 2.5 we can see similar values for E_a and n_p while the values for A_p and B_0 are different. This means that the thermodependency and nature of shape will be similar. Instead, it is the width and position of the peak, defined by A_1 and B_0 that will be the main difference between the two parametrizations. This is shown in Figure 2.3, where simulated polymerization heat flows are computed using Malkin and Camargo model (equation 2.29) with values from Table 2.2 for polymerization enthalpy. The results at temperatures where the polymerization peak is distinct from crystallization are compared with an experimental measurement of the synthesis heat flow.

$$\varphi_p(t) = \Delta H_p^{\infty} \dot{a}(t) = X_p^{\infty} \Delta H_p^{100\%} k_1 (1-a)^{n_p} (1 + B_0 a) \tag{2.29}$$

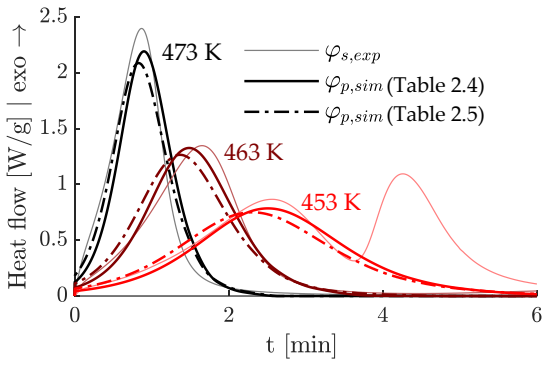

Figure 2.3. Comparison between one experimental measurement of the synthesis heat flow ($\varphi_{s,exp}$) and simulations of polymerization heat flows with parameters of Table 2.4 and Table 2.5.

2.3 Study of polymerization and crystallization coupling and proposition of a new coupling method

For this study, we use the crystallization kinetic parameters described in Table 2.3 for the Nakamura-Hoffman-Lauritzen model. For the polymerization kinetic parameters of Malkin and Camargo model, we chose the parameters in Table 2.4 as they were determined specifically with polymerization curves. Therefore, they perform slightly better for describing the polymerization heat flow (see Figure 2.3).

2.3.1 About crystallization influence on polymerization

In Figure 2.4, the variation of the final degree of polymer conversion X_p^∞ at each isotherm tested is shown with relation to the final degree of crystallinity X_c^∞. The values and standard deviation (error bars) come from Vicard et al. [15].

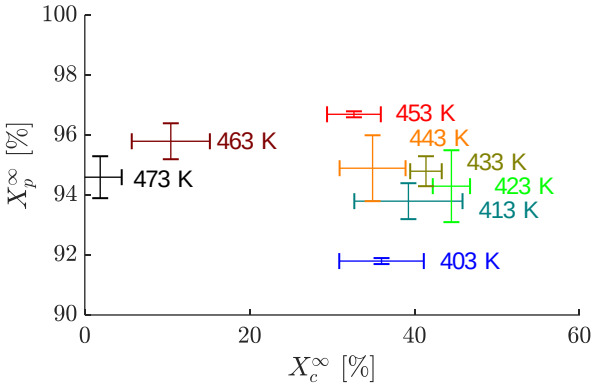

Figure 2.4. Average final degree of polymerization conversion compared to the average final crystallinity in synthetized DSC samples with error bars.

Interpretation of this figure can be done considering the hypotheses from the literature described in subsection 2.1.2. First, we observe the increase of the polymer conversion rate with the final crystallinity, between 453 K and 473 K. This would favor Wichterle et al. [87] hypothesis of PA6 crystals "not counting" in final monomer conversion, leading to a higher conversion rate. However, at temperatures lower than 453 K, as the final crystallinity stays in the 30-45% range, the polymer conversion rate decreases with temperature This suggests that reactants may be trapped by growing crystals as proposed by Davé et al. [94] and Van Rijswijk [2] which lowers conversion. Moreover, above 453 K, crystallization begins slowly towards the end of polymerization conversion if it is even still occurring. Instead, below 453 K, the lower the temperature, the earlier and the faster crystallization occurs relatively to polymerization [15].

Therefore, the following hypothesis seems likely: the presence of crystals is beneficial to polymer conversion only when the system has already mostly polymerized. Otherwise, the crystals will reduce the polymer conversion, probably by trapping reactants.

Even with these observations, the hypothesis of a constant mass ratio of polymerization was kept to simplify the subsequent models, and consequently that polymerization is mostly independent from crystallization. First, modelling crystallization influence on polymerization would need finer comprehension of the inhibition mechanisms and confirmation of Wichterle et al. [87] hypothesis. But more importantly, as the polymerization conversion is very high and has low variability between 413 K and 473 K, taking the average mass ratio of polymerization ($\overline{X_p^\infty} = 94.2 \pm 1.4 wt\%$) gives good description of the synthesis. However, there is a risk of slightly misestimating polymerization rate, notably at lower temperatures where the crystallinity is high throughout the synthesis.

2.3.2 Phenomena time scale

To highlight the cause of complexity in coupled polymerization crystallization modelling, characteristic times for the kinetics can be calculated. The first we are going to define is the crystallization initiation time $t_{c,0}$ (equation 2.18). The second and the third one are the modelled durations of each kinetic. The duration of polymerization kinetics $t_{p,f}$ is approximated with equation 2.30, which is an alternative form of the Malkin and Camargo model for $n_p = 1$ (see Annex 1). Since the time scale evolves exponentially with relation to temperature, it allows good approximation of the duration, even if underestimated. $a_f = 0.999$ defines the threshold at which we consider polymerization to be completed, which was defined for a 99.9% completion of the phenomena.

$$t_{p,f} \approx \frac{1}{K_p(T)} \ln\left(\frac{1 + B_0 a_f}{1 - a_f}\right) \tag{2.30}$$

The duration of local crystallization kinetics $t_{c,f}$ can be calculated with equation 2.31 which is the sum of the crystallization initiation time, and the time obtained from the isothermal form of Nakamura model (equation 2.21). The threshold for completed crystallization was defined with $\beta_f = 0.999$.

$$t_{c,f} = \frac{1}{K_c(T)} \left|\ln\left(1 - \beta_f\right)\right|^{\frac{1}{n_c}} + t_{c,0} \tag{2.31}$$

These characteristic times can be compared to the experimental time of the synthesis t_{exp}, by defining the synthesis enthalpy with relation to time with equation 2.32.

$$\Delta H_s(t) = \int_0^t \varphi_s \, \mathrm{dt} \tag{2.32}$$

In order to reduce the effect of measurement noise, t_{exp} was defined for 99.9% of the total enthalpy recorded by DSC during the synthesis ($\Delta H_s\left(t_{exp}\right) = 0.999 * \Delta H_{s,total}$).

In Figure 2.5, we can see a comparison between the different characteristic times and the measured duration of the syntheses. Below 423 K simulated kinetic of crystallization for polymerized material is more than a hundred time faster than simulated polymerization. It stays faster than polymerization until 455 K, temperature at which crystallization duration overtakes polymerization duration in this simulation. Another interesting temperature to note is 468 K, temperature at which $t_{c,0} > t_{p,f}$ and above which crystallization and polymerization can be considered fully decoupled. Finally, we can see that experimental times can be approximated by the slowest phenomena between local crystallization and polymerization, at least under 463 K. At 473 K, the experimental synthesis time hovers around the crystallization initiation time. This is most likely because of the very low crystallization at this temperature which means 99% enthalpy is reached with barely any crystallization. Depending on how much crystallinity is achieved, the 99.9% enthalpy value would be reached at a different time of the simulated crystallization kinetic.

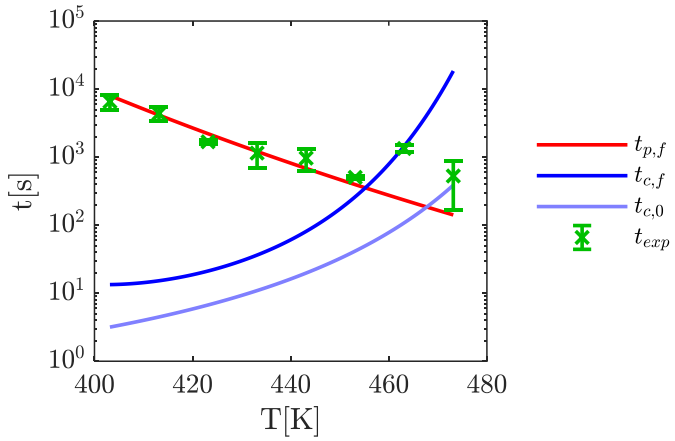

Figure 2.5. Comparison of the simulated different characteristic times and the experimental times of the syntheses.

2.3.3 Shortcomings of segregated and Bolgov-Malkin coupling

With the models described in subsection 2.2.2, the first two coupling models mentioned by Vicard et al. [16] are shown here to be unable to accurately describe synthesis. The first method is a basic segregated coupling model in equation 2.33 based on equation 2.6 which was employed as a basis of the model identification of Taki et al. [96]. In these methodologies, no difference is made between the global crystallization b and local crystallization β ($\dot{b} = \dot{\beta}$).

$$\varphi_s(t) = \varphi_p(t) + \varphi_c(t) = \Delta H_p^{\infty} \dot{a}(t) + \Delta H_c^{\infty} \dot{b}(t) \tag{2.33}$$

Similarly, what we will refer as the segregated Bolgov-Malkin coupling described in subsection 2.1.5 is defined following equation 2.34.

$$\varphi_s(t) = \varphi_p(t) + \varphi_c(t) = \Delta H_p^{\infty} \dot{a}(t) + \Delta H_c^{\infty} \dot{b}(t) a(t) \tag{2.34}$$

In these two methods, the crystallization rate is defined in equation with Nakamura-Hoffman-Lauritzen kinetics and with the crystallization initiation time, expressed with the Heaviside function $\mathcal{H}$.

$$\dot{b}(t) = \mathcal{H}\big(t - t_{c,0}\big) K_c\big(T(t)\big)(1-b) n_c \ln\left(\frac{1}{1-b}\right)^{\frac{n_c-1}{n_c}} \tag{2.35}$$

In Figure 2.6, the simulated heat flow shows that these two coupling methods do not resolve the different time scale between the synthesis kinetics and the local crystallization kinetics, as in both methods, crystallization finishes prematurely. Worse, because of the fast ending of local crystallization and the polymerization weight, the segregated Bolgov-Malkin coupling severely underestimates crystallization contribution to the heat flow.

This demonstrates the presence of a global crystallization kinetics spread along the advance of polymerization which cannot be described accurately by using local crystallization kinetics determined with bulk polymer in simple segregated coupling methods. Such methods can

only work when polymerization is nearly finished at the time crystallization starts. According to Figure 2.5, this threshold is around 468 K, temperature at which crystallinity is low (see Figure 2.4).

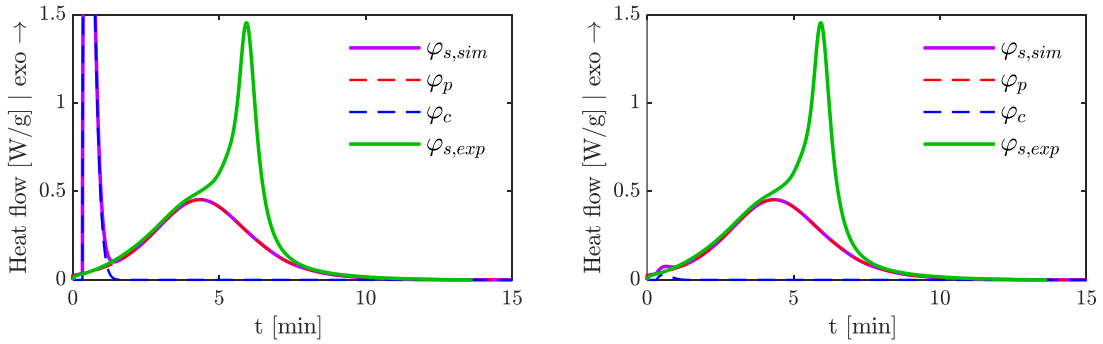

Figure 2.6. Comparison at 443 K between one experimental DSC heat flux and the simulated heat flux according to the segregated method (left) or the Bolgov-Malkin method (right) for polymerization, crystallization, and the synthesis.

Alternative interpretation of Bolgov-Malkin coupling

The segregated Bolgov-Malkin coupling seems to make little sense in its segregated form, as mentioned when discussing Figure 2.6, it gives worse result than the purely segregated method. To be more in line with the principle behind Bolgov and Malkin coupling, which is to weigh the crystallization rate with the polymerization progress, the crystallization rate should depend on the polymerization degree. Thus, instead of the form presented in the literature (equation 2.34), the Bolgov-Malkin coupling should also be defined using equation 2.36, but with an altered crystallization rate $\dot{b}$ dependent on polymerization as described with equation 2.37.

$$\varphi_s(t) = \varphi_p(t) + \varphi_c(t) = \Delta H_p^{\infty}\dot{a}(t) + \Delta H_c^{\infty}\dot{b}(t,a) \quad \text{with} \tag{2.36}$$

$$\dot{b}(t,a) = a(t)\mathcal{H}\left(t - t_{c,0}\right)K_c\left(T(t)\right)(1-b)n_c \ln\left(\frac{1}{1-b}\right)^{\frac{n_c-1}{n_c}} \tag{2.37}$$

This way, contrary to the form presented in equation 2.34, the crystallization kinetics will continue until b approaches one. Incidentally, equation 2.36 was most likely the de facto form that was identified by both Teuwen et al. [91] and Lee et al. [99], as they did not determine $\dot{b}$ from bulk polymer crystallization experiments, but by using the polymerization subtraction method from equation 2.7. Indeed, while crystallization can numerically be blocked from running its course, in a real situation, crystallization will occur regardless of the model flaws.

With crystallization kinetics defined independently from polymerization, (subsection 2.2.2), the simulated synthesis curves are obtained in Figure 2.7 at 443 K. However, as the evolution of $\varphi_{s,sim}$ shows, the crystallization simulation still occurs too early relatively to polymerization.

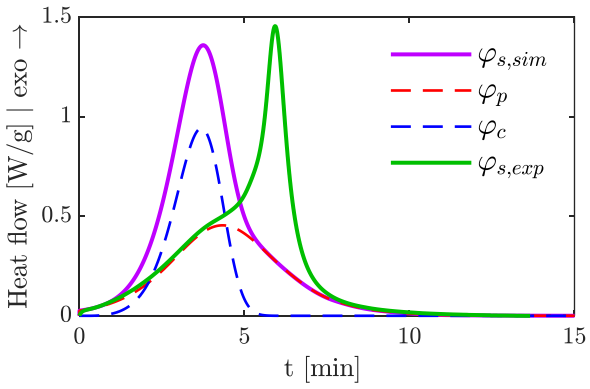

Figure 2.7. Comparison at 443 K between one experimental DSC heat flux and the simulated heat flux according to the alternative interpretation of Bolgov-Malkin method for polymerization, crystallization, and the synthesis.

The cause is that while the crystallization rate is weighted by the advancing polymerization, the Bolgov-Malkin method makes one questionable assumption. While the maximum crystallinity at the end of reaction will be the expected results, the method allows to have a degree of crystallization higher than the degree of polymerization ($b > a$). This means that at a given time, the crystallinity within the polymerized part can be higher than the final crystallinity ($X_c(T,t) > X_c^{\infty}(T)$). In other word, it defines the crystallization kinetics relatively to the whole reactive system as being crystallization ready, regardless of its polymerization status. This is in direct opposition with the postulate that crystallization only occurs within already polymerized chains.

2.3.4 A new coupling method for PA6 synthesis modelling

To solve the time scale difference between polymerization and crystallization phenomena, a solution was proposed by Vicard et al. [16] with the Hillier coupling method. It distinguishes between crystallization kinetics within each newly polymerized part, and global crystallization which is their sum as signified by the convolution integral (equation 2.16). However, because of the numerical difficulties involved with this convolution integral and the non-linear kinetic models (discussed in subsection 3.2.2), a more efficient coupling method is being sought.

This new coupling method is an improvement of the alternative Bolgov-Malkin coupling method with a similar delimitation between scales of crystallization considered by the Hillier-Vicard coupling model. Instead of starting a new crystallization kinetics at each time step, we relate the local crystallization degree β with the global crystallization degree b and a degree of polymer availability a_a with equation 2.38.

$$\beta(t) = \frac{b(t)}{a_a(t)} \tag{2.38}$$

Here, the degree of polymer availability a_a takes the crystallization initiation time into account to factor that newly formed polymerized chains need to reach a certain length before being available for crystallization. Then the global crystallization rate $\dot{b}$ is redefined in equation 2.36 with equation 2.40.

$$a_a(t) = a\big(t - t_{c,0}\big) \tag{2.39}$$

$$\dot{b}(t,a) = a_a \mathcal{H}\big(t - t_{c,0}\big) K_c\big(T(t)\big)(1-\beta) n_c \ln\left(\frac{1}{1-\beta}\right)^{\frac{n_c-1}{n_c}} \tag{2.40}$$

Thus, instead of considering the whole reactive system as polymerization ready, the local crystallization degree β defines how much crystallization has occurred within the polymerized part of the reactive system, while the global crystallization degree b defines how much crystallization has occurred relatively to the whole reactive mix. This is a slightly different definition of the local crystallization degree compared to the individual crystallization degree assigned to each newly polymerized part that make Hillier-Vicard coupling method so numerically heavy to compute. Instead, in equation 2.38, the value of the local crystallization degree is unified in the whole polymerized part, which is much more efficient calculation-wise.

In Figure 2.8, showing results of the new method, it can be observed that the crystallization heat flux $\varphi_c(t)$ is "subsequent" to the polymerization heat flux $\varphi_p(t)$. It is what was expected with equation 2.40 and which was not observed with previous coupling methods. However, the simulated heat flow $\varphi_{s,sim}(t)$ is still far from reproducing the shape of the experimental heat flow.

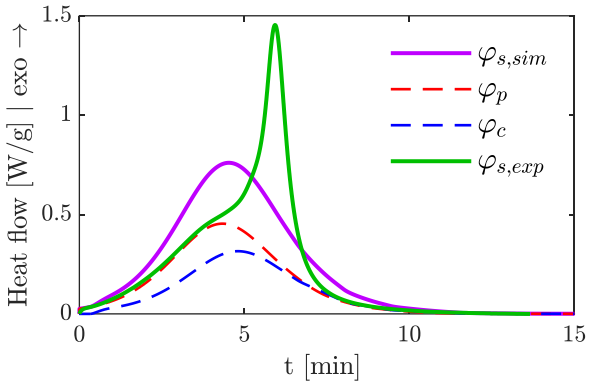

Figure 2.8. Comparison at 443 K between one experimental DSC heat flux and the simulated heat flux according to the new coupling method for polymerization, crystallization, and the synthesis.

Comparison with Hillier-Vicard coupling method

The global crystallization rate calculated by our new method with equation 2.40 can be compared with the global crystallization rate proposed by the Hillier-Vicard method without correction (equation 2.20 with $f_d = 1$). In Figure 2.9, we show the global crystallization rate for both methods at 443 K, 453 K and 463 K. Barring some numerical instabilities, it can be observed see that both methods have very similar curve shapes, with our new method modelling a slightly earlier crystallization compared to Hillier-Vicard. This is most evident at 453 K, where the two crystallization's rate curve can be clearly distinguished.

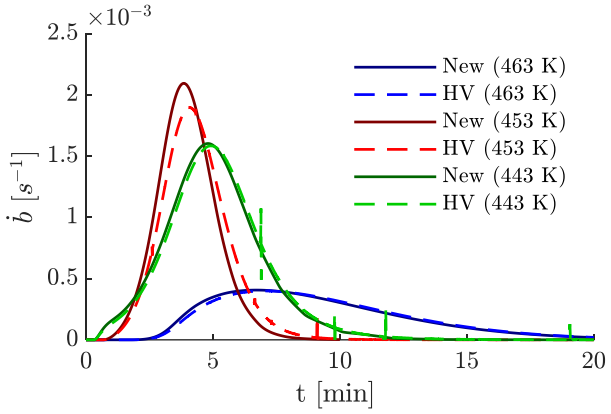

Figure 2.9. Comparison of global crystallization rate between the new crystallization coupled method and Hillier-Vicard (HV) coupling method at three isotherm (443 K, 453 K, 463 K).

To get more insight about the difference between the two models, we calculated both crystallization models at each degree between 403 K and 468 K and computed the coefficient of determination R^2 at these temperature between the two models. The results are shown in Figure 2.10 in which we can see that below 446 K, the coefficient of determination is higher than 0.995, demonstrating the very similar behaviour between the two methods at these temperatures. Over 446 K, the coefficient decreases until it reaches $R^2 = 0.9785$ at $T = 453\ K$ and then it increases and goes over 0.995 when $T = 463\ K$.

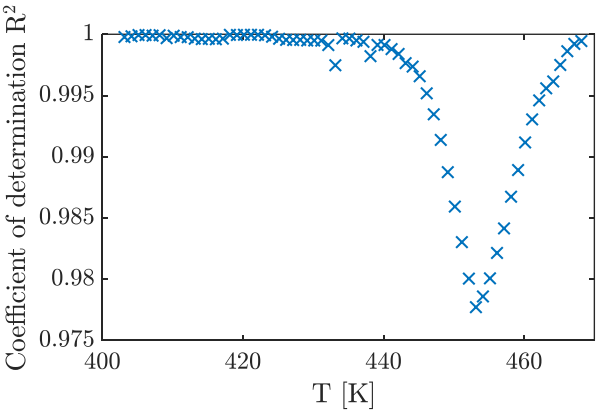

Figure 2.10. Coefficient of determination between equation 2.40 and 2.20 with $f_d = 1$ between 403 K and 468 K.

To interpret this curve, it is interesting to discuss the principle behind the two methods of modelling global crystallization. As mentioned before, with Hillier-Vicard method, the same local crystallization kinetic is attributed to each polymerized part, however its progress is dependent on its history. In the new method, the local crystallization kinetic is identical for the whole polymerized part and is instead dependent on the quantity of crystals relatively to the whole polymerized part. Therefore, while Hillier-Vicard coupling considers that each infinitesimal polymerized part will invariably crystallize the same way, the new coupling method considers that each new polymerized part will be taken along the ongoing crystallization kinetics. This means that in the new coupling model, existing crystals at a time slightly accelerate the crystallization kinetics as the local crystallinity density increases. It works in the same way than Wichterle et al. theory [87], in which crystallization increases polymerization conversion because of locally decreased amorphous polymer density.

As a direct consequence of the different crystallization mechanics described by the two methods, the correct way to explain Figure 2.10 should be by looking at where the duration of polymerization is compared to the duration of fully polymerized crystallization and the initiation time for crystallization. Below 442 K and above 468 K, the coefficient of determination is nearly equal to 1 (Figure 2.10). Figure 2.5 shows that below 442 K, the polymerized crystallization spans ten times less than polymerization. Therefore, the absence of difference between the two methods is explained by the speed at which polymerized materials crystallizes at these temperatures. On the other hand, above 468 K, Figure 2.5 shows that the crystallization initiation time overshoots the polymerization time, which means that the nearer the isotherm is to 468 K, the less coupling there is between crystallization and polymerization, and thus the less the coupling method matters. Hence, it is around 455 K that the coupling between crystallization and polymerization is most critical according to Figure 2.5. It is at these temperatures that crystallization starts early and slowly enough for the calculation method to visibly matter. However, even at these temperatures, the difference between the two methods is slight as $R^2 \geq 0.9785$ (Figure 2.10).

Diffusion factor

As our coupling method and Hillier-Vicard coupling method gives similar results, the diffusion factor described in equation 2.19 should also be able to improve our coupling method. As it works as a limiter of how much polymerized material is really available for crystallization, it can be integrated within a_a expression as described in equation 2.41 to slow the availability of polymer for crystallization, which in turn alters the calculation for local and global crystallization (equation 2.38 and 2.40).

$$a_a(t) = (f_d * a)\left(t - t_{c,0}\right) \tag{2.41}$$

Using Vicard et al. [16] parameters at 443 K for the diffusion factor ($C = 24.7$ and $D = 8.73$) we obtain the heat flow simulation shown in Figure 2.11, which offer the best description of the synthesis heat flow yet, and shows the necessity of reducing polymer availability for crystallization.

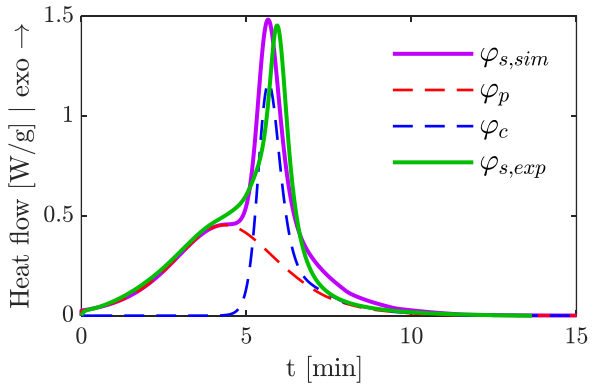

Figure 2.11. Comparison at 443 K between one experimental DSC heat flux and the simulated heat flux according to the new coupling method for polymerization, crystallization, and the synthesis.

2.4 Optimization of PA6 synthesis model

With the similarity of Hillier-Vicard and our proposed coupling method, it would be arguable to use the same parameters for the diffusion factor as proposed by Vicard et al. [16]. However, we observe different behaviour in measured DSC curves even within a same isotherm as shown in Figure 2.12 by the heat flow measurement realized at 433 K. Hence, chosen parameters were re-optimized to account for the diversity in experimental behaviour.

2.4.1 Variability of the measurements

The main cause of measurement variability is most likely residual humidity. Even with all the care in reducing moisture uptake before and during experimental measurement, drying components and working in inert atmosphere as much as possible, the reactive mix has proved to be very sensitive to water (see subsection 2.1.7 for other eventual possibilities).

However, comparing the average standard deviation of DSC measurements for the total heat of reaction ($\bar{\sigma}_{Q_{tot}} = 4.2\%$) and the synthesis duration ($\bar{\sigma}_{t_s(Q_{tot})} = 26.7\%$), we notice that only the synthesis speed is significantly variable. Moreover, looking at the values for each isotherm presented in Table 2.6, the magnitude of the standard deviations of reaction heat and synthesis duration show no significant correlation between themselves or temperature.

Since only the synthesis duration seems to be affected, as the heat flow curves seem to keep similar shape and area, we assumed that the cause of variability was solely caused by polymerization. Keeping the description of crystallization presented in subsection 2.3.4, in following optimizations local crystallization is assumed to occur regardless of polymerization rate variability. However, global crystallization is proportionally affected by polymerization rate variability because of its dependence on polymer chain availability.

Table 2.6. Total heat of reaction and crystallization enthalpy measured during the PA6 synthesis at different isothermal temperatures

Synthesis temperature T_{iso} [K]	**Total heat of reaction** Q_{tot} [J g^{-1}]	**SD of reaction heat** [%]	**Synthesis duration** $t(Q(t) = Q_{tot})$ [min]	**SD of synthesis duration** [%]
403	196.3 ± 11.1	5.7%	109.1 ± 27.4	25%
413	205.6 ± 14.5	7.0%	73.0 ± 16.5	23%
423	219.8 ± 3.3	1.5%	28.0 ± 1.9	6.8%
433	211.9 ± 1.8	0.9%	19.1 ± 7.6	40%
443	198.4 ± 8.3	4.1%	16.1 ± 5.7	35%
453	194.7 ± 6.3	3.2%	8.4 ± 0.4	4.4%
463	142.3 ± 10.1	7.1%	22.3 ± 2.7	12%
473	121.7 ± 4.5	3.7%	8.8 ± 6.0	68%

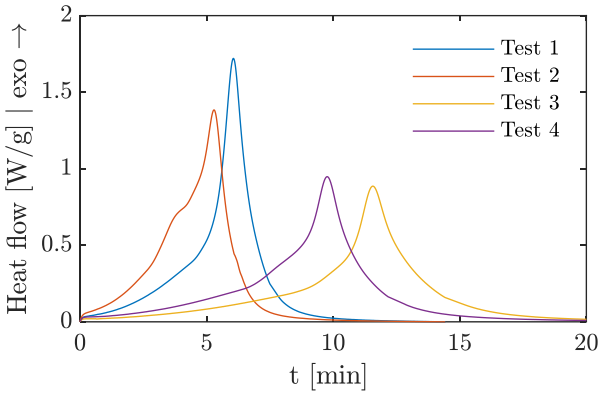

Figure 2.12. DSC measurements at 433 K.

2.4.2 Determination of parameters

As mentioned before, we suppose that local crystallization kinetics are not affected by the observed variability. Therefore, the phenomenon that may be susceptible to variability is polymerization, which will impact the polymerization model (Malkin and Camargo, equation 2.10) and the diffusion factor (equation 2.19) through polymer chains availability. Looking at Malkin and Camargo parameters, E_a is the least likely parameter to be affected by the variability factor, as a marker of temperature dependence of the reaction. Then, it is also unlikely that the reaction order n_p is affected much by the variability factor, as it indicates more a characteristic behaviour for the reaction than a characteristic speed. Accordingly, in Wendel et al.'s study [106] which so far is the only attempt found to take humidity into account in a polymerization model for anionically synthetized PA6 (subsection 2.1.7), the reaction order does not vary much ($1.05 < n_p < 1.14$). The most significant parameter they chose to modify is parameter A_1 while dismissing B_0 as independent from reactive molecules which is debatable (see equation 2.11 from Malkin et al. [103]). It is however the $A_1 B_0$ factorization that is the mathematical driving parameter of polymerization speed. As both Vicard [14] and Wendel et al. [106] parameters and models were determined simultaneously using strong numerical methods rather than mechanistic considerations, a similar approach was adopted to optimize the model.

Parameters t_i and a_i were introduced as respectively the initial time for polymerization initiation and the initial polymerization state. The former is added to investigate the possibility for an eventual polymerization initiation time as observed in experimental conversion curves conducted by Van Rijswijk et al. [20], while the latter is take into account eventual polymerization that could have happened during the preparation even if it was done at temperatures lower than 393 K. They also aim to correct eventual discrepancies in the measurements pre-processing. Then, parameter B_0 was used to account for the variability. As shown by Figure 2.13, optimizing B_0 rather than A_1 gives very slight improvement in the curve shape, which is not surprising given that A_1 is linearly linked to the model, while B_0 gap to linearity is $1/B_0$. Moreover, optimizing B_0 rather than A_1 allows to find an eventual thermodependency to the parameter missed by Vicard et al. [16] and which was considered by Teuwen et al. [91] with Kamal-Sourour model.

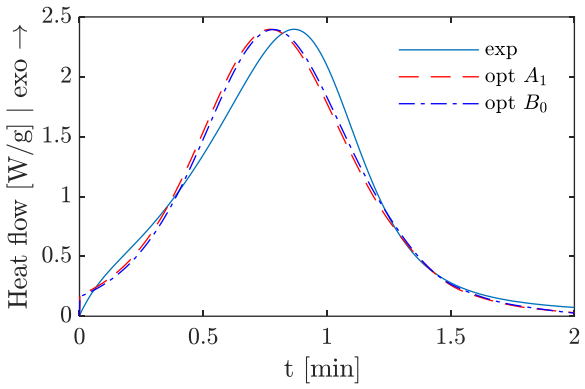

Figure 2.13. Comparison of A_1 and B_0 optimization for a DSC measurement at 473 K.

The basic equation for polymerization optimization is therefore described in equation 2.42.

$$\dot{a} = \mathcal{H}(t - t_i)A_1(1-a)^{n_p}(1 + B_0 a)\exp\left(-\frac{E_a}{RT}\right)$$
$$a(t=0) = a_i \tag{2.42}$$

The parameter C and D of the diffusion factor were also considered, because of perfectible optimization method employed by Vicard et al. (see Annex 2) eventual dependency to the variability factor and eventual need to adapt factor to the new coupling method.

2.4.3 Optimization method

The optimization method is detailed in this subsection and is summarized in Figure 2.14.

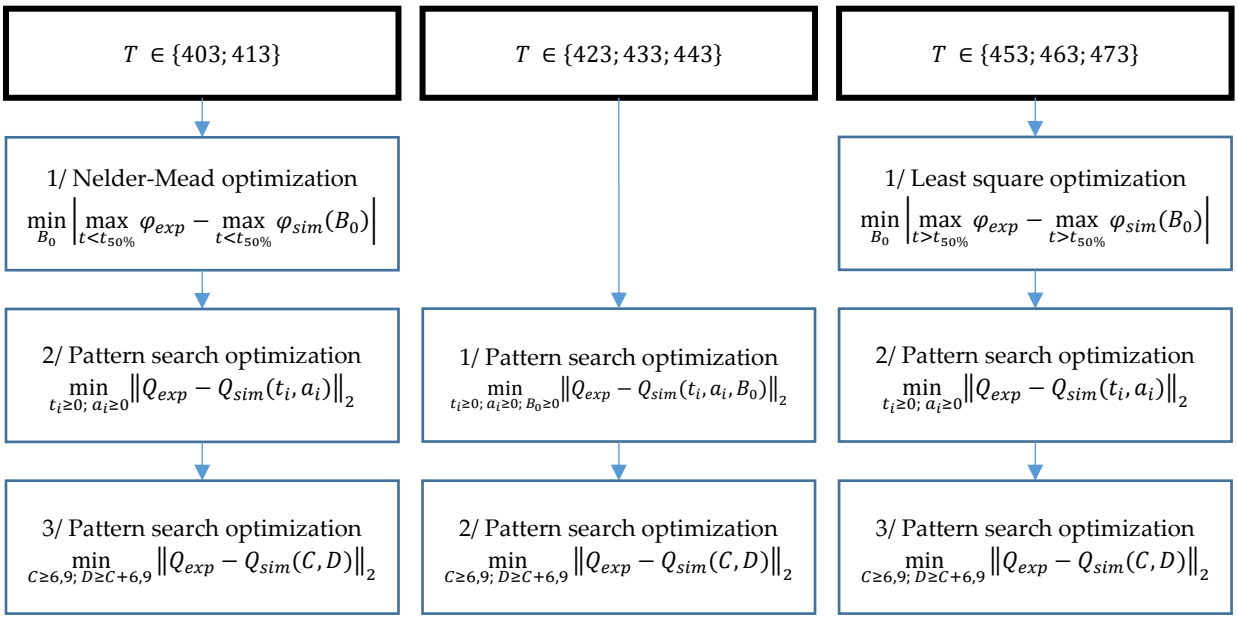

Figure 2.14. Model optimization method depending on temperature.

Autocatalytic parameter

B_0 was optimized using the polymerization spike for the maximum values of heat flow due to polymerization to coincide, when it was observable. At 423 K, 433 K and 443 K, the spikes respectively caused by polymerization and crystallization arise roughly at the same time, making the distinction between the two of them difficult, as such, its optimization has been conducted at the same time as t_i and a_i (see equation 2.46).

Thus, the objective functions f_{11} and f_{12} (respectively described in equation 2.43 and 2.44) to determine B_0 compared the maxima of the experimental heat flow to the maximum simulated heat flow caused by polymerization. At 453 K, 463 K and 473 K, the polymerization spike occurs before the crystallization spike (if any) so f_{11} is minimized in the first half of the reaction. Accordingly, $t_{50\%}$ defines the half-time of the synthesis ($Q(t_{50\%}) = 0{,}5 * Q_{tot}$).

$$f_{11}(B_0) = \left| \max_{t<t_{50\%}} \varphi_{exp}(t) - \max_{t<t_{50\%}} \varphi_{sim}(t, B_0) \right| \tag{2.43}$$

At 403 K and 413 K, the polymerization spike occurs after the crystallization spike so f_{12} is minimized in the second half of the reaction.

$$f_{12}(B_0) = \left| \max_{t>t_{50\%}} \varphi_{exp}(t) - \max_{t>t_{50\%}} \varphi_{sim}(t, B_0) \right| \tag{2.44}$$

The least-square method is efficient for f_{11} but not for f_{12}, presumably because of the high nonlinearity caused by the crystallization spike. The simplex method (Nelder-Mead method) has been used instead. B_0 initial value was 73.9 according to Table 2.4.

Reactive mix initial state: t_i, a_i

This optimization aims to shift the polymerization spike, so the optimization ignores the eventual variabilities caused by the initiation of polymerization, the already polymerized sample. Pattern search method has been used, and the parameters are constrained to be positive with t_i, a_i initial values were both fixed at 0. At most isotherms, it was done with objective function f_2 described by equation 2.45.

$$f_2(t_i, a_i) = \left\| Q_{exp}(t) - Q_{sim}(t, t_i, a_i) \right\|_2 \tag{2.45}$$

At 423 K, 433 K and 443 K, the height of the polymerization spike is also optimized as its experimental location is unclear and its location in the model is dependent of how the experimental data is interpreted (objective function f_{2B}, as described by equation 2.46).

$$f_{2B}(t_i, a_i, B_0) = \left\| Q_{exp}(t) - Q_{sim}(t, t_i, a_i, B_0) \right\|_2 \tag{2.46}$$

Diffusion factor optimization: C, D

The diffusion factor parameters were optimized thanks to equation 2.47, using initial values from Vicard et al. [16]. Pattern search method was also used here, following the optimization

method study discussed in Annex 1 which put it as the most efficient constrained optimization method. The chosen constraints are determined for the corrective factor to be valued during polymerization (if $a < 0.1\%, f_d = 0$, and if $a > 99.9\%, f_d = 1$). The initial value was sometime preconditioned with the simplex method for faster optimization.

$$f_3(C,D) = \left\| Q_{exp}(t) - Q_{sim}(t,C,D) \right\|_2 \tag{2.47}$$

2.4.4 Optimization results and average model for simulation

As shown by Figure 2.15 plotting the optimization results for each measurement at each temperature, no meaningful temperature dependency has been found for parameters t_i, a_i and B_0. We also observe that the induction time seems nearly inexistent at $T > 453K$ and low values for polymerization initial value ($\bar{a}_i = 1.3\%$).

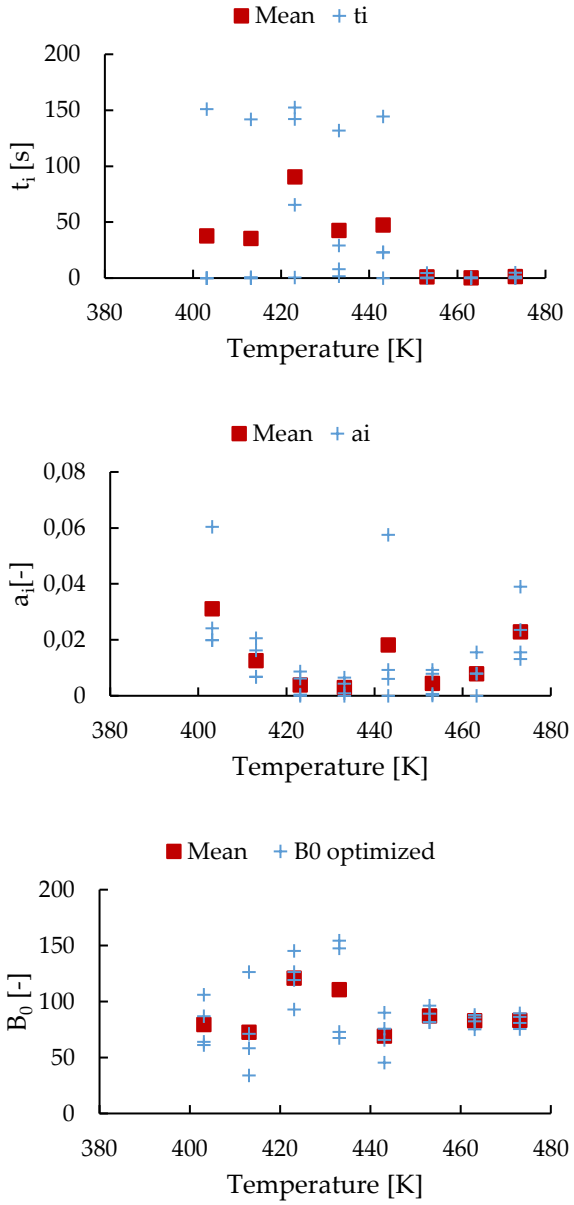

Figure 2.15. Results and average results for each parameter optimized in equation (2.42).

As a_i is determined as a mean to correct the curve shape and since no correlation has been observed with another parameter, every value was taken to calculate the mean. Looking at results for B_0 optimization, it can be observed that similarly to t_i, the optimized value does not vary a lot between 453 K and 473 K. It indicates that at high temperatures, the repeatability of the synthesis is good.

It is however more contrasted at lower temperatures, which may indicate that either crystallization, the synthesis speed affects the repeatability of measurement. The higher B_0 at 423 K and 433 K are especially interesting. They occur at temperatures where not only crystallization and polymerization occur in the same time frame, but it is also the temperatures where the final crystallinity is the highest. Therefore, this points to the beneficial influence of crystallization toward polymerization discussed in subsections 2.1.2 and 2.3.1. The lower values at 403 K and 413 K could then be associated either to the lower crystallinity, or to the fact that the virtually instantaneous (compared to polymerization) local crystallization of the polymerized chains is more likely to trap reactants. Nonetheless, it is very likely to be a coincidence instead, as the variation between measurements points at these temperatures is wider than the variation between the mean values.

Therefore, for these three parameters, we chose to take average values. As there are high discrepancies between values of t_i above and below 453 K, two mean values have been taken, as described in Table 2.7.

Table 2.7. Mean value of t_i, a_i and B_0.

Parameters	Value	Unit
B_0	$88.21 \pm 28{,}17$	$[-]$
a_i	0.0130 ± 0.0151	$[-]$
$t_i(T \geq 453K)$	1.04 ± 1.79	$[s]$
$t_i(T < 453K)$	50.2 ± 63.1	

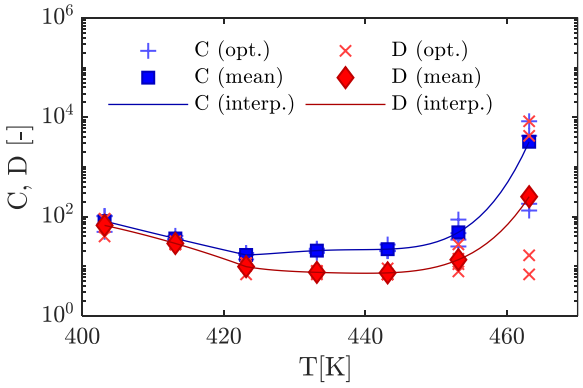

Figure 2.16. Interpolation described in compared to optimized values, signalled with a sign, of C (+) and D (x) for each experimental DSC curves. The mean value at each isotherm is described by a square for C and a diamond for D.

As shown by the optimization results for the slowest and fastest reaction for DSC tested in Figure 2.17, the optimization procedure can faithfully describe the heat flow caused from PA6 synthesis. With the bolded curves, a common average model is showcased at 413 K, 433 K and 453 K which parameters uses average values or expression presented in Table 2.7 and Table 2.8, and the enthalpies determined from experimental values detailed in Table 2.2. Because it takes the average of B_0 at all temperatures, it is as fast as the fastest synthesis at 453 K while it gives a good compromise at 413 K and 433 K.

However, the description of crystallization phenomenon tends to numerically average the heat flow integral and as such, description could still be improved, notably at 453 K. One possibility for better description would be to take secondary crystallization into account, as discussed by Vicard [14] which would further complicate modelling, but improve description.

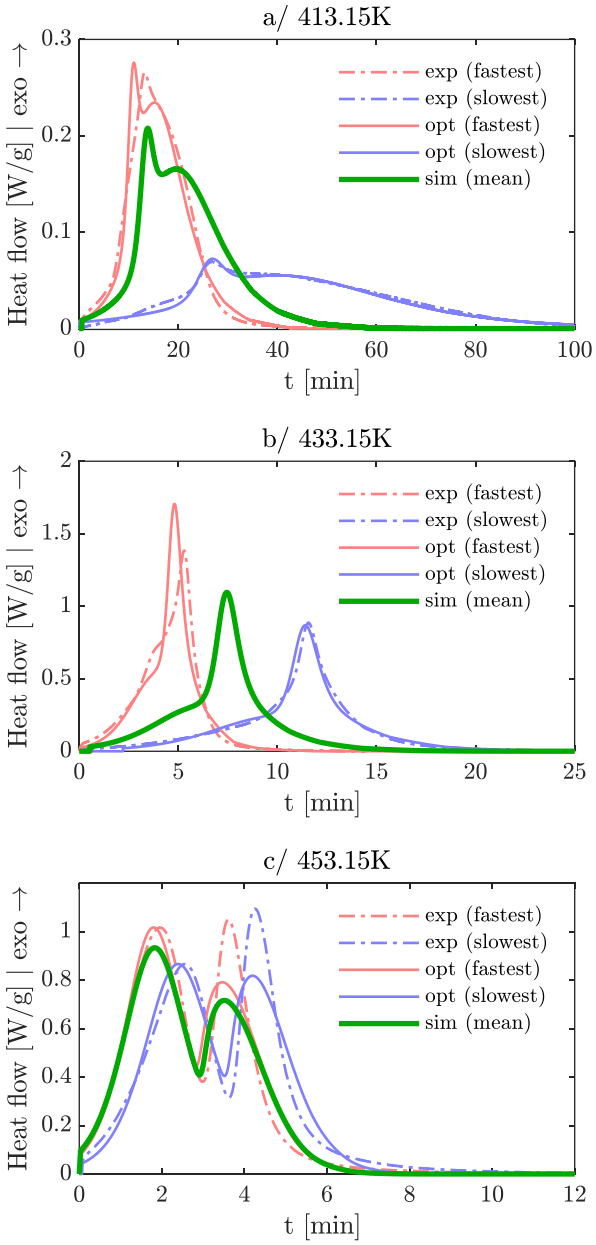

Figure 2.17. From top to bottom: DSC measurements compared to optimized model at 413 K, 433 K and 453 K.

Table 2.8. Interpolation of C and D from optimization results.

Temperature range	C and D expression	f_d
$T < 423K$	$C(T) = \exp(2.125 * 10^{-3}T^2 - 0{,}2541T + 72.30)$ $D(T) = \exp(-1.119 * 10^{-3}T^2 - 0{,}8889T - 160{,}5)$	Eq. (2.19)
$T \in [423K, 463K]$	$C(T) = \exp(7.739 * 10^{-6}T^4 - 0{,}01342T^3 + 8.728T^2 - 2.522 * 10^3T + 2.733 * 10^5)$ $D(T) = \exp(5{,}320 * 10^{-6}T^4 - 9.258 * 10^{-3}T^3 + 6{,}042T^2 - 1.753 * 10^3T + 1.907 * 10^5)$	Eq. (2.19)
$T > 463K$	−	$f_d = 1$

2.5 Rheokinetics of PA6 synthesis

In previous sections, the exothermic influence of the synthesis was studied with relation to polymerization and crystallization. However, the synthesis also affects the viscosity of the system which would influence the flow inside a reinforcement.

2.5.1 PA6 synthesis viscosity models

The chemoviscosity of thermosetting resins is usually considered to be dependent on temperature, cure, molecular weight, shear rate, pressure and filler effects [123]. The anionic polymerization can be considered to follow analogous mechanisms and therefore to follow the same dependencies. For this short literature review, the focus will be on empirical models used for the PA6 synthesis.

Viscosity of the monomer and temperature dependence

Usually, to model viscosity dependence on temperature for thermoset chemorheology, an empirical Arrhenius equation 2.48 is employed [123–125], with $\eta_{r,0}$ the reactive system initial viscosity and η_0, E_η the Arrhenius law parameters.

$$\eta_{r,0}(T) = \eta_0 \exp\left(\frac{E_\eta}{RT}\right) \tag{2.48}$$

For reactive anionic PA6 systems, it was notably used by Sibal et al. [90] who derived equation 2.49 for ε-caprolactam viscosity, which was also used by Davé et al. [126].

$$\eta_{r,0}(T) = 2.7 * 10^{-7} \exp\left(\frac{3525}{T}\right) \tag{2.49}$$

Dependence to synthesis parameters

To model the dependency on synthesis parameters, here again a model was proposed by Sibal et al. [90] following equation 2.50 with $K_{\eta,a} = 17.5$.

$$\eta(T, a) = \eta_{r,0}(T) \exp\left(K_{\eta,a} a\right) \tag{2.50}$$

Davé et al. [126], using a different reactive system, determined that a value of $K_{\eta,a} = 19.6$ gave good results compared to experimental measurement when the polymer conversion degree is inferior to 0.5.

Vicard [14] proposed equation 2.51 to take crystallization into account in viscosity modelling which is an extension of Sibal's model. While it was not able to reproduce the same speed in viscosity rise of experimental results, it showed potential in reproducing the shape of viscosity curve when crystallization is involved.

$$\eta(T, a, b) = \eta_{r,0}(T) \exp\left(K_{\eta,a} a\right) \exp\left(K_{\eta,b} b\right) \tag{2.51}$$

The Castro-Macosko model [127], described in equation 2.52 usually employed for thermoset resin was considered by Taki et al. [96] for reactive PA6. a_g is the gelation point, and A, B are empirically determined constants.

$$\eta(T, a) = \eta_{r,0}(T) \left(\frac{a_g}{a_g - a}\right)^{A+Ba} \tag{2.52}$$

They extended it in a similar way as equation 2.51, but with a confusing expression in which not only viscosity decreased with polymer conversion, but it also computed a singularity at the onset of crystallization. In their publication, it showed mixed performance when compared to experimental results.

2.5.2 Viscosity measurement methodology

Sample preparation and storage

In both Vicard's rheological study [14], and this rheological study, the samples have been prepared in a similar way. In a glovebox with nitrogen inerted atmosphere, the relative humidity is kept below 5%. There, the reactive mix has been melted, flattened, and solidified in a thin plate at ambient temperature. Then, it was broken into parts before storage.

For Vicard experimental measurements, all samples were kept in a sealed glass storage container. In our experimental measurements, samples were first put inside polyurethane vacuum sealed bags, which permeability to air proved to be important. Some of them were put inside a sealed glass storage container, other sealed bags were kept in ambient atmosphere. All samples were stored immediately after preparation inside the inerted glovebox. Silica gel was also put in every individual storage to try to keep humidity at a minimum.

Rheometers and measurement method

Vicard's measurements were conducted at the ICA laboratory, Albi, with a Thermo Scientific™ HAAKE™ MARS™ II rheometer. Since it was not able to give a stable measurement of the very low viscosity of the reactive mix, supplementary rheological measurements were carried out on two different plate plate rheometers: a Thermo Scientific™ HAAKE™ MARS™ 60 at Thermo Fisher Scientific, Courtaboeuf and an Anton Paar MCR302 at TPCIM laboratory at Douai (IMT Nord Europe). The characteristics, test configurations and the kind of sample used for each of the three rheometers are detailed in Table 2.9.

Table 2.9. Configuration of the rheometers.

Rheometer / **Parameters**	Anton Paar MCR302 (TPCIM)	Haake Mars 60 (Thermo Fischer Scientific)	Haake Mars II (ICAA,[14])
Plate diameter	50 mm	35 mm	35 mm
Minimum torque	10 nN.m	10 nN.m	50 nN.m
Torque resolution	0.1 nN.m	0.1 nN.m	<1 nN.m
Inerting gas	Nitrogen	Nitrogen	Argon
Gap	0.75 mm	0.75 mm or 1 mm	1 mm
Tested isotherms	453K, 473K	453K, 473K	423K, 443K, 453K, 473K
Heating speed	18K/min	Around 20K/min	Around 10K/min
Starting temperature	363K	Between 353K and 383K	363K
Test configuration	$\dot{\gamma} = 100\ \mathrm{s}^{-1}$	If $\eta < 0.1$ Pa s, $\dot{\gamma} = 10\ \mathrm{s}^{-1}$ else $f = 1$ Hz, $\gamma = 1\%$	If $\eta < 1$ Pa s, $\dot{\gamma} = 10\ \mathrm{s}^{-1}$ else $f = 1$ Hz, $\gamma = 1\%$
Sample storage	Sealed polyurethane bag and/or sealed glass container	Sealed polyurethane bag	Sealed glass container

In Figure 2.18, the heating step to reach the 453 K is shown for each test configurations. In this figure and the ones that follows, tests realized with the Anton Paar MCR302 (at Douai) are referred as "Do", tests realized with the Haake Mars 60 are referred as "Tf" and tests realized by Vicard [14] are referred as "Vi". With the Anton Paar MCR302 and the Haake Mars 60, the target temperature is obtained stably two time as fast as with older tests, thus giving more representative results for a given isotherm. The heating time for isotherms different from 453 K

is longer for higher isotherms and faster for lower isotherm, but the profile does not change for each configuration. For the Haake mars rheometers, the tests are ended when the observed viscosity reached a plateau, while for tests with the Anton Paar MCR302, they are stopped when max torque is reached.

In order to limit the influence of shear stress on polymerization, the Haake mars rheometer was configured to start with rotational shear before switching to oscillatory shear when the viscosity reaches 0.1 Pa.s. It is the same test configuration as Vicard, albeit with an earlier switch to oscillatory mode because of higher rheometer sensitivity. The Anton Paar MCR302 plate-plate rheometer was configured with high rotational shear in order to obtain precise measurement at very low viscosities approaching water viscosity.

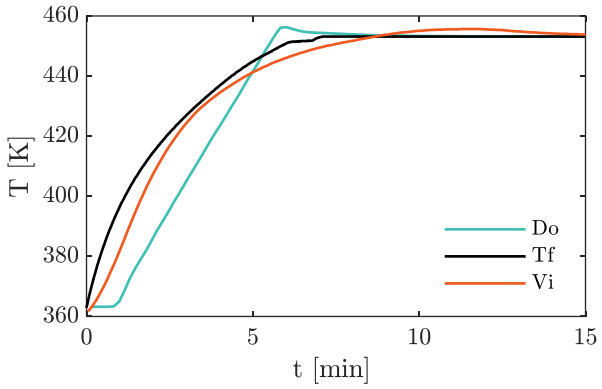

Figure 2.18. Temperature vs time during the heating step to the 453 K isotherm.

In subsections 2.5.3 and 2.5.4, the focus will be on measurements realized within the context of this study. Discussion about Vicard's results can be found on her PhD thesis [14].

2.5.3 Viscosity measurement results

In these viscosity measurements, a Newtonian behaviour has been assumed for the reactive systems. Indeed, the initial viscosity of the reactive mix does not seem to vary despite two different shear rates as the 10 s^{-1} and 100 s^{-1} tests show a roughly equivalent behaviour in Figure 2.19. Likewise, the study on the PA6 melt viscosity by Laun and Schmidt [128] suggests a Newtonian behaviour for polymerized chains at low shear rates ($< 1000\ s^{-1}$). To simplify, with the main components of the reactive system being Newtonian at low shear rates, we consider in the following that the reactive system is Newtonian even during the reaction, notably to be able to apply Cox-Merz equivalency (equation 2.53) between viscosity η and complex viscosity η^* [129]. $\dot{\gamma}$ is the strain rate, ω the oscillation and f the frequency.

$$\eta(\dot{\gamma}) = |\eta^*(\omega)| \text{ when } \dot{\gamma} = \omega = 2\pi f \tag{2.53}$$

Temperature dependence

In Figure 2.19, three viscosity measurements with relation to temperature are shown.

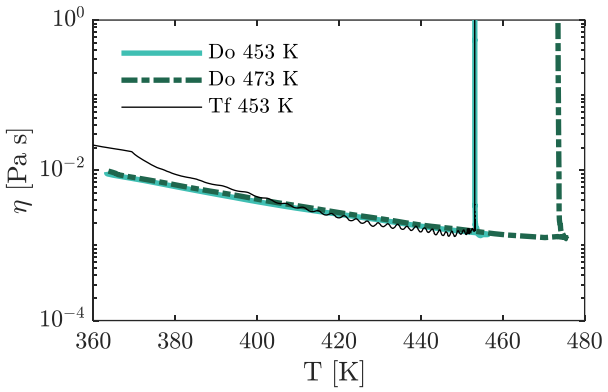

Figure 2.19 Viscosity measurement against temperature, during the heating part of the process.

As the displayed tests show, the temperature dependency of the reactive mix viscosity is faithfully reproduced during the heating phase. Such behaviour has been observed in every realized tests. In the tests realized with the Haake Mars 60, the viscosity starts at higher values than the tests realized with the MCR302 because the measurements were started before the full sample was melted. When the isotherm of the test is reached, the viscosity rise corresponds to the progress of the synthesis.

Dependence to synthesis at 453 K

Figure 2.20 shows a typical viscosity measurement after the heating phase realised with the Haake Mars 60. Other measurements have similar curve shape but different timeframes. It shows that the resin viscosity is directed by two growth regimes caused by the different time spans of the polymerization and the crystallization during the PA6 synthesis. Indeed, at 453 K the phenomena occur successively, which makes the lower slope between the two growth regimes the mark of the transition between these two phenomena.

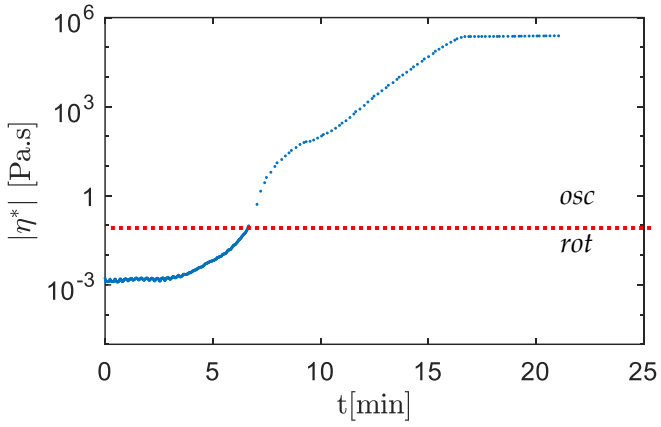

Figure 2.20. Typical isothermal viscosity rise behaviour during conversion at 453 K.

However, the viscosity rise occurs in a longer time span (around 16 minutes), than the expected duration of the synthesis (roughly 8 minutes according to Table 2.6).

2.5.4 Limits of the experimental campaign

Integrity of the measured sample during the reaction

Limits of the viscosity measurements included the difficulty to ensure that the gap between the plates is fully filled. This can be observed in Figure 2.21 where part of the sample polymerized outside the parallel plates. Another complication is that all reactants, and the monomer in particular, starts evaporating around 398 K [14]. This was observed in tests with the reactants' vapours condensing on colder surfaces (Figure 2.22). The last problem is that the changing phases in the sample will change the volume of the sample, as the crystalline PA6 phase has higher density than its amorphous phase, which in turn has higher density than ε-caprolactam [14,91]. The reactants' evaporation and the phases different densities are likely the causes behind the samples' porosity observed in Figure 2.23. This limits the representativity of the realized measurements.

Figure 2.21. Test with spilled reactive mix.

Figure 2.22. Reactants formed by condensation observed above the rheological test (Haake Mars 60 rheometer).

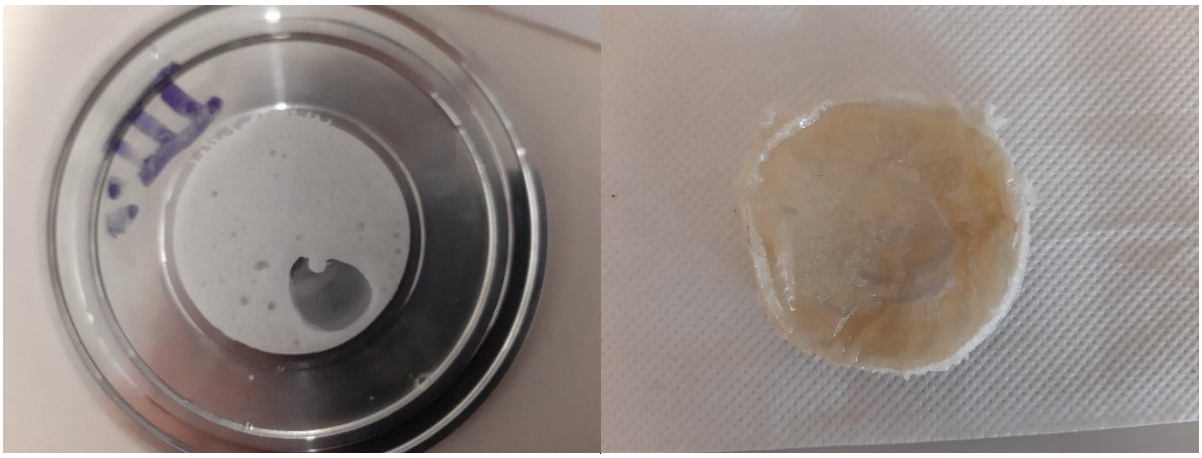

Figure 2.23. Example of sample appearance after polymerization.

Influence of sample storage and humidity

For most tests, despite inconstant sample integrity, the viscosity measurement produced curves with similar shape. However, high variability has been observed in the initiation time t_i of the full synthesis viscosity rises in tests ($t_i = 30 \pm 15\ s$). As this initiation time was not observed in DSC measurements, one likely reason is the variability in sample handling when setting the test up. Indeed, there is a time window between the instant the sample is taken out from a sealed storage and the start of the rheological test where the sample is directly exposed to ambient humidity. However, it is not the only cause of variability.

Before the tests, vacuum bag storage was considered as a more practical alternative than sealed glass containers. However, difference of behaviour depending on storage method was observed on tests realized with the Anton Paar MCR302. To compare the difference at 453 K, three rearranged curves representing the different observed behaviours depending on sample storage conditions are shown in Figure 2.24. The measurements realized before the start of the viscosity rise were removed by considering the part of the rheological test where $T > 451$ K and $\eta > 4$ mPa s. The viscosity condition was added to ignore minor viscosity jumps that sometimes occur at the beginning.

As mentioned before, every sample were sealed in a polyurethane bag. For "Polyurethane (6 days)", the vacuum bag was left in ambient air, and its test was realized around six days after sample fabrication. However, the curve "Glass" and "Polyurethane (1 day)" refers to measurement of samples in a polyurethane bag that were further stored in a glass container. As multiple samples were put inside one glass container, the "Glass" sample was tested immediately after opening the glass container, while the "Polyurethane (1 day)" was tested the day after. Therefore, the difference between these two curves shows that the glass container lost its inerted atmosphere during the short window of time the first sample of the container was removed. Then, the gap between the three samples behaviour demonstrates the influence of the polyurethane vacuum bag permeability to ambient humidity. The longer the bag was exposed to ambient humidity, the lower and the rougher the slope of the viscosity curve is. The slower viscosity rises are proof of the inhibition of the reaction caused by humidity, while the increased roughness may indicate that inhibition is uneven throughout the samples.

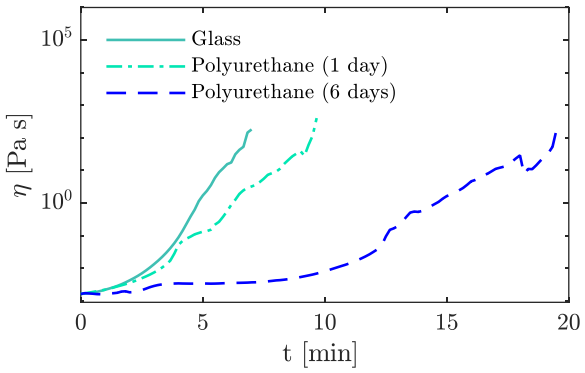

Figure 2.24. Rearranged viscosity curves with $t = 0$ when $T \approx 453K$ and $\eta > 4\ mPa$.

2.5.5 Elements for viscosity modelling and simulation

Although the quality of the rheological measurement could be improved, an attempt at modelling its behaviour was still realized. Indeed, some patterns could still be distinguished, and the synthesis model was shown to be adaptable in section 2.4.

In the literature review of subsection 2.5.1, the Sibal model 2.50 was used with good empirical results in at least two occurrences. The model extension to crystallization attempted by Taki et al. [96] and Vicard [14] essentially divide the viscosity law between the contribution of temperature, polymerization and crystallization, as described by equation 2.54 with η_0 being a non-physical theoretical value of the reactive system viscosity at infinite temperature.

$$\eta(T, a, b) = \eta_0 \eta_T(T) \eta_a(a) \eta_b(b) \tag{2.54}$$

Elements to model the influence of the three contributions equation 2.54 is presented. The validity of η_b dependency on the crystallization degree is notably discussed.

a. Temperature influence on viscosity

An induction time was experimentally observed before the polymerization starts and raises the viscosity. Moreover, the viscosity measured at high shear rate ($\dot{\gamma} = 100\ s^{-1}$) during the reactive mix heating showed good repeatability. Therefore, they were used to fit a model based on the Arrhenius law using equation 2.55, as shown in Figure 2.25.

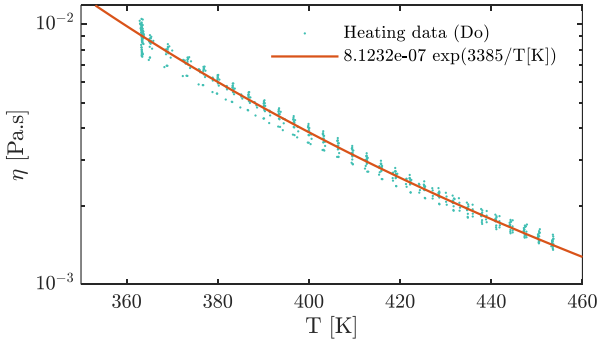

Figure 2.25. Experimental viscosity measured during the reactive mix heating compared to the fitted Arrhenius law.

$$\eta_{r,0}(T) = \eta_0 \eta_T(T) = 8.123 * 10^{-7} \exp\left(\frac{3385}{T}\right) \tag{2.55}$$

This model can be used in order to simulate the temperature dependency of the initial viscosity before PA6 synthesis.

b. Polymerization influence on viscosity

To model η_a, Sibal et al. [90] model was chosen 2.50. For polymerization, the Malkin and Camargo model was used (equation 2.42 with values from Table 2.4 for parameters A_1, E_a and n_p). The variability in viscosity measurement was approached the same way: B_0 was used to reduce the polymerization speed, while t_i, the polymerization initiation time was used to adjust the start of the viscosity rise.

At 473 K, in section 2.3 it was considered that crystallization was virtually non-consequential, meaning that $\eta(b) = 1$ is a reasonable enough assumption at this isotherm. Therefore, the Sibal model with $K_{\eta,a}$ (equation 2.56) could be tested and after adapting B_0 and t_i, and showed very good fit in Figure 2.26, when compared to tests from both Haake Mars rheometers. The model seems to work even when $a > 0.5$ contrary to Davé et al. observation [126].

$$\eta(473K, a) = \eta_{r,0}(473K)\eta_a(a) = \eta_{r,0}(473K) \exp(17.5 * a(t)) \tag{2.56}$$

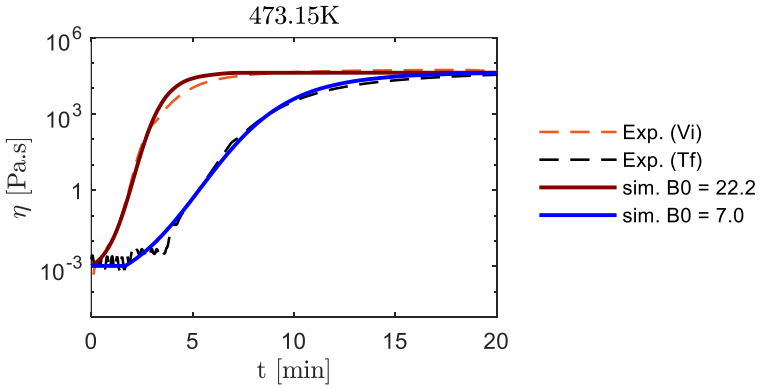

Figure 2.26. Viscosity simulation at 473K compared to some experimental measurement.

c. Crystallization influence on the system viscosity

In equation 2.54, it is assumed that polymerization and crystallization influence viscosity independently. However, this hypothesis is very unlikely, as with increased crystallinity, the ratio of amorphous polymer in the system decreases correspondingly. Therefore, a term depending on crystallinity should correct polymerization influence. To simplify model comprehension and writing, the crystallization influence will be described with the crystallinity X_c instead of the crystallization rate b. The crystallization influence on viscosity should then be written as following:

$$\eta_b(X_c) = \eta_c \eta_{X_c} \tag{2.57}$$

η_c is the crystallinity correcting factor, and its expression serves to correct the polymerization ratio (the ~5% unpolymerized monomer are ignored and therefore $X_p^\infty \approx 1$).

$$\eta_c = \exp\left(-K_{\eta,a}\,(1 - X_c)\right) \tag{2.58}$$

Then, simply reapplying Sibal model to crystallization as Vicard [14] suggested will increase the slope, which is not the behaviour observed. Therefore, an empirical model for crystallization viscosity proposed by Hieber et al. [130] was chosen instead.

$$\eta_{X_c} = \exp\left(K_{\eta,b}{X_c}^2\right) \tag{2.59}$$

Assuming that the end viscosity value can be used to determine the exponential constant, which is not aberrant in Figure 2.26, the following dependency was found for $K_{\eta,b}$:

$$K_{\eta,b}(T) = \frac{21}{X_c^\infty(T)} \tag{2.60}$$

It is a little counterintuitive as it would indicate that the system viscosity is affected by how much material can crystallize. Therefore, the full viscosity model simulated in Figure 2.27 follows equation 2.61.

$$\eta(T,a,b) = \eta_{r,0}\eta_a\eta_c\eta_{X_c} = \eta_{r,0}\eta_a\eta_c \exp\left(\frac{21}{X_c^\infty(T)}{X_c}^2\right) \tag{2.61}$$

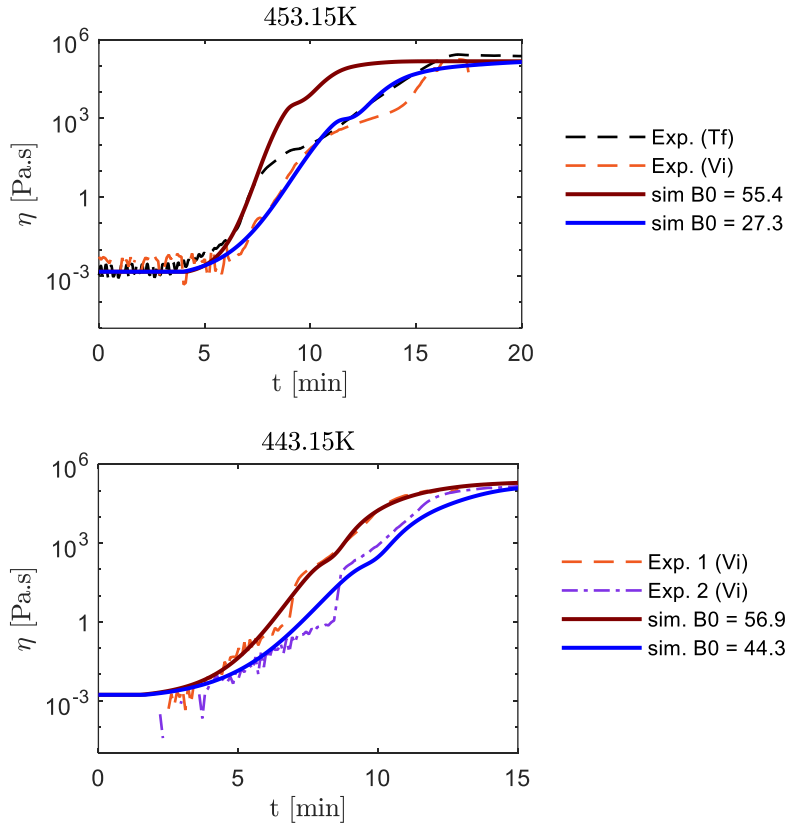

Figure 2.27. Viscosity simulation at 443K and 453K compared to some experimental measurements.

By repeating the same adaptation as before, adapting B_0 and t_i, it seems to compare well to experimental measurements at 443 K. It describes the same shape, with the slope variation at the right places. At 453 K however, the slope variation occurs too early compared to experimental curves, which maybe indicate a slower crystallization rate or initiation.

Chapter conclusion

While many studies of anionic synthesis of PA6 have been realized in the past, few works quantified the interaction between polymerization and crystallization. Here, the aim was to give elements of understanding of both phenomena from the interpretation of heat flow curves. The physical significance of the different coupling methods in the literature has been highlighted and compared to a new coupling method. This allowed to explain the relative performance of each method. Then, confronted with the variability of synthesis speed, the coupling method showed that crystallization taken alone is negligibly affected compared to polymerization. Parameters have been chosen and optimized to propose an average model for process simulation of the synthesis.

To improve the modelling method, multiple points could be studied further. An analytical study of the empirical model describing the phenomena may give more insight on the different role played by each parameter on the model and could both improve the model quality and reduce the number of parameters. Following Wichterle et al. hypothesis [87], the polymerization model could be tweaked to account for the increasing crystallinity during the synthesis. Having a better understanding of the mechanism of what we called local crystallization in polymerizing material would be a key point to improve the coupling method, notably on how polymerizing chains become ready for crystallization, and how the presence of crystal affect (or not) the crystallization kinetics.

Then, a brief review of existing models for reactive PA6 viscosity has been realized. Following an experimental rheological study, the limit of the experimental characterization was described. The influence of temperature has been derived from the study, and elements for modelling the influence of polymerization and crystallization have been given.

However, a more in-depth study needs to be realized, notably by devising a very rigorous and controlled experimental protocol for sample storing and handling to reduce variability as much as possible. To preserve the sample integrity, closed or pressurized environment system could be envisioned. The influence of strain rate on the synthesis will also be of interest, as it has shown to affect both polymerization [131] and crystallinity of thermoplastics [132].

Concerning rheology modelling, we mostly considered models that have been applied to the reactive PA6 in the past. While it showed good results, not enough attention has been given to rheological model applied for different polymer systems. Usually authors propose thermoset models as an alternative [125]. However, models for polymer solutions [133] have been used before to describe viscosity rise for polymerization processes. While we used Hieber empirical model [130] for crystallization, other empirical models for crystallization, or for colloid/suspensions have been used [134] and may also be suited, especially if the crystallization progress is understood structurally-wise.

Chapter 3

Process simulation for Fibre-Reinforced PA6 composites

The section 3.5 goes over the simulation presented in Han William, Quentin Govignon, Arthur Cantarel, et Fabrice Schmidt. « Efficient Polymerization and Crystallization Kinetics Coupling of Polyamide 6 Synthesis for Liquid Composite Molding Process Modeling ». *Polymer Engineering & Science* 62, nº 4 (04/2022): 999-1012. https://doi.org/10.1002/pen.25901.

For reactive process simulation, the synthesis model described in Chapter 2 need to be coupled with equations of flow in fibre preform described in Chapter 1. The aim is to predict the eventual influence of synthesis on the flow, and vice-versa. The resin may affect the flow with the advancing cure, which can also affect temperature, while dual-scale flow creates multiples resin fronts, meaning that each tow may be impregnated with resin of different age and characteristics.

In this chapter, the different methods employed for LCM process simulations are described, with the properties of the PA6 reactive mix necessary for non-isothermal reactive simulations. Then, integration of Chapter 2's synthesis model in 3D simulation is studied. Finally, elements for an experimental method to test simulations coupling fibrous media flow and non-isothermal reactive flow is proposed.

3.1 Simulation methods for LCM processes

Here, the focus will begin on simulation methods for resin filling during LCM processes. Then, methods for non-isothermal reactive simulations are reviewed.

3.1.1 LCM process simulations and resin tracking methods

For unsaturated flow, dual-scale flow has been represented only in more recent studies. Usually, LCM process simulations involve a flow equation (Stokes or Darcy depending on the scale) which is modelled throughout the domain. A resin tracking method is added to compute the flow front. Relation with dual-scale flow modelling has been done mainly on more recent studies, and their modelling strategies have been discussed in Chapter 1.

For macro-scale process simulation, the preferred method has been the control volume finite element method (CVFEM). The method consists in computing the Darcy Poisson equation within the finite element framework, and the filling of control volumes directly from the flow rate. It was proposed by Bruschke and Advani [135] and subsequently improved by Trochu et al. [136] to conform the control volumes with the finite elements. It is a well-established method for LCM simulations used in LIMS [24,137,138] and PAM-RTM [139]. However, to simulate the resin flow in gas during LCM processes, models from two-phase flow theory have been used, especially for micro-scale simulations. In this case, the dominant modelling approach also considers one fluid with weighted properties of the two immiscible phases and using an interface capturing method to separate them. Usually, the volume of fluid (VOF) or the level-set (LS) models are the preferred interface capturing methods, although the phase-field model has recently been considered. Other two-phase flow modelling methods worth mentioning are the Lattice Boltzmann method (LBM), based on Boltzmann kinetics giving statistical distributions for particle propagation and mesh-free Lagrangian particular methods. The first has been used for preform permeability determination [38,140] but has not been found to have been applied yet for LCM process simulation. The latter is briefly covered after describing the interface capturing methods.

Volume of fluid method

The volume of fluid (VOF) method was developed by Hirt and Nichols as a computationally efficient algebraic method for following free moving boundaries [141]. It follows the transport equation 3.1 where a colour function α designs one of the two fluid volume density within the considered volume space, as illustrated by Figure 3.1.

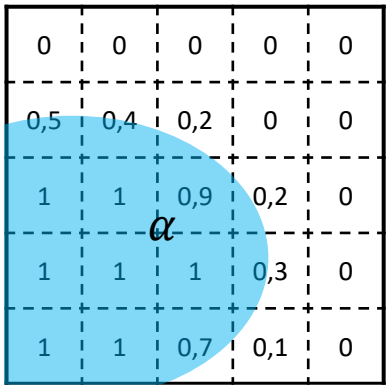

Figure 3.1. Algebraic description of fluid presence in a discretized domain according to the VOF method.

The method follows the same principle as Bruschke et Advani [135] and has also been integrated within the CVFEM method in Imbert et al. works [26,67,142]. However, it has usually been employed with the finite volume method (FVM), as it is the more popular computational fluid dynamics (CFD) discretization method. In addition, it is easy to rewrite equation 3.1 as a flow rate balance, simply by integrating over the volume, using the divergence theorem.

$$\frac{\partial \alpha}{\partial t} + \boldsymbol{\nabla} \cdot (\boldsymbol{u}\alpha) = 0 \tag{3.1}$$

The colour function can subsequently be used to weight fluid properties throughout space. Notably the surface tension force is often modelled using the continuum surface force (CSF) model proposed by Brackbill et al. [143]. To resolve the interface, two class of methods have been considered: algebraic methods and geometric methods.

The algebraic methods aim to reduce the spread of the fluid interface with slight modifications on the transport equation calculation method. Popular algebraic schemes include the compressive interface capturing scheme for arbitrary meshes (CICSAM) [144] available in commercial software Ansys Fluent®, the high resolution interface capturing scheme (HRIC) [145] present in STAR-CCM+®, the multidimensional universal limiter with explicit solution (MULES) implemented in OpenFOAM® [146], and more recently, the Iso-advector method [147]. Notably, the MULES method has been used multiple times in a finite volume method (FVM) framework for resin transfer moulding (RTM) simulations through OpenFOAM® use [148–151].

Instead, the geometric methods use the colour function to reconstruct the interface surface (or line for 2D simulations) in partially filled elements, usually following the piecewise linear interface calculation scheme (PLIC) [152] which usually direct the interface surface depending on the fraction phase gradient [153]. It has been assessed to be generally more accurate than its algebraic counterpart [147,154] and other interface capturing methods [154]. It is also becoming the more popular method, as it has recently replacing, or been associated with algebraic methods to improve the front sharpness [155,156].

Level set method

The level set (LS) method was proposed by Sethian, mainly for computational geometry, vision, materials science and fluid mechanics [157]. Instead of following the quantity of fluid inside the domain of interest, the colour parameter ϕ indicates the signed distance from the front location and is positive inside the phase of interest. Therefore, the calculations can be limited around the interface which makes it well suited for use with the boundary element method (BEM) framework as demonstrated in multiple works simulating LCM processes with Darcian flows using this combination [158–160].

$$\frac{\partial \phi}{\partial t} + \boldsymbol{u} \cdot \boldsymbol{n} |\nabla \phi| = 0 \tag{3.2}$$

The main advantages of the LS method is the great definition of the interface curvature [154] and potential efficiency when coupled with BEM [158]. However, mass conservation tends to be difficult to achieve, which led to conservative level-set formulation (as used by Spina et al. [161]) or to coupling with the VOF method [154].

Phase-field method

Contrary to the VOF and LS method, which usually use the continuum surface force theory to account for surface tension, the phase-field (PF) method is based on fluid free energy [162]. Therefore, here the colour parameter ψ is characteristic of the fluids free energy density and

varies between -1 and 1, each extrema representing each phase. In equation 3.3, $f(\psi)$ follows the Ginzburg-Landau-Wilson free energy functional which has various interpretations, with the Cahn-Hilliard equation being the most popular for two-phase flow simulations [154].

$$\frac{\partial \psi}{\partial t} + \boldsymbol{\nabla} \cdot (\boldsymbol{u}\psi) = f(\psi) \tag{3.3}$$

The method has been recently proposed by Dammann et Mahnken with two transport formulation for RTM simulations considering a Darcian flow interacting with deformable fibres [163]. They considered that the thermodynamical nature of the interface resolution was suited with the theory of porous media (TPM). However, their simulation for the phase parameters showed results with contrasting results in interface position and resolution. It was also used by Li et al. [54] for biphasic Stokes-Darcy with Beavers-Joseph-Saffman coupling simulation. It showed good result, albeit with diffusive interface in the porous part, when compared to non-averaged porous media.

Particular Lagrangian methods

Methods that follow interacting mesoscopic particles representative of a moving area permits fluid simulation in a Lagrangian framework. Notably, the smoothed particle hydrodynamics (SPH) and the moving particle semi-implicit method (MPS) have been respectively used by Lu et al. [164] and Yashiro et al. [165] to simulate injection in a fibrous area to predict potential micro-voids formation in LCM processes. These methods usually need huge calculation capacities as every particles behaviour need to be computed [140]. They are usually more suited for describing high discrepancy in fields in a microscopic scale (for instance, very high velocities gradient, or non-linear behaviour), where method involving a mesh may be to limitative or diffusive [166].

3.1.2 Non-isothermal reactive process simulation method

Non-isothermal reactive process simulation refers to process simulation that include the ongoing synthesis of the polymer of interest coupled with temperature.

Transport equation

The solution procedures in the literature usually includes scalar transport equations for temperature and cure as a Eulerian framework is usually used. Its general form is described in equation 3.4.

$$\frac{\partial x}{\partial t} + \boldsymbol{\nabla} \cdot (\boldsymbol{u}x) = \dot{s} + \boldsymbol{\nabla} \cdot (\boldsymbol{D_x} \cdot \boldsymbol{\nabla} x) \tag{3.4}$$

There is a transient term (time derivative), a convection term, and a diffusion term with $\boldsymbol{D_x}$ the diffusivity, which can be a scalar or a tensor. The source term $\dot{s}$ refers to the rate of change of scalar x. If the equation is used for polymerization modelling, the diffusivity has been neglected before [26], as it is usually not quantified in synthesis studies. If the equation is used

for temperature in incompressible settings (in which case $x = T$), the diffusivity can be defined by $D_T = \kappa/(\rho c_p)$.

Non-isothermal reactive process simulation

The solution algorithm for non-isothermal reactive simulation has been similar for most account in the literature. It usually realized by solving sequentially each value of interest in a time step. In non-isothermal reactive solution, it means that at least, pressure, velocity, synthesis or cure, and temperature need to be calculated. In Tan et Pillai [167], their proposed multiscale algorithm solves pressure and velocity first, and then temperature and pressure. In Nagy et al. [148,149], since OpenFOAM® is used, fluid phase transport is likely solved before the PISO algorithm for pressure and velocity described in subsection 1.1.2. Then temperature and polymerization were computed, with porous media influence in their second paper. In Imbert et al. works [67], the viscosity is updated before pressure and velocity computation. Then, fluid phase transport is solved before dual-scale resolution of polymerization and temperature.

Process simulation and crystallization

Crystallization does not seem to have been studied alongside polymerization in injection simulations for semi-crystalline thermoplastics synthesis. However, crystallization has been simulated during injection before, by Spina et al. for instance [161]. In their work, the different equations were also solved sequentially, and notably recorded stress history in order to predict crystalline microstructures resulting of both thermal and flow-induced crystallization.

3.2 Non-isothermal simulation of synthesis and integration of crystallization kinetics

The integration of the reactive PA6 synthesis model proposed in Chapter 2 is described here. For 3D simulations of the synthesis, the procedure for computing in Figure 3.2 is considered. In this section, the procedures suppose an incompressible resin flow or domain in non-porous media. If resin flow is included, PISO procedure for pressure and velocity, presented in subsection 1.2.1 is solved. If resin filling is simulated, the VOF method in OpenFOAM® is resolved first. It was introduced in subsection 1.3.4 and is written in its original, non-porous form in equation 3.5.

$$\frac{\partial \alpha_r}{\partial t} + (\boldsymbol{\nabla} \cdot \boldsymbol{u_r})\alpha_r + \boldsymbol{\nabla} \cdot \left((\boldsymbol{u_r} - \boldsymbol{u_g})\alpha_r \alpha_g \right) = 0 \tag{3.5}$$

The heat balance equation (equation 3.6) includes a source term where the heat flow of the synthesis is calculated. ρ, κ and c_p are the reactive and gas linearly mixed density, thermal conductivity, and thermal capacity. The source term $\dot{q}$ in equation 3.7 is calculated using the synthesis heat flux φ_s and the reactive mix thermal capacity $c_{p,r}$.

$$\frac{\partial T}{\partial t} + \boldsymbol{\nabla} \cdot (\boldsymbol{u}T) \; - \frac{1}{c_p} \boldsymbol{\nabla} \cdot (\kappa \boldsymbol{\nabla} T) = \dot{q} \tag{3.6}$$

$$\dot{q}(t) = \frac{\varphi_s(t)}{c_{p,r}} \tag{3.7}$$

The crux of the problem is to calculate the polymerization and crystallization heat flux φ_p and φ_c to obtain the synthesis heat flux φ_s (equation 2.6) and therefore how to adapt the synthesis model from Chapter 2 for 3D simulations.

$$\varphi_s(t) = \varphi_p\big(\dot{a}(t)\big) + \varphi_c\left(\dot{b}(t)\right) \tag{3.8}$$

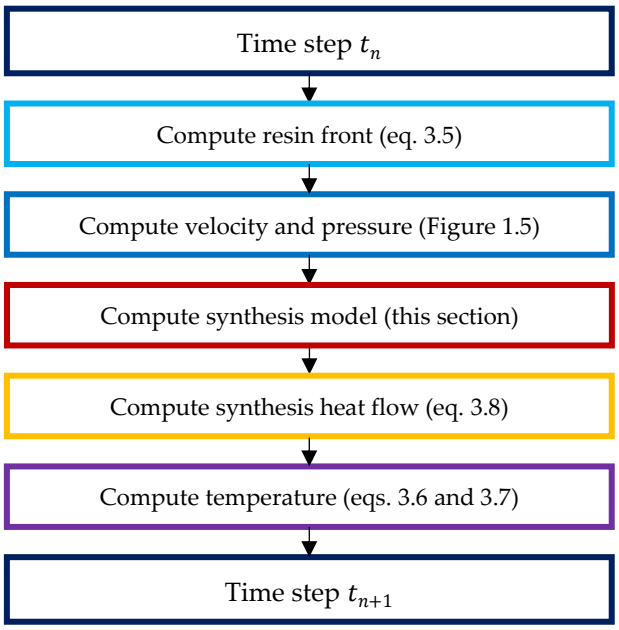

Figure 3.2. Basic procedure for non-isothermal reactive simulation.

In a first approach, the polymerization and crystallization degree are considered intensive properties. This hypothesis holds in simple unidirectional flows where no mixing of resin with different syntheses degrees are involved. By neglecting the dependence of the polymerization conversion rate X_p^∞ to temperature, the progress of polymerization can be solely determined by its degree a, as detailed in Chapter 2. Therefore, the polymerization rate can be obtained using equation 3.9. The eventual diffusion term is ignored here due to lack of knowledge about it. The polymerization rate $\dot{a}$ is calculated thanks to Malkin and Camargo equation 2.10.

$$\frac{\partial a}{\partial t} + \boldsymbol{\nabla} \cdot (\boldsymbol{u}a) = \dot{a} \tag{3.9}$$

However, not only has the final crystallinity X_c^∞ a noticeable dependency to temperature (Table 2.2), but section 2.3 showed that calculation of the crystallization degree b is nontrivial.

3.2.1 Method for non-isothermal crystallization computation

The need for adaptation of the kinetic models for non-isothermal reaction was discussed in Vicard's thesis [14]. The solution employed then was to use different weights for polymerization and crystallization heat flow according to constant non-isothermal DSC tests. This approach has a fundamental limitation. Since it assumes the model of the synthesis from the final crystallinity rather than the situation at each time step, it is unable to compute problems with a non-constant heating rate, where the final crystallinity of the PA6 has not been tested before. Therefore, it is not suited to simulate synthesis in an environment where the heating rate is not controlled.

Isothermal crystallization degree in non-isothermal simulations

The problem that arises during crystallization computation comes from the exothermic nature of PA6 synthesis. Let's consider the heat flow equation 2.34, where the global rate of crystallization $\dot{b}$, follows a polymerization dependant model as described in section 2.3.

$$\varphi_s(t) = \varphi_p\big(\dot{a}(t)\big) + \varphi_c\left(\dot{b}(t)\right) = \Delta H_p^{\infty}\dot{a}(t) + \Delta H_c^{\infty}\dot{b}(t,a) \tag{3.10}$$

In this equation $\dot{b}$ defines the time derivative of $b = X_c(t)/X_c^{\infty}$, the degree of crystallization.

The total heat of the reaction can also be considered instead (equation 3.11), with Q_p the heat of polymerization and Q_c the heat of crystallization.

$$Q_s(t) = Q_p(t) + Q_c(t) = \Delta H_p^{\infty}a(t) + \Delta H_c^{\infty}b(t,a) \tag{3.11}$$

However, according to Vicard et al. [16], the final crystallinity X_c^{∞} varies with temperature following equation 3.12.

$$X_c^{\infty}(T) = \frac{\Delta H_c^{\infty}(T)}{\Delta H_c^{100\%}} = \frac{-0.0354T^2 + 29.651T - 6107.5}{230} \tag{3.12}$$

Therefore, b is not only dependent on temperature from the crystallization model and the polymerization model, but also from how crystallisable the polymer chains are at a given temperature.

As the crystallization degree b defines the advance of crystallization relatively to the final crystallinity, it also has to take into account any temperature change. In this work, a method is detailed to update the crystallization degree following temperature change at each time step.

Procedure for update of crystallization progress

In order to propose a procedure to update the crystallization degree relatively to temperature changes, the following hypotheses are assumed:

1. Polymer chains that have crystallized remain crystallized throughout the whole synthesis (PA6 crystals are stable).
2. Temperature history does not affect polymerization and crystallization (only the current state of polymerization and crystallization determine the kinetics).

The first hypothesis is reasonable since it tends to be confirmed by isothermal and non-isothermal DSC studied by Vicard et al. [15]. Unless the fusion temperature of crystals is reached, they are not undone after heating or cooling. The second hypothesis simplifies the problem and may be assumed as data about such interaction has not been found. To describe the procedure, the following convention is adopted: the variable x_n define the value of parameter x updated at time step t_n. As such, as variable b varies with space (following the resin flow), time and temperature, the dependency of b has to be updated for each variable: b_n is defined by $b_n(T_n) = b(t_n, \xi_n, T_n)$. For crystallization enthalpy, it is supposed that enthalpy of already crystallized polymer does not vary with temperature, thus $\Delta H_{c,n} = \Delta H_c(t_n, \xi_n)$. For temperature, it does not only depend on time and space but also on the synthesis enthalpy and on thermal conductivity and capacity at t_n, and thus T_n is defined by $T_n = T\left(t_n, \xi_n, \kappa_n, c_{p,n}, \Delta H_{s,n}\right)$.

The procedure is written below, and starts after updating the polymerization degree to obtain a_{n+1} and $\Delta H_{p,n+1}$:

1. Crystallization degree is updated in time and space to obtain $b_{n+1}(T_n)$ (equation 3.13 with $b = b_n$ and $\dot{b} = \dot{b}_n$).

$$\frac{\partial b}{\partial t} + \boldsymbol{\nabla} \cdot (\boldsymbol{u} b) = \dot{b} \tag{3.13}$$

2. Quantity of enthalpy due to crystallization is updated spatially to obtain $\Delta H_c(t_n, \xi_{n+1})$ (equation 3.14 with $\Delta H_c = \Delta H_{c,n}$). Therefore, the material derivative is equal to zero as time is not updated for enthalpy in this step.

$$\frac{\partial \Delta H_c}{\partial t} + \boldsymbol{\nabla} \cdot (\boldsymbol{u} \Delta H_c) = 0 \tag{3.14}$$

3. Quantity of enthalpy due to crystallization is updated versus time as the product of the infinitesimal variation of crystallization degree during a time step ($\delta b_n = \dot{b}_n \delta t_n$) and crystallization potential at temperature T_n is defined by $\Delta H_c^{\infty}(T_n)$ (equation 3.15).

$$\Delta H_{c,n+1} = \Delta H_c(t_n, \xi_{n+1}) + \delta b_n * \Delta H_c^{\infty}(T_n) \tag{3.15}$$

4. The synthesis enthalpy $\Delta H_{s,n+1}$ and other needed parameters for temperature diffusion can be updated as the synthesis progress has been updated. This allows updating of temperature in time and space using the heat balance (equation 3.6) in order to obtain T_{n+1};

5. Crystallization degree is updated in temperature (equation 3.16). If $\Delta H_{c,n+1} \geq \Delta H_c^{\infty}(T_{n+1})$, the polymerized part has at least reached its crystallization potential, thus crystallization kinetics do not progress anymore.

$$\begin{aligned} &\text{If } \Delta H_{c,n+1} < \Delta H_c^{\infty}(T_{n+1}),\ b_{n+1},\\ &b_{n+1}(T_{n+1}) = b_{n+1}(T_n)\frac{\Delta H_{c,n+1}}{\Delta H_c^{\infty}(T_{n+1})}\\ &\text{If } \Delta H_{c,n+1} \geq \Delta H_c^{\infty}(T_{n+1})\\ &b_{n+1} = 1 \end{aligned} \tag{3.16}$$

The resulting non-isothermal procedure to follow the synthesis heat flow and temperature is described in Figure 3.3.

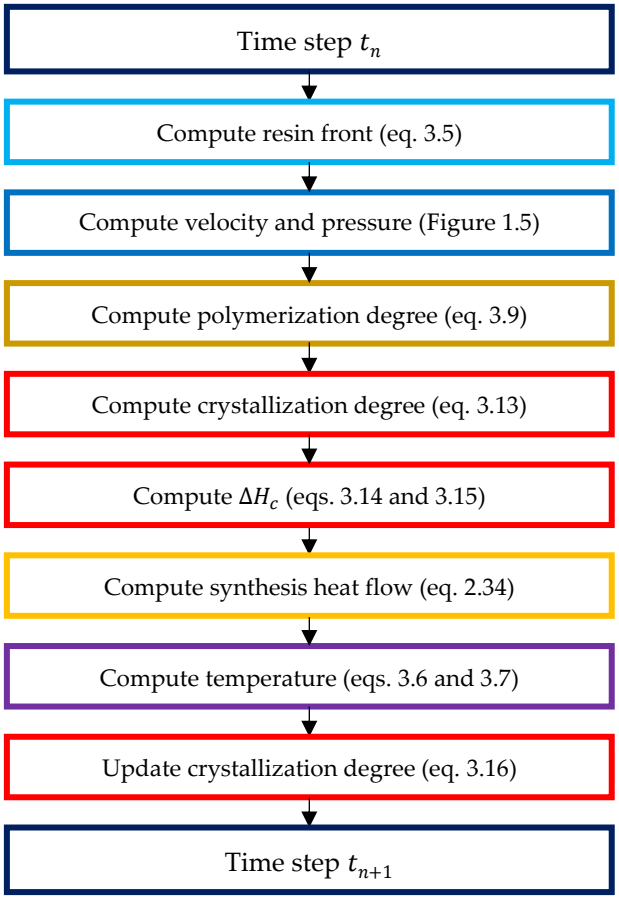

Figure 3.3. PA6 non-isothermal reactive simulation procedure.

Therefore, the history of crystallization is kept through summation of added crystallization enthalpy at each time step.

3.2.2 Crystallization model integration

The Hillier-Vicard crystallization model (equation 2.16) and the alternative crystallization model (equation 2.40) are both dependent on polymerization and have both shown to be able to reproduce the DSC behaviour of reactive PA6, with similar performances. Therefore, the choice of the crystallization model has been realized for practical reasons rather than physico-chemical reasons and is discussed here.

Barriers to integration of Hillier-Vicard crystallization model

In Vicard et al. [16], the global crystallization degree was defined by equation 2.16, in which $f_a = f_d * a$ to simplify expressions.

$$b(t) = \int_0^t \mathcal{H}(t - x_t - t_{c,0}) f_a(x_t) \frac{d\beta}{dx_t}(t - x_t - t_{c,0}) dx_t \tag{3.17}$$

As the Heaviside function nullifies any value higher than $t - t_{c,0}$, it is possible to displace the Heaviside function outside the integral (equation 3.18) and to define the convolution integral $I_b(u)$ in equation 3.19.

$$b(t) = \mathcal{H}(t - t_{c,0}) \int_0^{t-t_{c,0}} f_a(x_t) \frac{d\beta}{dx_t}(t - x_t - t_{c,0}) dx_t \tag{3.18}$$

$$I_b(u(t) = t - t_{c,0}) = \int_0^u f_a(x_t) \frac{d\beta}{dx_t}(u - x_t) dx_t \tag{3.19}$$

The presence of the convolution integral brings many problems in regard of its discretization. Firstly, resolution of convolution integral usually involve mathematical methods such as Laplace or Fourier transformation [168] which are less commonly used in FVM discretisation. Secondly, in non-isothermal synthesis, I_b varies depending on temperature, and therefore the convolution integral cannot be fully calculated in its integration limits without keeping the whole polymerization, crystallization, and temperature histories in memory. This would need extensive computational resources, and some solution to keep track of the reactive mix trajectory, which is difficult in a Eulerian framework.

Therefore, a preferable alternative is to discretize I_b. To be able to temporally discretize I_b on a time step, a relation between $I_b(u + \delta t)$ and $I_b(u)$ needs to be determined. However, additivity of the integral with relation to intervals (Chasles' relation) is not usable. Moreover, the highly non-linear form of both the polymerization model and the crystallization model complicates attempts of simplifying expressions. For instance, if a first order isothermal Avrami model is used instead of the local crystallization degree (equation 3.20), a method of resolution exists. It was initially proposed for a viscoelasticity model with a similar formulation [169].

$$\beta(t) = 1 - \exp(-K_c t) \tag{3.20}$$

In this case, from the relation in equation 3.21, equation 3.22 can be obtained.

$$\frac{d\beta(t + \delta t)}{dt} = -K_c \exp(-K_c(t + \delta t)) = \frac{d\beta(t)}{dt} \exp(-K_c \delta t) \tag{3.21}$$

$$I_b(u + \delta t) = \exp(-K_c \delta t) \int_0^{u+\delta t} f_a(x_t) \frac{d\beta}{dx_t}(u - x_t) dx_t \tag{3.22}$$

As such, $I_b(u + \delta t)$ can be rewritten with relation to $I_b(u)$ following equation 3.23.

$$I_b(u+\delta t) = \exp(-K_c\delta t)\left[I_b(u) + \int_u^{u+\delta t} f_a(x_t)\frac{d\beta}{dx_t}(u-x_t)dx_t\right] \tag{3.23}$$

Then, during temporally discretized reactive simulations, the value of the functions inside the remaining convolution integral will be known both at t and $t+\delta t$ during a time step. Therefore, it can easily be evaluated with the second order accurate trapezoidal rule to finally obtain b. If needed, the crystallization rate can also be calculated, either by applying the Leibniz integral rule, or by using the discretized relationship during a time step ($\delta b = \dot{b}\delta t$).

To use this integration procedure, the local crystallization cannot be used with its current parameters as the numerically identified crystallization order ($n_c = 1.59$) does not allow to separate δt like in equation 3.21.

Choice of the new crystallization model and calculation procedure

For the new crystallization model (equation 2.40), $\dot{b}$ and b are directly obtained by solving the differential equation.

Therefore, its integration does not need other mathematical methods, nor any simplification of the constituting polymerization or local crystallization model. As Chapter 2 showed that the apparent difference between the two domains is mostly negligible, it has been chosen over the Hillier-Vicard crystallization model.

However, in calculation of $\dot{b}$ and a_a, the model depends on comparison between the resin age t_r and $t_{c,0}$. The resin age is the timespan during which the resin was involved in the process, and if the resin is injected unreacted, it is distinct from the simulation time t. As mentioned above, the Eulerian framework of the simulation makes keeping history of parameters difficult. Therefore, for practical reasons, it is assumed that $t_{c,0}$ does not depend on temperature history but on the current temperature. Consequently, the delayed value a_{tc} is realized from the temperature and crystallization initiation time at time t rather than at $t_r - t_{c,0}\left(T\left(t_r - t_{c,0}\right)\right)$. These assumptions permit to limit difficulties in model integration; however, they are not verified.

Thus, the model is rewritten following equation 2.40 and uses the resin age t_r. The shifted polymerization degree parameter is $a_{tc} = a\left(t - t_{c,0}\left(T(t)\right)\right)$, needed to calculate polymer availability. Both parameters are kept in memory throughout the domain and are calculated using transport equations.

$$\dot{b}(t,a) = a_a(a_{tc})\mathcal{H}\left[t_r - t_{c,0}\left(T(t)\right)\right]K_c\left(T(t)\right)(1-\beta)n_c\ln\left(\frac{1}{1-\beta}\right)^{\frac{n_c-1}{n_c}} \tag{3.24}$$

The transport equation for t_r follows equation 3.25. The value of the material derivative is 1 since the resin age progresses linearly at the same rate as the process time t.

$$\frac{\partial t_r}{\partial t} + \boldsymbol{\nabla} \cdot (\boldsymbol{u} t_r) = 1 \tag{3.25}$$

Then, the transport equation for a_{tc} follows equation 3.26 and only aim to delay polymerization kinetics of the duration of the crystallization initiation time $t_{c,0}$. This step is necessary because of the absence of simple expression for the polymerization degree with relation to time.

$$\frac{\partial a_{tc}}{\partial t} + \boldsymbol{\nabla} \cdot (\boldsymbol{u} a_{tc}) = \mathcal{H}\left[t_r - t_{c,0}\left(T(t)\right)\right]\dot{a}(a_{tc}) \tag{3.26}$$

The steps for calculation of the crystallization degree are summarized and put in context of the rest of the procedure in Figure 3.4.

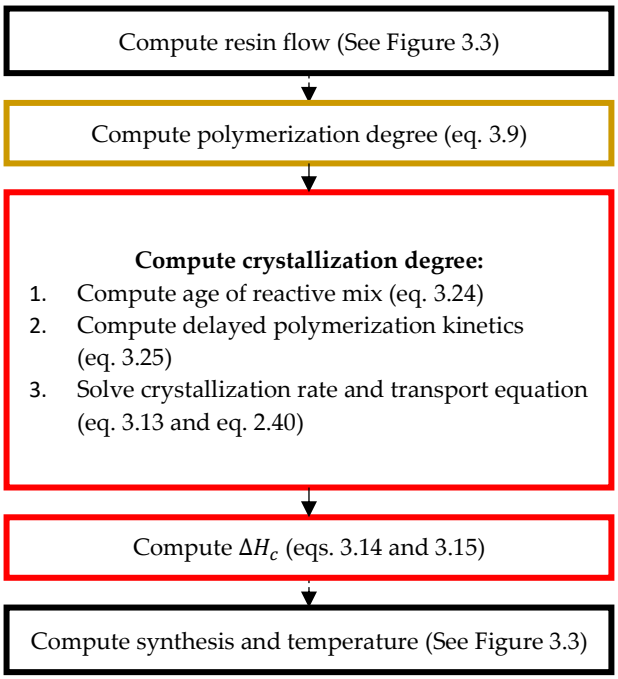

Figure 3.4. Detailed procedure for calculating the crystallization degree.

3.2.3 Properties for reactive PA6

In a first approach, the specific heat and the thermal conductivity are calculated using a mixture law between the different states of the reactive mix. The variation of density for various reasons (thermal dilatation, different phases density…) is ignored to stay within the incompressible framework of the simulation. The density is taken constant and rounded at $\rho_r = 1000\ \mathrm{kg\ m^{-3}}$ to conform with the incompressible continuity equation. It is a simplifying compromise between the lower ε-Caprolactam density at high temperature and the higher PA6 density (see Table 3.1).

Table 3.1: Density of different phases of the reactive mix with relation to temperature [170].

Phase	Parameter	Density [kg m^{-3}]
ε-Caprolactam	$\rho_{\varepsilon CL}$	$80.57\left(0.254^{1+\left(1-\frac{T[K]}{806}\right)^{0.286}}\right)^{-1}$
Amorphous PA6	ρ_{PA6a}	1080
Crystalline PA6	ρ_{PA6c}	1230

The relationship for the specific heat versus temperature for each phases in Table 3.2 are taken from Teuwen thesis [170]. The specific heat of the reactive mix $c_{p,r}$ is given by equation 3.27.

Table 3.2: Specific heat of different phases of the reactive mix with relation to temperature [170].

Phase	Parameter	Specific heat [J kg^{-1} K^{-1}]
ε-Caprolactam	$c_{p,\varepsilon CL}(T)$	$569.1 + 4.548 * T[K]$
Amorphous PA6	$c_{p,PA6a}(T)$	$1791.8 + 1.72 * T[K]$
Crystalline PA6	$c_{p,PA6c}(T)$	$206 + 4.24 * T[K]$

$$c_{p,r} = a * \left[X_c * c_{p,PA6c} + (1 - X_c) * c_{p,PA6c}\right] + (1 - a) * c_{p,\varepsilon CL} \tag{3.27}$$

The same kind of formulation is used for thermal conductivity (equation 3.28), however, without distinction between amorphous or crystalline phases for PA6. The values for each phase are compiled in Table 3.3.

Table 3.3: Conductivity of different phases of the reactive mix with relation to temperature [170].

Phase	Parameter	Thermal conductivity [J m^{-1} K^{-1}]
ε-Caprolactam	$\kappa_{p,\varepsilon CL}(T)$	$0.235 - 2.096 * 10^{-4} * T[K]$
PA6 (amorphous or crystalline)	$\kappa_{p,PA6}(T)$	0.258

$$\kappa_{p,r} = a * \kappa_{p,PA6} + (1 - a) * \kappa_{p,\varepsilon CL} \tag{3.28}$$

3.3 Comparison with DSC non-isothermal measurement

To check the capability of the method described above (Figure 3.3, Figure 3.4), it has been compared to Vicard et al. non-isothermal DSC measurement of PA6 synthesis with an ε-caprolactam based reactive mix [14,15]. The experimental procedure and materials were the same as for the isothermal DSC measurement discussed in section 2.2.1, however a constant rate of temperature is imposed instead of a constant temperature. The synthesis simulation uses the synthesis coupled model detailed in sections 2.3 and 2.4 with the non-isothermal simulation procedure of section 3.2.

3.3.1 Non-isothermal DSC measurements

One DSC measurement for each temperature rate and behaviour observed by Vicard are presented in Figure 3.5. In the figure, the heat flow has been normalized by dividing the temperature rate and is shown with relation to temperature. This permits for the surface under the curve to be representative of the reaction enthalpy. For each DSC measurement, only the interval of temperature relevant to the synthesis has been kept for this study. Therefore, the subsequent endothermic phenomena linked to the melting crystals [14] in the polymerized sample is not considered here.

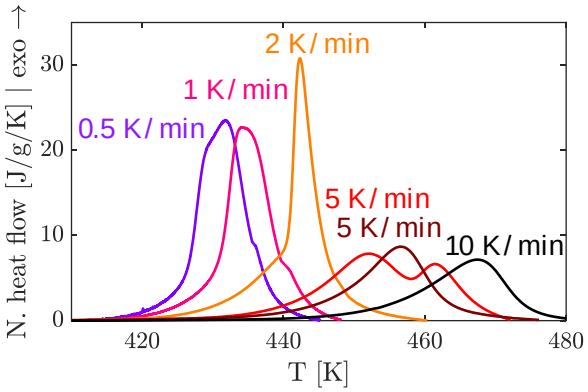

Figure 3.5. PA6 global synthesis kinetics measured with constant heating using DSC.

Similarly to both isothermal and rheological experiments, variability has been observed in these non-isothermal DSC measurement timeframe. Furthermore, at 5 K/min one measurement exhibited a different behaviour (red plot in Figure 3.5) in which the crystallization peak is distinct to the polymerization peak.

3.3.2 Constant temperature rate synthesis simulation

The synthesis model described in Chapter 2, including non-isothermal has been computed using OpenFOAM® 8. Therefore, the differential equations were resolved through the transport equations described in section 3.2 but with the velocity $\boldsymbol{u}$ set at $\mathbf{0}$ and without the pressure-velocity solving procedure. A simple adiabatic domain was used, and the time derivative was solved thanks to Euler explicit method with a time step $\delta t \leq 1$.

Instead of being calculated as a function of the synthesis, the source term $\dot{q}$ in equation (3.6) is taken constant, with the temperature rate of the corresponding DSC test. The synthesis model is taken as described in Chapter 2, without the polymerization initial parameters (a_i and t_i) because of the uncertainties on their validity, especially in a non-isothermal setting. The initial temperature has been set at 403 K.

The synthesis equations can result in non-real values as operations such as division by zero, negative fractional power or negative value inside logarithm can numerically happen. Thus, they have been corrected to avoid those cases. The corrections are shown in Annex 3.

Simulation results

A first simulation was realized using the mean value for the optimized autocatalytic parameter ($B_0 = 88.21$, see Table 2.7). As Figure 3.6 shows, it can predict the synthesis enthalpy reasonably well, albeit slightly underestimated at lower heating rates. Thus, the simulation can give a good estimation of the final crystallinity for a given heating rate. At 5 K/min heating rate, it is following the DSC results with two peaks behaviour rather than the other results.

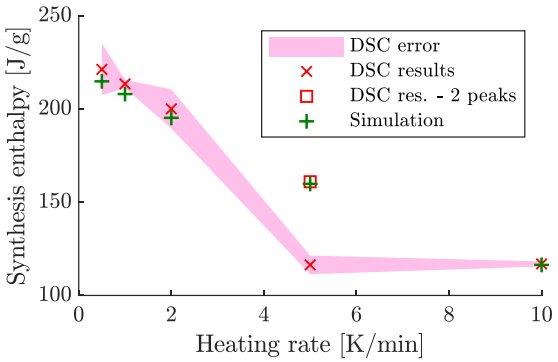

Figure 3.6. Comparison between the experimental synthesis enthalpy and the simulation enthalpy.

However, as shown in Figure 3.7 for the 1 K/min and 5 K/min heating, the simulation synthesis concluded faster than what is experimentally observed. This observation applies to every tested heating rate (see Annex 4). Moreover, at 1 K/min, the simulation peak is sharper and at 5 K/min, the simulation curve peaks are nearly merged. This suggests that in both cases, crystallization happens later relatively to polymerization than the simulation predicts.

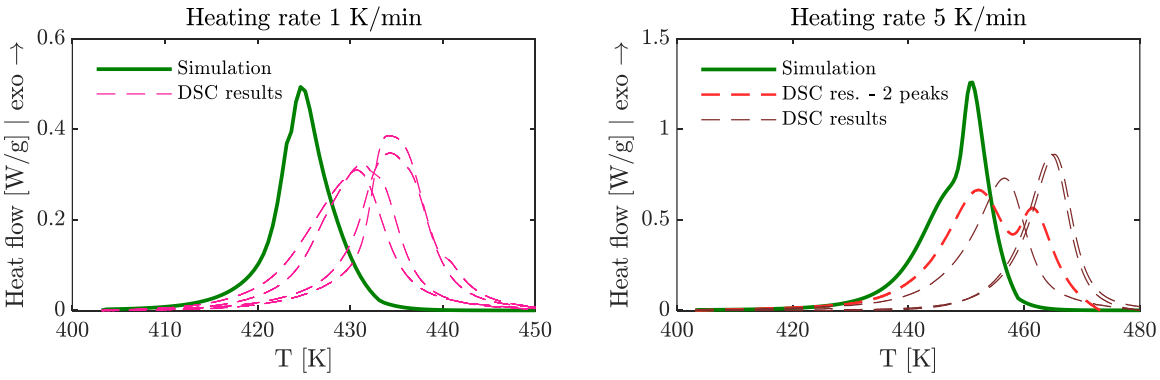

Figure 3.7. Comparison between the simulated heat flow and experimental heat flow at 1 K/min (left) and 5 K/min (right).

Following the synthesis study from section 2.4, the polymerization rate can be adjusted to account for slower polymerization by modifying the autocatalytic parameter B_0. Thus, two additional simulations have been realized with lower B_0. The two values used are indicated in equation 3.29. $\sigma_{B_0} = 28.17$ is the standard deviation of the optimized value ($B_0 = 88.21$).

$$\begin{aligned} B_{0,\sigma} &= B_0 - \sigma_{B_0} = 60.04 \\ B_{0,2\sigma} &= B_0 - 2\sigma_{B_0} = 31.87 \end{aligned} \tag{3.29}$$

However, as Figure 3.8 shows, the slower synthesis rate leads to a significant underestimation of the synthesis enthalpy at heating rates equal or slower than 2 K/min.

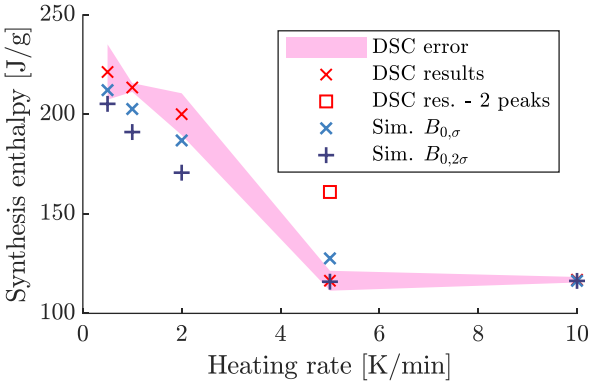

Figure 3.8. Comparison between the experimental synthesis enthalpy and the simulation enthalpy for $B_{0,\sigma}$ and $B_{0,2\sigma}$.

For some DSC measurements, the simulations are able to give the same behaviour but with some delay. In Figure 3.9, a compilation of such simulations and DSC results is given. *

The procedure has shown to be able to predict the total enthalpy. However, it happens early. Vicard proposed to add a polymerization initiation time, but the observed shifted behaviour of polymerization seems to indicate that it may be more a problem of inertia with the whole sample not heating as fast as the DSC. Temperature inertia may not be enough to describe the shift especially when considering lower heating rate. It may be because by the state of the matter (the reactive mix become gaseous at temperatures 403 K) or there could be a polymerization initiation condition. A 3D simulation of the DSC sample may give more information. Crystallization happens early in the simulation but does not seem to be misevaluated. One problem is the crystallization initiation time that may not be adapted to non-isothermal simulation. However, the inertial effects need to be quantified in order to conclude. The fact that the final simulated crystallinity and the final experimental crystallinity are similar in the 403-433 K range is either a coincidence, or it may indicate that temperature history is important for crystallization.

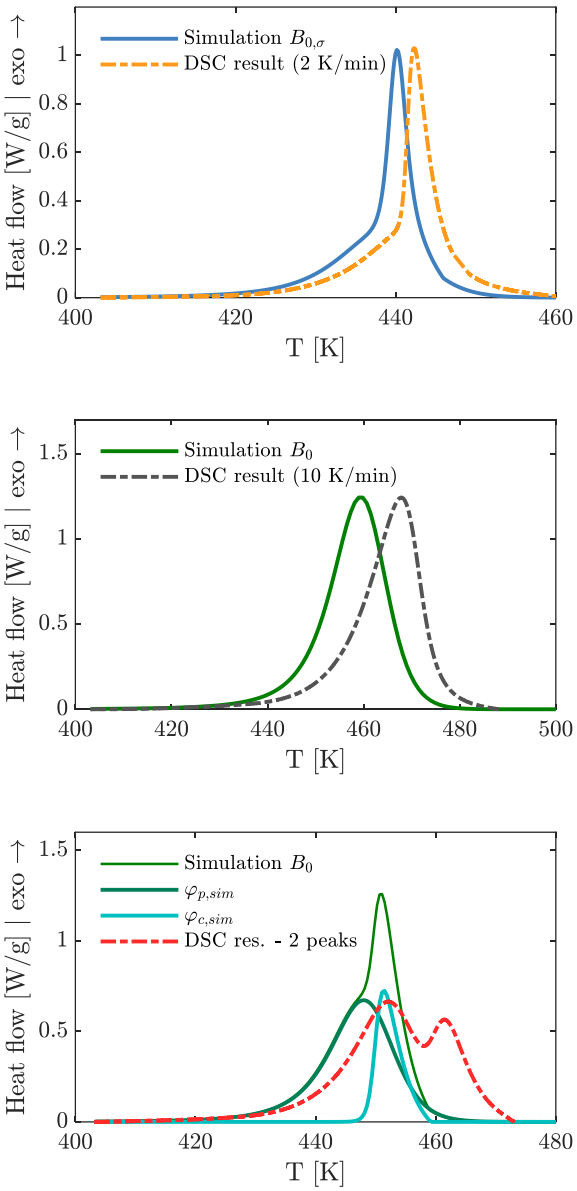

Figure 3.9. Comparison between simulation and DSC measurement that exhibit similar behaviour.

3.4 Reactive injection simulation

To simulate PA6 flow, OpenFOAM® has been used like in Chapter 1. As filling simulations are conducted, the VOF method for biphasic flow has been used (equation 3.5). The simulation procedure for biphasic incompressible simulation is presented in Figure 3.10.

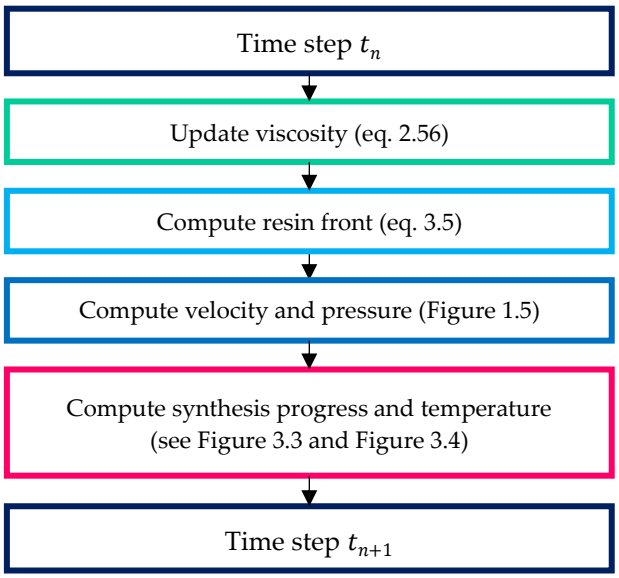

Figure 3.10. Procedure for a reactive injection simulation.

3.4.1 Simulation parameters

A first reactive injection simulation is realized with a geometry following Figure 3.11. The flow domain is a prism with a trapezoid base. It describes a half of an adiabatic mould with an inlet boundary from where the reactive mix is injected, and an outlet boundary for air rejection. The mesh includes 405 hexahedra for a quasi-2D simulation (one element in the thickness, with symmetry boundary conditions in the upper and lower face of the domain). The boundary conditions are described Table 3.4 : the reactive mix is injected with constant flow rate at a temperature of 413 K. The simulation duration of the injection has been set at 10 minutes, before stopping it for 20 minutes to monitor the synthesis progress. Thus, pressure and velocity calculation are omitted to avoid numerical instabilities.

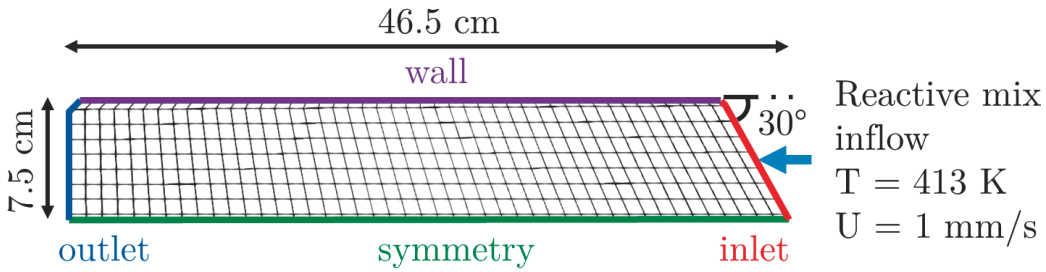

Figure 3.11. Description of the simulation geometry.

Table 3.4. Boundary conditions of the simulation

Parameters	Inlet	Outlet	Wall
$U(t \leq 10\ \text{min})$ $U(t > 10\ \text{min})$	$0.001\ \text{m s}^{-1}$ $0\ \text{m s}^{-1}$	$\frac{\partial U}{\partial n} = 0$	$U = 0$
p	$\frac{\partial p}{\partial n} = 0$	10^5 Pa	$\frac{\partial p}{\partial n} = 0$
$\alpha_{i\in\{r,g\}}(t \leq 10\ \text{min})$ $\alpha_{i\in\{r,g\}}(t > 10\ \text{min})$	0 $\frac{\partial \alpha_i}{\partial n} = 0$	$\frac{\partial \alpha_i}{\partial n} = 0$	$\frac{\partial \alpha_i}{\partial n} = 0$
$a(t \leq 10\ \text{min})$ $a(t > 10\ \text{min})$	0 $\frac{\partial a}{\partial n} = 0$	$\frac{\partial a}{\partial n} = 0$	$\frac{\partial a}{\partial n} = 0$
$b(t \leq 10\ \text{min})$ $b(t > 10\ \text{min})$	0 $\frac{\partial b}{\partial n} = 0$	$\frac{\partial b}{\partial n} = 0$	$\frac{\partial b}{\partial n} = 0$
$T(t \leq 10\ \text{min})$ $T(t > 10\ \text{min})$	$413\ K$ $\frac{\partial T}{\partial n} = 0$	$\frac{\partial T}{\partial n} = 0$	$\frac{\partial T}{\partial n} = 0$

3.4.2 Results and discussion

The front progresses mostly linearly following the constant reactive mix inflow as observed in Figure 3.12. The domain is 99.8% filled when the injection is stopped. Unsurprisingly, since the reactive mix is unreacted when it passes the inlet, the reaction has progressed more at the front than at the inlet. Therefore, Figure 3.13 a/ and b/ show that polymerization and crystallization most advanced near the outlet. Crystallization has not started in the inlet half of the domain, as the reactive mix has not been in the mould long enough. The temperature distribution in Figure 3.13 b/ shows the temperature rise caused by the start of the synthesis. At the corners near the outlet, the temperature is lower as some air is left.

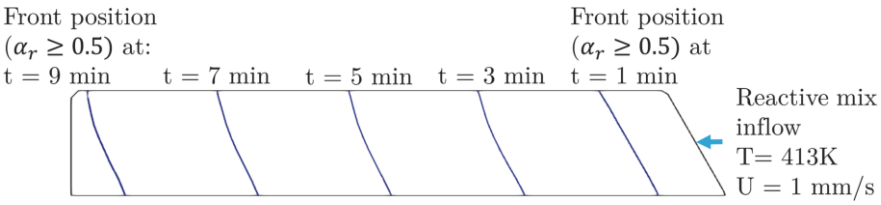

Figure 3.12. Reactive mix front position (determined at $\alpha_r > 0.5$) at different time of the simulation.

Figure 3.14 describes the proportion of fully polymerized and crystallized reactive mix in the domain relatively to time. It can be observed that polymerization and crystallization were both completed faster than the isothermal synthesis model (half an hour while DSC described in Figure 2.17 suggest an hour at 413 K). Moreover, due to the synthesis exothermy, the temperature rise prematurely stops crystallization.

Indeed, at t = 20 min, it can be observed (Figure 3.15) near the outlet that the temperature has reached 470 K at which crystallization is nearly non-existent. Thus, looking at Figure 3.15 c/, crystallinity is far from reaching the 43.6% crystallinity observed in isothermal synthesis at 413 K. Moreover, the distribution of crystallinity at the end of the reaction corresponds the temperature distribution in Figure 3.15 d/ (the temperature scale is narrowed for visibility compared to Figure 3.15 a/ and b/). Air left near the outlet does not heat as much as the reactive mix, and therefore causes lower temperature and higher crystallinity. They seem to lower the domain's core temperature (near the symmetry border) through conduction, which has less influence near the adiabatic borders.

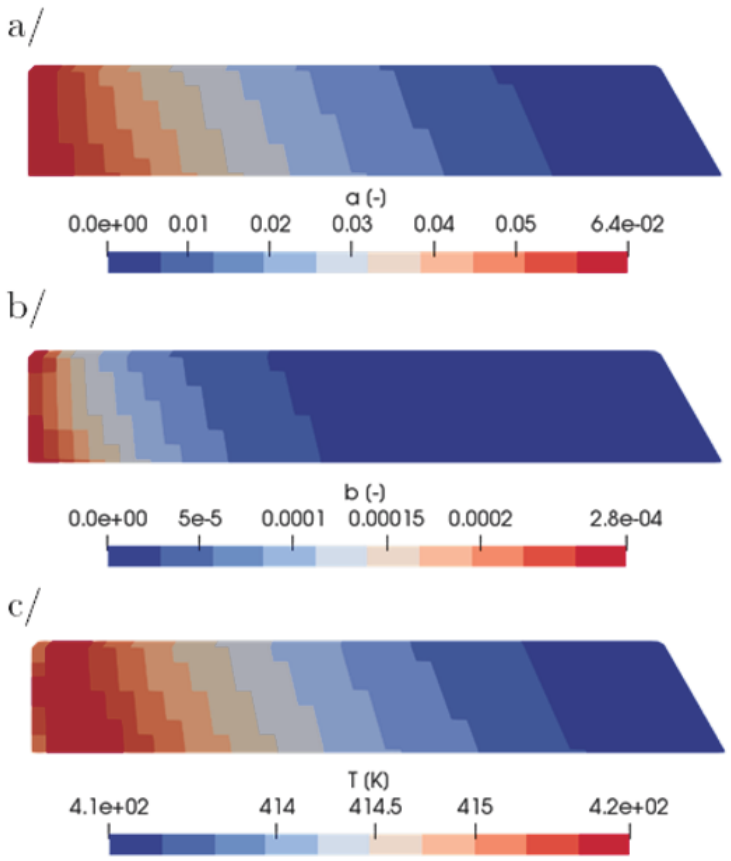

Figure 3.13. Distribution of the relative degree of polymerization a (a/), crystallization b (b/), the temperature T (c/) at the end of the injection (t = 10 min).

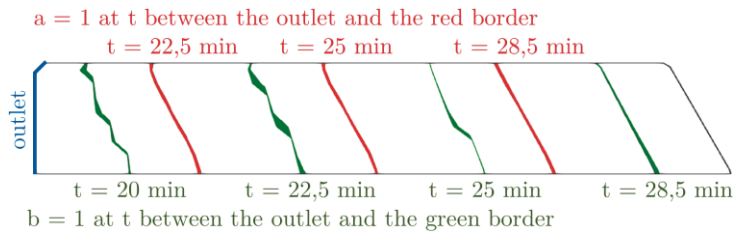

Figure 3.14: Proportion of the fully polymerized and fully crystallized part of the domain at different time, delimited between the outlet and the corresponding border.

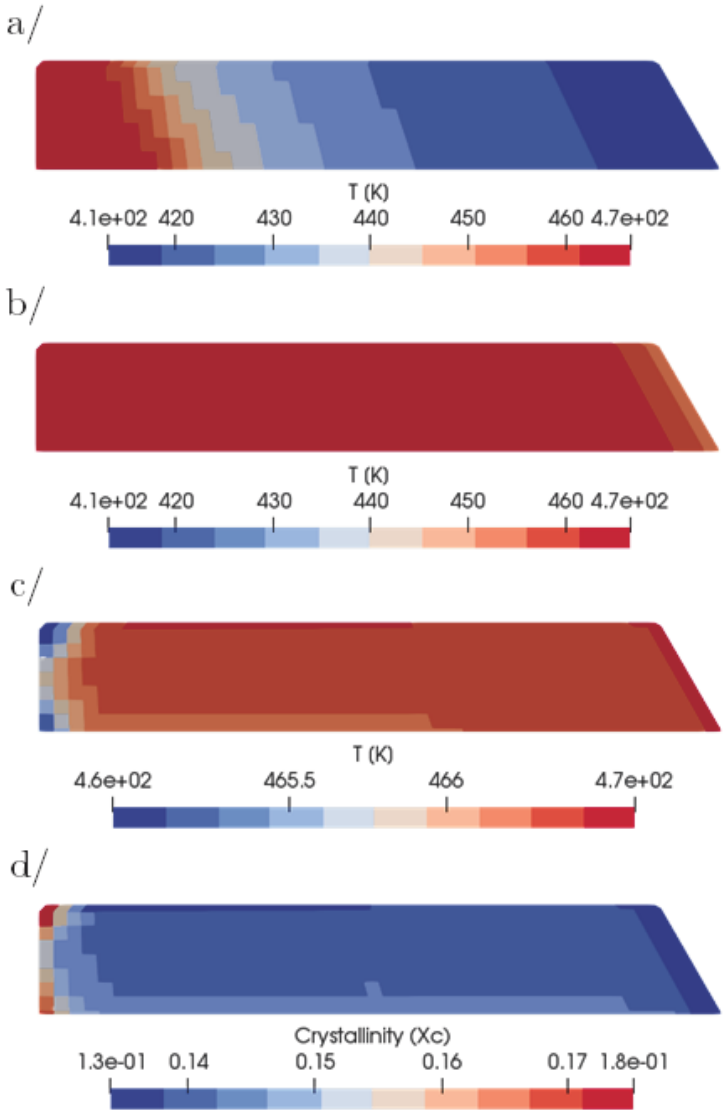

Figure 3.15: Temperature at a/ t = 20 min, b/ t = 28.5 min, c/ t = 30 min and crystallinity (d/) at t = 30 min.

3.5 Elements for experimental confrontation of the simulation

In the previous section, the possibilities of the simulation to give insights on effect of injection on the synthesis can be affected by the injection was presented. Namely, the age of the resin inside the domain varies along the injection duration, and with the eventual trapped air, it may influence the synthesis repartition. However, to confirm the relevance of the simulation, the observations need to be confirmed experimentally.

3.5.1 Experimental setup

An experimental setup for a resin injection was developed at Institut Clément Ader Albi. It was designed to be able to follow the resin front form above, while allowing thermocouple instrumentation inside the preform.

Mould

The mould is constituted by a 4 mm thick lower aluminium frame, with 9 mm diameter openings for the fluid inlet and outlet. Two vulcanized silicone sheets are placed on it and constitutes the shape of injection domain. The geometry of an individual sheet is shown in Figure 3.16. One sheet has a 2.3 mm thickness.

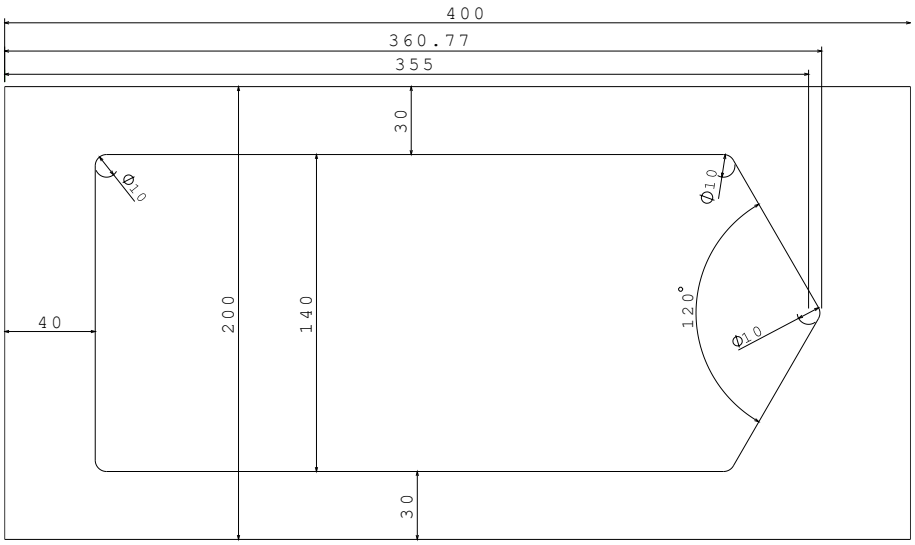

Figure 3.16. Vulcanized silicone sheets dimensions.

A 19 mm thick tempered glass panel is put on the silicone sheets and closes the injection domain. A transparent panel is chosen in order to allow visual tracking of the front. It was chosen over plastic materials such as polymethyl methacrylate (PMMA) to withstand temperatures that can go above 473 K. The mould is maintained in place with a 20 mm thick upper frame in aluminium fixed to the lower frame. It has two windows to observe the mould and has a minimal cross section of 20x20 mm². The high thickness of the glass panel and the upper frame ensure low deflection for reasonable pressure gradients (below 5 bars). Views of the setup are shown in Figure 3.17 and Figure 3.18, installed on a heating table.

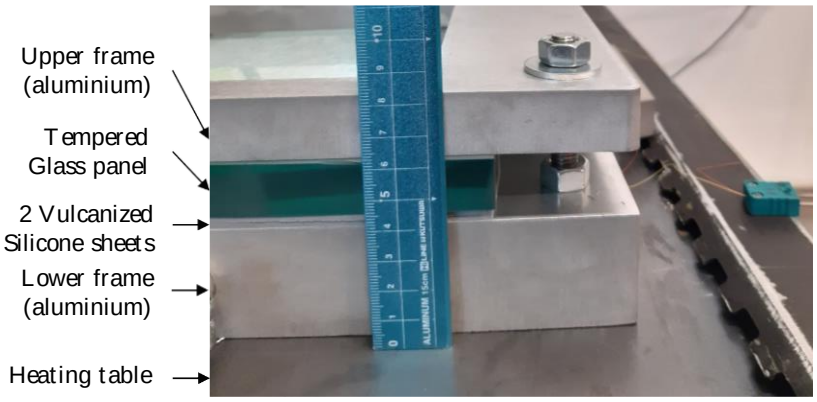

Figure 3.17. Side-view of the mould.

The mould is sealed by the two silicone sheets. The use of two silicon sheet allows to maintain a perfect seal when inserting thermocouples inside the cavity. To ensure a consistent thickness, some pockets are cut in the silicone sheets and 3.8°mm thick metallic spacers are placed (inserts can be observed in Figure 3.21).

Textile properties

The textile sample is the HexForce® 295g/m² 01102 1240 TF970 twill weave glass fiber woven fabric from Hexcel. Its nominal areal weight is $M_a = 295\ \mathrm{g/m^2}$ and is balanced between weft and warp direction. It was chosen as the fabric has been thoroughly characterised through three international benchmark exercises for in-plane and through thickness permeability measurement as well as compressibility measurement [30,31,171]. For the in-plane permeability measurement [30], nineteen different laboratories around the world participated, and multiple measurements at various FVF were realized with various experimental setup, all featuring unsaturated in-plane permeability characterization based on radial flow.

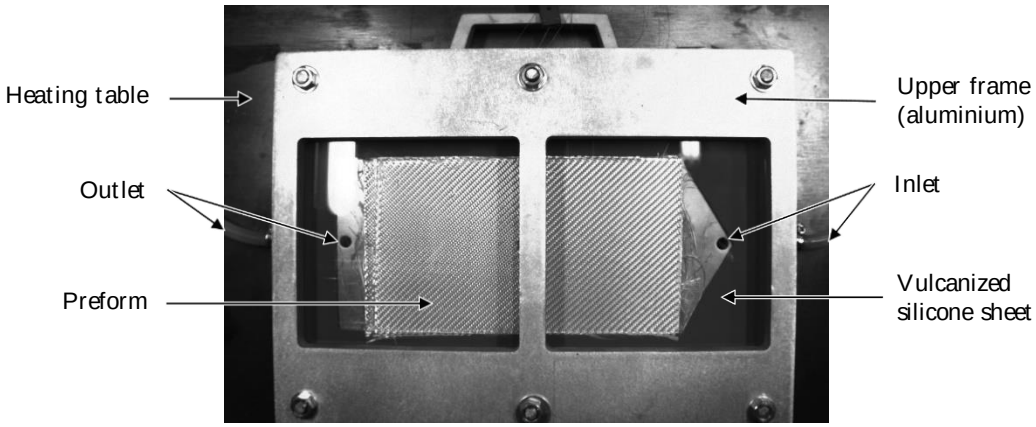

Figure 3.18. View from above of the mould.

To obtain permeability values for a specific FVF, a relation was derived from the measurements. Outlier results and those with an orientation angle between weft direction and K_1 greater than to 2° or unknown were omitted. Therefore, the 39 results (out of 66) used for interpolation are guaranteed to have been realized in similar conditions. Permeability results are shown relatively to the FVF in Figure 3.19.

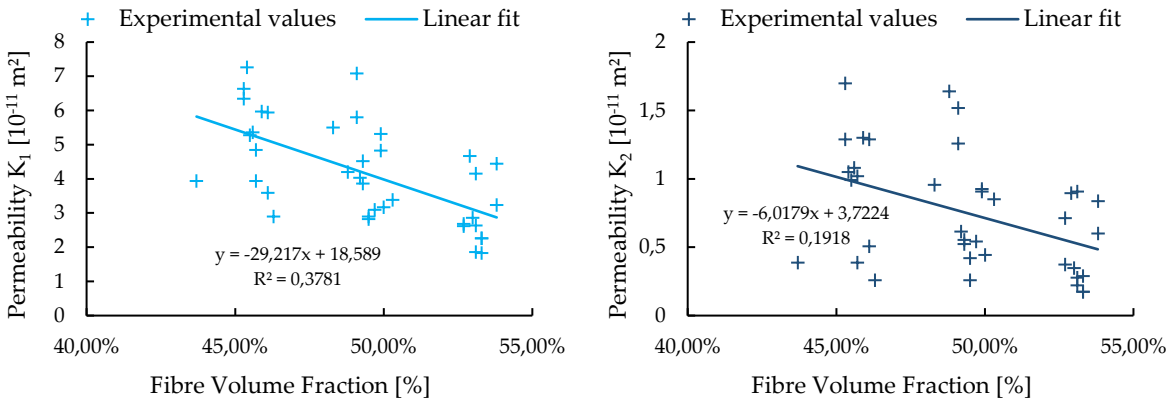

Figure 3.19. Permeability results for the woven fabric [30], and linear correlation.

Extrema for K_1 are $7.26 * 10^{-11}$ m^2 ($V_f = 45.4$ %) and $1.83 * 10^{-11}$ m^2 ($V_f = 53.3$ %). Extrema for K_2 are $1.70 * 10^{-11}$ m^2 ($V_f = 45.3$ %) and $1.76 * 10^{-12}$ m^2 ($V_f = 53.3$ %). Since there is a lot of variability, the results were correlated with a linear law for each permeability direction. This allows to obtain an average value for permeabilities for every V_f. The number of plies is linked to V_f using equation 3.30. h is the thickness and ρ_{gl} the glass fibre density, taken here at 2580 kg/m^3.

$$V_f = \frac{N_{ply}\rho_{gl}h}{M_a} \tag{3.30}$$

In the following text, 16 plies of textile were stacked, for a FVF of 48.1%. Therefore, the corresponding permeabilities can be extrapolated from the linear law in Figure 3.19. It gives $K_1 = 4.54 * 10^{-11}$ m^2 (warp direction) and $K_2 = 8.28 * 10^{-12}$ m^2 (weft direction). The through-thickness permeability was approximated from another benchmarking experiment for out of plane permeability of the same textile [31]. $K_3 = 2 * 10^{-12}$ m^2 was chosen for a FVF of 48.1%.

Test injection setup

A test injection was realized using water and is described here. Therefore, the inlet was placed in a water recipient and was weighted during injection for mass inflow. An air pump was linked to the outlet to control the pressure gradient in the mould. The heating is assured by the heating table, and a metallic assembly similar as used in Gantois [28] is used for stable image acquisition above the mould. A view of the setup excluding the inlet, outlet and acquisition system is shown in Figure 3.20.

5 thermocouples (Tc) of type K were were inserted inside the domain injection. Location of Tc3 and Tc4 are shown in Figure 3.21. Their diameter was chosen as small as available (0.75 µm) for minimal intrusiveness. Tc2 stopped working before injection, as such it will not be expanded on later. Tc1 and Tc5 are respectively placed on the lower aluminium frame and the 16th ply at a similar location as Tc3 (see Figure 3.22). A sixth thermocouple, Tc6 is used to measure the fluid temperature before injection.

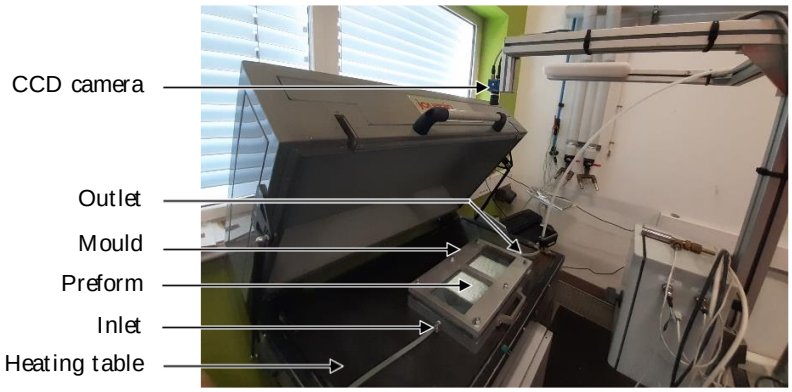

Figure 3.20. View of the mould and surroundings.

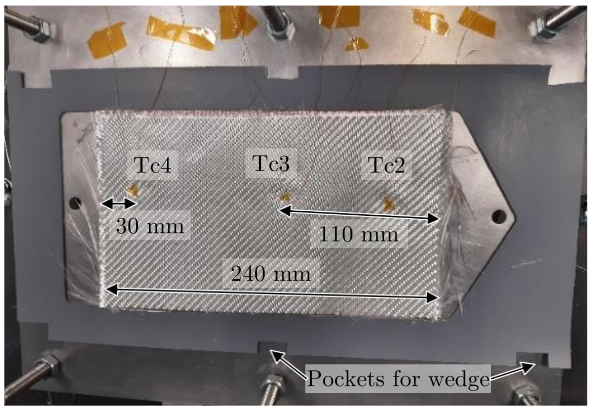

Figure 3.21. Thermocouples placement on the 8th ply.

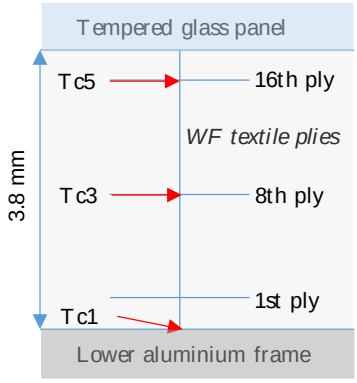

Figure 3.22. Thermocouple placement on the thickness (at Tc3 location).

3.5.2 Test injection with water experimental results

The program to synchronize acquisition of mass, temperatures and image was realized using LabVIEW.

Injection is realized with water with a pressure gradient of 0.2 bar imposed between the inlet and the outlet. The temperature of the injected water measured by Tc6 is constant, at 293.75 K. While the temperature of the heating table was set at 353 K, the injection was triggered before steady state is achieved inside the domain but was short enough for temperature variation in the aluminium frame to be negligible. The temperature of the lower frame at t=0 was 335.66 K, while it was 317.71 K near the glass panel. Compared to the PA6 reactive mix, water viscosity

is lower but in the same order of magnitude, while its surface tension is higher [172]. Thus, it is expected that the water front advances faster than if the reactive mix was used, but its impregnation inside the mesh may be slowed by the water's higher surface tension.

Image processing and visual front tracking

Because water is transparent, its injection front is not very distinguishable (see comparison of two frames in Figure 3.23 - injection is realized from the right).

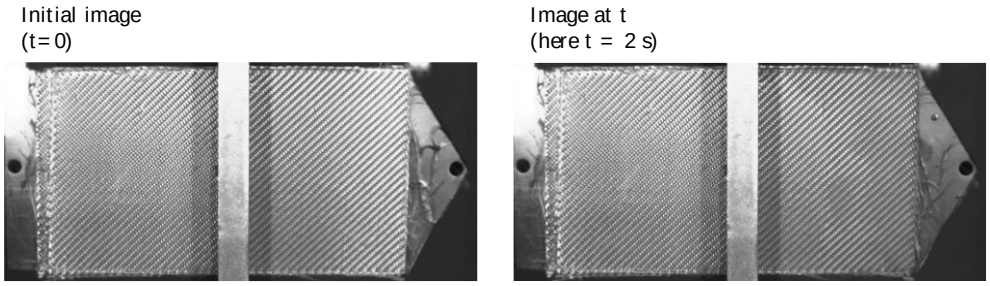

Figure 3.23. View of the injection domain at t = 0 s and t = 2 s.

To better observe differences, the initial image can be subtracted from the images at t, as without external interferences, only the front position changes between the frames (Figure 3.24). Then, Figure 3.24 has been added with itself, to obtain better contrast for the flow in the textile (Figure 3.25).

Figure 3.24. Subtraction of the two images from Figure 3.23.

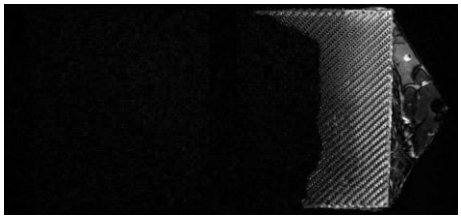

Figure 3.25. Figure 3.24 added with itself: post-processed injection frame at t = 2 s.

Views of the front at other times with the same post-processing method are presented in Figure 3.26.

The different contrasts at t = 2 s can be interpreted as a double front occurring in the preform, maybe caused by different infiltration speed inside or outside the tows, and between the plies. It becomes less visible as the injection advances since with constant pressure, the first front between tows and plies will catch up with the second front. Another observation is the race-tracking that occurs, mostly at the bottom of the frames in later injection times. It may be caused by defects during textile cutting.

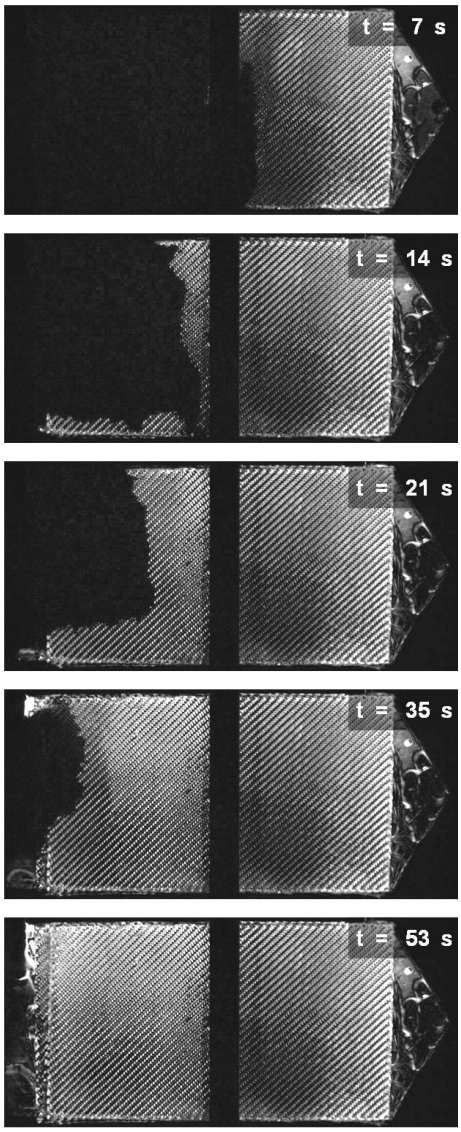

Figure 3.26. View of the post-processed frames for advancing water at different time of the injection.

Temperature measurements

The temperature measurements are shown in Figure 3.27.

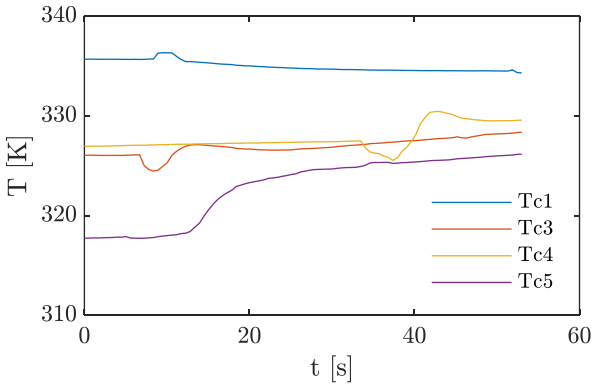

Figure 3.27. Temperature measurement during the injection

The passage of water over each thermocouple is detected by fluctuation in the curve. However, aside from Tc5 which see steady increase of temperature after the passage of water, it is complicated to explain. Another possibility is that some water near the glass panel was flowing faster, before going down because of gravity. It would also make the front near the glass to go slower, since it can't advance if the plies below are not impregnated yet, therefore explaining why the temperature of Tc5 increases slightly later. The temperature increase of Tc1 is especially difficult to explain since it happens only with the passage of the water's front. It may also be a result of different impregnation time through the thickness. Since the heating table was set at 353 K, the lower frame continues heating. If the water first arrived from below, it had been heated, before being cooled down by water arriving from above.

3.5.3 Simulation comparison

The preform is placed in the mould with the weft tows in the direction of the fluid flow. Therefore, the permeability tensor is defined using equation 3.31.

$$\boldsymbol{K} = \begin{bmatrix} 8.28 \cdot 10^{-12} & 0 & 0 \\ 0 & 4.54 \cdot 10^{-11} & 0 \\ 0 & 0 & 2 \cdot 10^{-12} \end{bmatrix} \mathrm{m}^2 \tag{3.31}$$

The simulation method is the same as in subsection 1.3.4. The volume averaged incompressible heat equation is calculated after the PISO algorithm. It is defined in equation 3.32. Parameters ρ and c_p are still the averaged fluid density and specific heat. As only the fluid is advected (assuming the fibres remains immobile), they direct the convection term. However, for the transient and diffusion term, $\bar{\rho}$, $\bar{c}_p$ and $\bar{\kappa}$ are introduced and calculated with the rule of mixtures. They are the volume averaged density, specific heat, and thermal conductivity between the glass fibres (ρ_{gf},$c_{p,gf}$ and κ_{gf}) and the fluid (ρ, c_p and κ).

$$\bar{\rho}\bar{c}_p \frac{\partial T}{\partial t} + \rho c_p \boldsymbol{\nabla} \cdot (\overline{\boldsymbol{u}} T) \; - \boldsymbol{\nabla} \cdot \bar{\kappa} \boldsymbol{\nabla} T = 0 \tag{3.32}$$

The chosen parameters for equation 3.32 are detailed in Table 3.5.

Table 3.5. Density and thermal properties.

Phase	Parameter	Value
Water	Density ρ_w	10^3 kg m^{-3}
	Specific heat $c_{p,w}$ [173]	4030 J kg^{-1}K^{-1}
	Thermal conductivity κ_w [174]	0.641 W m^{-1}K^{-1}
Air [175]	Density ρ_a	1 kg m^{-3}
	Specific heat $c_{p,a}$	10^3 J kg^{-1}K^{-1}
	Thermal conductivity κ_a	0.028 W m^{-1}K^{-1}
Glass Fibres [176]	Density ρ_{gf}	2580 kg m^{-3}
	Specific heat $c_{p,gf}$	802.5 J kg^{-1}K^{-1}
	Thermal conductivity κ_{gf}	1.275 W m^{-1}K^{-1}

Arrhenius law for viscosity dependency to temperature is already implemented in simulations (section 3.4). Thus, it was derived in equation 3.33 for water viscosity for the 313-333 K range, using data from Kestin et al. [177]. Extrapolated viscosity value and relative error with literature values are shown in Table 3.6. The very low errors indicates that at this temperature range, viscosity of water is well described.

$$\eta_{water\sim 320K}(T) = 2.6058 * 10^{-3} \exp\left(\frac{14372}{RT}\right) \tag{3.33}$$

Table 3.6. Water viscosity in simulation.

T [°C]	T [K]	Water viscosity (eq. (3.33)) [mPa s]	Relative error with [177] [%]
40	313.15	0.6506	-0.32%
45	318.15	0.5966	0.08%
50	323.15	0.5485	0.25%
55	328.15	0.5055	0.23%
60	333.15	0.4671	0.02%
65	338.15	0.4326	-0.30%

The simulation was done on a parallelepipedal domain representing half the fibre section of the injection domain, the other half being considered with a symmetry boundary condition. Its dimensions are therefore 240*70*3.8 mm^3 with a 48*14*10 mesh, represented in Figure 3.28. The lower wall cannot be seen but is located below the domain. All walls have no-slip boundary conditions for velocity, and zero normal gradient boundary condition for pressure and VOF equation.

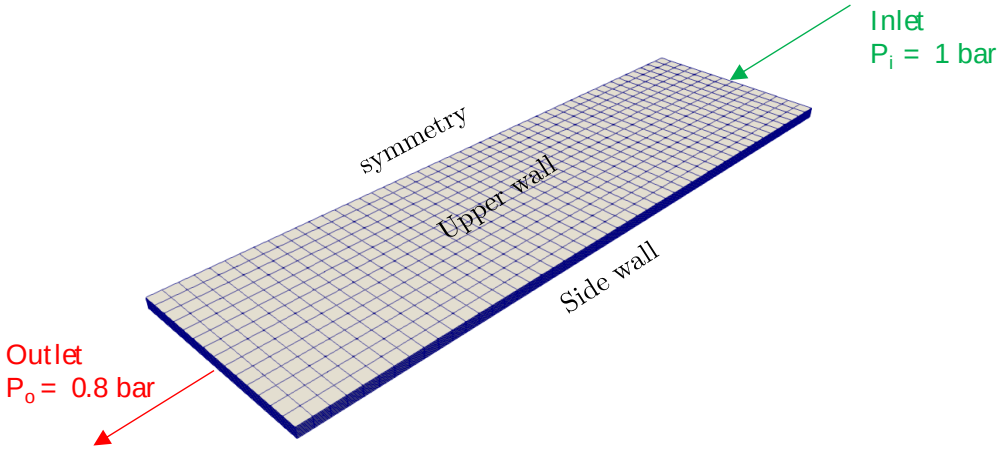

Figure 3.28. Domain geometry and mesh.

For temperature, the side wall is considered adiabatic (normal gradient is 0), while the lower wall is set with an isotherm at 335.66 K, obtained with the initial Tc1 value. The inlet temperature is set using Tc6, at 293.75 K. In order to obtain a realistic initial temperature distribution at the start in the domain a simulation is run with no flow and with the upper wall temperature initially set at 317.71 K (initial value of Tc5). The temperature in Figure 3.29

is therefore obtained when the simulation converges with a steady-state regime of temperature.

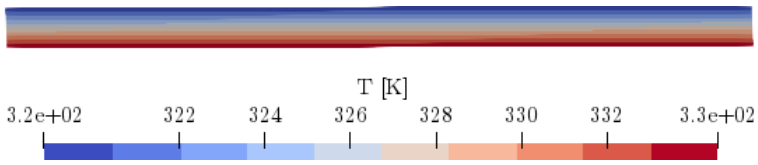

Figure 3.29. Initial temperature repartition through the domain thickness (seen from the inlet).

During the injection, a fixed temperature gradient is used for the upper wall. The value is given by calculations with a simplified 1D model in steady-state mode, which are detailed in Annex 5. For these conditions, $\frac{\partial T}{\partial n}(upper\ wall) = -381.52\ K/m$, n being the normal direction.

Figure 3.30 shows the temperature repartition at 7 s and 35 s in the middle of the injection domain, with the fully coloured elements representing water. At the inlet, water at ambient temperature is injected and is therefore colder. At both t = 7 s and t = 35 s, there is a concentration of temperature between the inlet and the flow front. It shows that the higher conductivity of water makes it much heat faster than air at the other side. Therefore, temperature at the front is slightly cooled by air.

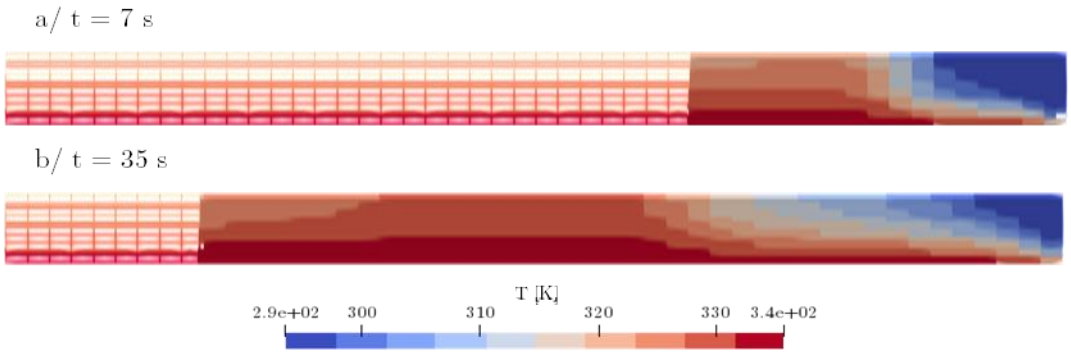

Figure 3.30. Temperature distribution at t = 7 s and t = 35 s seen at the symmetry plane (middle of the injection domain). The fully colored part represent element with a water saturation of at least 50%, the meshed part represent the rest of the domain. Injection was realized from the right side. Thickness scale is four times the length scale.

Water front comparison

In Figure 3.31, the simulated flow advance is qualitatively compared to the water front experimentally observed, on the side without race-tracking. Good agreement, albeit slightly underestimated from the simulation to the experience is observed. It could indicate that the simulation flow model is coherent with real conditions, but more tests are needed for confirmation, especially with the uncertainties on the textile permeability.

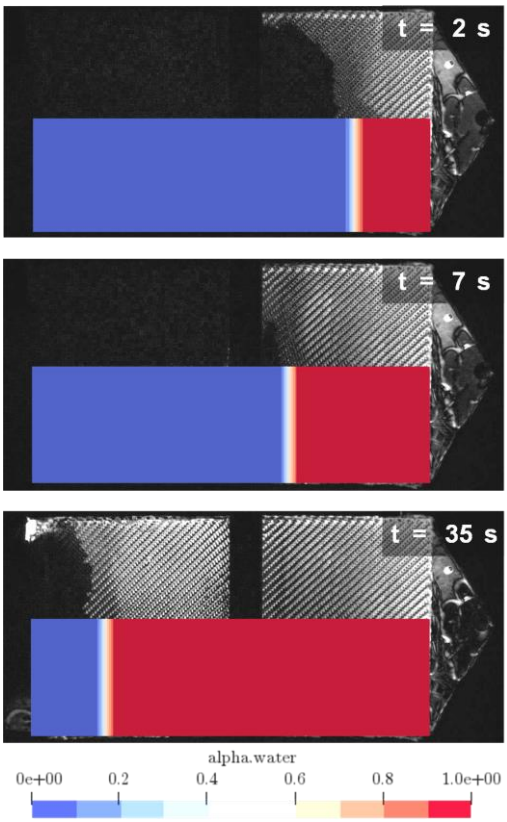

Figure 3.31. Comparison of water saturation during the simulation and experimental injection at three different times.

Temperature comparison

In order to compare experimental temperature and simulation, the value has been probed in the simulation at thermocouple locations (Figure 3.21 and Figure 3.22). However, the simulation value is not as punctual as the thermocouple, as it is the average temperature value inside the cell.

The temperature Tc at the thermocouples is compared to the simulation Ts in Figure 3.32, on the lower aluminium frame, is compared to simulation. Because of averaging, the simulated temperature Ts1 is lower than its counterpart at the beginning while Ts5 is higher. At the end of the injection, the temperature in the simulation is higher than the one measured by thermocouples, which suggest that the flux exiting the injection domain is underestimated. This is especially visible when comparing Tc3 and Tc5 to their simulated counterpart.

The odd temperature behaviour observed in Tc1, Tc3, and Tc4, are not reproduced by the simulation. Supposing the hypotheses above are correct, it is not surprising since gravity is not taken into account, and there is no reason for the flow front to advance faster near the glass panel. The contrary would be more likely to happen instead in the simulation because the viscosity would be lower near the hot aluminium frame. At the start, the simulated temperature Ts3 and Ts4 are higher than their experimental counterpart. Possible explanations are volume averaging, or incorrect modelling of the initial state since the regime is not completely permanent at the start of injection. However, the possibility that the thermocouples are lower than their location suggests cannot be dismissed.

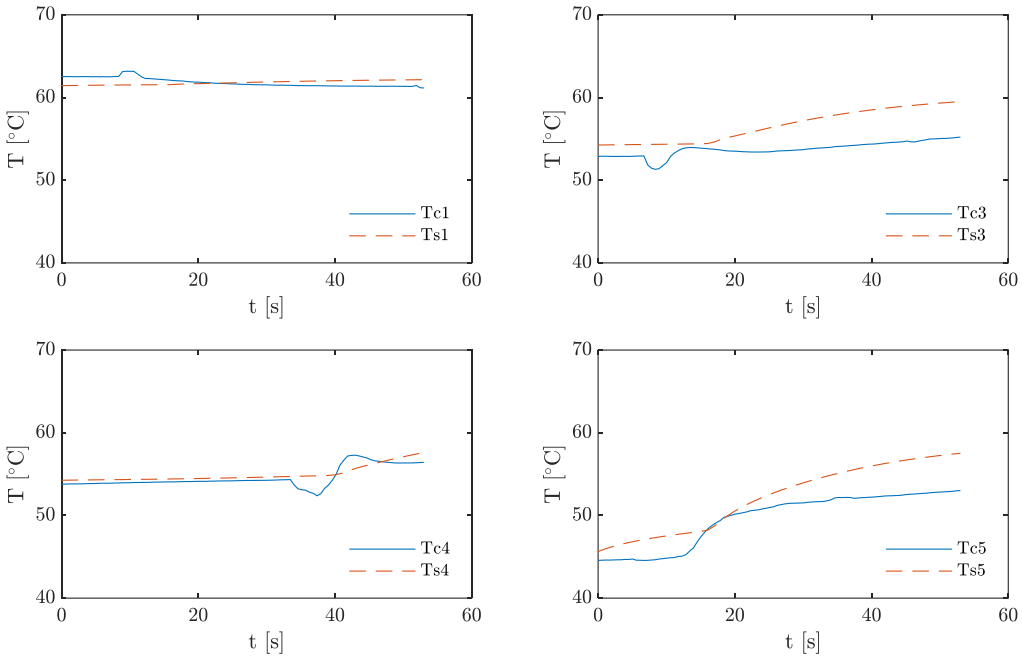

Figure 3.32. Temperature measured by thermocouple (Tc) compared to simulated value (Ts).

3.5.4 Prospective results with the reactive mix

Experimental comparison of water injection in the preform showed what can be expected of comparison in term of front and temperature. As shown in section 3.4, a time lag throughout the domain can be expected in temperature variation due to the kinetic model. The effect however is limited as the low viscosity of the monomer makes the injection time small compared to the synthesis duration, unless very high temperatures are used.

However, due to the different temperature conditions of the glass panel and the lower aluminium frame, variation in properties is expected. For instance, a simulation was realized using similar parameters as in subsection 3.5.3, but after a one-minute-long injection to fill the domain, simulation was continued, leaving the fluid at rest during 10 minutes until synthesis completion. The resin was injected unreacted at 383 K inside a domain with a lower frame temperature of 453.15 K, and a temperature gradient at the upper wall of $\frac{\partial T}{\partial n} = -2331\ K/m$.

The resulting temperature and crystallinity distribution is observed in Figure 3.33. The resulting crystallinity is generally higher near the top, because the exiting heat flux made the temperature go as low as 443 K. It is lower near the inlet (at the right of the figure) as the reaction ended later which kept the polymer hot.

Therefore, a gradient of crystallinity depending on temperature injection of the reactive mix with the presented setup may be observed even with the naked eye if it is high enough. However, with unaccounted flow parameters, the synthesis variability, the model perfectible accuracy and the potential reaction inhibition by the glass fibres [14] experimental synthesis after injection may not run as smoothly as predicted by the simulation.

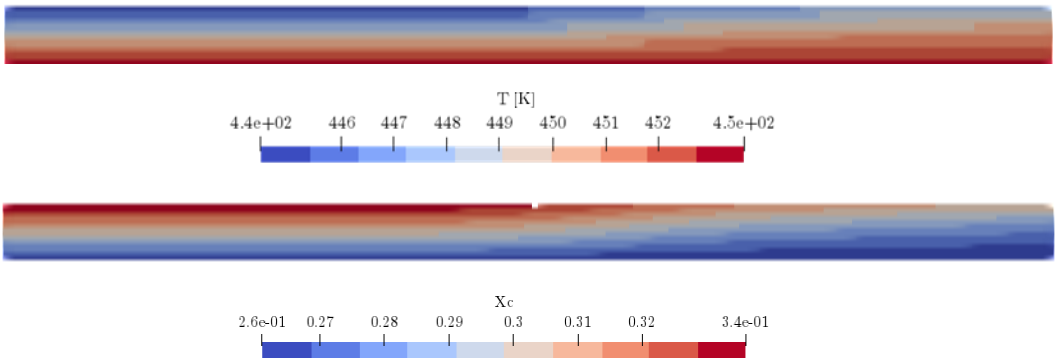

Figure 3.33. Temperature and crystallinity distribution at the end of the simulation. Injection was realized from the right side. Thickness scale is four times the length scale.

Chapter conclusion

Methods for numerical tracking of resin front and coupling with resin reaction and flow have been reviewed. Studies pertaining to integration of reactive PA6 system crystallization in process simulation are rare. Therefore, to propose such integration, elements for a non-isothermal reactive LCM process simulation are given here, by combining the flow model presented in Chapter 1 and the synthesis method from Chapter 2.

First, the transposition of the crystallization model to non-isothermal settings in a Eulerian framework has been studied. The proposed procedure has shown to reasonably describe the experimental behaviour measured using DSC, although a gap remains. It may be caused by temperature differences inside the DSC sample during measurement, but it is more than likely that some light still needs to be shed on the mechanisms that direct the start of polymerization and crystallization.

Then, the procedure for synthesis calculation including crystallization in a Eulerian framework is coupled with flow equations and heat equation. Results show how the time delay caused by injection can result in variations of temperature and crystallinity.

Finally, an experimental setup has been developed for fluid injection inside a fibrous preform, from which the front flow can be visually tracked. Thermocouples located inside the injection domain permit temperature measurement. A preliminary test has been achieved using water, and comparison with computation results show promising results. Numerical simulations can emphasis what results are expected with the experimental setup. However, injection using a reactive mix still need to be performed.

For reactive injections in this chapter, to simplify numerical integration, polymerization was assumed to be an intensive variable, or an intrinsic property of the resin. As mentioned in the chapter, the assumption is acceptable for simple flows. It also has the advantage to add no diffusion at the interface between resin and gas, since the reactive mix contribution is realized only on the heat transport and VOF equation. However, for numerical simulation using geometries where more complex flows can occur (for instance the textile sample in section 1.3), different portion of the polymerized reactive system can mix together. Thus, the transport equation for polymerization will also need to be volume averaged for these simulations.

Conclusion and prospects

In order to further understanding of reactive thermoplastic composites fabrication by LCM, the behaviour of the PA6 reactive mix during the process was investigated. Previous works on reactive PA6 realized at ICA (Clement Ader Institut) [14–16], derived data and models about the synthesis. To expand from these findings, the study focused on three main areas: simulation of resin flow in a fibrous preform, enhancement of the synthesis model, and its integration for full process simulation.

As interaction of the resin flow with the fibre is of capital importance in LCM process, a literature study revealed the numerous related studies. The Brinkman equation in OpenFOAM® framework can be readily used with minimal adaptation for both meso-scale simulations with tow modelled as a permeable media and for unsatured simulations. Tests using Gebart configurations with cylindrical tows showed the influence of tows permeability and the requirements for meshing and numerical convergence. Simulation with quasi-impermeable tows demonstrated the possibility to predict a given geometry permeability. Then, simulations on an experimentally acquired geometry [21] showed deviation on simulated permeability when compared to experimentally determined permeability. This highlighted the importance of cross-section and available channels on the flow. Showcase of dual-scale unsaturated simulation capability with the VOF method throughout the realistic geometry closes this part of the study.

Then, study of PA6 behaviour synthesis models has been realized. When polymerization and crystallization models are determined separately, older coupling methods fail to accurately describe the phenomena. The inadequacy of those methods is reaffirmed in this study. As a replacement, Vicard et al. [16] proposed a coupling model that temporally discretize the crystallization kinetics with relation to polymerization. However, as it involves a convolution integral which is inconvenient to compute, a new method has been proposed to describe the crystallization dependency to polymerization. It is based on averaging the local crystallization relative to the polymerization state in the whole domain of study and is much easier to differentiate and calculate. A comparative study between the methods followed and demonstrated similar description performances. The biggest gap was observed when the duration of local crystallization kinetics was similar to polymerization kinetics, around 453 K. With the observation of high measurement variability, an average model has finally been proposed derived from the whole DSC isothermal data derived from Vicard thesis [14].

The study is subsequently extended to its rheology. Due to difficulties linked to evaporation, atmosphere sensibility and very low viscosity of the monomer, which is barely higher than water's, studies have been scarce. Rheological measurements realized at a high shear rate

allowed to determine the temperature dependency of the reactive mix initial viscosity. Using previous [14] and new rheological measurements, a study was realized on the dependency of viscosity to polymerization and crystallization. A tentative integration of the synthesis model to describe the viscosity rise has been realized.

Then, the focus was extended to the integration of the synthesis model for LCM simulation. After a review of previous work on the subject, it was revealed that only few studies tackle the subject of reactive injection, and none have been found to include polymerization and crystallization coupling. At first, the problem of non-isothermal crystallization was investigated. Model based on crystallization degree turned out to be unsuited for non-isothermal situations, because they assume a final crystallinity which is dependent on temperature. To alleviate this issue, a resolution procedure to update crystallization at each time step is proposed. It requires memorization of crystallization history, which was done by integration of the crystallization enthalpy at each time step. Then, the temperature evolution caused by the reaction or external factors can be considered by updating the crystallization degree. With this proposed solution, integration of a synthesis model for reactive PA6 was possible. Choice of the new coupling model rather than Hillier-Vicard was based on ease of differential resolution and integration in a Eulerian framework. In order to account for the crystallization initiation time, transport equations to record the resin age in the domain, and a snapshot of polymerization history, are added. A comparison of the non-isothermal synthesis model procedure with previously realized DSC measurements [15] is subsequently proposed. It showed its ability to predict the synthesis enthalpy, and consequently the final crystallinity of the sample. Afterwards, a reactive injection simulation is presented and demonstrates the potential effect of temperature difference caused by the exothermic synthesis on crystallinity.

Finally, elements are provided for experimental confrontation of the simulation. An experimental setup has been developed. A preliminary injection of water inside a fibrous preform with known permeability was studied and used to test the simulation front and temperature tracking. However, the presence of a double front at the beginning of the injection and the variation of temperature showed interaction between flow and fibrous preform which are not described because of simplifying hypotheses. Results of simulation of injection and synthesis for the reactive mix including a porous media and a non-adiabatic domain is presented, to showcase the expected variation of crystallization that could be observed. This simulation can then be used to define the experimental parameters that would lead to noticeable variation in temperature and final degree of crystallinity and serve as basis for confrontation with experiment.

This thesis study attempts to propose a full simulation methodology for LCM processing of reactive PA6. Nonetheless, there are still subjects that need to be expanded on.

For flow simulation inside a textile, the influence of tow permeabilities and its volume fraction on the domain need a more in-depth study to better understand their interactions. Study on the realistic geometry showed that the influence of the channel cross-section is also important, and thus merit further investigation. This study also ignored the interaction between fibres and flow. However, not only multiple studies showed the influence of fluid surface tension on

infiltration and gas voids creation through capillary flow, but the injection momentum can also cause displacement of the tows. As the method employed here has been computationally expensive when dual-scale flow is calculated, it is not the most efficient for macro-scale calculations. However, simulations at meso-scale in a REV can give valuable information on flow behaviour at tow scale. They may be used to help parametrize computationally more efficient methods, such as sink-term modelling [18].

The study on PA6 synthesis gives a powerful tool for describing its behaviour, and it was demonstrated that it can be extended to rheology and non-isothermal settings. Some points still need elucidation. Better understanding of the initiation mechanisms of both polymerization and crystallization is needed. It may allow determination of more elegant models that rely less on numerical optimization and on empirical parameters to slow down crystallization and understanding of differences between non-isothermal simulation and experimental results. The latter would also benefit from simulations that faithfully reproduce the conditions of the DSC measurements. Mastery of the kinetics variability is also needed for better synthesis predictions. Coupled with a rigorous protocol of measuring the reactive mix rheology, a realistic chemorheological model could be determined. In this aspect, aside from the challenges coming from evaporation and humidity, issues that need to be resolved also includes the temperature in the sample and the influence of shear rate on the synthesis. The former is not as homogeneous as with DSC studies, while the latter is likely to slow down the synthesis especially at the edge of a parallel plate rheological experiment. Furthermore, fibres can have an adverse effect on PA6 synthesis. It is likely that the synthesis model can be adapted to fibres interaction similarly to what has been done for experimental variability, however confirmation would need experimental investigation. Studying microscopic observations of samples where experimental parameters are rigorously controlled could help elucidate the links between the different factors involved in the synthesis.

Finally, full process simulation comparison with experimentation was not completed in this study. Preliminary simulation results have shown that experimental reactive mix injection may be capable to shed more light on the shortcomings of the simulation, notably on flow description and synthesis prediction. However, tests risk to be hampered by the variable PA6 kinetics and its interaction with fibres. The synthesis model has also not yet been coupled with dual-scale flow simulations. After averaging the transport equation to account for more complex flows, it would allow to see the potential effects of slower tow impregnation on the overall synthesis and void formation.

Annexes

Annex 1 Analytic form of autocatalytic models for linear reaction order (np = mp = 1)

Following Malkin and Camargo model (2.10), if $n_p = 1$, it is written as follow

$$\dot{a} = \frac{da}{dt} = k_1(1-a)(1+B_0 a) \tag{0.1}$$

It is interesting to note that the following also apply for the Kamal-Sourour model 2.14, if $m_p = 1$ and B_0 follows an Arrhenius law.

By integrating the expression and isolating the polymerization dependant monomials, it can be rewritten for $a_x < 1$, and t_x its corresponding time:

$$\int_0^a \frac{1}{(1-a_x)(1+B_0 a_x)} da_x = \int_0^t k_1 dt_x \tag{0.2}$$

Using the partial fraction decomposition method, with $B_0 > -1$ and constant temperature, the following is obtained:

$$\int_0^a \frac{1}{1-a_x} + \frac{B_0}{1+B_0 a_x} da_x = (1+B_0)k_1 \int_0^t dt_x \tag{0.3}$$

The integration can be thus calculated.

$$-\ln(1-a) + \ln(1+B_0 a) = (1+B_0)k_1 t \tag{0.4}$$

Finally, the following analytical expression for a and t for linear autocatalytic models of polymerization can be obtained.

To simplify the expressions, we will write $K_p = (1+B_0)k_1$

$$\begin{cases} t(a) = \dfrac{1}{K_p}\ln\left(\dfrac{1+B_0 a}{1-a}\right) \\ a(t) = \dfrac{e^{K_p t} - 1}{e^{K_p t} + B_0} \end{cases} \tag{0.5}$$

For $a \in [0,1[$, and $n_p > 1$, we have the following inequalities, which could give some insight on the error of ignoring the reaction order.

$$1 - n_p a < (1 - a)^{n_p} < 1 - a \tag{0.6}$$

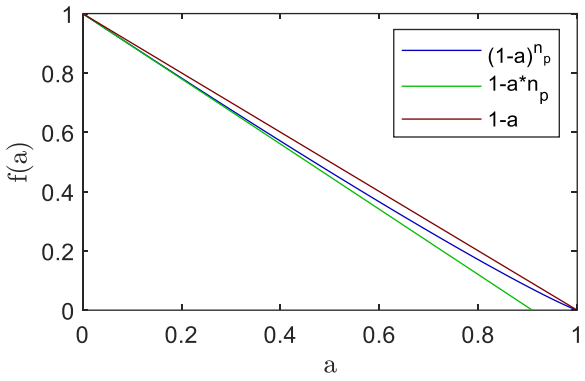

Figure 0.1: Comparison (0.6) between 0 and 1 for $n_p = 1.1$

Annex 2 Comparison of minimization algorithms

The diffusion factor parameters proved to be tricky to solve for iterative methods. Therefore, to optimize model parameters in section 2.4, different minimization algorithms present in MATLAB® were tested.

Multiple methods are implemented in MATLAB® R2018a through the Optimization Toolbox™ and the Global Optimization Toolbox. The tested MATLAB® functions can be divided in three categories: gradient based methods, direct search methods, and metaheuristics. They are listed and classified in Table 0.1.

Table 0.1 Optimization methods present in MATLAB® tested with equation (0.7)

Derivative based methods	Direct search methods	Metaheuristics methods
fmincon	*fminsearch*	*ga*
lsqnonlin	*patternsearch*	*simulannealbnd*
fminunc		

In the following text, the optimization test is described first and then the methods performance is discussed along a brief description of the function algorithm (based on MATLAB® R2018a documentation of the Optimization Toolbox™ and the Global Optimization Toolbox [178]).

Test optimization parameters

The optimization algorithms were tested on minimizing the following function (equation 2.47) in one measurement at 413 K, with φ_{sim} being calculated with the method detailed in 2.3.4.

$$f_{test}(C,D) = \left\| \varphi_{exp}(t) - \varphi_{sim}(t,C,D) \right\|_2 \tag{0.7}$$

The initial values were the one proposed by Vicard [14] (42 and 35 respectively), found using the *fmincon* function multiple times with randomized initial points.

Results

The full results are displayed in Table 0.2. The functions were tested with their default parameters without constraints and were all able to reach convergence aside from *patternsearch*. The optimization was considered converged if an exit parameter was reached (usually if the algorithm step size, the function variation, or a similar parameter varied less than 10^{-6}), which is mentioned in Table 0.3. The *patternsearch* function was tested both with default parameters, and with an extended limit for the number of iterations in order for the optimization to converge. The normalized objective function result was calculated from the ratio between the initial objective function results ($f_{test,i} = 1.17 \cdot 10^{-3}$) and the optimized objective function result.

Table 0.2 Results of optimization with different minimization algorithms

Function name	C	D	Calculation time [s]	Optimized objective function result
lsqnonlin	41.99	34.98	21.54	1.17E-03
fmincon	41.98	34.96	52.2	1.17E-03
fminunc	42	35	58.84	1.17E-03
fminsearch	20.42	16.67	125.19	5.07E-04
patternsearch	24.03	19.56	761.8	5.46E-04
patternsearch (converged)	21.35	17.42	1716	5.10E-04
ga	22.02	17.82	4209.8	5.21E-04
simulannealbnd	22.65	18.33	1514.6	5.26E-04

Table 0.3 Ending cause of optimization for each function and normalized value of objective function result

Function name	Ending cause	Normalized value of objective function result
lsqnonlin	step size <1e-6	0.999
fmincon	step size <1e-6	0.998
fminunc	objective function cannot be decreased	1.000
fminsearch	step size <1e-6 and function value variation < 1e-6	0.434
patternsearch	max. iterations reached (200)	0.467
patternsearch (converged)	mesh size <1e-6 (442 iterations)	0.436
ga	average change in the fitness value <1e-6	0.446
simulannealbnd	change in best function value <1e-6	0.450

In Figure 0.2 the normalized value of the objective function results is compared to the simulation time. It can be deduced from it that derivative-based methods are not able to minimize while direct search methods seem to be the most efficient. Indeed, *fminsearch* had overall the best performance in speed and minimization, and *patternsearch* could match the minimization performance of *fminsearch* with a slightly longer optimization time than *simulannealbnd*. The metaheuristic methods had decent performance, but for a much longer optimization time, especially for *ga*. However, it has to be noted that *fminsearch* and *patternsearch* converged results were more different than the similar minimization performance suggests. Indeed, the optimized parameters variation approaches 1 while the difference in optimized objective function value is only 0.002. In Figure 0.3 converged optimization results from *fminsearch*, *patternsearch* and *simulannealbnd*, are compared to the result obtained with initial parameters, and the experimental baseline. The figure shows the improvement given by the optimization algorithm, and the similarity between *fminsearch* and *patternsearch* converged minimization.

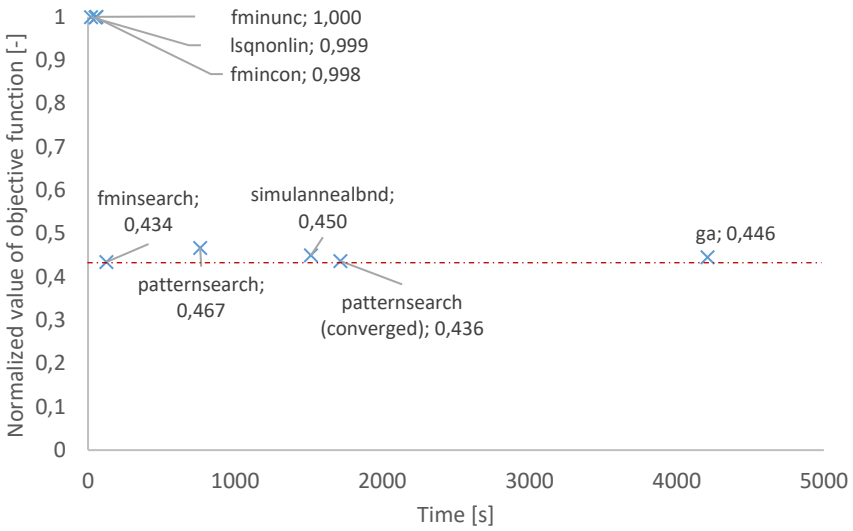

Figure 0.2 Value of the minimized objective function (normalized by the initial value) with relation to the computation time for each tested functions. The red dotted line indicates the best normalized objective function value (0.434)

a/

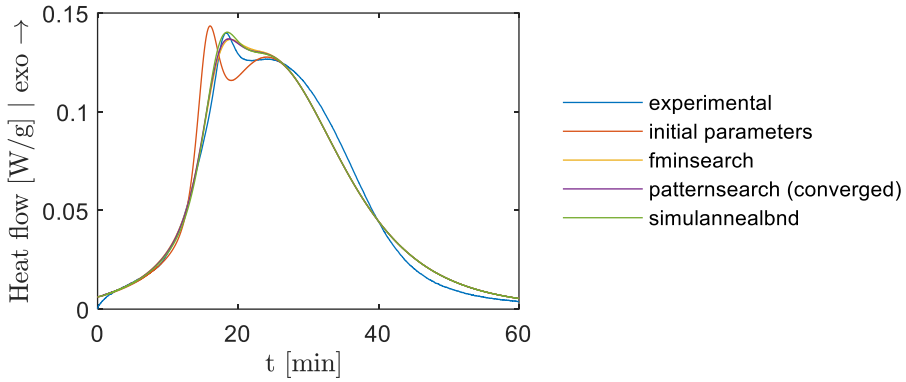

b/

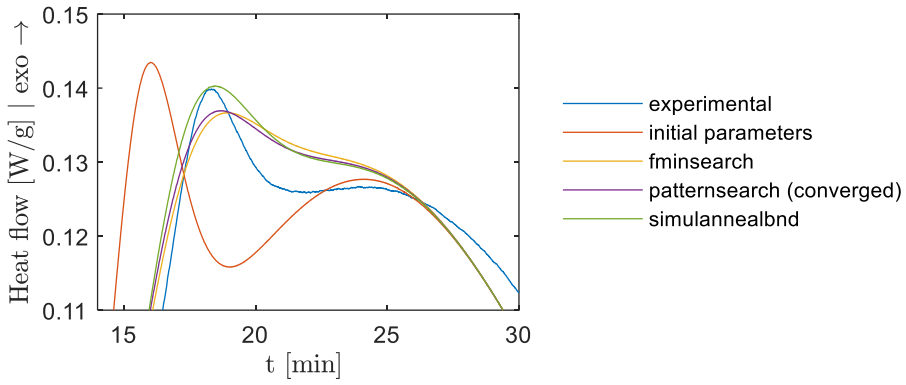

Figure 0.3 Comparison of heat flow curves between initial parameters, optimized parameters by fminsearch, patternsearch and simulannealbnd, and experimental measurement. a/ shows the whole measurement, b/ zooms in the area of interest

Optimization algorithms and results discussion

1/ Derivative based methods results

Derivative methods refer any algorithm that uses derivatives of the objective function to find the minimum, through gradients or hessians. It includes the *fmincon* function uses the "interior-point" algorithm while the *lsqnonlin* is based on the Levenberg-Marquardt method. As they are constrained non-linear solvers, the unconstrained quasi-newton based function *fminunc* was also tested.

Neither algorithm managed to improve the solution, which is not surprising concerning *fmincon* as it was the source of the initial points. However, the bad performance of the two other algorithms showed that derivative based methods are at the very least unsuited to this problem formulation.

2/ Direct search methods results

Direct search methods use algorithms which iteratively reduce the interval space solution to minimize the function instead of using derivative based iterations. It includes both *fminsearch* for unconstrained optimization and *patternsearch* which allows constrained optimization. The *fminsearch* function uses the Nelder-Mead method (also called downhill simplex method) while *patternsearch* uses the generalized pattern search algorithm which finds a minimum by iteratively moving and shrinking a mesh.

They proved to be the most performant methods for our problems, with the Nelder-Mead method showing unparalleled speed and performance. The pattern search method was much slower and required more iterations than proposed by default to approach the optimization performance of the Nelder-Mead method. However, as mentioned before, with the difference between the optimized parameters set not matching the minimization performance, they have likely reached two different local minima. Still, their quality is better than the initial local minima.

3/ Metaheuristic methods results

Metaheuristic methods are unconventional optimization methods used for complex problems where methods are either unusable, or unable to give a satisfying solution. The principle for solution research and selection greatly varies between different metaheuristic methods. The tested functions, *ga* and *simulannealbnd* are respectively based on the genetic algorithm and the simulated annealing heuristic which apply some degree of randomization to avoid local extrema trapping as much as possible.

The methods were used to ensure that the solution range obtained with the direct search methods are not another local extremum, even if they do not guarantee it. The similar results obtained compared to the direct search method show that the results obtained with direct search methods give "high-quality" local minima. However, the methods require to compute

the objective function in an enormous number of points, and consequently have a comparatively bad time/performance ratio.

Conclusion

As the derivative-based methods seem to be trapped in a local minimum while the metaheuristic methods take long calculation time without better performance, direct search methods were privileged for our minimization problem. Despite the better performance of *fminsearch*, the *patternsearch* function was often preferred to *fminsearch* because the latter does not allow the inclusion of optimization constraints. However, while the aforementioned tests showed the potential for direct search methods based optimization for our problem, the results difference between the two methods show that minor local minima are plenty and thus, a more comprehensive study of the problem may give better model parameters.

Annex 3 Synthesis model numerical protection

Equations obtained from trial and error to stop OpenFOAM® simulations from crashing because of unsupported operations. They include division by zero, logarithm and root of negative numbers, and unsupported huge numbers usually caused by exponentials of big numbers. They are neither optimized nor efficient. However, finding the optimal formulations would not noticeably improve results, while requiring need a more in-depth study.

Corrected crystallization time

$t_{c,0} = A_t \exp\left(\frac{E_t}{R\left(T_m^0 - T_p\right)}\right)$		(0.8)
$T_p =$ $\mathcal{H}\left(T - T_{p1}\right)\mathcal{H}\left(T_{p2} - T\right)T$ $+\left(1 - \mathcal{H}\left(T - T_{p1}\right)\right)T_{p1}$ $+\left(1 - \mathcal{H}\left(T_{p2} - T\right)\right)T_{p2}$	$T_{p1} = 328.55\ K,\ T_{p2} = 485.95\ K$ if $T \in \left]T_{p1}, T_{p2}\right[, T_p = T$ if $T \leq T_{p1}, T_p = T_{p1}$ if $T \geq T_{p2}, T_p = T_{p2}$	(0.9)

Corrected Hoffman – Lauritzen

$K_c(T) = K_0 \exp\left(-\frac{U^*}{R\left(T_p - T_\infty\right)}\right)\exp\left(\frac{-K_g\left(T_m^0 + T_p\right)}{2T_p^2\left(T_m^0 - T_p\right)}\right)$	(0.10)

Corrected Malkin & Camargo

The same modification are realized for a_r with $t_{c,0}$.

$a > 0$ $\dot{a} = [\mathcal{H}(1-a)(1-a)]^{n_p}(1 + B_0 a)A_1 \exp\left(\frac{E_{a,1}}{RT}\right)$	For $n_p = 1.1$, $(1-a)^{n_p} \in \mathbb{R} \Leftrightarrow$ $1 - a \geq 0$	(0.11)

Corrected diffusion parameter

$f_d(a_r) = 1 - \mathcal{H}\left(T_{f2} - T\right)\frac{1}{1 + \exp\left(C\left(T_{pf}\right)(a_r - 1) + D\left(T_{pf}\right)\right)}$		(0.12)
$T_{pf} =$ $\mathcal{H}\left(T_{f2} - T\right)T$ $+\left[1 - \mathcal{H}\left(T_{f2} - T\right)\right]T_{f2}$	$T_{f2} = 463.15\ K$ if $T < T_{f2}, T_{pf} = T$ if $T \geq T_{f2}, T_{pf} = T_{f2}$	(0.13)

Corrected crystallization

With $\epsilon = 10^{-6}$

$a_a(t) = f_d a_r \mathcal{H}(f_d a_r - \epsilon)$ $+ \epsilon[1 - \mathcal{H}(f_d a_r - \epsilon)]$	If $f_d a_r > \epsilon, a_a = f_d a_r$ else $a_a = \epsilon$	(0.14)

$\beta(t) = \frac{\mathcal{H}(a_a - b)b}{a_a} + 1 - \mathcal{H}(a_a - b)$	If $a_a > b, \beta(t) = \frac{b}{a_a}$ If $a_a \leq b, \beta(t) = 1$	(0.15)
$\beta_p(t) = \mathcal{H}(\beta - \epsilon)\mathcal{H}(1 - \epsilon - \beta)\beta + [1 - \mathcal{H}(\beta - \epsilon)]\epsilon + [1 - \mathcal{H}(1 - \epsilon - \beta)](1 - \epsilon)$	If $\beta \in]\epsilon, 1 - \epsilon[, \beta_p = \beta$ If $\beta \leq \epsilon, \beta_p = \epsilon$ If $\beta \geq 1 - \epsilon, \beta_p = 1 - \epsilon$	(0.16)

Now f_b can be written, as with $1 - \beta_p \in [\epsilon, 1 - \epsilon]$ the logarithm is always a real positive.

$f_b = n_c(1 - \beta_p)\ln\left(\frac{1}{1 - \beta_p}\right)^{\frac{n_c - 1}{n_c}}$	(0.17)

Equation (0.19) is written to satisfy Levy robust formulation of Nakamura's model.

$f_{b,m} = n_c \epsilon \ln\left(\frac{1}{\epsilon}\right)^{\frac{n_c - 1}{n_c}}$	(0.18)
$f_{b,p} = \mathcal{H}(\beta - \epsilon)\mathcal{H}(1 - \epsilon - \beta)f_b + [1 - \mathcal{H}(\beta - \epsilon)]\epsilon + [1 - \mathcal{H}(1 - \epsilon - \beta)]\frac{(1 - \beta)f_{b,m}}{1 - \epsilon}$	(0.19)

Annex 4 Full non-isothermal DSC results

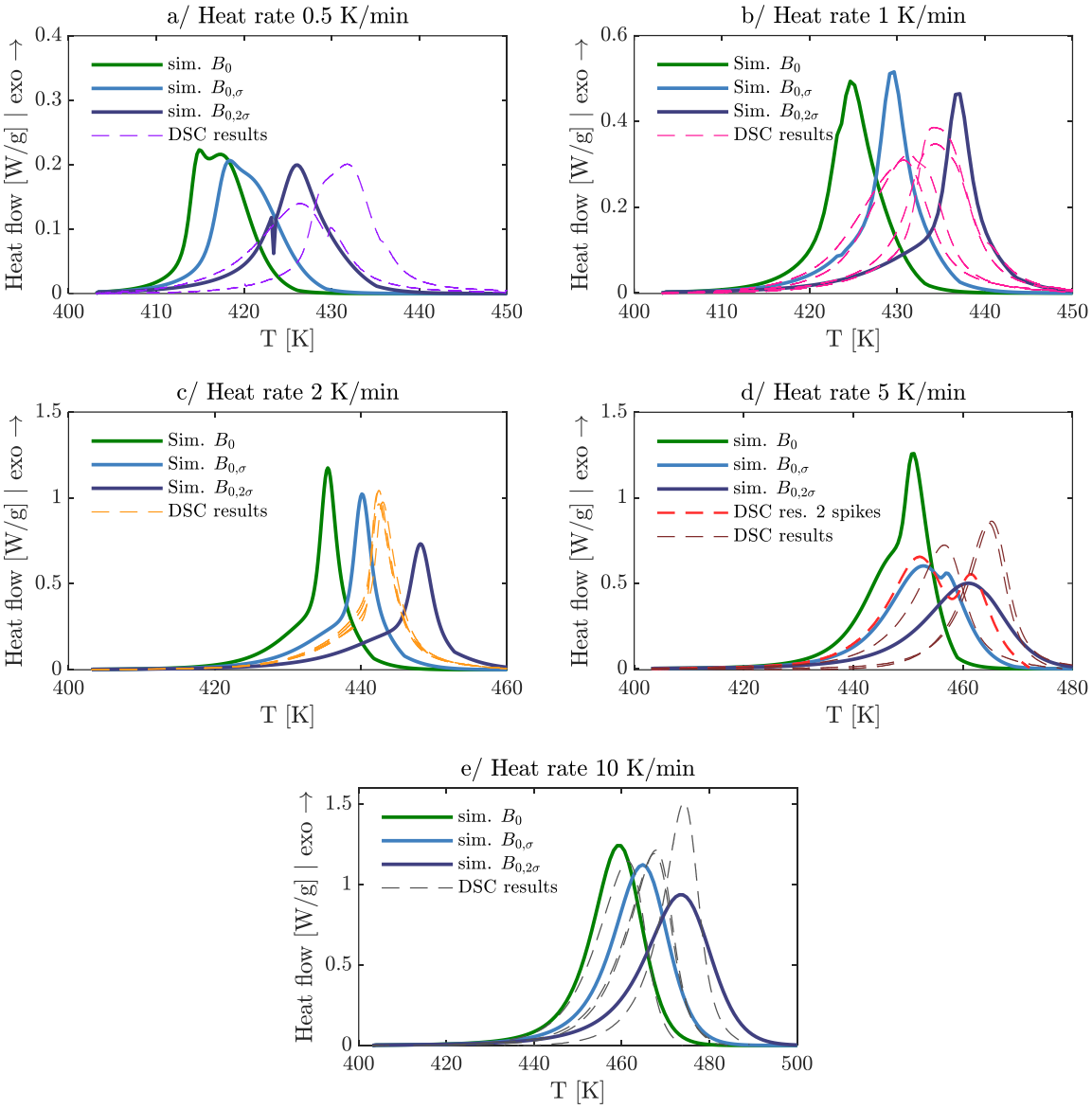

Table 0.4: Enthalpy results (experimental from [14])

Heat rate [K min^{-1}]	Simulated enthalpy [J g^{-1}]		Experimental enthalpy [J g^{-1}]
0.5	$B_0 = 88.21$	214.88	221.3 ± 13.9
	$B_{0,\sigma} = 60.04$	212.19	
	$B_{0,2\sigma} = 31.87$	205.29	
1	$B_0 = 88.21$	208.06	213.5 ± 2.2
	$B_{0,\sigma} = 60.04$	202.71	
	$B_{0,2\sigma} = 31.87$	191.17	
2	$B_0 = 88.21$	195.29	200.1 ± 10.5
	$B_{0,\sigma} = 60.04$	186.90	
	$B_{0,2\sigma} = 31.87$	170.70	
5	$B_0 = 88.21$	159.88	161.0 (two spikes) 116.4 ± 5.0 (one spike)
	$B_{0,\sigma} = 60.04$	127.63	
	$B_{0,2\sigma} = 31.87$	115.91	
10	$B_0 = 88.21$	116.41	116.9 ± 1.4
	$B_{0,\sigma} = 60.04$	116.38	
	$B_{0,2\sigma} = 31.87$	116.32	

Annex 5 Temperatures in the mould at permanent regime

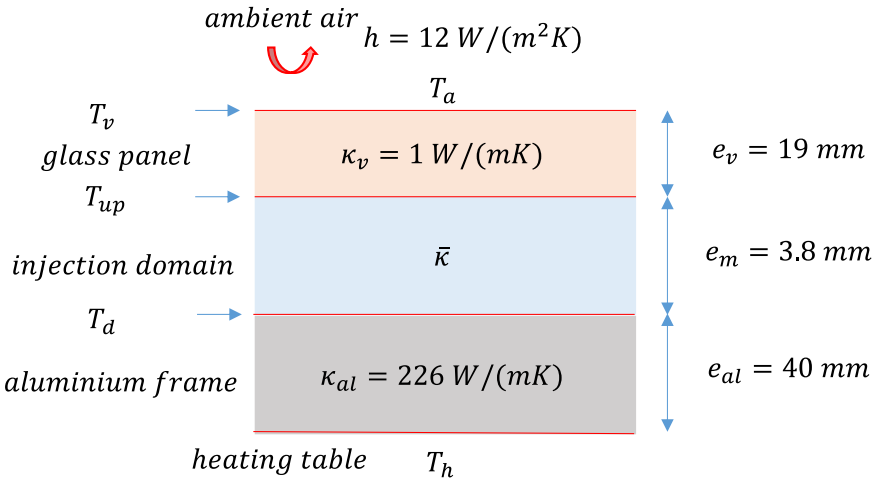

Figure 0.4. Schematic with parameters for permanent regime calculation.

In steady-state regime, only the heat conduction term and the heat transfer term are relevant. Other influencing parameters such as contact resistances are not considered. To simplify, the problem is studied only through the thickness i.e., the different strata are considered infinite. In this problem $\bar{\kappa} = V_f \kappa_{gf} + (1 - V_f)\kappa_{air}$.

Therefore :

$$\frac{\kappa_v}{e_v}(T_{up} - T_v) = h(T_v - T_a) \tag{0.20}$$

$$\frac{\kappa_v}{e_v}(T_{up} - T_v) = \frac{\bar{\kappa}}{e_m}(T_d - T_{up}) \tag{0.21}$$

$$\frac{\kappa_{al}}{e_{al}}(T_h - T_d) = \frac{\bar{\kappa}}{e_m}(T_d - T_{up}) \tag{0.22}$$

From (0.20),

$$T_v = \frac{\kappa_v}{he_v + \kappa_v} T_u + \frac{he_v}{he_v + \kappa_v} T_a = A_1 * T_{up} + A_2 * T_a \tag{0.23}$$

From (0.21),

$$T_{up} = \frac{\bar{\kappa} e_v}{\bar{\kappa} e_v + \kappa_v e_m} T_d + \frac{\kappa_v e_m}{\bar{\kappa} e_v + \kappa_v e_m} T_v = B_1 * T_d + B_2 * T_v \tag{0.24}$$

Thus, with (0.23)

$$T_{up} = B_1 * T_d + B_2 * (A_1 * T_{up} + A_2 * T_a) \tag{0.25}$$

$$T_{up} = \frac{1}{1 - B_2 A_1}(B_1 * T_d + B_2 A_2 * T_a) \tag{0.26}$$

From (0.22),

$$T_h = \frac{e_{al}\bar{\kappa}}{\kappa_{al}e_m}\left(T_d - T_{up}\right) + T_d \tag{0.27}$$

Because $\frac{e_{al}\bar{\kappa}}{\kappa_{al}e_m} \approx 0$, $T_h \approx T_d$: in permanent regime, the temperature in the lower aluminium frame is nearly homogeneous.

Two temperatures are needed to solve the rest of the equation system.

In studied simulations, the temperature gradient from the mould to the glass is of particular interest. By grossly simplifying the transfert coefficient with κ_v/e_v, it is given by:

$$\frac{\partial T}{\partial n} = \kappa_v \frac{T_v - T_{up}}{\bar{\kappa}e_v} \tag{0.28}$$

Parameters for subsection 3.5.3

For simulation in subsection 3.5.3, $\kappa_{air} = 0.028\ W/(mK)$ and thus $\bar{\kappa} = 0.6337\ W/(mK)$. The air temperature was measured giving $T_a = 293.8\ K$. With $T_u = 317.71\ K$, $T_v = 313.27\ K$ according to equation (0.23). This gives the experimental temperature gradient in the tempered glass panel. Applying all equations give $T_{up} = 323.41\ K$ and finally, $\frac{\partial T}{\partial n} = -381.52\ K/m$. This value is likely to be underestimated, as the temperature gradient in the mould is much higher in the experiment than in permanent regime.

Parameters for subsection 3.5.4

For simulation in subsection 3.5.4, $T_u = 453.15\ K$, $T_a = 293.15\ K$ and $\kappa_{air} = 0.037\ W/(mK)$. The calculated thermal gradient is $\frac{\partial T}{\partial n} = -2331\ K/m$.

List of figures

List of tables

References

[1] K. van Rijswijk, H.E.N. Bersee, Reactive processing of textile fiber-reinforced thermoplastic composites – An overview, Composites Part A: Applied Science and Manufacturing. 38 (2007) 666–681. https://doi.org/10.1016/j.compositesa.2006.05.007.

[2] K. van Rijswijk, Thermoplastic composite wind turbine blades: vacuum infusion technology for anionic polyamide-6 composites, PhD Thesis, Technische Universiteit Delft, 2007.

[3] T. Ishikawa, K. Amaoka, Y. Masubuchi, T. Yamamoto, A. Yamanaka, M. Arai, J. Takahashi, Overview of automotive structural composites technology developments in Japan, Composites Science and Technology. 155 (2018) 221–246. https://doi.org/10.1016/j.compscitech.2017.09.015.

[4] C. Latorre, BMW i3: carbon fiber body, (2013). https://www.plastix-world.com/bmw-i3-carbon-fiber-body/ (accessed October 9, 2019).

[5] J. Mackie, Modélisation de la phase de fusion/imprégnation dans le procédé de fabrication de tape composite thermoplastique, PhD Thesis, IMT Mines Albi - University of Toulouse, 2021.

[6] L. Feuillerat, O. De Almeida, J.-C. Fontanier, F. Schmidt, Effect of poly(ether ether ketone) degradation on commingled fabrics consolidation, Composites Part A: Applied Science and Manufacturing. 149 (2021) 106482. https://doi.org/10.1016/j.compositesa.2021.106482.

[7] L. van Lieshout, Visualization from the RTM (Resin Transfer Molding) process., 2006. License: Public Domain, https://commons.wikimedia.org/wiki/File:RTM_process.png (accessed April 1, 2022).

[8] P. Ó Máirtín, P. McDonnell, M.T. Connor, R. Eder, C.M. Ó Brádaigh, Process investigation of a liquid PA-12/carbon fibre moulding system, (2001) 9.

[9] M.D. Wakeman, L. Zingraff, P.-E. Bourban, J.-A.E. Månson, P. Blanchard, Stamp forming of carbon fibre/PA12 composites – A comparison of a reactive impregnation process and a commingled yarn system, Composites Science and Technology. 66 (2006) 19–35. https://doi.org/10.1016/j.compscitech.2005.06.001.

[10] L. Zingraff, V. Michaud, P.-E. Bourban, J.-A.E. Månson, Resin transfer moulding of anionically polymerised polyamide 12, Composites Part A: Applied Science and Manufacturing. 36 (2005) 1675–1686. https://doi.org/10.1016/j.compositesa.2005.03.023.

[11] J.J. Murray, C. Robert, K. Gleich, E.D. McCarthy, C.M. Ó Brádaigh, Manufacturing of unidirectional stitched glass fabric reinforced polyamide 6 by thermoplastic resin transfer moulding, Materials & Design. 189 (2020) 108512. https://doi.org/10.1016/j.matdes.2020.108512.

[12] G. Cazaux, Faisabilité des procédés LCM pour l'élaboration de composites renfort continu à matrice thermoplastique polyamide, PhD Thesis, Université du Havre, 2016.

[13] D. Salvatori, Strategies for faster impregnation in melt thermoplastic resin transfer molding process, PhD Thesis, École Polytechnique Fédérale de Lausanne, 2018.

[14] C. Vicard, Étude et modélisation de la synthèse du polyamide 6 pour la mise en œuvre de composites thermoplastiques par voie liquide réactive, PhD Thesis, IMT Mines Albi - University of Toulouse, 2018.
[15] C. Vicard, O. De Almeida, A. Cantarel, G. Bernhart, Experimental study of polymerization and crystallization kinetics of polyamide 6 obtained by anionic ring opening polymerization of ε-caprolactam, Polymer. 132 (2017) 88–97. https://doi.org/10.1016/j.polymer.2017.10.039.
[16] C. Vicard, O. De Almeida, A. Cantarel, G. Bernhart, Modeling of the polymerization and crystallization kinetic coupling of polyamide 6 synthesized from ε-caprolactam, Polymer. 180 (2019) 121681. https://doi.org/10.1016/j.polymer.2019.121681.
[17] H. Tan, K.M. Pillai, Multiscale modeling of unsaturated flow in dual-scale fiber preforms of liquid composite molding I: Isothermal flows, Composites Part A: Applied Science and Manufacturing. 43 (2012) 1–13. https://doi.org/10.1016/j.compositesa.2010.12.013.
[18] M. Imbert, High speed reactive RTM with on-line mixing in dual-scale fibrous reinforcements: Experimental and numerical developments and investigations, PhD Thesis, Université Bretagne Loire, 2017.
[19] V. Michaud, A Review of Non-saturated Resin Flow in Liquid Composite Moulding processes, Transp Porous Med. 115 (2016) 581–601. https://doi.org/10.1007/s11242-016-0629-7.
[20] K. van Rijswijk, H.E.N. Bersee, W.F. Jager, S.J. Picken, Optimisation of anionic polyamide-6 for vacuum infusion of thermoplastic composites: choice of activator and initiator, Composites Part A: Applied Science and Manufacturing. 37 (2006) 949–956. https://doi.org/10.1016/j.compositesa.2005.01.023.
[21] W. Wijaya, Permeability of 2D Woven Composite Textile Reinforcements: Textile Geometry and Compaction, and Flow Modelling, PhD Thesis, The University of Auckland, 2020.
[22] W. Han, Q. Govignon, A. Cantarel, F. Schmidt, Efficient polymerization and crystallization kinetics coupling of polyamide 6 synthesis for liquid composite molding process modeling, Polymer Engineering & Sci. (2022) pen.25901. https://doi.org/10.1002/pen.25901.
[23] H. Darcy, Les fontaines publiques de la ville de Dijon, V. Dalmont, Paris, 1856.
[24] P. Simacek, S.G. Advani, A numerical model to predict fiber tow saturation during liquid composite molding, Composites Science and Technology. 63 (2003) 1725–1736. https://doi.org/10.1016/S0266-3538(03)00155-6.
[25] K.M. Pillai, M.S. Munagavalasa, Governing equations for unsaturated flow through woven fiber mats. Part 2. Non-isothermal reactive flows, Composites Part A: Applied Science and Manufacturing. 35 (2004) 403–415. https://doi.org/10.1016/j.compositesa.2004.01.001.
[26] M. Imbert, E. Abisset-Chavanne, S. Comas-Cardona, D. Prono, Efficient dual-scale flow and thermo-chemo-rheological coupling simulation during on-line mixing resin transfer molding process, Journal of Composite Materials. 52 (2018) 313–330. https://doi.org/10.1177/0021998317706536.
[27] D.A. Nield, A. Bejan, Convection in Porous Media, Springer New York, New York, NY, 2013. https://doi.org/10.1007/978-1-4614-5541-7.
[28] R. Gantois, Contribution à la modélisation de l'écoulement de résine dans les procédés de moulage des composites par voie liquide, PhD Thesis, IMT Mines Albi - University of Toulouse, 2012.

[29] R. Arbter, J.M. Beraud, C. Binetruy, L. Bizet, J. Bréard, S. Comas-Cardona, C. Demaria, A. Endruweit, P. Ermanni, F. Gommer, S. Hasanovic, P. Henrat, F. Klunker, B. Laine, S. Lavanchy, S.V. Lomov, A. Long, V. Michaud, G. Morren, E. Ruiz, H. Sol, F. Trochu, B. Verleye, M. Wietgrefe, W. Wu, G. Ziegmann, Experimental determination of the permeability of textiles: A benchmark exercise, Composites Part A: Applied Science and Manufacturing. 42 (2011) 1157–1168. https://doi.org/10.1016/j.compositesa.2011.04.021.

[30] D. May, A. Aktas, S.G. Advani, D.C. Berg, A. Endruweit, E. Fauster, S.V. Lomov, A. Long, P. Mitschang, S. Abaimov, D. Abliz, I. Akhatov, M.A. Ali, T.D. Allen, S. Bickerton, M. Bodaghi, B. Caglar, H. Caglar, A. Chiminelli, N. Correia, B. Cosson, M. Danzi, J. Dittmann, P. Ermanni, G. Francucci, A. George, V. Grishaev, M. Hancioglu, M.A. Kabachi, K. Kind, M. Deléglise-Lagardère, M. Laspalas, O.V. Lebedev, M. Lizaranzu, P.-J. Liotier, P. Middendorf, J. Morán, C.-H. Park, R.B. Pipes, M.F. Pucci, J. Raynal, E.S. Rodriguez, R. Schledjewski, R. Schubnel, N. Sharp, G. Sims, E.M. Sozer, P. Sousa, J. Thomas, R. Umer, W. Wijaya, B. Willenbacher, A. Yong, S. Zaremba, G. Ziegmann, In-plane permeability characterization of engineering textiles based on radial flow experiments: A benchmark exercise, Composites Part A: Applied Science and Manufacturing. 121 (2019) 100–114. https://doi.org/10.1016/j.compositesa.2019.03.006.

[31] A.X.H. Yong, A. Aktas, D. May, A. Endruweit, S. Advani, P. Hubert, S.G. Abaimov, D. Abliz, I. Akhatov, M.A. Ali, T. Allen, D.C. Berg, S. Bickerton, C. Brauner, D. Brütsch, B. Caglar, H. Caglar, P. Causse, A. Chiminelli, A. Cohades, S. Comas-Cardona, M. Danzi, J. Dittmann, C. Dransfeld, P. Ermanni, E. Fauster, J.A. Garcia-Manrique, A. George, R. Graupner, V. Grishaev, A. Guilloux, M. Hancioglu, W. Harizi, T. Herman, W. Huang, M.A. Kabachi, A. Keller, K. Kind, M. Laspalas, O.V. Lebedev, M. Lizaranzu, A.C. Long, K. Masania, V. Michaud, P. Middendorf, D. Salvatori, R. Schubnel, N. Sharp, M. Sozer, J. Thomas, F. Trochu, R. Umer, J. Valette, J.H. Wang, B. Willenbacher, Out-of-plane permeability measurement for reinforcement textiles: A benchmark exercise, Composites Part A: Applied Science and Manufacturing. 148 (2021) 106480. https://doi.org/10.1016/j.compositesa.2021.106480.

[32] B.R. Gebart, Permeability of Unidirectional Reinforcements for RTM, Journal of Composite Materials. 26 (1992) 1100–1133. https://doi.org/10.1177/002199839202600802.

[33] M. Bodaghi, S.V. Lomov, P. Simacek, N.C. Correia, S.G. Advani, On the variability of permeability induced by reinforcement distortions and dual scale flow in liquid composite moulding: A review, Composites Part A: Applied Science and Manufacturing. 120 (2019) 188–210. https://doi.org/10.1016/j.compositesa.2019.03.004.

[34] A. Geoffre, Y. Wielhorski, N. Moulin, J. Bruchon, S. Drapier, P.-J. Liotier, Influence of intra-yarn flows on whole 3D woven fabric numerical permeability: from Stokes to Stokes-Darcy simulations, International Journal of Multiphase Flow. 129 (2020) 103349. https://doi.org/10.1016/j.ijmultiphaseflow.2020.103349.

[35] I. Verpoest, S. Lomov, Virtual textile composites software : Integration with micro-mechanical, permeability and structural analysis, Composites Science and Technology. 65 (2005) 2563–2574. https://doi.org/10.1016/j.compscitech.2005.05.031.

[36] X. Zeng, L.P. Brown, A. Endruweit, M. Matveev, A.C. Long, Geometrical modelling of 3D woven reinforcements for polymer composites: Prediction of fabric permeability and composite mechanical properties, Composites Part A: Applied Science and Manufacturing. 56 (2014) 150–160. https://doi.org/10.1016/j.compositesa.2013.10.004.

[37] W. Wijaya, M.A. Ali, R. Umer, K.A. Khan, P.A. Kelly, S. Bickerton, An automatic methodology to CT-scans of 2D woven textile fabrics to structured finite element and

voxel meshes, Composites Part A: Applied Science and Manufacturing. 125 (2019) 105561. https://doi.org/10.1016/j.compositesa.2019.105561.
[38] M. Röding, P. Svensson, N. Lorén, Functional regression-based fluid permeability prediction in monodisperse sphere packings from isotropic two-point correlation functions, Computational Materials Science. 134 (2017) 126–131. https://doi.org/10.1016/j.commatsci.2017.03.042.
[39] L. Silva, P. Laure, T. Coupez, H. Digonnet, Multiphysics for Simulation of Forming Processes, in: N. Boyard (Ed.), Heat Transfer in Polymer Composite Materials, John Wiley & Sons, Inc., Hoboken, NJ, USA, 2016: pp. 269–300. https://doi.org/10.1002/9781119116288.ch9.
[40] G.S. Beavers, D.D. Joseph, Boundary conditions at a naturally permeable wall, J. Fluid Mech. 30 (1967) 197–207. https://doi.org/10.1017/S0022112067001375.
[41] P.G. Saffman, On the Boundary Condition at the Surface of a Porous Medium, Studies in Applied Mathematics. 50 (1971) 93–101. https://doi.org/10.1002/sapm197150293.
[42] I.P. Jones, Low Reynolds number flow past a porous spherical shell, Math. Proc. Camb. Phil. Soc. 73 (1973) 231–238. https://doi.org/10.1017/S0305004100047642.
[43] H.C. Brinkman, A calculation of the viscous force exerted by a flowing fluid on a dense swarm of particles, Flow, Turbulence and Combustion. 1 (1949). https://doi.org/10.1007/BF02120313.
[44] J.A. Ochoa-Tapia, S. Whitaker, Momentum transfer at the boundary between a porous medium and a homogeneous fluid—I. Theoretical development, International Journal of Heat and Mass Transfer. 38 (1995) 2635–2646. https://doi.org/10.1016/0017-9310(94)00346-W.
[45] J. Bear, Modeling Phenomena of Flow and Transport in Porous Media, Springer International Publishing, Cham, 2018. https://doi.org/10.1007/978-3-319-72826-1.
[46] D.A. Nield, The limitations of the Brinkman-Forchheimer equation in modeling flow in a saturated porous medium and at an interface, International Journal of Heat and Fluid Flow. 12 (1991) 269–272. https://doi.org/10.1016/0142-727X(91)90062-Z.
[47] K. Vafai, S.J. Kim, On the limitations of the Brinkman-Forchheimer-extended Darcy equation, International Journal of Heat and Fluid Flow. 16 (1995) 11–15. https://doi.org/10.1016/0142-727X(94)00002-T.
[48] J.-L. Auriault, On the Domain of Validity of Brinkman's Equation, Transp Porous Med. 79 (2009) 215–223. https://doi.org/10.1007/s11242-008-9308-7.
[49] D.A. Nield, Discussion of a Discussion by F. Chen and C. F. Chen (Chen, F., and Chen, C. F., 1996, ASME J. Heat Transfer, 118, pp. 266–268), Journal of Heat Transfer. 119 (1997) 193–194. https://doi.org/10.1115/1.2824090.
[50] K. Vafai, S.J. Kim, Closure to "Discussion of a Discussion by K. Vafai and S. J. Kim" (1997, ASME J. Heat Transfer, 119, pp. 195–196), Journal of Heat Transfer. 119 (1997) 196–197. https://doi.org/10.1115/1.2824093.
[51] N.D. Ngo, K.K. Tamma, Microscale permeability predictions of porous fibrous media, International Journal of Heat and Mass Transfer. (2001) 11.
[52] Y.S. Song, J.R. Youn, Asymptotic expansion homogenization of permeability tensor for plain woven fabrics, Composites Part A: Applied Science and Manufacturing. 37 (2006) 2080–2087. https://doi.org/10.1016/j.compositesa.2005.12.002.
[53] E. Syerko, C. Binetruy, S. Comas-Cardona, A. Leygue, A numerical approach to design dual-scale porosity composite reinforcements with enhanced permeability, Materials & Design. 131 (2017) 307–322. https://doi.org/10.1016/j.matdes.2017.06.035.

[54] C. Li, A. Cantarel, X. Gong, A two phases coupling free and porous flow method at multi-scales of LCM process, in: Proceedings of the 2019 International Conference on Composite Materials, Melbourne, Australia, 2019: p. 8.
[55] OpenFOAM v8, (2020). https://openfoam.org/news/v8-patch/.
[56] J.-L. Auriault, About the Beavers and Joseph Boundary Condition, Transp Porous Med. 83 (2010) 257–266. https://doi.org/10.1007/s11242-009-9435-9.
[57] C.-H. Bruneau, I. Mortazavi, Numerical modelling and passive flow control using porous media, Computers & Fluids. 37 (2008) 488–498. https://doi.org/10.1016/j.compfluid.2007.07.001.
[58] F.J. Carrillo, I.C. Bourg, C. Soulaine, Multiphase flow modeling in multiscale porous media: An open-source micro-continuum approach, Journal of Computational Physics: X. 8 (2020) 100073. https://doi.org/10.1016/j.jcpx.2020.100073.
[59] Chung Hae Park, L. Woo, Modeling void formation and unsaturated flow in liquid composite molding processes: a survey and review, Journal of Reinforced Plastics and Composites. 30 (2011) 957–977. https://doi.org/10.1177/0731684411411338.
[60] J. Bréard, Y. Henzel, F. Trochu, R. Gauvin, Analysis of dynamic flows through porous media. Part I: Comparison between saturated and unsaturated flows in fibrous reinforcements: Analysis of Dynamic Flows. I, Polym Compos. 24 (2003) 391–408. https://doi.org/10.1002/pc.10038.
[61] L. Gascón, J.A. García, F. LeBel, E. Ruiz, F. Trochu, A two-phase flow model to simulate mold filling and saturation in Resin Transfer Molding, Int J Mater Form. 9 (2015) 229–239. https://doi.org/10.1007/s12289-015-1225-z.
[62] L. Gascón, J.A. García, F. LeBel, E. Ruiz, F. Trochu, Numerical prediction of saturation in dual scale fibrous reinforcements during Liquid Composite Molding, Composites Part A: Applied Science and Manufacturing. 77 (2015) 275–284. https://doi.org/10.1016/j.compositesa.2015.05.019.
[63] K.M. Pillai, Governing equations for unsaturated flow through woven fiber mats. Part 1. Isothermal tows, Composites Part A: Applied Science and Manufacturing. 33 (2002) 13. https://doi.org/10.1016/S1359-835X(02)00034-9.
[64] H. Tan, K.M. Pillai, Fast liquid composite molding simulation of unsaturated flow in dual-scale fiber mats using the imbibition characteristics of a fabric-based unit cell, Polym Compos. 31 (2010) 1790–1807. https://doi.org/10.1002/pc.20971.
[65] I.D. Patiño-Arcila, J.D. Vanegas-Jaramillo, Modeling and simulation of filling in dual-scale fibrous reinforcements: state of the art and new methodology to quantify the sink effect, Journal of Composite Materials. 52 (2018) 1915–1946. https://doi.org/10.1177/0021998317734038.
[66] M. Imbert, S. Comas-Cardona, E. Abisset-Chavanne, D. Prono, Experimental investigation of intra-tow fluid storage mechanisms in dual-scale fiber reinforcements, Composites Part A: Applied Science and Manufacturing. 107 (2018) 70–82. https://doi.org/10.1016/j.compositesa.2017.12.015.
[67] M. Imbert, S. Comas-Cardona, E. Abisset-Chavanne, D. Prono, Introduction of intra-tow release/storage mechanisms in reactive dual-scale flow numerical simulations, Journal of Composite Materials. 53 (2019) 125–140. https://doi.org/10.1177/0021998318780498.
[68] W.K. Chui, J. Glimm, F.M. Tangerman, A.P. Jardine, J.S. Madsen, T.M. Donnellan, R. Leek, Process Modeling in Resin Transfer Molding as a Method to Enhance Product Quality, Society for Industrial and Applied Mathematics. 39 (1997) 15.

[69] H. Jasak, Error Analysis and Estimation for the Finite Volume Method with Applications to Fluid Flows, Imperial College London, 1996.
[70] H.G. Weller, G. Tabor, H. Jasak, C. Fureby, A tensorial approach to computational continuum mechanics using object-oriented techniques, Comput. Phys. 12 (1998) 620. https://doi.org/10.1063/1.168744.
[71] OpenFOAM: User Guide v2012, (n.d.). https://www.openfoam.com/documentation/guides/latest/doc/index.html (accessed December 15, 2021).
[72] H.K. Versteeg, W. Malalasekera, An introduction to computational fluid dynamics: the finite volume method, 2nd ed, Pearson Education Ltd, Harlow, England ; New York, 2007.
[73] OpenFOAM Foundation repository for OpenFOAM version 8, (2021). https://github.com/OpenFOAM/OpenFOAM-8.
[74] R.I. Issa, Solution of the implicitly discretised fluid flow equations by operator-splitting, Journal of Computational Physics. 62 (1986) 40–65. https://doi.org/10.1016/0021-9991(86)90099-9.
[75] G. Puaux, Simulation numérique des écoulements aux échelles microscopique et mésoscopique dans le procédé RTM, PhD Thesis, École nationale supérieure des mines de Paris, 2011.
[76] C. Greenshield, OpenFOAM 2.1.0: Arbitrary Mesh Interface, CFD Direct. (2011). https://openfoam.org/release/2-1-0/ami/ (accessed December 9, 2021).
[77] P.E. Farrell, J.R. Maddison, Conservative interpolation between volume meshes by local Galerkin projection, Computer Methods in Applied Mechanics and Engineering. 200 (2011) 89–100. https://doi.org/10.1016/j.cma.2010.07.015.
[78] W. Wijaya, S. Bickerton, P.A. Kelly, Meso-scale compaction simulation of multi-layer 2D textile reinforcements: A Kirchhoff-based large-strain non-linear elastic constitutive tow model, Composites Part A: Applied Science and Manufacturing. 137 (2020) 106017. https://doi.org/10.1016/j.compositesa.2020.106017.
[79] W. Wijaya, P.A. Kelly, S. Bickerton, A novel methodology to construct periodic multi-layer 2D woven unit cells with random nesting configurations directly from μCT-scans, Composites Science and Technology. 193 (2020) 108125. https://doi.org/10.1016/j.compscitech.2020.108125.
[80] N.Q. Thanh, Analyse expérimentale et numérique de la compaction des renforts fibreux. Application pour la perméabilité, PhD Thesis, INSA de Lyon, 2011.
[81] S.P. Bancora, C. Binetruy, S.G. Advani, E. Syerko, S. Comas-Cardona, Effective permeability averaging scheme to address in-plane anisotropy effects in multi-layered preforms, Composites Part A: Applied Science and Manufacturing. 113 (2018) 359–369. https://doi.org/10.1016/j.compositesa.2018.07.025.
[82] T. Ahmed, Reservoir Engineering Handbook, Elsevier, 2019. https://doi.org/10.1016/B978-0-12-813649-2.00001-3.
[83] J.E. Warren, H.S. Price, Flow in Heterogeneous Porous Media, Society of Petroleum Engineers Journal. 1 (1961) 153–169. https://doi.org/10.2118/1579-G.
[84] K.E. Wardle, H.G. Weller, Hybrid Multiphase CFD Solver for Coupled Dispersed/Segregated Flows in Liquid-Liquid Extraction, International Journal of Chemical Engineering. 2013 (2013) 1–13. https://doi.org/10.1155/2013/128936.

[85] M. Deléglise, C. Binétruy, P. Krawczak, Solution to filling time prediction issues for constant pressure driven injection in RTM, Composites Part A: Applied Science and Manufacturing. 36 (2005) 339–344. https://doi.org/10.1016/j.compositesa.2004.07.001.
[86] W. Han, Q. Govignon, A. Cantarel, C. Samuel, F. Schmidt, Modeling the reactive PA6 flow for LCM processes, ESAFORM 2021. (2021). https://doi.org/10.25518/esaform21.4351.
[87] O. Wichterle, J. Šebenda, J. Králíček, The anionic polymerization of caprolactam, Advances in Polymer Science. 2 (1961) 578–595. https://doi.org/10.1007/BF02189480.
[88] T. Kōmoto, M. Iguchi, H. Kanetsuna, T. Kawai, Formation of Spherulites During Polymerization of Lactams, Makromol. Chem. 135 (1970) 145–164. https://doi.org/10.1002/macp.1970.021350115.
[89] V.P. Wittmer, H. Gerrens, Über die anionische schnellpolymerisation von caprolactam, Makromol. Chem. 89 (1965) 27–43. https://doi.org/10.1002/macp.1965.020890103.
[90] P.W. Sibal, R.E. Camargo, C.W. Macosko, Designing Nylon-6 polymerization systems for RIM, Polymer Process Engineering. 1 (1984) 147–169.
[91] J.J.E. Teuwen, A.A. van Geenen, H.E.N. Bersee, Novel Reaction Kinetic Model for Anionic Polyamide-6, Macromol. Mater. Eng. 298 (2013) 163–173. https://doi.org/10.1002/mame.201100457.
[92] J. Humphry, N. Yang, L.-J. Vandi, B.V. Hernandez, D.J. Martin, M.T. Heitzmann, Isothermal differential scanning calorimetry analysis of the anionic polymerisation of polyamide-6: Separation by dual asymmetric gaussians, Materials Today Communications. 25 (2020) 101473. https://doi.org/10.1016/j.mtcomm.2020.101473.
[93] Z. Rainer, Lamellenbildung bei der Kristallisation von Polymeren, 2009. License: Attribution only, https://commons.wikimedia.org/wiki/File:Lamellenbildung_bei_der_Kristallisation_von_Polymeren.svg (accessed November 10, 2021).
[94] R.S. Davé, R.L. Kruse, L.R. Stebbins, K. Udipi, Polyamides from lactams via anionic ring-opening polymerization: 2. Kinetics, Polymer. 38 (1997) 939–947. https://doi.org/10.1016/S0032-3861(96)00567-8.
[95] J. Karger-Kocsis, L. Kiss, Thermograms of Activated Anionic Polymerization of ε-Caprolactam, Makromol. Chem. 180 (1979) 1593–1597. https://doi.org/10.1002/macp.1979.021800621.
[96] K. Taki, N. Shoji, M. Kobayashi, H. Ito, A kinetic model of viscosity development for in situ ring-opening anionic polymerization of ϵ-caprolactam, Microsystem Technologies. 23 (2017) 1161–1169. https://doi.org/10.1007/s00542-016-3045-6.
[97] S.A. Bolgov, V.P. Begishev, A.Ya. Malkin, V.G. Frolov, Role of the functionality of activators during isothermal crystallization accompanying the activated anionic polymerization of ε-Caprolactam, Polymer Science U.S.S.R. 23 (1981) 1485–1492. https://doi.org/10.1016/0032-3950(81)90118-0.
[98] A.Ya. Malkin, V.P. Beghishev, S.A. Bolgov, The exothermal effects of superimposed processes of activated anionic polymerization of ε-Caprolactam and crystallization of the polymer formed, Polymer. 23 (1982) 385–390. https://doi.org/10.1016/0032-3861(82)90340-8.
[99] K.H. Lee, S.C. Kim, Reaction-Induced Crystallization Kinetics During the Anionic Polymerization of ϵ-caprolactam, Polymer Engineering and Science. 28 (1988) 8. https://doi.org/10.1002/pen.760280104.

[100] R.Z. Greenley, J.C. Stauffer, J.E. Kurz, The Kinetic Equation for the Initiated, Anionic Polymerization of ε-Caprolactam, Macromolecules. 2 (1969) 7.
[101] A.Ya. Malkin, V.G. Frolov, A.N. Ivanova, Z.S. Andrianova, The nonisothermal anionic polymerization of caprolactam, Polymer Science U.S.S.R. 21 (1979) 691–700. https://doi.org/10.1016/0032-3950(79)90296-X.
[102] R.E. Camargo, V.M. Gonzalez, C.W. Macosko, M. Tirell, Bulk Polymerization Kinetics by the Adiabatic Reactor Method, Rubber Chemistry and Technology. 56 (1983) 774–783.
[103] A.Ya. Malkin, V.G. Frolov, A.N. Ivanova, Z.S. Andrianova, L.A. Alekseichenko, The kinetics of anionic polymerization of caprolactam in the presence of carbamylcaprolactams, Polymer Science U.S.S.R. 22 (1980) 1097–1103. https://doi.org/10.1016/0032-3950(80)90207-5.
[104] D.J. Lin, J.M. Ottino, E.L. Thomas, A kinetic study of the activated anionic polymerization of ε-caprolactam, Polym. Eng. Sci. 25 (1985) 1155–1163. https://doi.org/10.1002/pen.760251808.
[105] S. Sourour, M.R. Kamal, Differential scanning calorimetry of epoxy cure: isothermal cure kinetics, Thermochimica Acta. 14 (1976) 41–59. https://doi.org/10.1016/0040-6031(76)80056-1.
[106] R. Wendel, P. Rosenberg, M. Wilhelm, F. Henning, Anionic Polymerization of ε-Caprolactam under the Influence of Water: 2. Kinetic Model, J. Compos. Sci. 4 (2020) 8. https://doi.org/10.3390/jcs4010008.
[107] V.V. Korshak, T.M. Frunze, S.P. Davtyan, V.V. Kurashev, T.V. Volkova, V.A. Kot'Elnikov, R.B. Shleifman, Kinetics of activated anionic polymerization of ε-Caprolactam under non-isothermal conditions, Polymer Science U.S.S.R. 21 (1979) 2161–2169. https://doi.org/10.1016/0032-3950(79)90154-0.
[108] I.H. Hillier, Modified avrami equation for the bulk crystallization kinetics of spherulitic polymers, J. Polym. Sci. A Gen. Pap. 3 (1965) 3067–3078. https://doi.org/10.1002/pol.1965.100030902.
[109] J. Fournier, G. Williams, C. Duch, G.A. Aldridge, Changes in Molecular Dynamics during Bulk Polymerization of an Epoxide−Amine System As Studied by Dielectric Relaxation Spectroscopy, Macromolecules. 29 (1996) 7097–7107. https://doi.org/10.1021/ma9517862.
[110] M. Avrami, Kinetics of Phase Change. I General Theory, The Journal of Chemical Physics. 7 (1939) 1103–1112. https://doi.org/10.1063/1.1750380.
[111] J.D. Hoffman, J.I. Lauritzen, Crystallization of bulk polymers with chain folding: theory of growth of lamellar spherulites, J. RES. NATL. BUR. STAN. SECT. A. 65A (1961) 297. https://doi.org/10.6028/jres.065A.035.
[112] J. Magill, Crystallization kinetics study of nylon 6, Polymer. 3 (1962) 655–664. https://doi.org/10.1016/0032-3861(62)90113-1.
[113] C. Schick, V. Mathot, Fast Scanning Calorimetry, Springer International Publishing, Cham, 2016. https://doi.org/10.1007/978-3-319-31329-0.
[114] I. Kolesov, D. Mileva, R. Androsch, C. Schick, Structure formation of polyamide 6 from the glassy state by fast scanning chip calorimetry, Polymer. 52 (2011) 5156–5165. https://doi.org/10.1016/j.polymer.2011.09.007.
[115] K. Nakamura, K. Katayama, T. Amano, Some aspects of nonisothermal crystallization of polymers. II. Consideration of the isokinetic condition, J. Appl. Polym. Sci. 17 (1973) 1031–1041. https://doi.org/10.1002/app.1973.070170404.

[116] R.M. Patel, J.E. Spruiell, Crystallization kinetics during polymer processing—Analysis of available approaches for process modeling, Polym. Eng. Sci. 31 (1991) 730–738. https://doi.org/10.1002/pen.760311008.
[117] O. Wichterle, J. Šebenda, J. Tomka, Adiabatic crystallization of amorphous polycaprolactam, J. Polym. Sci. 57 (1962) 785–791. https://doi.org/10.1002/pol.1962.1205716562.
[118] C.N. Velisaris, J.C. Seferis, Crystallization kinetics of polyetheretherketone (peek) matrices, Polym. Eng. Sci. 26 (1986) 1574–1581. https://doi.org/10.1002/pen.760262208.
[119] K. Ueda, K. Yamada, M. Nakai, T. Matsuda, M. Hosoda, K. Tai, Synthesis of High Molecular Weight Nylon 6 by Anionic Polymerization of e-Caprolactam, Polym. J. 28 (1996) 6.
[120] M. Wilhelm, R. Wendel, M. Aust, P. Rosenberg, F. Henning, Compensation of Water Influence on Anionic Polymerization of ε-Caprolactam: 1. Chemistry and Experiments, J. Compos. Sci. 4 (2020) 7. https://doi.org/10.3390/jcs4010007.
[121] S. Pillay, U.K. Vaidya, G.M. Janowski, Liquid Molding of Carbon Fabric-reinforced Nylon Matrix Composite Laminates, Journal of Thermoplastic Composite Materials. 18 (2005) 509–527. https://doi.org/10.1177/0892705705054412.
[122] V.K.-H. Illers, H. Haberkorn, Schmelzverhalten, struktur und kristallinität von 6-polyamid, Makromol. Chem. 142 (1971) 31–67. https://doi.org/10.1002/macp.1971.021420103.
[123] P.J. Halley, M.E. Mackay, Chemorheology of thermosets - An overview, Polym. Eng. Sci. 36 (1996) 593–609. https://doi.org/10.1002/pen.10447.
[124] M.B. Roller, Rheology of curing thermosets: A review, Polym. Eng. Sci. 26 (1986) 432–440. https://doi.org/10.1002/pen.760260610.
[125] Ageyeva, Sibikin, Kovács, A Review of Thermoplastic Resin Transfer Molding: Process Modeling and Simulation, Polymers. 11 (2019) 1555. https://doi.org/10.3390/polym11101555.
[126] R.S. Davé, L. Kruse, Polyamides from Iactams via anionic ring- opening polymerization: 3. Rheology, Polymer. 38 (1997) 949–954.
[127] J.M. Castro, C.W. Macosko, Studies of mold filling and curing in the reaction injection molding process, AIChE J. 28 (1982) 250–260. https://doi.org/10.1002/aic.690280213.
[128] H.M. Laun, G. Schmidt, Rheotens tests and viscoelastic simulations related to high-speed spinning of Polyamide 6, Journal of Non-Newtonian Fluid Mechanics. 222 (2015) 45–55. https://doi.org/10.1016/j.jnnfm.2014.08.018.
[129] W.P. Cox, E.H. Merz, Correlation of dynamic and steady flow viscosities, J. Polym. Sci. 28 (1958) 619–622. https://doi.org/10.1002/pol.1958.1202811812.
[130] C.A. Hieber, Modeling/simulating the injection molding of isotactic polypropylene, Polym. Eng. Sci. 42 (2002) 1387–1409. https://doi.org/10.1002/pen.11039.
[131] A.Ya. Malkin, S.G. Kulichikhin, Chemical transformations and phase transitions in polymer rheology and technology, Makromolekulare Chemie. Macromolecular Symposia. 68 (1993) 301–322. https://doi.org/10.1002/masy.19930680123.
[132] T. Parenteau, G. Ausias, Y. Grohens, P. Pilvin, Structure, mechanical properties and modelling of polypropylene for different degrees of crystallinity, Polymer. 53 (2012) 5873–5884. https://doi.org/10.1016/j.polymer.2012.09.053.
[133] H.U. Moritz, Increase in viscosity and its influence on polymerization processes, Chem. Eng. Technol. 12 (1989) 71–87. https://doi.org/10.1002/ceat.270120112.

[134] G. Lamberti, G.W.M. Peters, G. Titomanlio, Crystallinity and Linear Rheological Properties of Polymers, IPP. 22 (2007) 303–310. https://doi.org/10.3139/217.2006.
[135] M.V. Bruschke, S.G. Advani, A finite element/control volume approach to mold filling in anisotropic porous media, Polym. Compos. 11 (1990) 398–405. https://doi.org/10.1002/pc.750110613.
[136] F. Trochu, R. Gauvin, D.-M. Gao, Numerical analysis of the resin transfer molding process by the finite element method, Adv. Polym. Technol. 12 (1993) 329–342. https://doi.org/10.1002/adv.1993.060120401.
[137] P. Simacek, S.G. Advani, Desirable features in mold filling simulations for Liquid Composite Molding processes, Polym Compos. 25 (2004) 355–367. https://doi.org/10.1002/pc.20029.
[138] P. Simacek, S.G. Advani, Resin flow modeling in compliant porous media: an efficient approach for liquid composite molding, International Journal of Material Forming. 11 (2018) 503–515. https://doi.org/10.1007/s12289-017-1360-9.
[139] F. Trochu, S. Chatel, S. Maison - Le Poëc, Y. Benoit, P. de Luca, P. Baisch, D. Roger, P. Guerin, Skills Synergy Leading to RTM Flow Simulation Success Story, SAE Int. J. Aerosp. 4 (2011) 1021–1030. https://doi.org/10.4271/2011-01-2629.
[140] A. Nabovati, E.W. Llewellin, A.C.M. Sousa, A general model for the permeability of fibrous porous media based on fluid flow simulations using the lattice Boltzmann method, Composites Part A: Applied Science and Manufacturing. 40 (2009) 860–869. https://doi.org/10.1016/j.compositesa.2009.04.009.
[141] C.W. Hirt, B.D. Nichols, Volume of fluid (VOF) method for the dynamics of free boundaries, Journal of Computational Physics. 39 (1981) 201–225. https://doi.org/10.1016/0021-9991(81)90145-5.
[142] M. Imbert, High Speed Reactive Resin Transfer Moulding (RTM) Process Simulation for Mass Production of Automotive Structural Parts, SAE Int. J. Mater. Manf. 8 (2015) 503–515. https://doi.org/10.4271/2015-01-0722.
[143] J.U. Brackbill, D.B. Kothe, C. Zemach, A continuum method for modeling surface tension, Journal of Computational Physics. 100 (1992) 335–354. https://doi.org/10.1016/0021-9991(92)90240-Y.
[144] O. Ubbink, R.I. Issa, A Method for Capturing Sharp Fluid Interfaces on Arbitrary Meshes, Journal of Computational Physics. 153 (1999) 26–50. https://doi.org/10.1006/jcph.1999.6276.
[145] S. Muzaferija, M. Peric, Computation of free-surface flows using the finite-volume method and moving grids, Numerical Heat Transfer, Part B: Fundamentals. 32 (1997) 369–384. https://doi.org/10.1080/10407799708915014.
[146] S.S. Deshpande, L. Anumolu, M.F. Trujillo, Evaluating the performance of the two-phase flow solver interFoam, Computational Science & Discovery. 5 (2012) 014016. https://doi.org/10.1088/1749-4699/5/1/014016.
[147] J. Roenby, H. Bredmose, H. Jasak, A computational method for sharp interface advection, Royal Society Open Science. 3 (2016) 160405. https://doi.org/10.1098/rsos.160405.
[148] J. Nagy, L. Reith, M. Fischlschweiger, G. Steinbichler, Modeling the influence of flow phenomena on the polymerization of ϵ-Caprolactam, Chemical Engineering Science. 111 (2014) 85–93. https://doi.org/10.1016/j.ces.2014.02.020.
[149] J. Nagy, L. Reith, M. Fischlschweiger, G. Steinbichler, Influence of fiber orientation and geometry variation on flow phenomena and reactive polymerization of ϵ-caprolactam, Chemical Engineering Science. 128 (2015) 1–10. https://doi.org/10.1016/j.ces.2015.01.046.

[150] H. Grössing, N. Stadlmajer, E. Fauster, M. Fleischmann, R. Schledjewski, Flow front advancement during composite processing: predictions from numerical filling simulation tools in comparison with real-world experiments, Polymer Composites. 37 (2016) 2782–2793. https://doi.org/10.1002/pc.23474.
[151] J. Seuffert, L. Kärger, F. Henning, Simulating Mold Filling in Compression Resin Transfer Molding (CRTM) Using a Three-Dimensional Finite-Volume Formulation, Journal of Composites Science. 2 (2018) 23. https://doi.org/10.3390/jcs2020023.
[152] R.B. DeBar, Fundamentals of the KRAKEN code. [Eulerian hydrodynamics code for compressible nonviscous flow of several fluids in two-dimensional (axially symmetric) region], California Univ., Livermore (USA). Lawrence Livermore Lab., 1974. https://doi.org/10.2172/7227630.
[153] W.J. Rider, D.B. Kothe, Reconstructing Volume Tracking, Journal of Computational Physics. 141 (1998) 112–152. https://doi.org/10.1006/jcph.1998.5906.
[154] S. Mirjalili, S.S. Jain, M.S. Dodd, Interface-capturing methods for two-phase flows: An overview and recent developments, Annual Research Briefs, Center for Turbulence Research. (2017) 117–135.
[155] H. Scheufler, J. Roenby, Accurate and efficient surface reconstruction from volume fraction data on general meshes, Journal of Computational Physics. 383 (2019) 1–23. https://doi.org/10.1016/j.jcp.2019.01.009.
[156] C. Greenshield, Interface Capturing in OpenFOAM, CFD Direct. (2020). https://cfd.direct/openfoam/free-software/multiphase-interface-capturing/ (accessed October 8, 2021).
[157] J.A. Sethian, Level set methods and fast marching methods: evolving interfaces in computational geometry, fluid mechanics, computer vision, and materials science, 2nd ed, CAMBRIDGE UNIVERSITY PRESS, 1999.
[158] S. Soukane, F. Trochu, Application of the level set method to the simulation of resin transfer molding, Composites Science and Technology. 66 (2006) 1067–1080. https://doi.org/10.1016/j.compscitech.2005.03.001.
[159] R. Gantois, A. Cantarel, B. Cosson, G. Dusserre, J.-N. Felices, F. Schmidt, BEM-based models to simulate the resin flow at macroscale and microscale in LCM processes, Polym. Compos. 34 (2013) 1235–1244. https://doi.org/10.1002/pc.22531.
[160] M.-Q. Thai, F. Schmidt, G. Dusserre, A. Cantarel, L. Silva, BEM computation of 3D Stokes flow including moving front, Int J Mater Form. 10 (2017) 567–580. https://doi.org/10.1007/s12289-016-1302-y.
[161] R. Spina, M. Spekowius, C. Hopmann, Multiphysics simulation of thermoplastic polymer crystallization, Materials & Design. 95 (2016) 455–469. https://doi.org/10.1016/j.matdes.2016.01.123.
[162] D. Jacqmin, Calculation of Two-Phase Navier–Stokes Flows Using Phase-Field Modeling, Journal of Computational Physics. 155 (1999) 96–127. https://doi.org/10.1006/jcph.1999.6332.
[163] C. Dammann, R. Mahnken, Simulation of a resin transfer molding process using a phase field approach within the theory of porous media, Composites Part A: Applied Science and Manufacturing. 120 (2019) 147–160. https://doi.org/10.1016/j.compositesa.2019.02.022.
[164] G. Lu, L. He, D. Chen, W. Li, Smoothed particle hydrodynamics simulation of dual-scale flow during resin transfer molding, Journal of Reinforced Plastics and Composites. 36 (2017) 1431–1438. https://doi.org/10.1177/0731684417709950.

[165] S. Yashiro, D. Nakashima, Y. Oya, T. Okabe, R. Matsuzaki, Particle simulation of dual-scale flow in resin transfer molding for process analysis, Composites Part A: Applied Science and Manufacturing. 121 (2019) 283–288. https://doi.org/10.1016/j.compositesa.2019.03.038.
[166] L.D. Libersky, A.G. Petschek, T.C. Carney, J.R. Hipp, F.A. Allahdadi, High Strain Lagrangian Hydrodynamics: A Three-Dimensional SPH Code for Dynamic Material Response, Journal of Computational Physics. 109 (1993) 67–75. https://doi.org/10.1006/jcph.1993.1199.
[167] H. Tan, K.M. Pillai, Multiscale modeling of unsaturated flow in dual-scale fiber preforms of liquid composite molding III: reactive flows, Composites Part A: Applied Science and Manufacturing. 43 (2012) 29–44. https://doi.org/10.1016/j.compositesa.2011.08.008.
[168] C. Lubich, Convolution quadrature and discretized operational calculus. I, Numerische Mathematik. 52 (1988) 129–145. https://doi.org/10.1007/BF01398686.
[169] J.C. Simo, T.J.R. Hughes, Computational inelasticity, Springer, New York, 1998.
[170] J.J.E. Teuwen, Thermoplastic Composite Wind Turbine Blades - Kinetics and Processability, PhD Thesis, Technische Universiteit Delft, 2011.
[171] A.X.H. Yong, A. Aktas, D. May, A. Endruweit, S.V. Lomov, S. Advani, P. Hubert, S.G. Abaimov, D. Abliz, I. Akhatov, M.A. Ali, S. Allaoui, T. Allen, D.C. Berg, S. Bickerton, B. Caglar, P. Causse, A. Chiminelli, S. Comas-Cardona, M. Danzi, J. Dittmann, C. Dransfeld, P. Ermanni, E. Fauster, A. George, J. Gillibert, Q. Govignon, R. Graupner, V. Grishaev, A. Guilloux, M.A. Kabachi, A. Keller, K. Kind, D. Large, M. Laspalas, O.V. Lebedev, M. Lizaranzu, A.C. Long, C. López, K. Masania, V. Michaud, P. Middendorf, P. Mitschang, S. van Oosterom, R. Schubnel, N. Sharp, P. Sousa, F. Trochu, R. Umer, J. Valette, J.H. Wang, Experimental characterisation of textile compaction response: A benchmark exercise, Composites Part A: Applied Science and Manufacturing. 142 (2021) 106243. https://doi.org/10.1016/j.compositesa.2020.106243.
[172] N. Ogata, Surface Tension and Spinnability of Molten Poly-ε-capramide, BCSJ. 33 (1960) 212–216. https://doi.org/10.1246/bcsj.33.212.
[173] Water - Specific Heat vs. Temperature, Engineering ToolBox. (2004). https://www.engineeringtoolbox.com/specific-heat-capacity-water-d_660.html (accessed March 28, 2022).
[174] Water - Thermal Conductivity vs. Temperature, Engineering ToolBox. (2018). https://www.engineeringtoolbox.com/water-liquid-gas-thermal-conductivity-temperature-pressure-d_2012.html (accessed March 28, 2022).
[175] Dry Air - Thermodynamic and Physical Properties, Engineering ToolBox. (2005). https://www.engineeringtoolbox.com/dry-air-properties-d_973.html (accessed March 28, 2022).
[176] E-Glass Fibre, AZO Materials. (n.d.). https://www.azom.com/properties.aspx?ArticleID=764 (accessed March 28, 2022).
[177] J. Kestin, M. Sokolov, W.A. Wakeham, Viscosity of liquid water in the range −8 °C to 150 °C, Journal of Physical and Chemical Reference Data. 7 (1978) 941–948. https://doi.org/10.1063/1.555581.
[178] MATLAB®, The MathWorks Inc., Natick, Massachusetts, United States of America, 2018.

Mise en œuvre de composites par injection de résine thermoplastique réactive dans une préforme fibreuse

L'utilisation de systèmes réactifs permettant la synthèse in-situ du polyamide 6 (PA6) à base d'ε-caprolactame est une voie prometteuse pour la fabrication de pièces composites à matrices thermoplastiques par des procédés voie liquide (LCM) grâce à leur faible viscosité initiale. Cependant, il a été montré à certaines températures que la cristallisation du PA6 se déroule simultanément avec sa polymérisation. Dans ces conditions, la cristallisation du PA6 dépend alors de sa cinétique de polymérisation. D'une part, ces phénomènes influent sur la viscosité, la température et la répartition entre les phases non polymérisée, amorphe et cristalline du système réactif durant le procédé. D'autre part, l'écoulement est rendu complexe par la présence de deux échelles de pores dans une préforme fibreuse. Ainsi, le couplage de ces écoulements avec la cinétique de synthèse du PA6 va influencer l'homogénéité et la qualité des pièces fabriquées avec ces procédés.

De manière à comprendre et à prédire ces phénomènes et leur effet sur la qualité de fabrication des composites, un modèle prenant en compte l'influence de la réactivité de la résine sur les écoulements dans la préforme a été développé. Une simulation numérique du procédé basée sur la méthode des volumes finis (FVM) et la résolution de l'équation de Brinkman en milieu fibreux est proposée. Elle inclut un nouveau modèle de couplage de polymérisation-cristallisation du PA6 qui a été développé afin de permettre la simulation de ces phénomènes dans des géométries 3D. Les avantages de ce modèle sont présentés par comparaison avec des modèles existants. Un modèle prenant en compte l'influence de ces phénomènes sur la viscosité a aussi été élaboré en se basant sur des essais rhéologiques. Un pilote d'injection est développé afin de pouvoir comparer les résultats de la simulation du procédé d'injection de thermoplastiques réactifs avec des observations expérimentales.

Mots clés : Couplage polymérisation/cristallisation, Modélisation rhéocinétique, Ecoulement double-échelle, Ecoulement réactif anisotherme, Simulation procédé voie liquide.

Composites manufacturing by injection of reactive thermoplastic resin in a fibrous preform

In order to manufacture thermoplastic composites using liquid composite moulding processes (LCM), the use of reactive systems for in-situ synthesis of polyamide 6 (PA6) with ε caprolactam has proved itself a promising possibility due to its low initial viscosity. However, at certain temperatures, crystallization of PA6 has been shown to occur simultaneously with its polymerization. Therefore, in these conditions, crystallization of PA6 depends on its polymerization kinetics. These phenomena affect the viscosity, the temperature, and the repartition between the non-polymerized, the amorphous and the crystallized phases of the reactive system during the process. Furthermore, the dual scale of porosity present in a fibrous preform complicates description of the flow. Therefore, the coupling of these different scales with PA6 synthesis kinetics is source of variabilities in homogeneity and quality of LCM processes manufactured composites.

To understand and predict these phenomena and their effects on the quality of manufactured composites, a modelling method taking into account both the resin reactivity and the presence of the preform has been developed. A simulation method of flow in a fibrous preform using Brinkman's equation within the finite volume method (FVM) framework is proposed. At the same time, a new coupling model for polymerization and crystallization is elaborated in order to enable their simulation in 3D geometries. The advantages of this model are demonstrated comparatively to existing models. A viscosity model taking these phenomena into account is also proposed with the help of rheological tests. An experimental injection setup is developped to compare results of the process simulation of reactive thermoplastics injection in a fibrous preform to observations obtained from experimental injections.

Keywords: Polymerization/crystallization coupling, Rheokinetic modelling, Dual-scale flow, Reactive non-isothermal flow, Liquid composite moulding simulation.